Muon tracks through ATLAS

Een wetenschappelijke proeve op het gebied
van de Natuurwetenschappen, Wiskunde en Informatica.

Proefschrift

ter verkrijging van de graad van doctor
aan de Katholieke Universiteit Nijmegen,
op gezag van de Rector Magnificus prof. dr. C.W.P.M. Blom,
volgens besluit van het College van Decanen
in het openbaar te verdedigen op
vrijdag 21 maart 2003,
des namiddags om 1:30 precies,
door

Erik Joost Visser

geboren op 11 januari 1969 te Rosmalen.

Promotor: **Prof. dr. E.W. Kittel**

Manuscriptcommissie:

Prof. dr. C. Daum	Universiteit Twente
Prof. dr. ing. B. van Eijk	Universiteit Twente
Dr. A. Nisati	Istituto Nazionale di Fisica Nucleare, Sezione di Roma

ISBN 90-9016664-5

To whom will read this thesis,
(that you may learn from it, like I did)

Front cover: False colour, three-dimensional representation of the percentage of well-fitted muon tracks (as mapped on one quarter of the muon spectrometer, see also Fig. 7.36).

Back cover: Muon spectrometer, inner detector and combined performance for the charged inverse transverse momentum muon track parameter (see also Fig. 7.42) and the logo of the ATLAS detector with four tracks emanating from its centre.

Contents

Introduction

The muon was discovered in 1936[1] by Anderson and Neddermeyer. It came as a complete surprise and is one of the first particles found that is not normally present in matter on earth. Its discovery was preceded by the discovery of the positron in 1932[2], also by Anderson. Both types of particles were found in cosmic radiation, the only high-energy laboratory available at that time.

The discovery of muons was actually the result of a rigorous search for the pion, which was predicted in 1935[3] by Yukawa as the mediator of the strong interaction. However, though the discovered muons had the predicted mass, they did not have the predicted strong interaction. On the other hand, it had become clear that the newly discovered positron, the electron or the proton could not account for all phenomena found within the cosmic radiation. Thus, on theoretical grounds, the investigation was started how to account for the phenomenon that a proportion of cosmic-ray particles is highly penetrating. These particles pass through thick layers of heavy matter and lose their energy mainly through ionization. Furthermore, it had been observed that these penetrating particles had to have a mass intermediate between the masses of the proton and the electron. The unexplained phenomena were unravelled by the notion that a muon is like an electron (or positron), but without any strong interaction in matter and about two-hundred times heavier. The pion was discovered only much later, namely in 1947[4] by Powell.

There are various ways to detect muons. The technique chosen typically depends on expected momentum range, applied readout technique, required detection efficiency, limitations on cost and size, and thus on applicability. For example, the Wilson cloud chamber[5–7], used for the cosmic-ray experiments of the early days, serves well to introduce some of the general principles.

First of all, a medium is needed that signals the passage of a charged particle. Already for this purpose, a number of alternatives exist. Several of them will be encountered in the next chapters. In case of the cloud chamber, an under-cooled vapour is used as detection medium. Whenever a charged particle passes, it leaves a condensation trail showing up as a visible track.

Secondly, it is important to register the exact position coordinates of this track. There are numerous registration techniques, depending on the medium and the particular setup used. Taking a photographic image of the condensation trails makes subsequent processing possible. Other techniques use different ways to produce such

"images".

The trajectory of a charged particle is influenced by the component of a magnetic field perpendicular to its direction of flight. By using strong magnets, the particle path is bent inside the magnetic field. Typical parameters as charge and momentum can be inferred from the curvature. Subsequent chapters describe how the muon track parameters are obtained within the ATLAS sub-detectors of interest.

The ATLAS detector[8] (A Toroidal LHC ApparatuS) is one of the general-purpose detectors designed for an experiment with the LHC[9] (Large Hadron Collider) at CERN, the European Laboratory for Particle Physics. The aim of this experiment is to probe further into the fundamental forces of nature than has been currently possible. Since the LHC opens up an unexplored energy region, the general-purpose detectors also have to be able to deal with the unexpected. In order to get there, lots of research has been undertaken to prove that the detectors can cope at least with a broad variety of expected physics processes. Here, a strong emphasis lies on the physics process in which the Higgs boson decays exclusively into two pairs of muons. In the currently used theory, which is called minimal Standard Model, the Higgs boson is responsible for giving mass to elementary particles. It is presently the most important phenomenon to be investigated and, henceforth, its discovery of prime importance to the LHC experimental programme.

This thesis comprises of two parts. In the first part, issues are discussed where the physics of interest is typically dealt with on a per-track, i.e. single-muon, basis. The physics that deals with multiple muons is covered in the second part. A number of appendices give detailed insight into several important topics.

Part I consists of seven chapters. Chapter 1 is meant to introduce a historical view of particle detection techniques. Track parameters are analysed in Chapter 2. Muon detection techniques specifically used by ATLAS are examined in Chapter 3. Chapter 4 provides insight into the magnetic field configuration of ATLAS. The detection chamber configuration is described in Chapter 5. Chapter 6 delves deep into the software tools provided by the ATLAS software community. This provides the crucial knowledge needed for the application of the tools in Chapter 7. Here, the MuFit software, developed by the author of this thesis, is described and analysed. It is used to reconstruct muon tracks, on the basis of the described detection techniques, magnetic field and detection chamber configurations, to obtain muon track parameters. Chapter 7, therefore, is the heart of this thesis as it forms the documentation of the MuFit package, which is the main contribution to ATLAS by the author of this thesis. Even though mainly standard analysis methods and tools have been used for Chapters 6 and 7, the results presented therein are novel, as they describe the interplay between the virtual ATLAS detector and the tools used, e.g. the MuFit software. It has been the intention of the author to be as thorough as possible in preparing the data and subsequent results as to ensure their reproducibility.

Part II consists of four chapters. The first of them (Chapter 8) provides the background for the Standard Model. This theory is explained in Chapter 9. Modern labora-

tories do not rely on cosmic radiation only to produce interesting particle interactions, but particle colliders are used instead, such as the future LHC. Its features are summarized in Chapter 10 to provide the necessary information. This information is used in Chapter 11 by the author to calculate new discovery potentials of LHC for the Higgs boson. Here, special attention goes to the Higgs boson decay into four muons, which is the main subject of this thesis. The analysis shows that the ATLAS detector is well suited for this physics channel. Again, great effort has been undertaken by the author to prepare reproducible data, i.e. Higgs boson decay interactions, and results. These results, obtained through the use of the author's MuFit tool, are carefully compared with previous studies (performed within the ATLAS community).

Chapter 12 summarizes the conclusions that follow from the analyses presented in parts I and II. It has been the author's purpose to reserve his gritty opinions till the end and present them in this chapter, which is primarily meant for expert readers. This can also be said of the appendices. Appendix A reviews possible settings for the GEANE software tool to tune its behaviour with respect to energy loss recuperation. Appendix B provides the data flow within the MuFit software package. It also explains the method used for fitting the muon track parameters to the position coordinates. A mathematical formulation of the Standard Model is given in appendix C. In appendix D, numerous distributions are shown and analysed, from which important parameters of the Higgs boson decay are extracted. Acronyms and abbreviations, which have been introduced and used throughout the thesis, are summarized in appendix E.

The thesis ends with two summaries, namely one in English and one in Dutch.

Part I

Single muons

Chapter 1

Particle detection techniques

In order to be able to study elementary particle interactions, one has to design particle detectors. We, therefore, start with a short historical overview describing the major detection techniques used to this purpose. A rough selection of available techniques has been made to show the development as well as the advantages and disadvantages. The short overview in this chapter is loosely based on the first chapter of a book by Shutt[10]. Typical timing quantities have been taken from Table 2 of the first chapter of a book by Ferbel[11].

1.1 Photographic emulsions

The oldest detection technique uses photographic emulsions. Chemical reactions, namely the forming of silver oxide (AgO), take place in the emulsion along the trajectory of the charged particle. A visible blackening of the emulsion along the track is the result. After development, the emulsion is scanned for this blackening in a microscope.

Both advantages and disadvantages of this technique are enormous. The obvious disadvantage is that the emulsion only gets developed after some time. This means that all timing information is lost and a lot of tracks from numerous events run through the same emulsion. Furthermore, it is painstaking and time consuming, thus expensive, work to search for the microscopic blackening. Its important advantage is the precision of the technique, since the position of the track can be measured within a few micrometres. This gives the possibility to perform very specialized and/or precise measurements. For instance, nowadays emulsion is still being used in the CHORUS experiment[12] at CERN, which uses detectors taking care of timing information and additional detectors predicting the location where to search for the tracks.

1.2 Cloud chambers

A completely different technique is the Wilson cloud chamber[5–7], though, again, a trail of ionizations is left behind by charged particles during their passage through a sensitive volume. In order to obtain the sensitivity to charged particles, a volume is

filled with a mixture of non-condensible gas and vapour in equilibrium with a small amount of liquid. A sudden adiabatic drop in pressure decreases the temperature, which results in a supersaturation of the gas-vapour mixture. In this situation, condensations will form along the track of the charged particle due to the ionizations. However, these condensations are also formed wherever other cores for condensation, like gas impurities, are present. A stereographic picture is made to record the event.

This technique has the disadvantage that the chamber needs to be brought back to its initial condition after the event recording. During this dead time, which takes about one to two minutes, no further events can be recorded. Also practically no contamination may be present, since this would mean that the condensations form in wrong places. The low matter density of the gas-vapour mixture might be disadvantageous as well as this prevents the Wilson cloud chamber to act as a target to induce elementary particle reactions. A prime advantage is the fact that the ionizations stay present for quite some time, which gives ample of opportunity for the condensation drops to grow and to take a picture. Actually, the drops continue growing if the positive charge is not removed actively, e.g. by performing a voltage sweep. The drops would otherwise start drifting downwards, due to gravity, until they reach the liquid at the bottom. It is possible to lower the pressure only at the moment when external detectors, for instance counters, have registered the passage of a charged particle. In general, each photographic picture will then show an event of interest.

1.3 Bubble chambers

The operating principles of the bubble chamber can be seen almost as inverse to the cloud chamber. In 1952, Glaser[13–15] suggested the application of a superheated liquid as a particle detector. Here, a liquid is brought above its boiling point by a sudden decrease in pressure. Upon passage of the charged particle characteristic bubbles will be formed at the ionizations[(1)]. Again, a stereographic picture is made to record the event. Afterwards, the pressure is raised in order to get rid of the bubbles and to prepare for the next superheating and recording cycle.

A difficulty is that the liquid should not be boiling before the picture is taken. However, rough surfaces are always present at the faces of the volume and serve as/cause boiling centres. This means that only a very short time window is available in which the event has to take place. Thus, the bubble chamber is sensitive only for a limited amount of time, which is a few milliseconds. If the short sensitive time causes no problem, then a nice advantage is that it does not matter much which material is being used for construction. This opens the possibility to build really big chambers[(2)] that can fully contain the elementary particle reaction, i.e. the event.

[(1)] This process can be compared very well to what happens when someone stirs liquid which has been heated well above its boiling point in a microwave oven; it suddenly starts to boil fiercely (mainly at the rough surface of the spoon).

[(2)] One of the most important big chambers was Gargamelle[16] at CERN, which has led to major physics discoveries, one of which is the discovery of neutral currents[17] in 1973.

1.4 Spark chambers

Another often used detection technique is the spark chamber[18–20]. Here, the principle of detection is based on a spark (discharge) between two electrodes. Basically, the chamber consists of a number of parallel plate electrodes with a gas in between. The ionizations along the trail of the highly energetic charged particle cause the creation of positive ions and free electrons. A discharge occurs when applying a large potential difference between the plates because of a multiplication of the ionizations by the potential field. The visible effect is a spark of which a stereographic picture can be taken. Two fully different types of operation are available for the spark chamber, each with its specific merits and demerits.

If the electric field is continuously present, then every passing charged particle will cause a discharge. This makes it rather impossible to select any particular type of event or particle beforehand. Furthermore, spontaneous discharges can occur, but should be avoided, because the operating voltage of 5 kV/mm is close to the electric breakdown of the gas. A big advantage is that in this mode of operation no external detectors are needed to signal the passage of a charged particle. The chamber itself detects the particle and can as such be used as trigger for other systems. We shall see in Sect. 3.2 that the ATLAS detector uses this technique in a slightly adapted form.

To explain this, we need to study the multiplication stage somewhat better[21]. With a sufficiently low electric field, only further ionization by the free electrons will occur. This results in an avalanche towards the positively charged electrode, i.e. the anode. The chamber is said to work in avalanche or proportional mode. The charge of the electrons is collected within a few nanoseconds, but the charge of the ions takes a factor thousand longer to be collected by the cathode. Though, the positive charge can also be removed using Freons and a gas recycling system. When the electric field has passed a certain threshold, which is gas dependent, then there will also be secondary processes, like photon emission, causing the generation of additional avalanches. This process is additional to and slower than the primary avalanche since a column of ions has been created to link the anode and cathode. The chamber is said to work in streamer or Geiger mode. The total charge is collected within a microsecond. Increasing the electric field further results in a breakdown because of space charge deformation of the electric field. The chamber[(3)] is said to work in discharge or spark mode.

The other possibility is to apply the electric field only when an external reference system has signalled the passage of an interesting particle. This is possible, since the potential difference can be generated extremely fast. Since the high-voltage pulse lasts for a number of nanoseconds, only short streamer discharges develop, typically of a few millimetres. Compared to the bubble chamber, the main benefit is that the short time window of sensitivity can always be made to overlap with the event. The sensitivity is of the order of a microsecond in which the event takes place, while the sensitivity in case of a bubble chamber lasts for about a millisecond in which more

[(3)] Proportional counters and Geiger counters, which also detect the passing charged particle themselves, had been developed already before the spark chambers. The ATLAS detector utilizes the avalanche mode for muon track measurement.

events can overlap. This superb time resolution has the consequence that the events become very clean, i.e. without a background superimposed. The large build-up of charge makes the chamber insensitive for almost one second after the event, however.

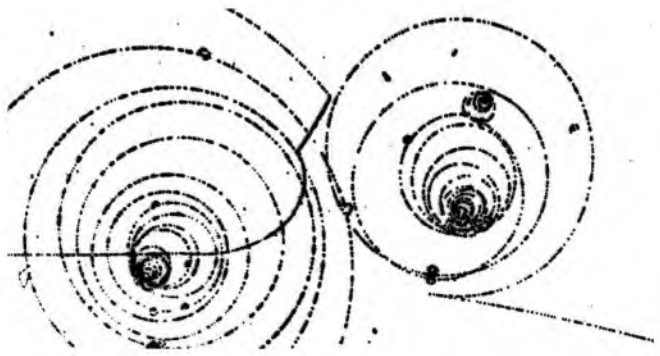

Figure 1.1: Fragment of bubble chamber photo showing several charged tracks.

A disadvantage of the techniques described in Sect. 1.1 to Sect. 1.3 above is the need to use photographic recording material, of which an example can be found in Fig. 1.1. The films have to be developed, scanned, and measured, before the track information is available in digital form. Only then are the events available for analysis. If in a certain experiment millions of pictures have been taken, then this signifies that a lot of time and work is needed to get useful information out. In order to obtain the information cost effectively, a fully automated recording of the events is preferred as soon as more than just a few events are expected. The spark chamber technique makes this possible, since the exact conductor at which the discharge current pulse has occurred can be pinpointed by properly segmenting the plate electrodes. This automatically gives the location of the track, which then can be processed further in a digital manner. As we shall see further on, precisely this technique is used in modern-day detection chambers, although in a number of variations.

1.5 Scintillation counters

In the previous section we saw that two electrodes with an electric field between them can serve as a counter. Another technique which is often used as trigger is the scintillation counter[22]. Here, the principle of operation is based on the excitation of atoms of the scintillating medium. Light is emitted at the end of the scintillation process, either directly or through the use of wavelength shifters. In inorganic crystals, the excitation is achieved by freeing electrons and (electron) holes which then will move through the crystal until they reach an activator. This activator is actually an impurity in the crystal lattice with which the medium has been doped. The activator goes into an excited state, with higher energy levels, during the recombination and falls back to its ground state while emitting light. This scintillation process needs quite a period

of time to complete, namely in the order of a microsecond[23], which is temperature dependent. On the other hand, in organic scintillators the time to fall back into the ground state is of the order of a few nanoseconds only, because molecular levels are excited here. To be more precise: most of the excitation energy is transformed into vibrations and only a small fraction into UV-radiation. However, to detect the light in these scintillators, the radiation needs to be transformed into visible light afterwards using photoluminescence in wavelength shifting solutes, i.e. the so-called wavelength shifters. An advantage is that one can produce (plastic) scintillators in any arbitrary form.

Quite often the scintillator itself can take care of the light transportation because of its transparency. In this case a photomultiplier tube[11], coupled to the end of a slab of scintillation material, can be used to transform the photons into an electronic signal. Actually, the technique of scintillation is much older than the photomultiplier, but at that time it was only possible to detect the light flashes by naked eye. Consequently, the Geiger-Müller tube[(4)], which is based on an electric discharge, was preferentially used to detect the passage of a charged particle.

Many of the techniques described above have been developed further. So, in the detectors that are currently used, those ideas come back, though in slightly adapted forms. One subject that has not been addressed yet is the detection of non-charged elementary particles, i.e. electrically neutral particles. These particles can not be measured directly, since they are non-ionizing, but their energy can be absorbed and, therefore, measured by calorimeters. This thesis does not deal any further with either neutral particles or calorimetry.

[(4)] A counter operated in Geiger mode.

Chapter 2

Track Parameters

Apart from the need to identify the particle, it is also necessary to know the so-called track parameters. This means that every point on the particle trajectory has to be known, together with the corresponding momentum. When the particle moves in vacuum through a uniform static magnetic field, with magnitude $|\vec{B}|$, then a solution to the Maxwell equations[24] can easily be obtained:

$$\vec{r}(t) = \vec{r}_0 + v_{\parallel} t\hat{e}_{\parallel} + a(\hat{e}_{\perp,1}\sin\omega_B t + \hat{e}_{\perp,2}\cos\omega_B t) \quad .$$

This expression represents a helix with starting point at location $\vec{r}_0$ and radius a. Furthermore, $\hat{e}_{\parallel}$ denotes the unit vector parallel to the direction of the magnetic field $\vec{B}$, and $\hat{e}_{\perp,1}, \hat{e}_{\perp,2}$ are the two unit vectors perpendicular to it. The initial velocity component along the magnetic field is given by $v_{\parallel}$ and can be obtained from the relation $\vec{p}(t) = \gamma m\vec{v}(t)$. Alternatively, the momentum follows from $\vec{v}(t) = v_{\parallel}\hat{e}_{\parallel} + \omega_B a(\hat{e}_{\perp,1}\cos\omega_B t - \hat{e}_{\perp,2}\sin\omega_B t)$.

The important parameters for physics are ω_B, the gyration or precession frequency, and a, the radius of the helix. By definition: $\omega_B = e|\vec{B}|/\gamma mc = ec|\vec{B}|/E$ with E the conserved energy of the particle. If the energy, or velocity, of the charged particle is low, then the possibility exists that it will start to spiral in the magnetic field. This makes it almost impossible or at least very hard to detect the particle. To the contrary, a highly energetic particle will move along a small part of the arc of a helix with large radius a. For very high energies, however, this can even go as far as that the particle seems to move along a straight line, despite the bending power of the magnetic field. The radius holds a direct relation to this and is given by the important formula: $e|\vec{B}|a = cp_{\perp}$. Here, $p_{\perp}$ denotes the amount of momentum of the particle perpendicular to the magnetic field. This quantity already determines to a large extent the movement of the particle and does as such provide useful information. The notation p_{T} is used in the remainder of this thesis, to denote the transverse momentum, instead of using the academic form ($p_{\perp}$). As we will see in the next sections, there is more information available about the track which helps in its final definition/specification.

2.1 Detectable particles

Since the early days of cosmic radiation research, an enormous spectrum of elementary particles has been discovered. They all have certain properties, which allow us to identify them uniquely. Among these properties are: mass, charge and lifetime[(1)]. Many particles decay practically immediately, i.e. within about 10^{-23} seconds after their creation, by means of the so-called strong interaction. One normally refers to those particles as resonances. Therefore, it is not useful to speak of the lifetime of the particle; the width of the resonance[(2)] is being used instead. Most of the other particles decay by means of the weak interaction. Here, no typical lifetime can be given since it varies from about 10^{-17} to 10^{-8} seconds, and in case of the free neutron even 10^3 seconds. Only very few elementary particles are stable[(3)]. Table 2.1 gives some properties[25] of a very limited number of particles. The measurement inaccuracy, or quoted error, on every number is much smaller than the last decimal given, except for the lifetimes of the neutron and neutral pion, which are more precisely presented as $\tau_n = 886.7 \pm 1.9$ s and $\tau_{\pi^0} = 8.4 \pm 0.6 \times 10^{-17}$ s respectively.

particle name	symbol	charge Q (in units of e)	lifetime τ (in s)	mass m (in MeV/c^2)
electron	e^-	-1	stable	0.511
proton	p	$+1$	stable	938.3
neutron	n	0	887	939.6
photon	γ	0	stable	0.0
muon	$\mu^\pm$	± 1	$2.2 \cdot 10^{-6}$	105.7
pion(s)	π^0	0	$8.4 \cdot 10^{-17}$	135.0
	$\pi^\pm$	± 1	$2.6 \cdot 10^{-8}$	139.6
kaon(s)	$K^\pm$	± 1	$1.2 \cdot 10^{-8}$	493.7
	K_L	0	$5.2 \cdot 10^{-8}$	497.7
	K_S	0	$8.9 \cdot 10^{-11}$	497.7

Table 2.1: Some properties of a limited number of elementary particles.

It is common knowledge that atoms consist of protons, neutrons and electrons, while electromagnetic radiation, such as light, consists of photons. Furthermore, every particle has an accompanying anti-particle with exactly the same lifetime and mass but opposite charge. This means that certain neutral particles can be identical to their anti-particles.

(1) For instance, the lifetime is needed for distinction in the K_L-K_S system where the mass difference is minimal. It is also important to note that the average or mean lifetime is fundamentally different from the half-life of a sample of radioactive material, though the values differ by the constant factor $\ln(2)$, for particles at rest.

(2) Typical widths are $\Gamma = 10$-100 MeV, with a corresponding lifetime, according to $\Gamma = \hbar/\tau$, of order 10^{-23} seconds.

(3) Stability denotes a measured, average lifetime larger than the current age of the universe.

2.1.1 Interaction with matter

In reality, the particle will never move in complete vacuum; there will always be some matter present. That is why it is useful to look further into possible interactions of charged particles with various media. All matter consists of more or less regularly placed atomic nuclei with bound and even free electrons circling around them. Although the material looks homogeneous and electrically neutral on a macroscopic scale, this definitely is not true when looked at on a microscopic scale. The charged particle will experience the material mostly as empty space during its passage through it. The presence of positively charged nuclei and negatively charged electrons is mainly noticed by the prevalence of Coulomb forces. Different elementary particles undergo the influence of these forces in matter differently. We will not go into detail on all of these processes and on which elementary particles exactly participate in them, but concentrate on the two major processes concerning muons. Full details can be found in texts by Sauli[21] and by Jackson[24].

2.1.2 (Ionization) energy loss

Firstly, we discuss the interaction of muons with the electrons present in the material. The Coulomb force has a repellent effect between μ^- and e^-, while it has an attractive effect between μ^+ and e^-. This means that the muon and (bound) electron push each other away or draw together at close proximity. Since the muon is many times more massive than the electron, its direction practically is not changed by this interaction. The electron, on the contrary, can change its trajectory completely .

Several things can happen, depending on the energy or momentum transfer. Bound electrons can change their orbit thus leading to an excited state of the atom, or they can be knocked out completely thus leaving the atom ionized. The maximum energy transfer can be computed from relativistic kinematics and is given by the expression: $E_M = 2m_e c^2 \gamma^2 \beta^2$, where m_e denotes the electron mass, c the speed of light, β the velocity of the incident particle divided by c, and $\gamma = 1/\sqrt{1-\beta^2}$. The expression is only valid for $\gamma \lesssim 10$, corresponding to a maximum energy transfer of 100 MeV for a muon with momentum 1 GeV/c. This amount of energy will in general not be transfered because of its high improbability, i.e. the probability falls off exponentially for increasing energy transfers. Still, an energy transfer higher than the minimum ionizing energy of typically 20 eV is extremely likely. The liberated electrons are called δ-rays when they have acquired an energy of a few keV or more, of course with a maximum of E_M. As we have seen in the previous chapter, the detection of charged particles is based on this kind of interaction, namely the ionization of atoms. Figure 2.1 shows a qualitative example(4) of the excitation or ionization probability by 100 keV electrons in water.

(4)To get a more quantitative feeling, it would be good to refer to the GEANT manual[26] which explains how these processes can be simulated. For now it suffices to say that the chance for an atom to get into an excited state, rather than being ionized, increases at increasingly larger distances to the passing charged particle, up to a certain maximum distance.

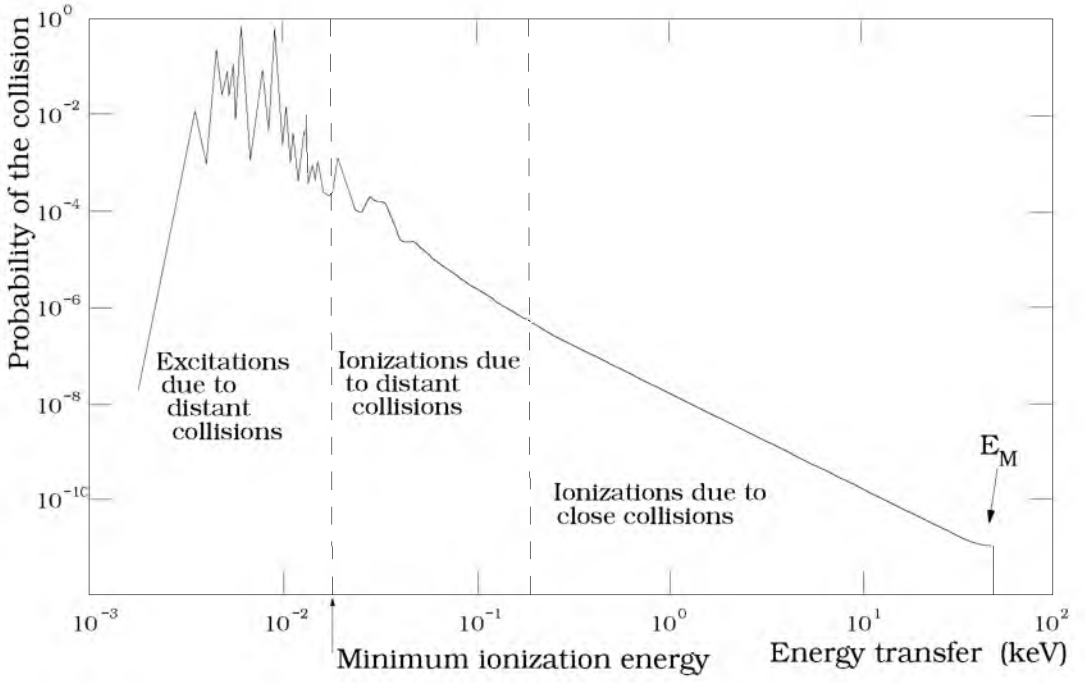

Figure 2.1: Relative probability of excitations and ionizations due to 100 keV *electrons in water as a function of the energy transfer (in* keV*).*

Although the initial track direction of the muon does not change much, the muon still can transfer a substantial amount of energy to the electron. The net effect of this interaction is called energy loss, which effectively means that the velocity of the muon decreases. A catastrophic energy loss inside the material will have the consequence that the track parameters change considerably.

2.1.3 (Coulomb) multiple scattering

Secondly, we discuss the interaction of muons with the atomic nuclei present in the material. Now the μ^- experiences an attractive Coulomb force, and the μ^+ a repellent one. The atomic nucleus is a massive cluster of protons and neutrons completely immobile compared to the fast moving muon. The influence of the passing muon on the nucleus, therefore, is almost nil: the energy transfer is small as well. Instead, the muon itself will be pushed, or pulled respectively, from its trajectory. So, after each scattering the track direction of the muon will have changed. The muon encounters not one but many nuclei during its traversal through the material. This results in successive scatters. The consequence of this multiple scattering process is not only a change of the track direction but also a shift of the track compared to the location of the original helix.

The change in track parameters depends on the density of the medium. Air and other gases can be considered as vacuum. Experience has shown that the theoretical

helix still represents a good approximation for such low matter densities. Even for material of high density, the net angular deflection due to multiple scattering is not large, unless the amount of material traversed becomes really huge. However, in any material sometimes large angle scattering does occur, but this should be attributed to rare single scatters. It has the consequence that the typical Gaussian statistical distribution of the multiple scattering process exhibits additional tails due to these single scatters.

2.2 Decay in flight

Energy loss (through ionization) and multiple scattering can be seen as examples of rather continuous processes which the muon experiences when interacting with matter. An example of a discrete process is the decay of a muon. The chance for this to happen inside the detector is highly unlikely for fast moving muons. A muon with a momentum of 1.5 GeV/c has an apparent average lifetime of $\tau/\sqrt{1-\beta^2} = 0.03$ ms (using $\beta = |\vec{p}|c/E$). On average, it will have travelled a distance[27] of slightly more than 9 km through vacuum during this time. Using this as the minimum detection energy, together with an exponential decay distribution[(5)], one can calculate that at most 0.2 percent of the muons have a chance to decay inside the ATLAS spectrometer, which has a maximum span of $d = 20$ m. It should be reminded that this calculation gives the worst case scenario, i.e. in reality the percentage is lower[(6)].

[(5)]The expressions $f(t,\tau) = \exp(-t/\gamma\tau)/\gamma\tau$, with $\gamma\tau$ the apparent lifetime, and $\int_0^{d/v} f(t,\tau)\mathrm{d}t = 1 - \exp(-dm/p\tau)$, with $v = p/\gamma m$, give the probability that an individual muon will decay[28] at time $t = d/v$ while travelling a distance d.

[(6)]Substituting more common values like, e.g. $d = 15$ m and $p = 40$ GeV/c gives less than a 0.01 percent decay chance.

Chapter 3

Spectrometer detection techniques

Several techniques exist to detect (charged) muons. In the following, it will be indicated which choices have been made for the ATLAS detector and what determined these particular choices. Since the detector has to operate in an unexplored energy range, the necessity arises to build in as much safety as possible. Therefore, the first decision was to build a muon detection system that can work in a stand-alone fashion, i.e. independently from the rest of the ATLAS detector. Furthermore, it has been decided to split the system in two manners.

Firstly, precision chambers are used, for an accurate position measurement of the track, together with fast (trigger) chambers, to signal the passage of interesting muons. These trigger chambers also help the precision chambers with the measurement of the track position.

Secondly, the flux of ionizing particles is not the same everywhere. The largest contribution to this flux does not come from muons but from background. This calls for the use of different technologies in specific parts of the spectrometer. Chambers positioned in high flux regions of the detector have a finer segmentation, and thus a higher cost. The change in technology applies to both precision and trigger chambers. As a result of this a total of four different types of chambers are used in ATLAS.

3.1 Charge drift

Before going into a detailed study of the four technologies, it is necessary to explain how the ionizations, caused by the passage of the charged particles, can be measured electronically. A good, theoretical description can be found in texts by Tolsma[29] and by Sauli[21]. Only the most important points will be reviewed here.

We concentrate on gases for which the number of ionizations is 5 to 50 per centimetre, which corresponds to mixtures with average atomic numbers of 2 to 30. These primary ionizations are fully localized near the track; the initial direction of their movement is completely random due to multiple scattering. The ionizations are not distributed uniformly along the track but appear as clusters. The size of the cluster depends on the energy of the primary emitted electron: it is one when the energy is below

the ionization potential of the gas; it is larger than one when the energy of the primary electron is big enough to ionize additional atoms. The clusters are also distributed randomly along the track.

Now it is necessary to pick up a signal. For this purpose, a potential difference is applied over the gas volume. The ionization products move due to the resultant electric field. The positively charged ions move along the electric field lines to the cathode, while the electrons are accelerated in the direction of the anode. Figs. 3.1(a), 3.1(b), and 3.1(c) below show electric field contours and charge drift lines for three common configurations of the electrodes. The influence of a magnetic field is shown in the case of the drift tube, where the bending of the drift lines is clearly visible. The bending automatically has the consequence that the path has become longer, thus resulting in a larger drift time. This effect is quantified by the angle (Lorentz angle) through which the drift lines are bent towards the anode.

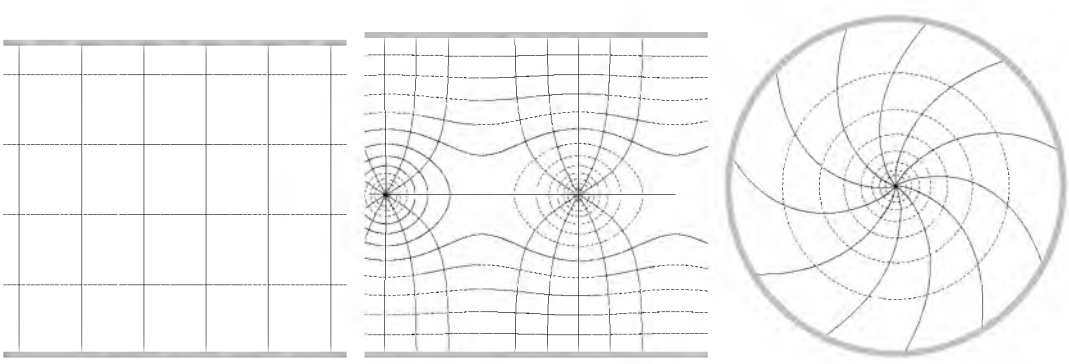

(a) Two parallel plate electrodes, the upper one at $+8.9$ kV and the lower one at earth potential.

(b) Two parallel plate electrodes at earth potential and sense wires at $+3.1$ kV.

(c) A drift tube, with the tube wall at earth potential and the sense wire at $+3.3$ kV.

Figure 3.1: Electric field contours or equipotential lines (shown as dashed lines) and charge drift lines (shown as full lines) for a number of different electrode configurations (shown as grey objects).

Due to the acceleration caused by the electric field, the electrons obtain more than enough momentum to escape from the ion. However, it is not necessarily so that their velocity is fully directed along the field lines. When the energy supplied by the field is sufficient, the electrons will cause secondary ionizations, or even a completely new track of ionizations in case of a δ-ray production. So, diffusion will occur, which results in a sideways growth of the cluster with additional ions and electrons. All these additional electrons are also accelerated towards the anode. The energy obtained through the acceleration in the electric field is used for, again, further ionizations of gas atoms. Hereby, an avalanche of electrons can be created, or even a discharge (spark) to the anode. The whole process described above develops extremely fast, in a fraction of

a nanosecond, and gives rise to an electric signal (current) of typically 10^5 electrons[(1)]. This number is usually called the gas amplification factor, or simply the gain.

At the same time, the ions move towards the cathode, but much slower because of their mass. So, this movement does not result in the creation of an avalanche (to the cathode). Instead, a slowly moving, positively charged cloud is formed. It takes a few microseconds before the ion cloud reaches the cathode. During this time, the properties of the drift cell are influenced by the space charge as caused by the cloud which decelerates the ions. Luckily, it could be shown by Tolsma[29] that the influence is not large. The long signal tail measured at the anode can be attributed to the induction caused by the moving positively charged ions.

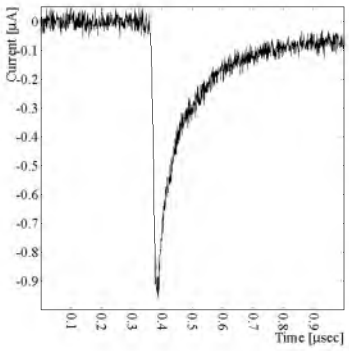

Figure 3.2: Pulse shape, as seen by the preamplifier, of a single cluster consisting of a very large number (> 200) of electrons.

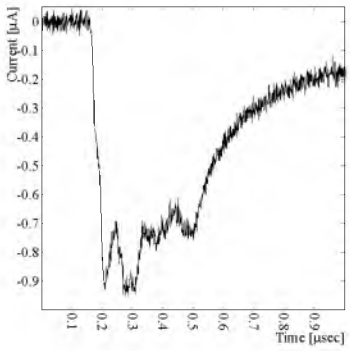

Figure 3.3: Possible pulse shape, as seen by the preamplifier, of a superposition of clusters coming from a 170 GeV muon track.

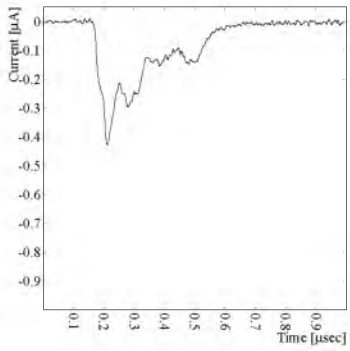

Figure 3.4: Example of a signal, as seen by the discriminator, after processing by specialized electronics performing tail cancellation.

In the end, a typical signal resulting from one cluster is shown in Fig. 3.2. However, since many clusters have been formed, one has to add up their individual contributions in order to get the final signal shape. An example is shown in Fig. 3.3. The apparent typical signal time is a few hundred nanoseconds[(2)]. Normally, special electronics are needed to transform the capricious signal into a smooth one. An example is shown in Fig. 3.4 where we can see that it is possible to decrease the signal time, using specially designed electronics. It would go too far to fully describe the electronics, so the idea is given instead.

At some point, all charge carried by electrons and ions has reached either anode or cathode. During that time, the drifting charge has induced currents in the electrodes, which are either wires and/or strips (as plate electrodes are usually segmented

[(1)] 10^5 electrons$\times 1.6 \cdot 10^{-19}$ C/electron$\approx$ 16 fC.

[(2)] This signal time is smaller than the time needed for the ions to reach the cathode because the closer the ions get to the cathode, which is at earth potential, the slower they move and thus the less their induction.

in strips). These currents are picked up and fed into a preamplifier, where the amplification ensures the possibility to really measure the signal/charge/current. Electronic noise, which is a statistical process due to the motion of electrons in the conducting medium and a function of temperature, is always present and amplified as well. Therefore, a discriminator is used to compare the incoming signal with a certain threshold. If the signal stays below this minimum then it will be ascribed to noise. On the other hand, a possibly interesting event has occurred as soon as the signal exceeds the threshold. It would now be possible to sample the shape of the current, or to clock the moment at which the threshold was exceeded, but there are many other measurement methods which give useful information about the signal.

Detailed simulation studies have been performed to understand this signal development. The ATLAS simulation and reconstruction software does not use these simulations, but uses parametrizations[3], instead. Hereby, several independent steps are, and can be, combined into one parametrization describing the process.

One important process which adds to the signal has not been mentioned yet. Not only the electrons contribute to the diffusion of the clusters, but also the photons which have been produced during the avalanche. Their subsequent avalanches, however, are not necessarily located in close proximity of the original avalanche. In order to prevent the signal from diffusing too much, one normally adds a quenching component to the gas. This quencher has many vibrational and rotational degrees of freedom, which absorb the photons and thus prevent them from traveling too far.

In this paragraph, the most important demands[30] regarding the detection system are summarized. Two fundamental limits cannot be circumvented, namely diffusion, which means that clusters can yield different drift times even when circumstances do not differ, and ionization, which can yield strongly varying cluster sizes so that the threshold exceeding cluster does not always come from the nearest ionization. The operating point will be chosen such that the most accurate position measurement is obtained. As we have seen, the potential difference determines how fast electrons and ions drift towards the anode and cathode, respectively. It also influences the gain, which needs to be sufficiently high, in order to be able to discriminate a signal from noise. Furthermore, it governs the operating regime, i.e. the system operation in proportional, streamer or even discharge mode. Close to the wire, the electric field, resulting from the potential difference, can be extremely dense, which can cause gas breakdown. The gain is highly affected by the choice of gas mixture, where a high fraction of a noble gas is favourable. However, a fraction of quencher is needed to prevent spurious avalanches. Furthermore, a low minimum ionization energy is helpful for the creation of a large number of clusters. The gas also needs to be non-flammable to prevent a possible explosion. Addition of electronegative gases helps to clean up the ions and allows for higher gain operation. A magnetic field is necessary to obtain the track parameters, but increases the drift time. On the other hand, addition of

[3]This is necessary for speed of execution; simulations of the models would be too much time consuming, while a parametrization of a model only involves a few additions and multiplications.

carbon dioxide helps in reducing the resultant Lorentz angle. The gain influences the choice of threshold for the discriminator, which in turn influences the track resolution. A temperature below room temperature would be useful but not practical to achieve, but a constant temperature is important so that the resolution does not degrade. Applying an overpressure improves the resolution because cluster diffusion and fluctuation is reduced as more ionizations occur along the track. The mechanical system needs to withstand that pressure, though. Finally, in regions of high flux, aging should not occur too soon, so that the system can remain in operation for a fair number of years. This aging is actually defined as the process whereby a polymeric coating is deposited on the electrodes due to chemical radicals that are formed by the ionization process. It has the effect that the electrodes will function less and less as the years go by, due to the increasing resistance of the electrode surfaces. The polymers also cause an increased release of secondary electrons thus leading to more secondary ionizations and spurious avalanches.

It is clear that a lot of requirements restrict possible choices. Some requirements are more or less conflicting, so in the end concessions had to be made.

3.2 Resistive Plate Chamber (RPC)

The first detection technique used for the spectrometer that we shall look at is the RPC[31–33]. It is a good example of the improved spark chamber technique and also the easiest to describe. In ATLAS[34], the RPCs cover a surface of about 3650 m^2 with a total of 355,000 active channels. Figure 3.5 shows the schematic setup of this detection technique.

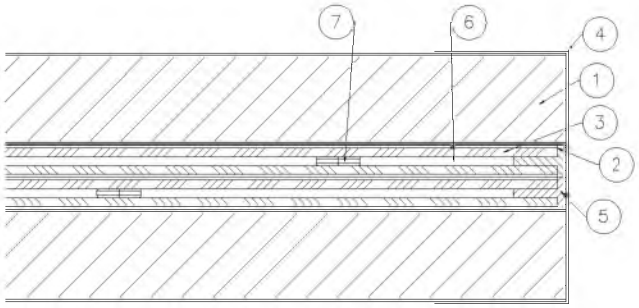

Figure 3.5: Schematic cross section of a double gas gap RPC. 1: polystyrene structures; 2. insulating polyethylene; 3. Bakelite™; 4. aluminium sheets and support; 5. polycarbonate frame; 6. gas gap; 7. polycarbonate spacers.

The basic principle is a uniform electric field applied between two plate electrodes, see Fig. 3.1(a). The ionizations, caused by the passage of a muon, give rise to the occurrence of an avalanche. Streamers should not occur, since they spoil the time resolution, but cannot be banned completely because of the small distance (2 mm) and high potential difference (8.9 kV) between the electrodes. The sensitive part of

the cell is the gas volume, which has variable areal dimensions up to a maximum of 108×249 cm^2. A prototype exists with dimensions 50×50 cm^2. The gas mixture used is 97%/3% tetrafluoroethane ($C_2H_2F_4$)/iso-butane (C_4H_{10}). The chamber does not have a very high gain, as the gain is highly distance dependent, i.e. the maximum gain exists for a cluster at 2 mm distance from the anode. However, the charge produced (0.3 pC) is enough for a signal to be picked up by the preamplifier. Furthermore, the gas has the property that it absorbs UV-radiation, thus making sure that the emitted photons stay localized.

The electrodes are two thin layers of conducting graphite painted on Bakelite™ material, which have the same dimensions as the gas volume. This material has a very high resistivity (ρ) in the order of 10^{10} Ω cm. The high resistivity ensures that the signal charge will not leak away sideways. So, both discharge and signal stay very much localized near the original track. This high resistivity, in combination with the highly quenching gas, prevents the creation of sparks, which occurs when the gas gap is made smaller than 2 mm.

A polycarbonate frame makes sure that the gas volume is properly sealed off. With the help of additional spacers it also takes care of keeping the resistive plates at a fixed distance of 2 mm. The high voltage is applied on the graphite paint. These layers are protected by a film of insulating PET (polyethylene-terephthalate). Copper strips are used to measure the signal. These strips are glued on the cell and collect the charge. Placing the strips orthogonal to each other in the two planes, the possibility of a two-coordinate[4] read-out system is achieved. Even though the avalanche takes place mostly within the 3-4 cm width of the strips, it still has advantages to read out the neighbouring strips as well. The resulting signals can then be used for a charge centre-of-gravity calculation. This method leads to a position determination which is more accurate than the strip width.

The chamber described above has a rate capability of 1 kHz/cm^2. It is possible to increase this rate by decreasing the total charge of the signal. To achieve this, one would have to choose either a different gas with a lower multiplication factor (gain), or resistive plates with a lower resistance. In conclusion, the important parameters of the RPC are:

signal charge	0.3	pC
rate	1	kHz/cm^2
time resolution	1.5	ns
signal duration	< 20	ns
position resolution	1	cm

Another option is a so-called double-gap RPC, as shown in Fig. 3.5. This is actually the option used for the ATLAS RPCs. It has the advantage of an optimized time resolution since non-Gaussian tails disappear, when combining the time measurements of both gaps. Furthermore, the efficiency of 97% of the single gap RPC is enlarged to

[4] It is three dimensional actually since the position of the gas volume is well known.

practically 100% for the double gap RPC due to the fact that the dead space caused by the polycarbonate frame and spacers is reduced. A further reduction comes from the staggering of the chambers, as shown in Fig. 3.6, resulting in a minimal dead space overlap.

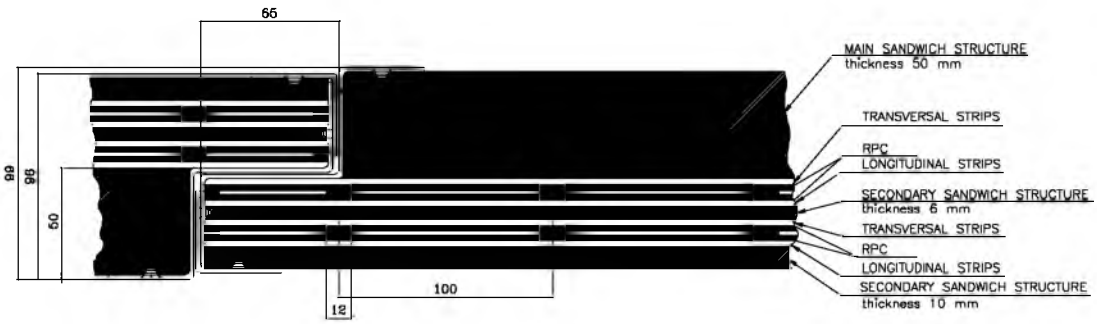

Figure 3.6: Cross section showing two staggered double-gap RPCs.

The space resolution of a full ATLAS RPC chamber becomes as good as 6.5 mm, see Fig. 3.7. Structures of 50 mm and 10 mm thick polystyrene, sandwiched between 0.5 mm thick aluminium sheets, provide the mechanical stability of the staggered chambers.

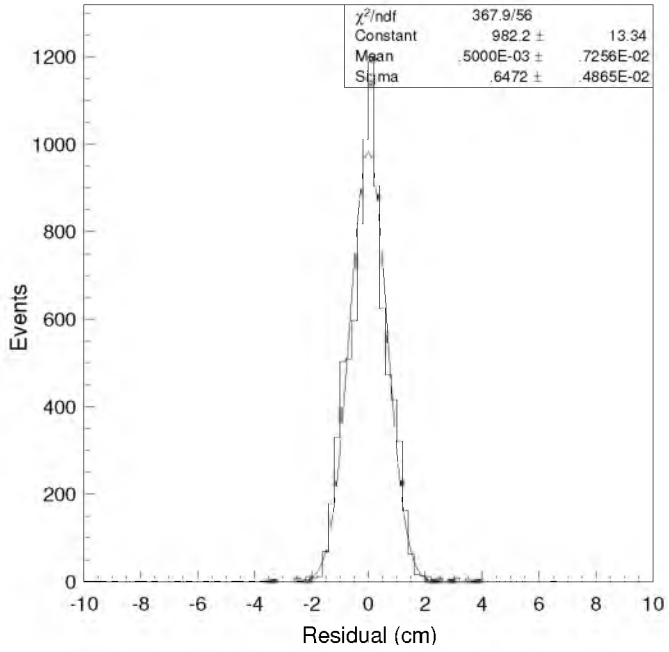

Figure 3.7: Position resolution obtained from a double-gap RPCs.

3.3 Thin Gap Chamber (TGC)

The TGC[35, 36] is a chamber technology that uses high amplification factors, typically 10^6, but which still operates in proportional mode. In ATLAS[34], the TGCs cover a surface of about 2900 m^2 with a total of 440,000 active channels. Figure 3.8 shows the schematic setup of this detection technique.

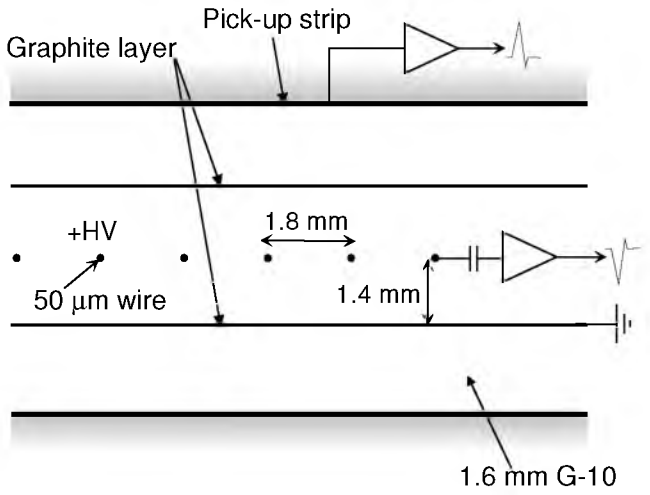

Figure 3.8: Schematic cross section of a TGC, showing its components and a read-out strip orthogonal to the wires.

The basis here are again two plate electrodes, though they both act as cathodes this time. These electrodes are made of 1.6 mm thick doubly printed G10 (printed circuit board) on which a layer of graphite has been painted. In order to obtain enough mechanical stability, a 5 mm thick support of low-cost paper honeycomb is used, with an additional layer of 500 μm thick G10. Facing the gas volume, a copper cladding is used to electrically earth the chamber, while patterns of read-out strips or pads are etched into the copper facing the honeycombs. Gold plated tungsten wires of 50 μm diameter provide the anode. An anode "plane" is made by placing the wires in precise 1.8 mm intervals, between the two plate cathodes. The resulting drift field has already been sketched in Fig. 3.1(b). It is obtained by the application of a 3.1 kV potential difference between anode and cathode. The high gain results from the strong field and gives rise to a fast signal development. Since the gas gap is small, i.e. the distance between the cathodes is only 2.8 mm, it ensures a restricted drift time for the ions. Together, these advantages explain the very good time resolution of the TGC. Normally, the gas mixture 55%/45% carbon dioxide (CO_2)/n-pentane (n-C_5H_{12}) is used because of the elaborate experience[(5)] gained with it. This gas mixture is highly quenching and provides a good signal without causing streamers in its saturated mode. It has the disadvantage that it is highly flammable and, therefore, requires adequate

[(5)]Mainly with the OPAL detector[37] at CERN.

safety measures. Using another gas, 80%/20% CF_4/iso-butane (C_4H_{10}) would reduce the flammability and improve the timing resolution. However, the final choice has not been made for this gas, since it is electronegative and thus reduces the detection efficiency.

As with the RPCs, the sensitive area of the TGC varies from 39×104 cm^2 to 167×216 cm^2. Prototypes of 10×10 cm^2 as well as 1.6×1.2 m^2 do exist. In principle, the anode wires can be read out to obtain a very precise position measurement. However, this will not be done with the TGCs used in ATLAS, since we are primarily interested in the trigger function of these chambers. So, the copper strips and the wires ganged in groups of 4 to 20 wires are read out and this coarse position measurement helps the first-level trigger in getting a better momentum definition. The important parameters of the TGC are summarized in the table given below:

signal charge	0.5	pC	
rate	20	kHz/cm^2	
time resolution	1.3	ns	
signal duration	< 25	ns	
position resolution	$2-10$	mm	depending on the number of wires grouped together
	$4-14$	mm	depending on the strip width (for second coordinates)

Furthermore, it needs to be noted that the signal is quite independent of external influences; the rate (up to 20 kHz/cm^2), the angle of incidence, and the externally applied magnetic field have no large effect. The efficiency of the chamber is 100%, except for the area taken up by the wire support, which accounts for a dead space of about 3-4%. This can be improved by using double or triple chambers, as has been done for the ATLAS TGCs, see Fig. 3.9.

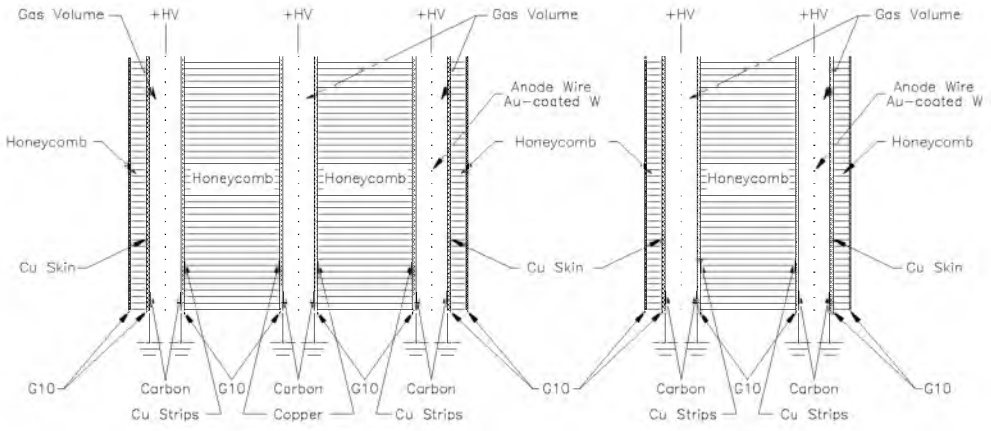

Figure 3.9: Cross section showing a triplet and a doublet TGC. The scale of the gas gap is highly exaggerated and the thickness of the honeycomb between two TGCs is 20 mm.

The prime task of the two types of trigger chambers described above is the determination of the time at which the muon passes. This time stamp is needed by the precision chambers to identify the correct event corresponding to the measured muon track. Later on it will be explained why a coarse position measurement is needed in addition.

Since the fast detection techniques have been described, we can now turn to the precision techniques for an accurate position measurement. Actually, from the previous table one derives that the TGC combines position and time measurement.

3.4 Cathode Strip Chamber (CSC)

The CSC[38] is a chamber technology that combines a high position accuracy with a very short ion drift time. These properties are useful for position measurement chambers which have to operate in high flux regions. This is the case for ATLAS, where high amounts of ionizing radiation are expected close to the beam pipe. The choice has been made to use the CSCs in that area, instead of the standard position measurement chambers (MDTs), which can only cope with a certain flux of ionizing particles. This standard measurement technique will be described in the next section. The transition between the two techniques is chosen such that a safety is built in against unexpected situations, especially against an underestimation of the flux levels from poorly understood sources. In ATLAS[34], the CSCs will cover a surface of about 27 m^2 with a total of 67,000 active channels. The schematic setup of this chamber is shown in Fig. 3.10.

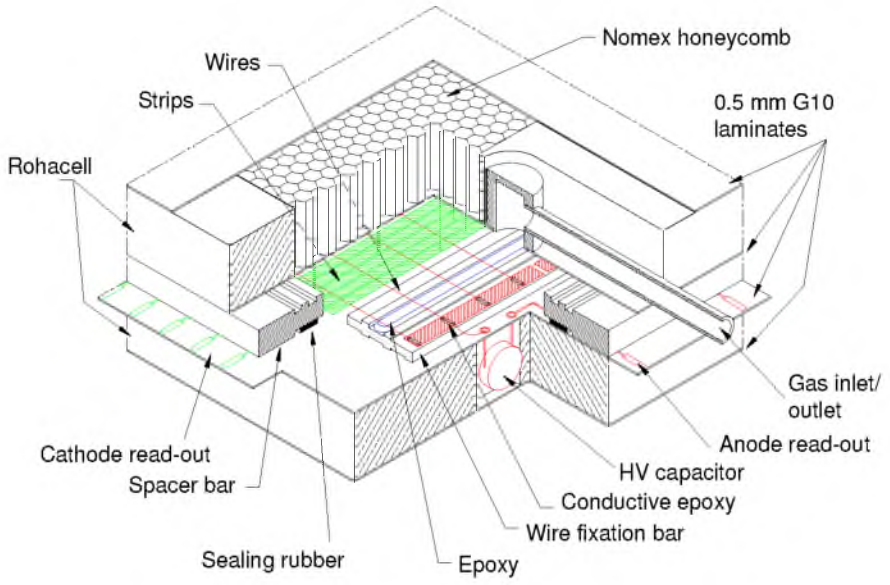

Figure 3.10: Single CSC layer showing construction details.

Again, the CSC technique is based on plate electrodes as the cathodes and planes of

wires as the anodes, see Fig. 3.1(b). The basis for the multilayer modules are sheets of 18.75 mm thick NOMEX®[39] honeycomb (hexcel). The properties of this lightweight polymer are, amongst others, very good mechanical stability, easy mouldability, and low conductivity. A 0.5 mm thick layer of printed circuit board, FR-4 fibreglass laminate with 17 μm copper cladding, is put on both sides of the hexcel sheet. The copper forms the cathodes of the chamber. Five of these panels are hung into a rohacell frame in order to obtain a four-layer chamber, e.g. see Fig. 3.11. The copper claddings at the outside of the chamber, where no gas is present, serve as electromagnetic shield. The panels and frames are lightweight, merely 1 kg/m^2, but still strong enough to withstand the tension on the wires, with a force of about 40 kg/m. It is for this reason that the 30 μm diameter gold-plated tungsten wires are connected directly to this frame.

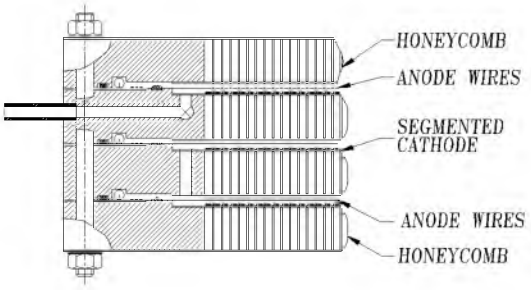

Figure 3.11: Design of a three-layer CSC chamber.

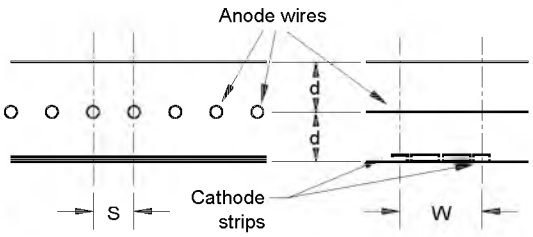

Figure 3.12: Layout of wires and strips in CSC with $d = S = W/2 =$ 2.54 mm.

Typical for the CSC is that a so-called symmetric cell layout has been chosen. This means that the distance between the anode wires and the distance between anode and cathode planes are equal, see Fig. 3.12. The distance is only 2.54 mm, i.e. 5.08 mm between cathode planes, which results in very short drift times, namely less than 30 ns for the ions. A non-flammable gas mixture, 30%/50%/20% argon (Ar)/carbon dioxide (CO_2)/tetrafluoromethane (CF_4) is used, which gives a proportional amplification gain factor of $4 \cdot 10^4$ at a potential difference of 2.6 kV.

Though prototypes are working with a sensitive area of 45×37 cm^2, in principle every desired width and length can be chosen for the geometry. For ATLAS, the CSCs come in two types, see Fig. 3.13, with variable dimensions of 40-114 $\times$ 120 cm^2. The same flexibility applies to the read-out: the copper can be etched along any direction. In ATLAS, the orientation of the chamber will be such that the wires run in radial direction towards the beam pipe.

One of the two cathode planes has strips etched in the direction orthogonal to the wires. This gives the accurate position measurement, where a strip read-out pitch of 5.08 mm results in a position resolution of 60 μm using the centre-of-gravity method. Actually, the excellent resolution can not be explained by the wire pitch and centre-of-gravity method alone. A special trick has been used, which is shown schematically in Fig. 3.14. The width of the actual read-out strips is only 1.07 mm but they have two 1.63 mm wide intermediate strips between them, thus explaining the 5.08 mm pitch, see Fig. 3.14(a). Reading out all strips would introduce too many active channels, so

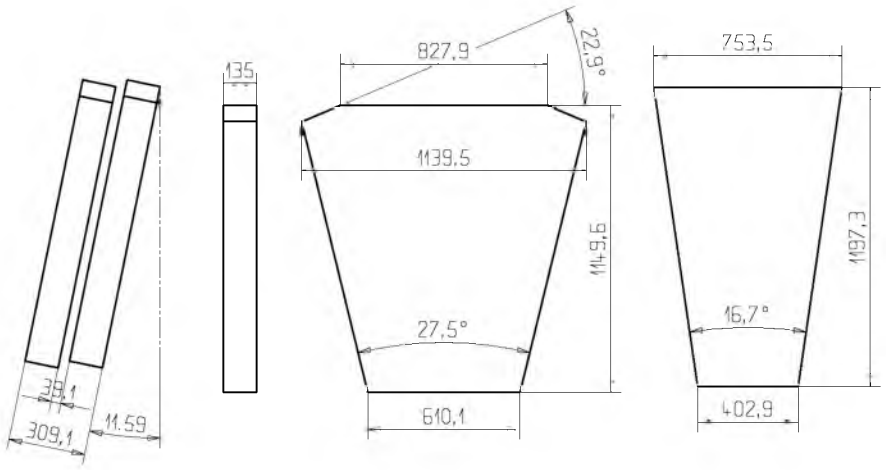

Figure 3.13: Dimensions (in mm*) of the two types of CSC module and the orientation of two modules towards the beam interaction point.*

capacitive coupling of intermediate strips to read-out strips is used, see Fig. 3.14(b). Now, the excellent resolution is obtained by (charge) integration over a number of strips. For the four-layer chamber, even a position resolution of 40 μm is feasible, see Fig. 3.15.

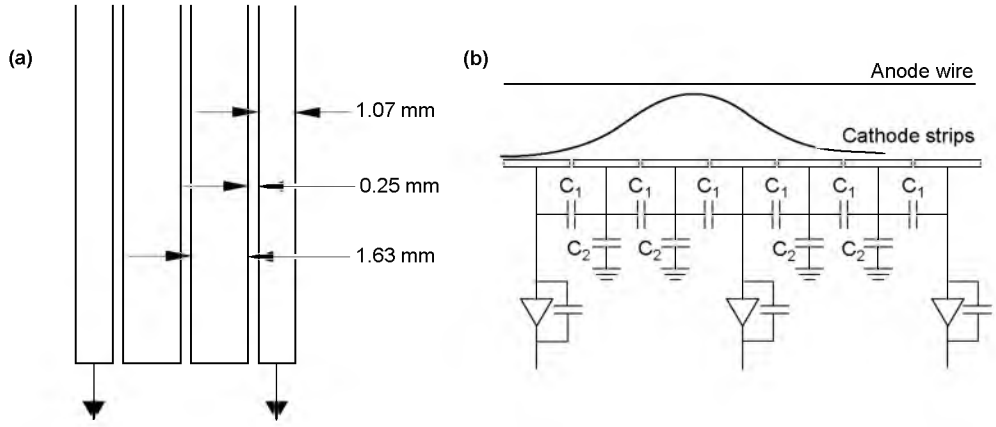

Figure 3.14: (a) Widths of read-out and intermediate strips. (b) Circuit showing the capacitive coupling of strips.

In principle, it is possible to read out the wires for a second coordinate measurement. This would result in a position resolution of approximately 1 mm if no drift time measurement is used. A number of wires could be ganged together to reduce the number of read-out channels at the cost of a less accurate position measurement. In ATLAS, this wire read-out will not be used. Instead, it has been decided to etch the copper in the second cathode parallel to the wires, in order to obtain another set of strips that will give a second coordinate measurement of 5 mm precision. Here, the

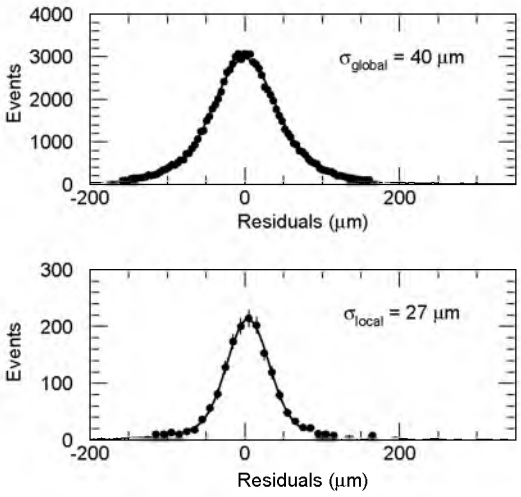

Figure 3.15: Position resolution obtained by prototype chamber (upper plot) and by the best performing layer (lower plot).

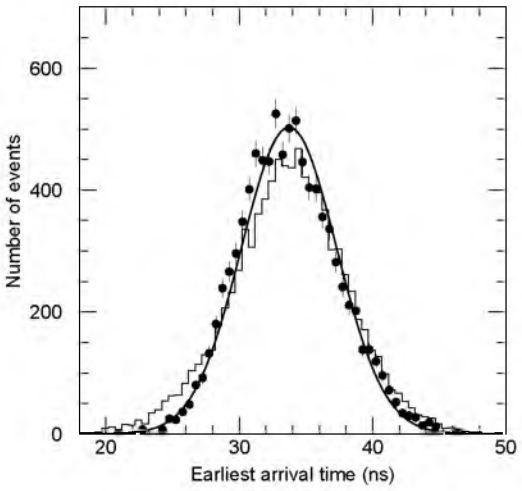

Figure 3.16: Time resolution obtained by prototype chamber for the arrival time that was registered first.

strip segmentation is much coarser than in the first cathode, such that the number of read-out channels is kept to a minimum. This set of strips is also used for the timing of the bunch crossing. The maximum drift time of 30 ns is practically within the 25 ns bunch crossing time of LHC. Selecting the plane with the earliest time of arrival, one can obtain a time resolution of 3.6 ns, see Fig. 3.16, which is good enough to correctly identify the event to which a muon belongs[34].

The conclusion is that the CSCs are able to operate in a high flux environment with rates going up to possibly 5 kHz/cm^2 (including a safety factor of 5), while providing good position measurements. It has to be remarked that this is achieved by tilting the chambers towards the beam interaction point, as shown in Fig. 3.13 in order to let, on the average, tracks pass perpendicular through the chambers, thus reducing the track inclination and, therefore, the degradation of the resolution. The CSC performance is summarized in the table below:

signal charge	1.15	pC	
time resolution	3.6	ns	
signal duration	< 30	ns	
position resolution	40	μm	bending coordinate
	5	mm	second coordinate

3.5 Monitored Drift Tubes (MDT)

The MDT[40, 41] chamber is a novel technology that was developed fully within the ATLAS muon collaboration. It came forward as the result of a combined effort to

integrate several competing techniques[42–44]. In ATLAS[34], the MDTs will cover a surface of about 5500 m^2 with a total of 370,000 active channels. A schematic representation of two complete chambers is given in Fig. 3.17.

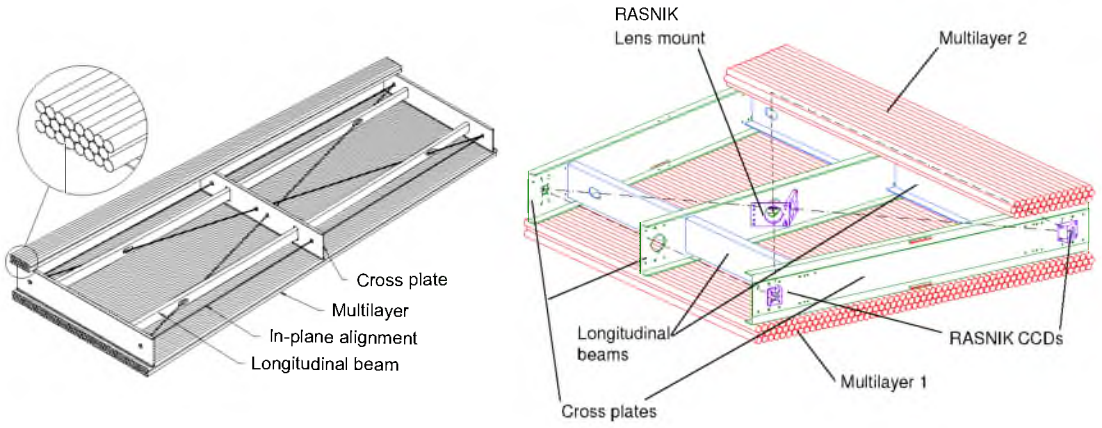

Figure 3.17: Schematic representations of a barrel and an endcap MDT chamber.

Starting-point is the use of a tube as a drift cell, see Fig. 3.1(c). The tube acts as cathode and is made of a hard aluminium alloy of the AlMn-type (ALUMAN 100). It has an outer diameter of 3 cm where the wall has a thickness of 400 μm. These tubes can be produced by the industry such that they satisfy stringent tolerance requirements. For instance, the outer diameter does not exceed $30,000^{+0}_{-30}$ μm, the wall thickness satisfies the dimensions 400 ± 20 μm and the maximum eccentricity is 15 μm. The anode is a gold-plated 97%/3% tungsten (W)-rhenium (Re) wire of 50 μm diameter operated at a potential of 3.27 kV. It is fixed at the outer ends of the tube by endplugs of which a conceptual design is shown in Fig. 3.18. The tube length can vary from 0.7 m to 6.3 m, depending on its position in the spectrometer. An additional wire locator is inserted in the middle of the tube as soon as its length exceeds 4 m, in order to avoid that the wire is moved out of the centre of the tube by electrostatic forces, vibrations, or chamber deformations.

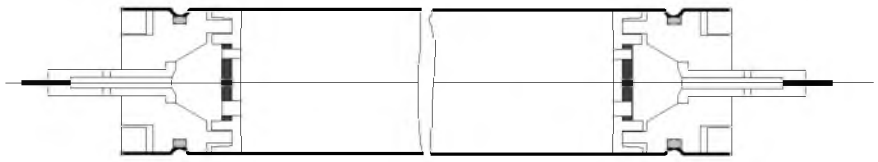

Figure 3.18: Schematic representation of an MDT tube with endplugs at both ends. The tube is cut in two, so that the largest part of the wire is not shown.

In comparison to the other techniques described before, the MDT chamber utilizes completely different concepts developed to obtain a technology which is cheap and which can cover a large area. This detection technology is specialized in an accurate position measurement of a muon track in the direction of its deflection caused by the

externally applied magnetic field. The need to cover a large area requires the use of long tubes. However, it was found that, in practice, no support structure exists to keep the tubes rigid enough. The simplest solution to this problem was to allow the chamber sag due to gravity, but to give the wire such a tension that it has an equal sag. Because of deviations to the chamber geometry which are caused by air flow, temperature differences, vibrations, and other external influences, the necessity arises to continuously monitor the chamber. It is floppy by nature and the deviations are accurately registered in order to guarantee a high precision position measurement. Figure 3.17 shows the support structure and monitoring system (RASNIK).

No final choice has been made yet for the drift gas, though the requirements have become clear. Lots of research has come up with a gas mixture of 91%/4%/5% argon (Ar)/nitrogen (N_2)/methane (CH_4) being the best candidate found[(6)] since the 'Technical Proposal'[8]. The choice has been made to operate under an absolute[(7)] gas pressure of 3 bar. This has the advantage that the resolution of a single tube is much better than under normal atmospheric pressure. Furthermore, the Lorentz angle diminishes and the overpressure ensures that the tube stays round to a higher precision.

The following list of specifications is taken as the operating point. First of all, the gas gain will be $2 \cdot 10^4$. This choice ensures that the wires will function long enough to detect the signal during the lifetime of the experiment. Namely, the efficiency of detection by the wires diminishes in time because of a polymeric coating that forms upon them. This aging is caused by chemical radicals formed with the charge build-up, binding into larger molecules, i.e. the polymers. The low gas gain infers that the potential difference between anode and cathode has to be low. This, in turn, has the effect that the drift time becomes longer. Especially for the maximum drift time, i.e. for tracks which pass at a distance of 1.5 cm from the wire, this is of importance. It should not exceed 500 ns, because otherwise the association of the muon to the correct event becomes too difficult and/or there can be other muons or ionizing particles (background radiation) also passing through the same tube at a distance closer to the wire, which spoil the drift time measurement. An important point to note is that the gas gain should still be such that the gas is operated in proportional mode.

The previous discussion implies that a fast gas needs to be used. Almost in contrast to this is the need that the Lorentz angle is less than 10° for practical reasons. Namely, the Lorentz angle depends on the magnetic field component along the wire, which varies in a long tube thus making it too hard to choose the proper drift time to drift distance (*r*-*t*) relation for large (unknown) Lorentz angles.

Probably the most strict demand is that, for safety reasons, the gas should be non-flammable. In practice, this means that the amount of flammable components in the gas is at most at a one percent level.

---

(6) The fall-back options of using pure argon (Ar)/carbon dioxide (CO_2) mixtures is under study, but also a different mixture of the standard gas, namely 92%/5%/3% argon (Ar)/nitrogen (N_2)/methane (CH_4), is being studied.

(7) An absolute pressure of 3 bar implies that the overpressure is practically 2 bar, or 2 atmospheres.

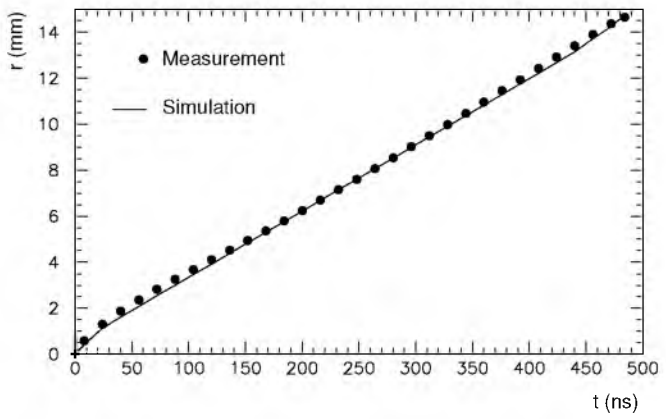

Figure 3.19: The r-t relation of MDTs, but without a magnetic field.

Upon final choice of the gas[8], a precise *r-t* relation is made, as shown in Fig. 3.19. This is an accurate correlation of the distance to the wire perpendicular to the muon track, which is the shortest distance and called drift distance (r), and the difference in the (triggered) time of passage of the muon and arrival time of the signal, which is called drift time (t). The *r-t* relation is used to obtain a position measurement from the time measurements. The accuracy of the drift distance determined in a single tube averages around 80 μm, see Fig. 3.20. However, the orientation of the muon track with respect to the tube is still fully undetermined and consequently a mattress or multi-layer which consists of several staggered planes of tubes is used. The combination of information from neighbouring tubes now determines the angle of the muon track, e.g. with respect to the mattress.

A problem still arises with the configuration of three or four layers of tubes such as has been chosen for the ATLAS experiment. The angle with which the muon crosses the mattress is not always unambiguous because of the inaccuracy in the drift time to drift distance measurement. Furthermore, the tubes are not hundred percent efficient and sometimes fail to register a signal. Additionally, areas of dead space exist which are caused by the walls of the tubes. Because of these considerations, it has been found useful to mount another mattress of MDTs on the other side of a spacer. This spacer or support frame has been preformed to follow the natural sag of MDTs and houses the monitoring system. It has been kept as lightweight as possible. The result is a stable structure with highly necessary redundancies, as is shown in Fig. 3.21. Additionally, the statistical precision on the measured coordinate is improved to about 40 microns by this combined structure.

[8] A linear *r-t* relation is provided by pure gas mixtures of Ar/CH_4, where the single tube resolution is independent of the background. This gas is subject to aging though. A pure Ar/CO_2 gas mixture does not age, but it is too slow and non-linear. In practice, this means that the drift tube properties change too much due to the space charge effects, which worsens the single tube resolution in high background regions. So, the gas of interest will be a mixture of argon, carbon dioxide and methane with a possible additional gas component.

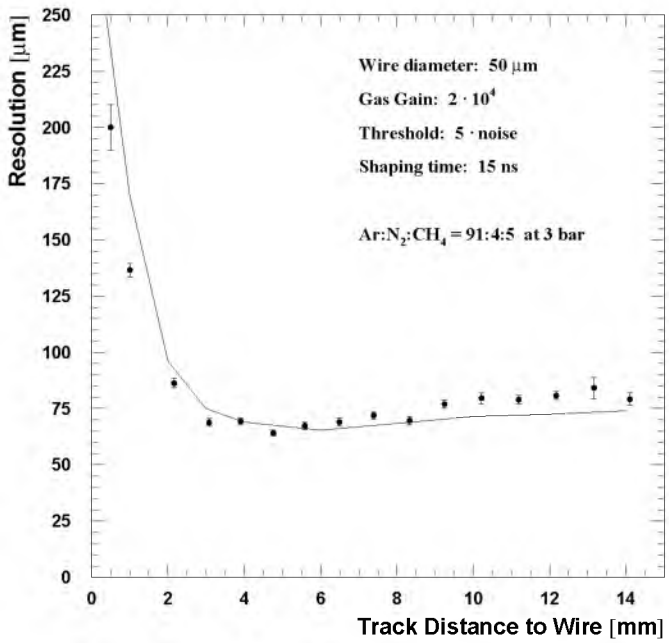

Figure 3.20: Single-tube MDT position resolution versus drift distance.

The position of the muon track along the wires is not measured by the MDT chambers at all. Instead, the MDTs depend on the trigger chambers (RPCs, described in Sect. 3.2, and TGCs, described in Sect. 3.3) to provide this second coordinate, i.e. the position along the wire.

We conclude with a table showing the MDTs parameters of importance:

signal charge	1.7	pC	
signal duration	< 480	ns	
position resolution	40	μm	bending coordinate
	$4-14$	mm	second coordinate
angular precision	0.3	mrad	bending coordinate

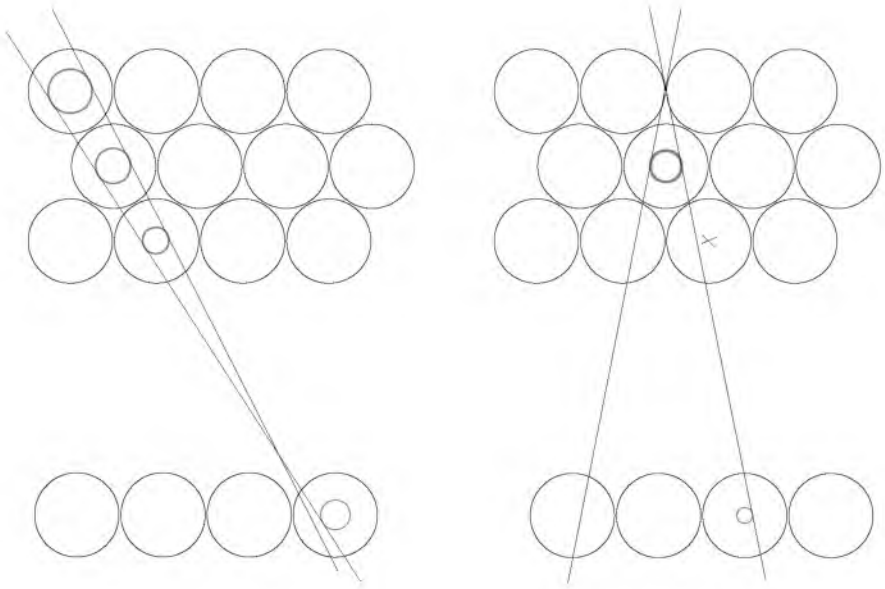

Figure 3.21: Pictures showing part of an MDT chamber where the spacer structure has not been drawn; the distance between the multilayers is not to scale. Only the top layer of tubes for the lower multilayer is shown. The solid straight lines correspond to infinite momentum muon track possibilities while the grey circles represent the approximate drift distance. The left picture shows a situation where the top multilayer cannot decide on the possible track, but it becomes clear from the lower multilayer. The picture on the right shows tracks running through dead areas and one tube that failed to register a signal; again, the lower multilayer is decisive on the correct track.

Chapter 4

Spectrometer magnets

In order to be able to do relevant physics, criteria have to be set on the precision with which the track parameters are measured. The purpose of the muon spectrometer is to measure muons with a minimal transverse momentum p_T of 5 GeV/c and a maximum p_T of 1 TeV/c, or even beyond. To be more precise, the target is a momentum resolution of $\Delta p_T/p_T \approx 2\%$ at $p_T = 100$ GeV/c, and $\Delta p_T/p_T \approx 10\%$ at $p_T = 1000$ GeV/c[8]. These criteria can be directly translated into demands for the precision of the muon detection chambers and the strength of the magnetic field which is used to bend the particle trajectory, depending on its track parameters.

The ATLAS community has chosen to adopt a global coordinate system with its origin at the (nominal) beam collision point in the centre of the ATLAS detector. The x-axis points parallel to the plane of the collider ring towards its centre. The y-axis points towards the earth surface, while keeping perpendicular to the x-axis. The z-axis lies along the direction of the proton beams, in such a way that a proper right-handed coordinate system is obtained. Often, a diameter $R = \sqrt{x^2 + y^2}$ is used which defines the radial distance from the collision point. Roughly speaking, between the longitudinal boundaries -6.75 m $< z < 6.75$ m, the space available for the muon spectrometer starts at a diameter of 4.25 m going outward. Beyond $|z| > 6.75$ m, in principle, the complete area can be used.

Now, two fully distinct options exist. In the first option, The available space can be filled with iron in order to slow down the muons appreciably. Advantageous to this option are the facts that the very energetic muons can be bent off easily because they lose velocity and that the whole structure remains compact[(1)]. However, it becomes more difficult to adhere to the momentum resolution, because the combined effect of multiple scattering and energy loss is not exactly known along the muon track. This makes the combinability of measurements less effective.

With the other option, the space available stays practically empty, such that an open structure is formed. In order to bend the highest-energetic muons, the necessity arises

[(1)] It is worthwhile to note that the other general purpose LHC experiment has chosen for the solid iron mode of operation as can also be inferred from its name: CMS[45] stands for Compact Muon Solenoid. ATLAS stands for A Toroidal Lhc ApparatuS. From a technical and economical point of view, it is impossible to build a solenoid with the same volume as the ATLAS toroids.

for the muon to travel a long distance through a strong magnetic field. Within the ATLAS community the choice has been made for this second option[46–48].

The bending of the muon track occurs in the $R-z$ plane, because use is made of a magnet system that produces a toroidal field.

4.1 Magnet Systems

Elaborate research and much deliberation has led to the conclusion that an eightfold symmetry would be the most cost-effective approximation of a torus. Both a large muon barrel magnet as well as two muon endcap magnets show this eightfold segmentation, see Fig. 4.1.

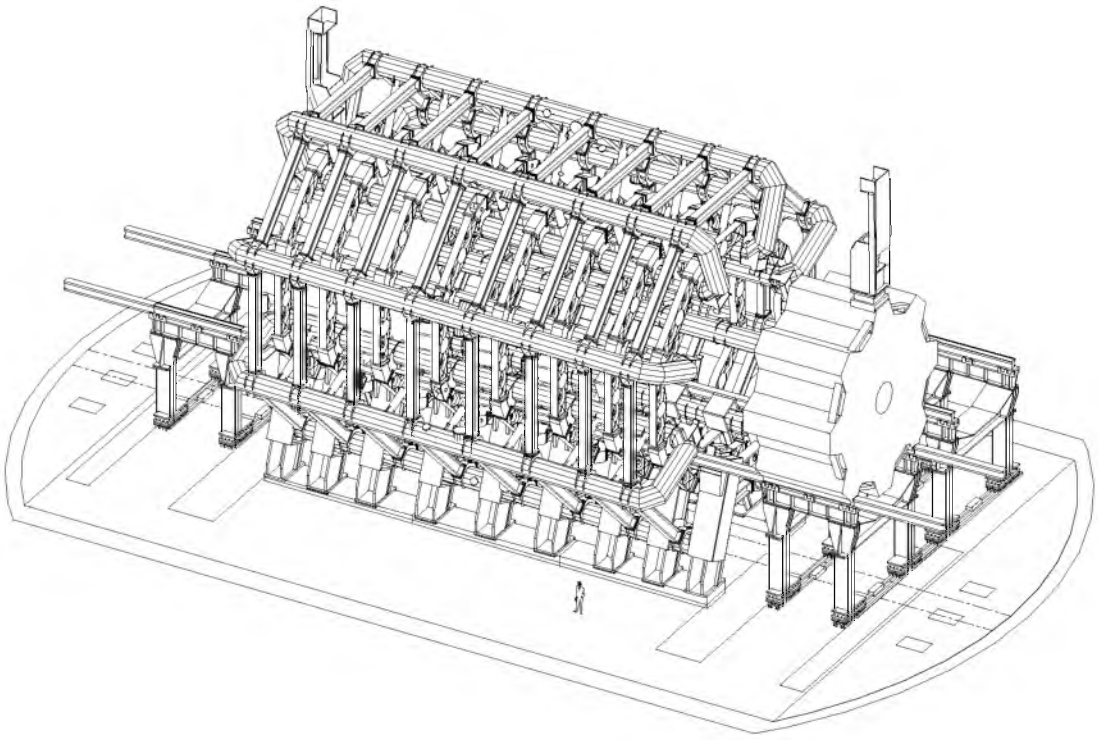

Figure 4.1: Barrel and endcap cryostats supported by feet and rails. The right-handed endcap cryostat has been moved from its position out of the barrel cryostat.

The eight coils which comprise the barrel toroid[49], individually look like racetracks, as can be seen in Fig. 4.2. The windings are made of a superconducting material, namely 20 kA aluminium stabilized niobium-titanium (NbTi). They are stacked in a so-called winding house, as shown in Fig. 4.3, which has been pre-formed as a racetrack. It has a height of 4.98 m and a length of 24.95 m.

Additional stiffening ribs are installed in the winding house to prevent the coils from becoming circles under the large magnetic forces. Small asymmetries between

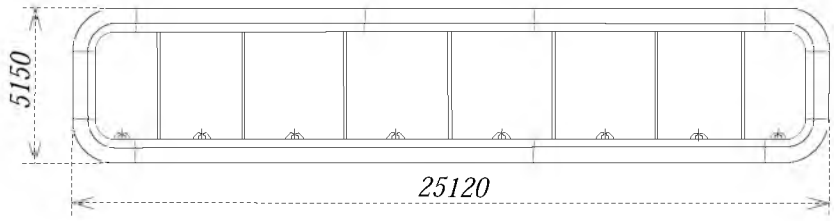

Figure 4.2: Barrel racetrack casing.

the coils give rise to large forces, so that their relative positions need to be fixed. This is ensured by housing each coil in a separate cryostat. It maintains an inside temperature of 4.5 K, needed for the NbTi to be superconducting. Voussoirs are mounted between the cryostats in order to hold them at equal distances. Furthermore, struts at the radial end of the cryostats also serve the purpose to carry the forces of asymmetries between the coils. The struts run parallel to the voussoirs, as can be seen in Fig. 4.4.

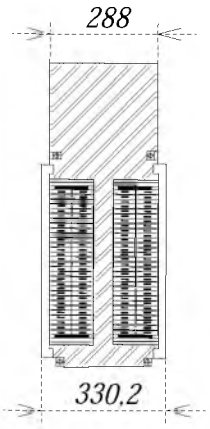

Figure 4.3: Cross section of winding house showing double pancakes of conductors.

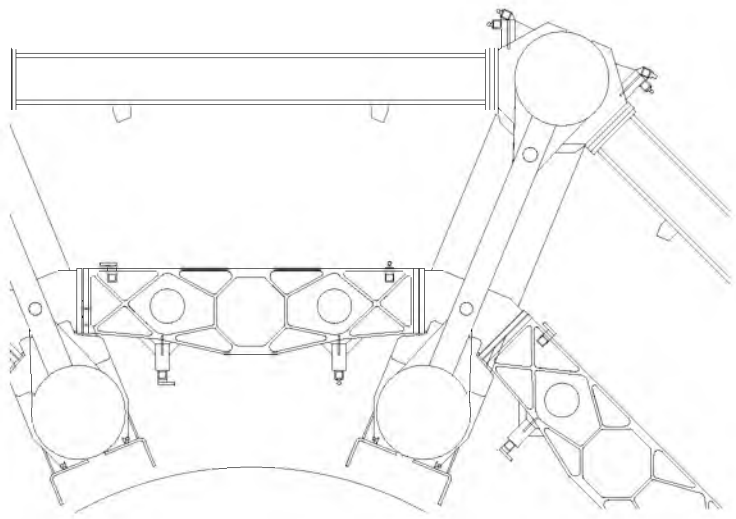

Figure 4.4: Voussoirs (at the inside) and struts (at the outside) keeping each barrel cryostat in position.

The total dimensions of the barrel toroid come down to an inner bore of 9.44 m and an outer diameter of 20.08 m (radially from 4.72 m to 10.04 m) with a length of 25.26 m.

The barrel toroid by itself does not suffice to bend muons throughout all the available space. To give more coverage, use will be made of two additional endcap toroids [50] to be pushed inside the barrel toroid from either end. Muons moving close to the beam pipe are now bent much more by the additional (forward/backward) magnetic field. In the endcaps, the eight coils sit together inside one cryostat. The whole structure has been rotated by 22.5° with respect to the barrel toroid, in order to fit in. Inside the cryostat are support frames to keep the coil structures in place. The support

frames are kept in fixed position by support webs to prevent any asymmetry between coil positions, see Fig. 4.5.

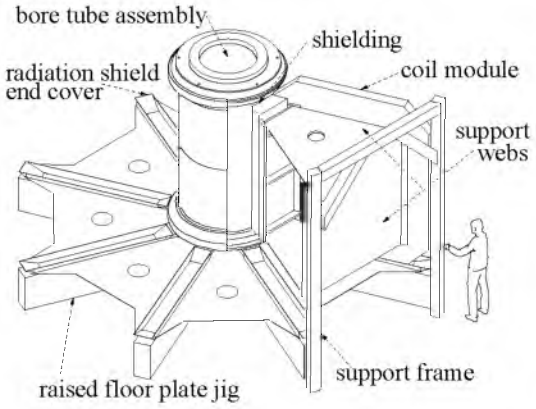

Figure 4.5:
Support structures of endcap coils.

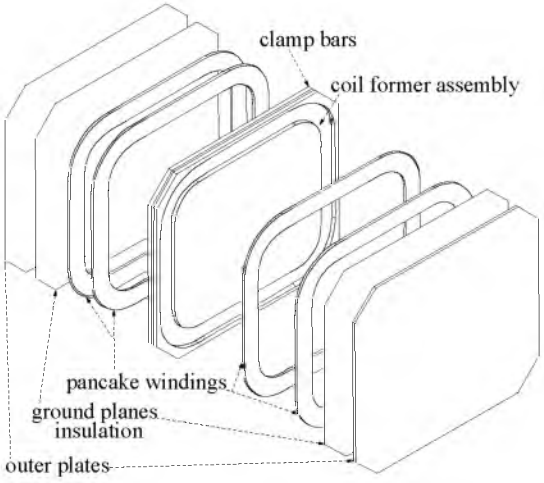

Figure 4.6:
Assembly of one endcap coil.

The coil structure is shown in Fig. 4.6. It consists of a central plate with a pre-formed groove and additional cover plates. The double pancake racetrack windings of superconducting material are placed inside the grooves. The windings are again made of aluminium stabilized niobium-titanium. Dimensions of the endcap cryostats are: an inner bore of 1.65 m, an outer diameter of 10.70 m (radially from 0.825 m to 5.35 m) with a length of 5.00 m each. The endcaps have a peculiar shape in order to fit inside the barrel magnet system, i.e. the outer diameter of the endcap cryostats is larger than the bore of the barrel cryostat, but, because of the rotation, the effective outer diameter is 9.13 m. Figure 4.1 already showed the right-hand of the endcap cryostats, the other one being barely visible inside the other end of the barrel structure.

One has to consider that the cold elements shrink in size while the temperature is brought down from room temperature to 4.5 K, so the dimensions previously given are only valid after this cool down.

Because the magnetic field provided by the toroid magnets does not reach far into the central volume ($|z| < 6.75$ m, $R < 4.25$ m), an additional solenoid[51] is used to provide the bending of charged particles close to the interaction point. The windings are made of the familiar niobium-titanium superconductor. They constitute one coil, which has a solenoidal shape of 2.44 m diameter and 5.30 m length. It is operated at 4.5 K inside a cryostat that houses a calorimetric sub-detector as well.

In conclusion, Fig. 4.7 shows the superconducting material, i.e. the windings, of the complete magnet system[52].

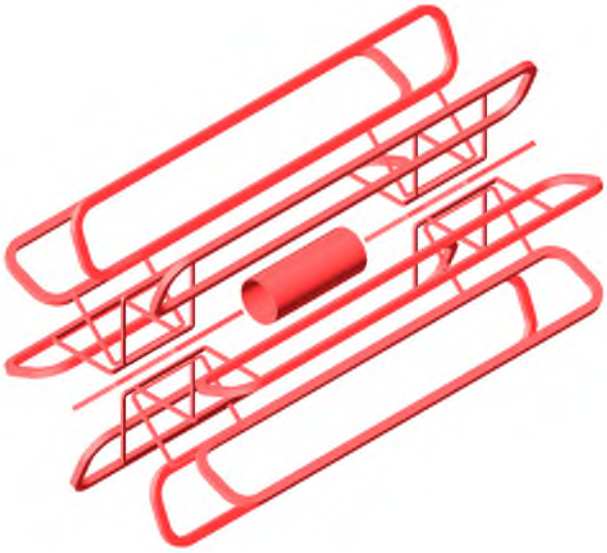

Figure 4.7: Distribution of coil material, showing eight large barrel coils, sixteen endcap coils and the central solenoid.

4.2 Magnetic field

It would normally be possible to calculate the magnetic field components, i.e. direction and size, from the distribution of magnetic windings at every desired point in space. To do this, all magnetic material has to be taken into account. However, Fig. 4.7 does not show all magnetic material in the ATLAS detector. Especially in the area between the solenoid and the barrel toroid, a large amount of ferromagnetic material is present that needs to be included into the calculation. Furthermore, there are many small deviations in material position during operation of the detector, originating from temperature changes, vibrations, and deformations. This would mean that the magnetic field map would have to be recalculated continuously, which is impossible to do. So instead, about 2000 cubes of size $1 \times 1 \times 1$ cm^3 are placed at strategic locations inside the detector to measure the local magnetic field. Three orthogonal faces of the cubes are equipped with Hall probes, which perform the actual measurement of field components in three directions, see Fig. 4.8. This helps in the field map reconstruction only if the position of the probes within the detector is exactly known. So, the cubes are placed on precision instruments.

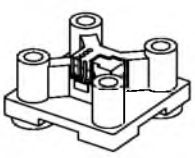

Figure 4.8: Measuring cube showing one Hall probe (out of three) and four fixation points.

Because of symmetry reasons, the components of the magnetic field $\vec{B}$ are denoted

$\vec{B} = (B_R, B_\phi, B_z)$. In a perfect toroidal field, only the B_ϕ component is non-zero, while only the B_z component is non-zero in a perfect solenoidal field. The ATLAS magnetic field has a transition from a (length limited) solenoidal field to an approximately toroidal field, so that all components are present at every point in space, though some component values can be very small. So, the bending of a charged particle track occurs mainly in the $x-y$ plane within the solenoid, mainly in the $R-z$ plane within the toroids, and there is almost no bending in the space in between. Figure 4.9 shows a number of representations of the magnetic field, but only projections can be drawn since it is a three dimensional vector field.

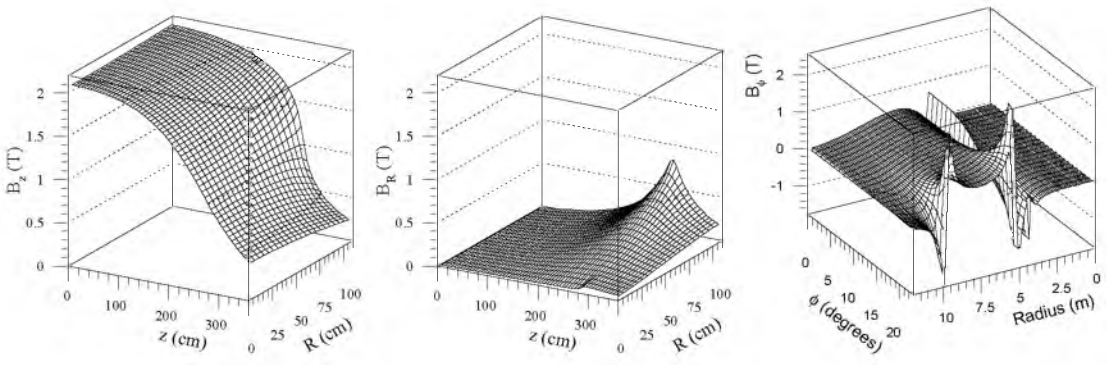

Figure 4.9: Strength of magnetic field components in Tesla. B_z and B_R as function of z and R in the central region, and B_ϕ as function of ϕ and R at $z = 0$ in the whole detector.

The solenoid provides a field of 2 T strength which peaks to 2.6 T on the superconducting material. The peak fields on the superconductor for barrel and endcap toroids are 3.9 T and 4.1 T, respectively.

4.3 Sagitta measurement

In Chapter 2 is explained how to define the muon transverse momentum p_{T}, which is the main parameter of interest. The magnetic field as obtained from the toroids is absolutely non-uniform. Only at large distances from the coils does the approximation of a perfect toroidal field hold. Nevertheless, it is quite useful to start from the simplest, most ideal, situation in order to explain some mathematics. So, for demonstration purposes, a homogeneous magnetic field and a muon track in perfect vacuum is used, see Fig. 4.10.

The figure shows a muon following a perfect helix (where the bending by the magnetic field is exaggerated). The figure represents the projection of the helix onto a plane perpendicular to the direction of the magnetic field, which means that only an arc with radius a remains. Furthermore, three measurement stations have been drawn, denoted by the numbers 1, 2, and 3. The muon enters the spectrometer at station 1 and leaves it at station 3. The real distance traversed by the muon between these stations is called

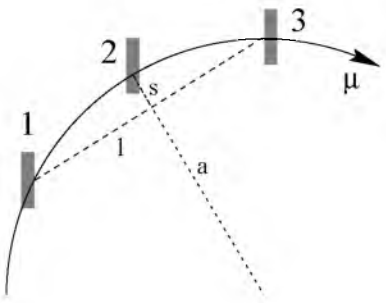

Figure 4.10: Definition of sagitta measurement showing a muon track going through measurement stations 1 *to* 3*. The radius of the arc (a) is shown by the dotted line.*

the track length. With the symbol *l* we only denote the shortest distance between the two stations in a projection onto the plane mentioned above. Halfway between these stations, the track has the largest deviation from *l*. This deviation (the sagitta) is usually denoted by the parameter *s*. It is advantageous to place a measurement station at this position, in order to achieve the best measurement of the sagitta, itself. In the figure, this station is denoted 2.

A bit of geometry leads to the equation:

$$l = 2 \cdot \sqrt{a^2 - (a-s)^2} = 2\sqrt{2as - s^2} \ .$$

In reality, the arc will look much more like a straight line. Mathematically seen, this means that $a \gg s$, and thus an approximation can be made, i.e.

$$a \approx l^2/8s \qquad , \qquad \text{or} \qquad p_T = \frac{e}{c}|\vec{B}|\frac{l^2}{8s} \ . \tag{4.1}$$

These quantities are all well measurable. Usually, the direction of travel of the muon and the direction of the magnetic field will not be perpendicular to each other. Using the angle θ between both directions, it is still possible to calculate the momentum. The relation is: $p_T = p\sin\theta$, so that $p = (e/c)(l^2/8s)(B/\sin\theta)$. The same factor applies to the relation between the track length L and l, namely $L \approx l/\sin\theta$, although in this case the approximation $l \gg s$ had to be made, which certainly holds for virtually straight, high momentum tracks.

However, the real situation is far from ideal. Firstly, the magnetic field is not homogeneous and actually not even properly toroidal either. This can be seen from Fig. 4.11, where the inhomogeneous transition from barrel to endcap magnetic fields is drawn. The magnetic field is of such complexity that besides the B_ϕ component, B_Z and B_R components exist also. This results in the observation that actually no plane of projection exists in which the muon is bent along the arc of a circle. Only by rough approximation does the muon follow a helical trajectory through space. To solve this, use is made of the bending power that the muon experiences. The bending

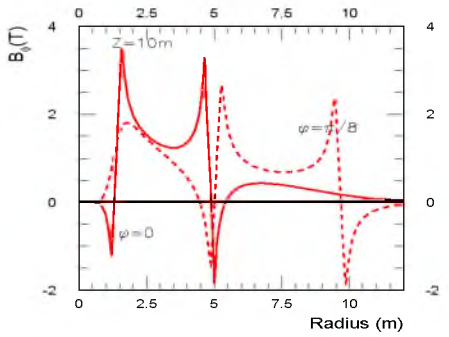

Figure 4.11: Magnetic field component B_ϕ for $\phi = 0$ and $\phi = \pi/8$ at $z = 10$ m as a function of R showing the inhomogeneity of the magnetic field.

power is the integrated field strength along the muon track from entrance to exit of the tracking volume, i.e. the part of the spectrometer between stations 1 and 3. This field integral is evaluated as $\int \vec{B} \cdot \mathrm{d}\vec{l}$ for muons with an infinite momentum, thus moving along a straight line. Because of these considerations, one should remark that the peak field of the magnets does not matter. Figure 4.12 shows the bending power of the B_ϕ (or $B_\perp$) component for different inclinations of the track. Here, θ is the angle between the beam pipe and the muon track. It is represented as the pseudo-rapidity quantity $\eta \equiv -\ln(\tan\theta/2)$ in the graph.

Secondly, another non-ideal complication is that the muon does not move through vacuum but through a space filled with matter. Structures such as magnets and detection chambers cause difficulties through multiple scattering and energy loss processes. Actually, all material between measurement stations 1 and 3 influences the precision of the muon spectrometer, especially for muons with momentum below 100 GeV/c, where multiple scattering has the most prominent influence, or below 20 GeV/c where energy loss fluctuations are most important. We will deal with the momentum resolution, in great detail, in Chapter 7.

One can perform a back-of-the-envelop calculation in order to get an idea of the size of the sagitta. At $\eta \approx 0$, one has $\theta \approx 90^\circ$ which means that p_T equals p. The lever arm in the detector is about 5 to 6 m and, according to Fig. 4.12, the integrated field is about 2 Tm. Rewriting formula (4.1) to obtain the sagitta in terms of known quantities gives: $s(\text{in mm}) = 37.5 \cdot BI(\text{in Tm}) \cdot l(\text{in m})/p_\mathrm{T}(\text{in GeV}/c)$, which yields $s = 3.5$–4.0 mm for a $p_\mathrm{T} = 100$ GeV/c muon[(2)]. It is also possible to calculate the error in momentum determination from the error in sagitta measurement. Assuming the sagitta measurement error to be 60 μm, which is a 1.7% relative error compared to 3.5 mm, gives a relative error of 1.7% on the transverse momentum determination, since $\Delta s/s = \Delta p_\mathrm{T}/p_\mathrm{T} = \Delta p/p$.

[(2)]This value is in agreement with figure 4 in the ATLAS Internal Note MUON-NO-150[53].

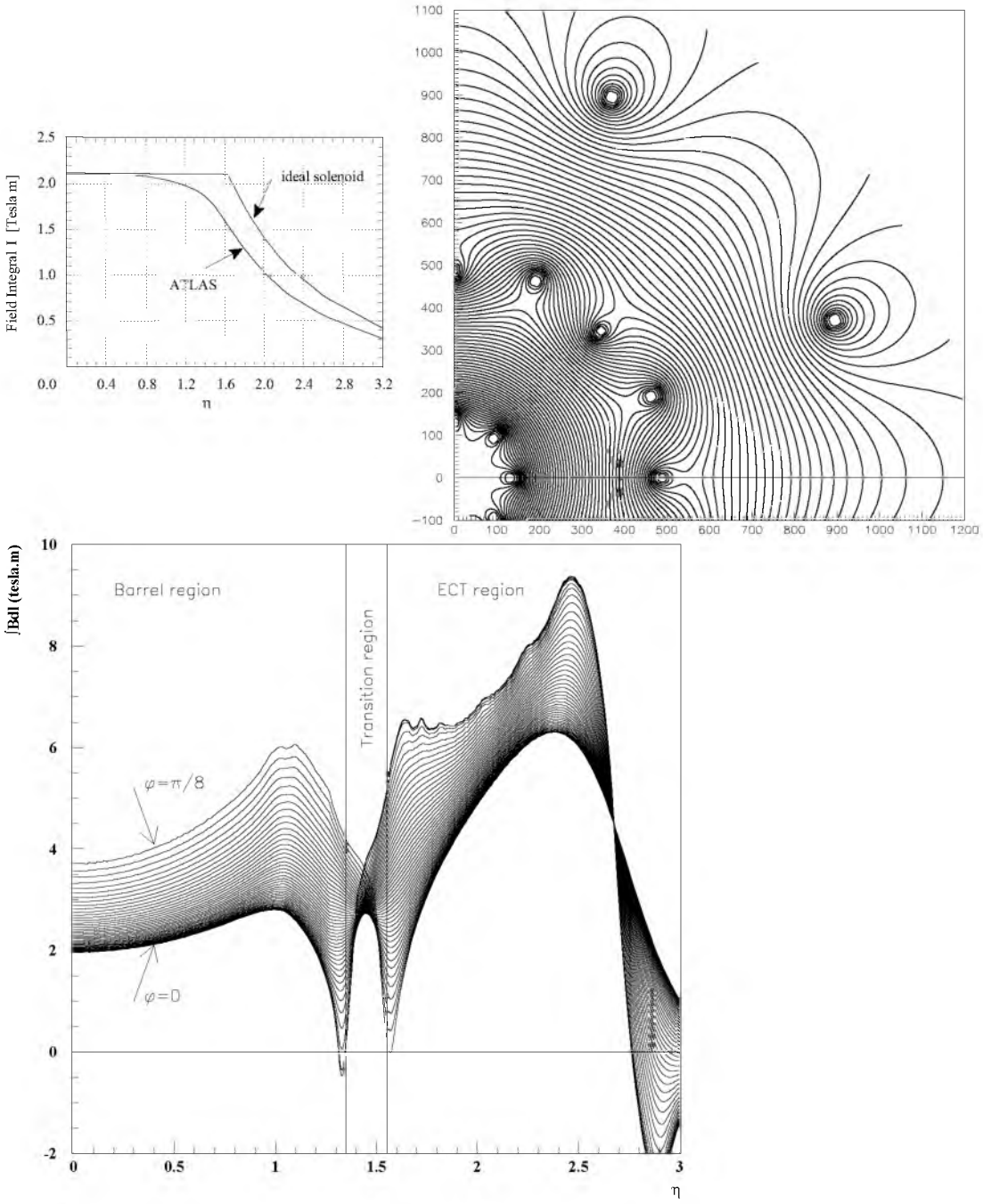

Figure 4.12: Integrated magnetic field for the central region (top left graph) and the full detector (left graph) for charged particles with infinite momentum. The top graph shows the magnetic field map in the transition region, along the EE-station (see next chapter), with an interval of 0.1 Tm.

Chapter 5

Spectrometer layout

With the magnet structures fixed, as described previously and shown in Fig. 4.1, all remaining space can, in principle, be used to house detection chambers. This statement is not strictly true, since there are many other, even rather stringent, restrictions that can impose precise demands on the chamber layout. An example of a precise restriction is the location of the support feet that keep the whole ATLAS detector lifted off the ground. The full muon barrel apparatus, i.e. precision chambers, trigger chambers, support structures, cabling, pipelines et cetera, is connected via the barrel toroid cryostats to the feet. Furthermore, the support feet also have a support rail attached to them. Not only the muon endcaps but all other detector components rest on these rails. This includes the calorimeters with an overall total weight of about 4000 tons, as well as the inner detector. In the end, the ATLAS detector will weigh about 7000 tons.

Space is also needed for the cabling of the spectrometer, the calorimeters, and the inner detector. This comprises of power lines (both low and high voltage), of readout channels (mostly fiber transmission lines), and of trigger lines which run between chambers and/or detectors. However, most intrusive are the pipelines, which have to satisfy certain safety rules. Especially the cryogenic cooling pipes cause difficulties, since they may neither be flexible nor may they have many bends or bridge a large height difference. The supply and waste pipes of the water cooling can be a lot smaller, while gas in- and outlets are supplied by flexible tubes. During an experimental run, calamities can occur, possibly causing a quick temperature rise. Over-dimensioned waste pipes and valves have been built into the system in order to avert explosions in such an event.

Every change in the layout has to deal with the points mentioned above. In addition, it is necessary to have access to every part of the ATLAS detector after it has been installed inside the cavern. For this purpose, the muon endcaps and the calorimeters have been placed on the rail support system, so that they can be moved out of position. The dimensions of the muon chambers, which are manufactured on production sites all around the world and transported to Geneva, have to be such that they are transportable. Furthermore, we want to position the chambers such as to take maximum use of the effective bending power of the magnetic field.

Many rounds of adjustments were needed in order to obtain the final layout of the

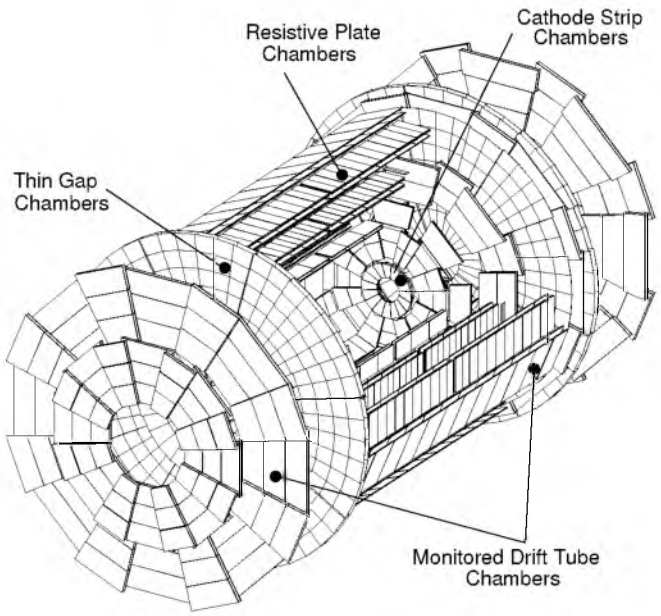

Figure 5.1: 3D-view of chamber positioning. RPCs or TGCs are always positioned together with MDTs. Part of the barrel has been cut out.

muon spectrometer, as shown in Fig. 5.1. It turned out to be possible to maintain a rather full coverage around the interaction point while fulfilling every other requirement. Actually, the strategies according to which chambers are placed in the barrel and in the endcaps differ. So, both systems will be treated separately. This reflects the trigger chambers also, where different technologies are used in barrel and endcaps. Finally, a point which has not been mentioned yet but which also follows the explicit distinction between barrel and endcaps, is the alignment system dealing with (deviations of) the detector element positions in the spectrometer. This alignment system follows the chamber layout closely as will be explained later on.

5.1 Muon barrel

The barrel muon spectrometer uses just one strategy. The precision measurement is performed by the MDT chambers already described in Sect. 3.5. For trigger purposes, the RPCs are used as described in Sect. 3.2. The open structure of barrel magnet and cryostats gives a very good opportunity for a proper sagitta measurement. This can be seen from Figs. 5.2 and 5.3, which show cross sections of the chambers along with the magnet structures.

Visible are three shells around the centre of the detector. Hereby, every shell represents a measurement station as given in Fig. 4.10. The first station, which is denoted as BI (Barrel Inner), has large chambers (L) between the lower ends of the barrel coil cryostats and small chambers (S) which fit precisely between the calorimeters and the

bottom of the coils. The outer shell of chambers (BO) can be placed easily. Again, the small chambers are positioned close to the cryostats, but this time on top of the outer ends, while the large chambers are placed further inward along the struts, even though this decreases the so-called lever arm. This lever arm equals more or less the distance the muon travels through the magnetic field. Positioning the middle station, denoted as BM (Barrel Middle), is a lot more difficult since the stiffening ribs of the coils are in the way. This is not much of a problem yet for the large chambers, because they are placed between the ribs along the voussoirs. However, the small chambers end up right inside these structures. The solution is to give these chambers a shorter length.

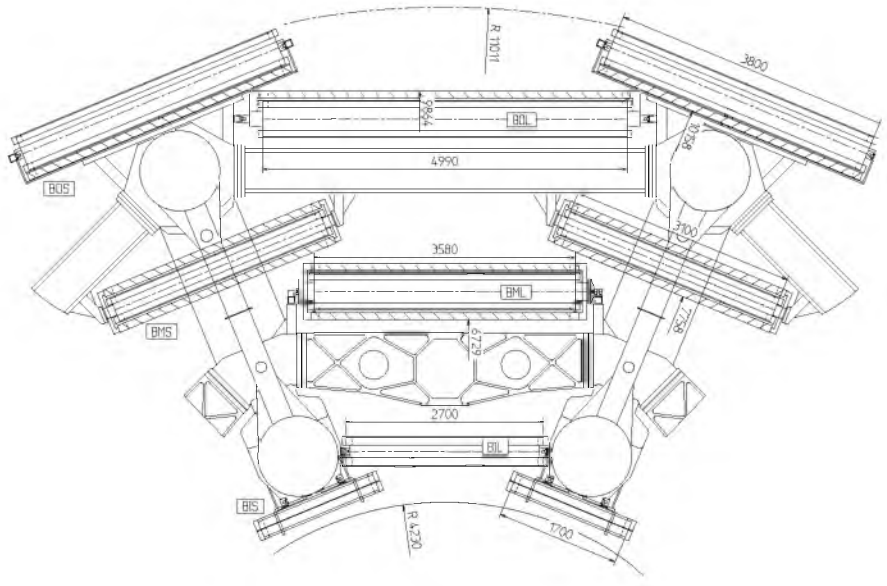

Figure 5.2: Cross section in $x-y$ plane of a barrel standard sector.

There are a few chambers in the setup which have exceptional dimensions. The BIL chambers next to the rails cannot have the same dimensions as in the other sectors and are therefore narrowed. As this would introduce an unacceptable loss in coverage, this is recovered by placing BIR (R for rails) chambers below the rails. Though some of the barrel cryostats have been integrated with the feet, this is not possible to accomplish with the chambers. Also some BML chambers are special. So, the BMF (F for feet) chambers between the feet are shorter than the standard BML chambers. This loss in coverage cannot be recovered. Also some of the BOL chambers are replaced due to the presence of the feet. It is possible to introduce two types of chamber (BOG and BOH), which together form a BOF chamber which, inserted in the (hollow) feet structure, recover practically all space. Figure 5.4 shows the different shapes of BIR, BMF, BOG, and BOH chambers.

A small overlap exists between every large and small chamber within a station, in order to warrant the best possible coverage. This also helps for the alignment, since muons traversing the overlap are detected by both types of chamber, from which a

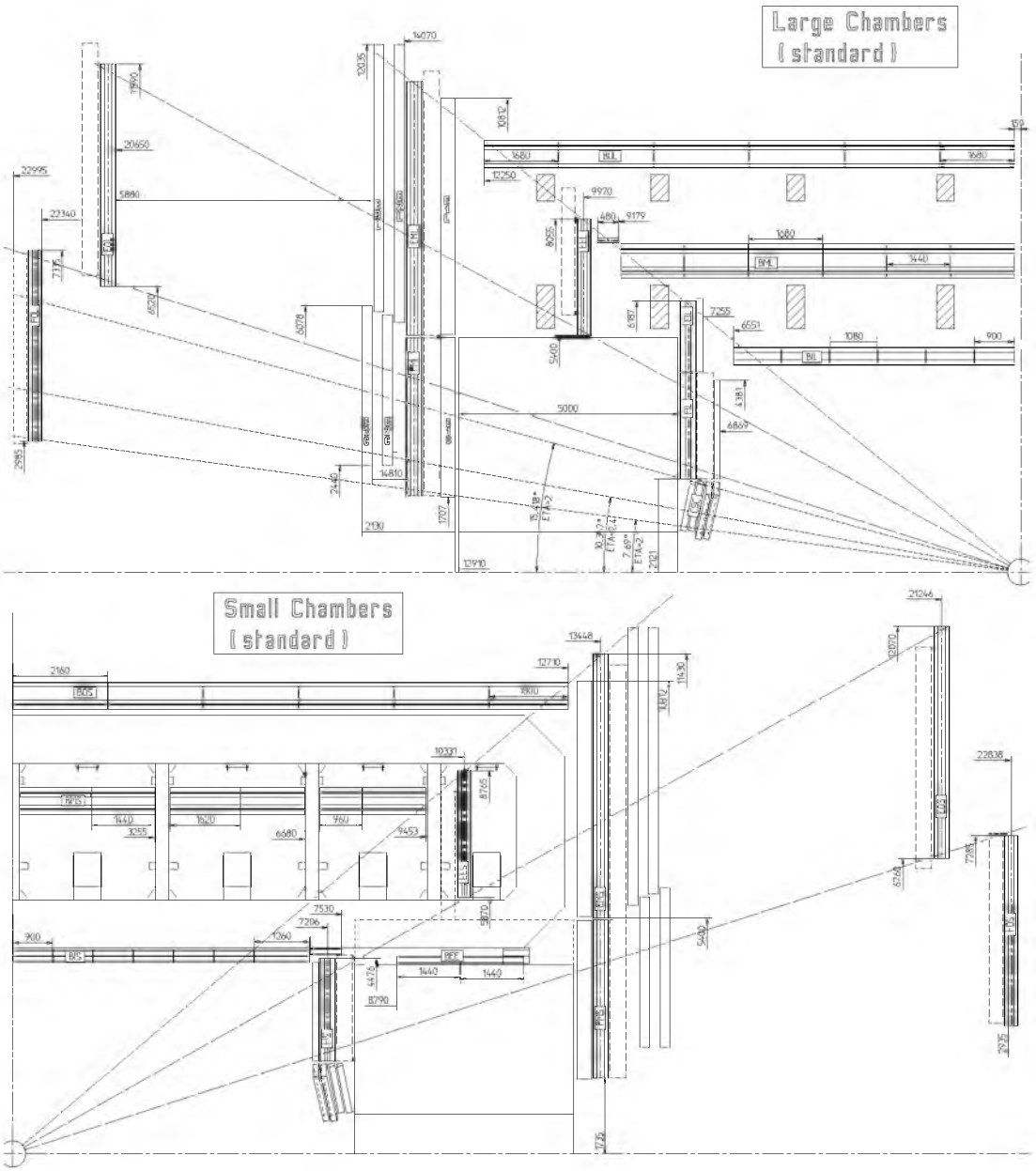

Figure 5.3: Longitudinal view of standard sectors showing large (L) chambers and small (S) chambers. Dashed lines show the projection of endcap chambers and cryostat from the other view.

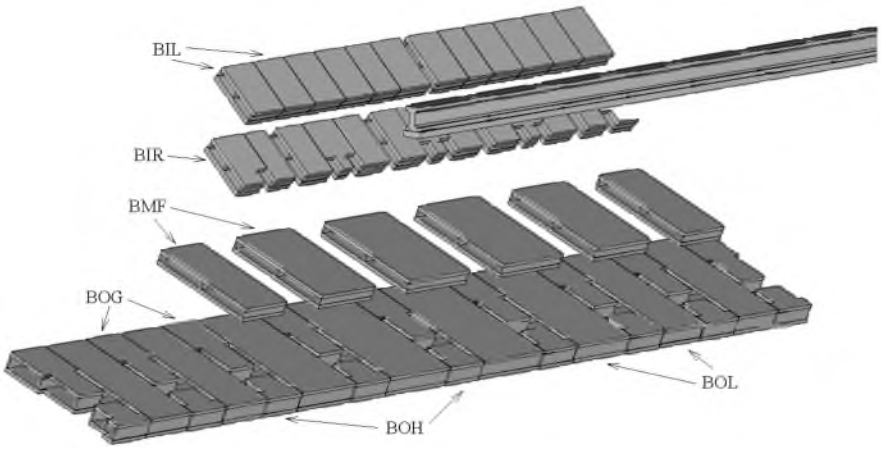

Figure 5.4: Shapes of BIL, BIR, BMF, BOG, BOH, BOL chambers and half a support rail in one of the feet/rail sectors.

relative positioning can be inferred, off-line. Four rows of tubes are stacked in each multilayer of the BI-station, while the multilayers of all other stations are equipped with three rows of stacked tubes.

A last point to note about the muon spectrometer barrel is that it has been decided to lead all services (i.e. cables, pipelines, et cetera) out in a radial plane around the interaction region. That is why a cutout has been made for the full barrel at $z \approx 0$ as can be seen in Fig. 5.3.

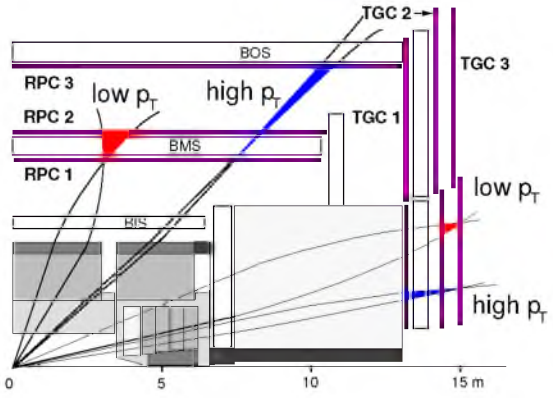

Figure 5.5: Logic of low and high p_T trigger schemes in barrel and endcap.

The barrel trigger chambers (RPCs) follow the layout of the precision chambers (MDTs) together with which they are placed in one overall chamber structure. The precise placement of the MDTs, RPCs and support structures can be taken from Fig. 5.2. Double gap RPCs are fastened both on top and below the MDTs of the BM-station, while they are only fixed underneath or on top of the MDTs of the BOS- and BOL-stations, respectively. This has to do with the trigger logic[54] as presented in Fig. 5.5.

The figure shows a so-called low-p_T trigger, with a threshold of 6 GeV/c, where at least three of the four RPC layers around the BM-station have to give a signal within a prescribed coincidence window. A high-p_T trigger, from 20 GeV/c upwards, demands an additional coincidence with a signal in at least one of the two RPC layers in the BO-station. This way, the trigger logic takes into consideration that an RPC is not 100% fully efficient, while the incidental trigger rate as caused by random background radiation is kept very low. Using other trigger window sizes, it is possible to reconfigure the barrel muon trigger for another threshold value in the range of 6 to 35 GeV/c.

It is impossible to keep the structure of the magnet cryostats with the chambers connected to them rigid[(1)]. So, the necessity arises to register any deformation. This is precisely the task of the alignment system[55–57], which measures and combines all deformations. As remarked already in Sect. 3.5, every MDT chamber houses its own in-plane alignment system with RASNIK[57] monitors. These monitors register every deviation of the middle (cross-)plate with respect to the ends of the chamber. The alignment of the chambers with respect to each other can be done due to the fact that the chambers in the three stations mutually form a projective tower. The four corners of the middle chamber are now monitored by radial, projective light rays with respect to those of the inner and outer chambers. In addition, the mutual positions of the projective towers are registered by proximity sensors and axial light rays. Figure 5.6 shows the alignment scheme without the RASNIK monitors.

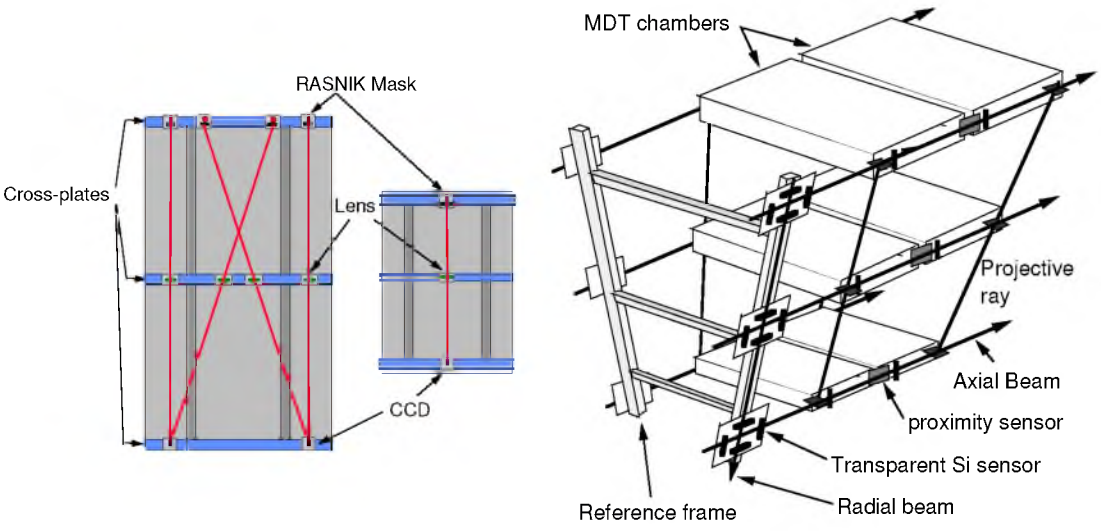

Figure 5.6: Alignment scheme of muon barrel showing the in-plane and overall chamber alignment.

A remark is that the wires of the MDTs run perpendicular to the beam pipe/z-axis. All deformations measured have to be calculated back to deviations on the positions of the wires. Additionally, the RPCs take care of a rough position-finding along the wires,

[(1)]The task to actively reposition the chambers to exactly known locations is too arduous.

which is called second coordinate measurement. The combined resolution needed here is about 6 mm, in order to know the magnetic field strength with sufficient precision. With this knowledge, i.e. the wire position, the second coordinate, the magnetic field and the drift time, it now becomes possible to determine the track position coordinates accurately.

5.2 Muon endcaps

The strategy chosen for the muon endcaps differs from that of the muon barrel, because the cryostat is now a closed structure which makes it impossible to position chambers inside, see Fig. 4.1. Therefore, no direct sagitta measurement can be accomplished in the largest part of the muon endcaps. Still, in order to profit most from the magnetic field, the inner station EI (Endcap Inner) and the middle station EM (Endcap Middle) are placed as close as possible to the endcap cryostats. Using a third measurement station, it becomes possible to measure the angle under which the muon leaves the middle station. Placing the outer station EO (Endcap Outer) further away from the interaction point improves the precision on this measurement. That is why the EO-station is placed against the walls of the cavern in which the ATLAS detector is housed.

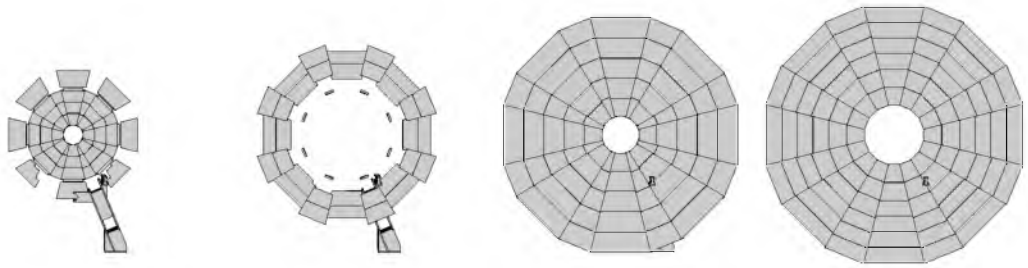

Figure 5.7: The shells of the endcap showing the inner, extra, middle and outer stations. In one sector, the support feet and rail are shown as well.

The EI-station has a double segmentation. There is a radial segmentation in two rings, namely an inner FI-ring (F for forward) and an outer EI-ring (E for external). An eightfold segmentation in azimuth is used for both rings where small (S) and large (L) chambers overlap in the FI-ring. This is not possible for the EI-ring, because the barrel magnet coils are in the way. So only EIL-chambers exist which have the proper cutouts for the support rails. Since the occupancy for an MDT chamber would be too high for chambers close to the beam pipe, CSC chambers are used instead for the FI-station. They are segmented in small and large chambers too, and extend in pseudorapidity over the range $2.0 \lesssim |\eta| \lesssim 2.7$. Figure 3.13 already showed the two types of CSC chamber.

The EM-station is a complete shell extending radially from 173.5 to 1134 cm, with only two cutouts for the rails. Also this station has the eightfold segmentation with large and small chambers in an EM-ring and FM-ring.

The two rings that make up the EO-station are not placed on top of each other, see Fig. 5.3, because the cavern can not be made large enough to allow for this. Actually, only the EO-ring is fixed directly to a support structure on the cavern wall. A trench is made in the cavern floor in order to prevent cutouts to the lowest EOL- and EOS-chambers. The FO-ring is placed even further away from the interaction point, at the end of the beam pipe shielding, which means that it ends up inside the support structure of the EO-ring. Again, both rings show the familiar eightfold segmentation in large and small chambers.

There is a small range[2] in pseudorapidity $1 \lesssim |\eta| \lesssim 1.4$ where it is possible to perform a sagitta measurement in the endcaps. This possibility is supported by the use of an extra station, which is placed on top of the endcap cryostats. Its shape is completely adapted to the space available. There are two semi-rings with an eightfold segmentation. The EE-ring consists of small chambers that fit inside each barrel coil, and of large chambers placed between two barrel coils. A very peculiar BEE-ring consists of small chambers that are placed in the castellations of the endcap cryostats, i.e. in the very small remaining space between endcap cryostat and barrel cryostat, with an orientation similar to the barrel chambers (which explains the B), see Fig. 5.7.

A small overlap exists between every large and small chamber within a station to ensure the best possible coverage. In certain regions, the muon will pass both through endcap chambers and barrel chambers. These regions are denoted as the intermediate or transition region. It is very easy now to lead all services out radially since there is sufficient space between the stations.

The trigger uses an adapted strategy as well, though the logic stays more or less the same. As there is no room inside the cryostats, there is also no use to place trigger chambers at both sides of the endcap magnets. The bending of the muon track by the magnetic field cannot be measured this way. Instead, all trigger chambers are placed behind the magnets, as shown in Fig. 5.8, so that use is made of the fringe field. Since the background radiation is rather high in most part of the endcaps, the decision has been made to use the TGC technology for the trigger chambers. There are double-gap TGCs in front of the EI-station but are used for second coordinate measurement. A triple-gap TGC layer is placed in front of the EM-station, while two double-gap TGC layers are placed behind it. All TGC chambers follow the segmentation of the MDT chambers except for the FM-ring where eight large chambers provide the full coverage. Figure 5.3 already showed the schematic build-up of the endcap. This is clarified in a spatial sense by the pictures in Fig. 5.7.

Figure 5.5 demonstrates the trigger logic. The requirements for a low-p_T and a high-p_T trigger remain practically the same as in the barrel case. Namely, three out of four TGC layers behind the middle station and, additionally, one out of three TGC layers of the inmost station should give a signal in a specified coincidence window. Actually, the sizes of these windows vary because of the very complex magnetic field. The complex magnetic field also necessitates a resolution of 1.1 to 1.6 cm on the sec-

[2]This rapidity range translates into two ranges for the θ-angle, namely $27.7^\circ < \theta < 40.4^\circ$ and $139.6^\circ < \theta < 152.3^\circ$.

ond coordinate measurement, which in fact implies a high granularity for the TGCs. This high granularity makes it easier to obtain sharp thresholds at 6 GeV/c and at 20 GeV/c, while it keeps the incidental trigger rate sufficiently low also, even though the flux of background radiation is considerably larger than in the barrel. Because of the complexity of the magnetic field, there are also trigger windows needed in the non-bending direction. These windows are required to be 100% efficient for all muons. In practice, trigger windows of 13 cm going down in size to 3 cm, in regions far from the coils, need to be used. These values can be compared to the barrel trigger windows, which are 30 to 50 cm depending on the pseudo-rapidity.

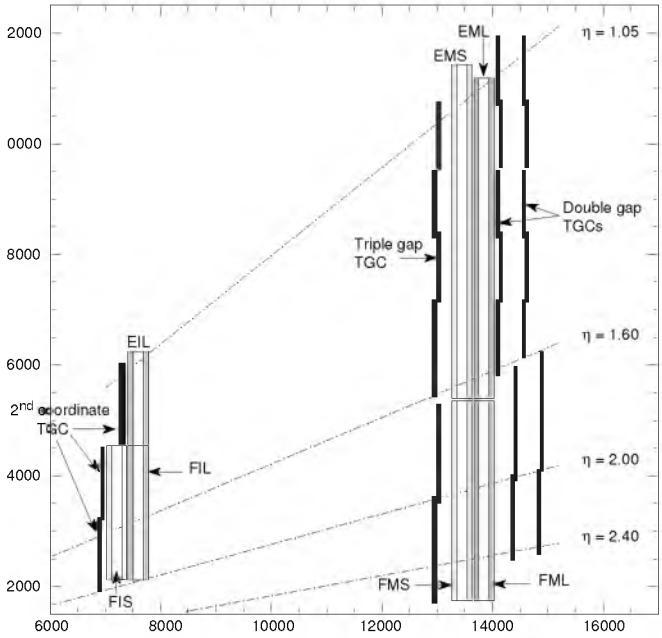

Figure 5.8: Position of TGC chambers in the endcap. Some MDT stations are shown for comparison. The scale of both axis is in mm.

Also the alignment strategy uses a modified concept. Projective towers cannot be realized since not many light rays can be guided through the cryostat. The basic assumption adopted here is that chambers within a plane form a rigid structure. Every chamber is precisely defined and connected by alignment bars to its plane. These planes themselves are placed with respect to reference bars which, in turn, are monitored very precisely. Figure 5.9 shows the concept.

Every displacement of any bar can be translated directly into an appropriate chamber deviation. The bars themselves are made of a carbon fibre composite which has no thermal expansion at room temperatures. Possible deformations of the bars resulting from, for instance, gravity are monitored by on-bar RASNIK systems. There are axial light rays that connect the chamber bars to the reference bars.

A final remark is that triggering with TGCs is foreseen for only part of the angle where CSCs take over from MDTs. This means that the CSCs need to provide the

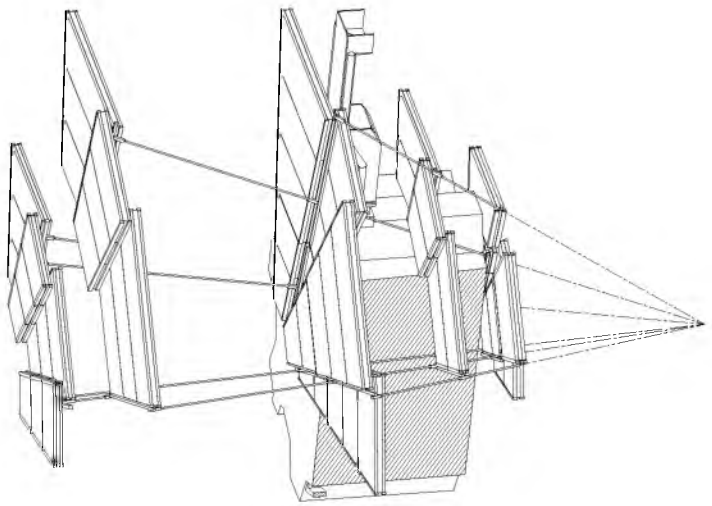

Figure 5.9: Scheme of endcap alignment showing part of the cryostat and measurement stations. The reference bars are barely visible. The station to station alignment bars have a common, virtual point of projectivity.

second coordinate measurement. Consequently, the coverage of the precision measurement chambers is slightly larger than the coverage of the trigger chambers, i.e. $|\eta| < 2.7$ and $|\eta| < 2.4$, respectively.

Chapter 6

Software packages

The software, used for the analyses in this thesis, consists of a fair number of packages. Most of these packages have been made available by the ATLAS software community[58] in the 1.0.1 production release[(1)]. Several packages are part of software releases that are provided by the CERN software community. The dependence on packages of external vendors has been kept to an absolute minimum. Though, it is clear that all software needs to be compiled, i.e. translated into machine executable code, at some stage where the dependence on the machine architecture and (native) compiler support is paramount.

One can order the software packages into a more or less layered model. The lowest layer consists of packages dealing directly with the machine architecture, for instance I/O, graphical and mathematical functions. On top of this is another support layer with packages that provide more elaborate and extended, machine independent I/O, graphical and mathematical functionality. This is CERN software in the form of ZEBRA[60], HIGZ[61] and CERNLIB[62], respectively. Another layer can be said to consist of toolbox packages with well defined interfaces and functionality, like SLUG[63] and GEANT[26], which provide frameworks for event manipulation, i.e. I/O, and detector simulation, respectively. Then, a large number of packages written by the ATLAS users exist, which perform specific duties, like building parts of the detector geometry, collecting signals in parts of the detector, reconstructing the track parameters of certain particles, et cetera. These packages change often since the demands and insights into their functionality are not everlasting. The topmost layer consists of the user applications which are in fact relatively small packages that bind the user packages together into useful programs, as a simulation or a reconstruction program. However, also application programs can be huge, as in case of PAW[64] or other analysis programs.

In the time period from mid 1993 to the production release (and later), which is the time period during which work has been done for this thesis, most of the software packages have gone through an (enormous) transition. This means that functionality has been added, removed, or changed, which in turn means that possible "bugs" have

[(1)] Actually, the 1.0.1 production release is the only production release available. It is in use since 26 May 2000[59]. All releases before and after this one, until 2 August 2001, are development releases which are less well defined.

been introduced and/or corrected. Several packages will be dealt with in greater detail in the next sections and the changes that have been made to them with respect to the production release will be described. Some of these changes have entered in subsequent development releases, others are just for private use.

6.1 Overview of simulation software

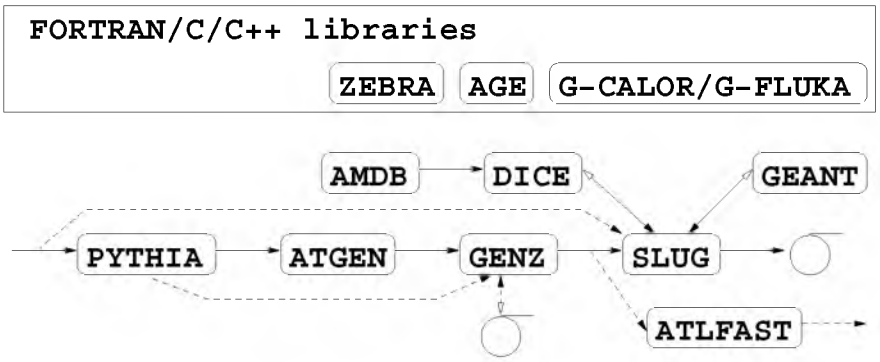

Figure 6.1: Data flow through various packages going from physics (data) to simulated detector data. The dashed lines represent alternatives to the most general data flow which is denoted by solid lines, while the directions of major over minor data flows are given by solid and transparent arrowheads, respectively.

Starting point is an executable program, for instance DiceMain[65], with version tag 00-00-06, which takes a data card file as primary input. Data flow through the executable program is presented in Fig. 6.1. The data cards influence the precise definition of the detector and the physics simulation. Table 6.1 gives a condensed summary of the data card file used for single-particle data generation. Operational data cards for the number of events to be generated (TRIG), random seed initialization (RNDM) and debugging purposes (TRAP, TIME, DEBUG) have been left out for clarity. The file differs from the default data card file[66] proposed by the ATLAS software community.

The first change introduced is an extension to the SLUG package[63], with version tag 01-23-35. The SLUG package is an additional layer on top of GEANT[26], with version tag 21-08-33, and provides unified services to that. In practice, this means that it allows all sub-detectors to be treated in the same way. It also defines the program flow based on the options specified in the data card file. Furthermore, it takes care of the internal data flow, as well as that from and to external files. These duties make SLUG the skeleton of the full ATLAS software.

The subroutine SLBEAM[67] is extended in such a way that there are more possibilities for single-particle generation. The default data card for this purpose is: *KINE* 0 *type* E_{min} E_{max} η_{min} η_{max} φ_{min} φ_{max} *mode*, where *type* stands for the PDG

dicejob_higgsdistribution_single_muons_no_secondaries.dat Page 1/2

```
C------------------------------------------------------------C
C                                                            C
C------- Datacard File for DICE Version 3.21 ----------------C
C                                          27th October 98C
C                                                            C
C------- All detectors are activated                         C
C                                                            C
C------- Muon database should be  M2.8                       C
C                                                            C
C------------------------------------------------------------C
LIST
C GENERATE event: kine(2): electron=11, mu=13, pi=211 g=22 pi0=111
C kine(2)=0: mu+=13 and mu-=-13 alternate
C Higgs distribution in the full detector with mass 150GeV
KINE 0  0.  10.  50.  -2.7  2.7  0.0  6.2831853  150.
C
C ----  digitization and simulation and analysis status
SIMULATION    1
DIGITIZATION  1
RECONSTR      0
ANALYSIS      1
OUTP          1
C allow for larger ZEBRA.0 file of 2G approx. 200000 events
FZLI 2000
*BKIO '0' 'EVNT'
*BKIO '0' 'KINE'
*BKIO '0' 'HITS'
*BKIO '0' 'DIGI'
C
C ------- GEANT TRACKING CARDS -----------------
AUTO 0
OPTI 2
DCAY 2
MULS 2
PFIS 2
MUNU 2
LOSS 3
PHOT 2
COMP 2
PAIR 2
BREM 2
DRAY 2
ANNI 2
C atrecon does not contain hadronic packages
HADR 2
ABAN 0
C  100 keV as a first speed compromize
CUTS 1=.0001 2=.0001 3=.0001 4=.0001 5=.0001
CUTS 6=.001  7=.001  8=.001  9=.001 10=.01
CUTS 11=100.E-9
```

dicejob_higgsdistribution_single_muons_no_secondaries.dat Page 2/2

```
*MODE 'SLUG' 'DEBU' 0 'PRIN' 0 'GRAP' 0
C------------------------------------------------------------------
C
C-GEOMETRY DEFINITION OF ATLAS  (FULL LAR + COIL IN FRONT+ AIR T)-
C
C------------------------------------------------------------------
C
*MODE 'INIT' 'PRIN' 0
*MODE 'GEOM' 'PRIN' 0
*MODE 'DOCU' 'PRIN' 0
*MODE 'CLOS' 'PRIN' 0
*MODE 'DIGI' 'PRIN' 0 'RAND' 1
*MODE 'RECO' 'PRIN' 0
*MODE 'ANAL' 'PRIN' 0
*MODE 'CONS' 'PRIN' 0
*MODE 'GENE' 'PRIN' 0 'RAND' 1 'HIST' 0
*MODE 'INPU' 'PRIN' 0
*MODE 'OUTP' 'PRIN' 0
C  Magnetic field
*MODE 'MFLD' 'GEOM' 1 'MFLD' 0 'PRIN' 1 'HIST' 0
C  The Atlas geometry
*MODE 'ATLS' 'GEOM' 1 'PRIN' 1 'GRAP' 0 'MFLD' 1
*MODE 'PIPE' 'GEOM' 1 'PRIN' 1 'GRAP' 0 'MFLD' 1 'SIMU' 1
*MODE 'CRYO' 'GEOM' 1 'PRIN' 1 'GRAP' 0 'MFLD' 1 'SIMU' 0 'DIGI' 0
*MODE 'COIL' 'GEOM' 1 'PRIN' 1 'GRAP' 0 'MFLD' 1 'SIMU' 0 'DIGI' 0
C      Inner tracker - version 95-1 on   (Morges layout)
*MODE 'PIXB' 'GEOM' 1 'PRIN' 1 'GRAP' 0 'MFLD' 1 'SIMU' 1 'DIGI' 1
*MODE 'PIXE' 'GEOM' 1 'PRIN' 1 'GRAP' 0 'MFLD' 1 'SIMU' 1 'DIGI' 1
*MODE 'SCTT' 'GEOM' 1 'PRIN' 1 'GRAP' 0 'MFLD' 1 'SIMU' 1 'DIGI' 1
*MODE 'ZSCT' 'GEOM' 1 'PRIN' 1 'GRAP' 0 'MFLD' 1 'SIMU' 1 'DIGI' 1
*MODE 'XTRT' 'GEOM' 1 'PRIN' 1 'GRAP' 0 'MFLD' 1 'SIMU' 1 'DIGI' 1
*MODE 'INAF' 'GEOM' 1 'PRIN' 1 'GRAP' 0 'MFLD' 1
C      Calorimetry
*MODE 'CALO' 'GEOM' 1 'PRIN' 0 'RECO' 0 'ANAL' 0
*MODE 'COPS' 'GEOM' 1 'PRIN' 1 'GRAP' 0 'MFLD' 1 'SIMU' 0 'DIGI' 0
*MODE 'ACCB' 'GEOM' 1 'PRIN' 1 'GRAP' 0 'MFLD' 1 'SIMU' 0 'DIGI' 0
*MODE 'ENDE' 'GEOM' 1 'PRIN' 1 'GRAP' 0 'MFLD' 1 'SIMU' 0 'DIGI' 0
*MODE 'HEND' 'GEOM' 1 'PRIN' 1 'GRAP' 0 'MFLD' 1 'SIMU' 0 'DIGI' 0
*MODE 'TILE' 'GEOM' 1 'PRIN' 1 'GRAP' 0 'MFLD' 1 'SIMU' 0 'DIGI' 0
C      Muon  (Parameters read from AMDB muon database)
*MODE 'AMDB' 'GEOM' 1 'PRIN' 1 'GRAP' 0 'MFLD' 0 'SIMU' 0 'DIGI' 0
*MODE 'MINT' 'GEOM' 1 'PRIN' 1 'GRAP' 0 'MFLD' 0 'SIMU' 0 'DIGI' 0
*MODE 'MUCH' 'GEOM' 1 'PRIN' 1 'GRAP' 0 'MFLD' 1 'SIMU' 1 'DIGI' 1
C
STOP
STOP
```

Table 6.1: Data cards of a typical DiceMain job.

particle type[68], e.g. $type = \pm 13$ for a $\mu^{\pm}$, and *mode* defines whether E stands for the momentum p ($mode = 0$) or the transverse momentum p_{T} ($mode = 1$). This way, single particles of one given type are generated with uniform distribution in η, φ and p (or p_{T}). The first extension is to allow $type = 0$ to generate positively and negatively charged muons alternately. The second extension is an attempt to simulate a more physical distribution. To do this, a "Higgs mass" is specified with $mode = 150$, which then results in a single-particle distribution consisting of both μ^{+} and μ^{-} moving out isotropically, i.e. uniformly in θ and φ, from the interaction region with transverse momenta mainly in the range from 15 to 40 GeV/c and an exponential tail falling off to the Higgs mass specified. Figure 6.2 shows the relevant distributions for 400.000 generated single muons, where the tail for p_{T} above 50 GeV/c has been cut off.

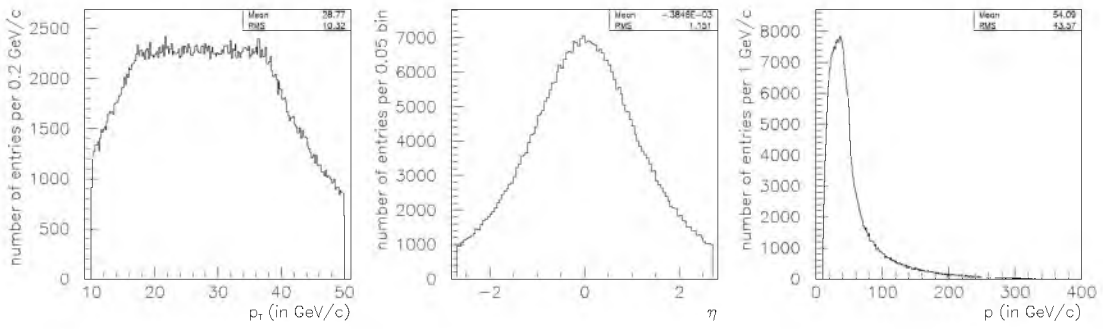

Figure 6.2: Muon track parameter distributions resembling physical events.

The next set of data cards makes clear to SLUG that the simulation, digitization and (simple) analysis stages should be performed for every event and that the output of the generated event and tracks (EVNT, KINE) and simulated signals (HITS, DIGI) should be kept in a separate file for further processing. An additional data card (FZLIMIT 2000) was needed in order to override the default and allow for files greater than 200 MB.

The remaining data cards of the first column help in optimizing GEANT, e.g. so that it orders all volumes/detector elements along the most profitable axis[(2)] (OPTI). Furthermore, the tracking of a particle stops when its momentum is below 100 keV/c (CUTS 1 to 5), thereby releasing the remaining energy into the current medium. This does not hold for electrons, which are treated more carefully (ABAN). Several discrete physics processes (DRAY, BREM, PAIR) are approximated by continuous energy loss calculations for electrons and muons which have momenta below 1 MeV/c (CUTS 6 to 10). Multiple scattering (MULS) is taken into account using the Molière theory[69, 70]. Continuous energy loss (LOSS) due to ionization is applied to particle momenta below 1 MeV/c where restricted Landau-fluctuations are used. δ-rays are generated for particles with higher momenta.

It has been decided not to generate secondary particles originating from discrete processes (DCAY, PFIS, MUNU, PHOT, COMP, PAIR, BREM, DRAY, ANNI), but only to alter the muon track parameters according to these processes. The advantage is a profound speed increase: the simulation of a single muon is, on average, 6 to 7 times faster than in a full physics simulation. This increase will be even larger in case of complex multi-particle events. It is, of course, necessary to perform a number of studies in order to quantitatively understand the disadvantages of this procedure, but they are summarized qualitatively first.

Very important to note is that no electrons originating from δ-ray production are generated and simulated. This means that there will be far less tracks in the detectors that could spoil good signals. The same applies to photons which are suppressed completely and thus cannot generate tracks in other parts of the detector. Signals in calorimeters are obtained from particle showers. These showers are now neither generated nor simulated, so that the calorimeters measure meaningless signals. By default though, many other effects that would spoil signals are already not reproduced, like minimum bias, pile-up, (background/electronics) noise, inefficiencies and chamber deformations.

This thesis concentrates on the muon spectrometer and energy loss corrections along the full track length. So, it was decided to study the difference in energy loss (ΔE) obtained for simulated and non-simulated generation of secondaries in discrete processes. To this purpose, two single-muon samples were generated with $p =$ 45 GeV/c, $\eta = 0.084$, $\varphi = 1.4865$ rad ($\theta \approx \varphi \approx 85.2^\circ$): one with, the other without secondaries. Both samples were generated without multiple scattering contributions (MULS 0) and without a magnetic field (MFLD 0), in order to obtain straight tracks.

[(2)] Given the cylindric nature of the detector, the axis most profitable to increase the tracking speed of GEANT is the z-axis.

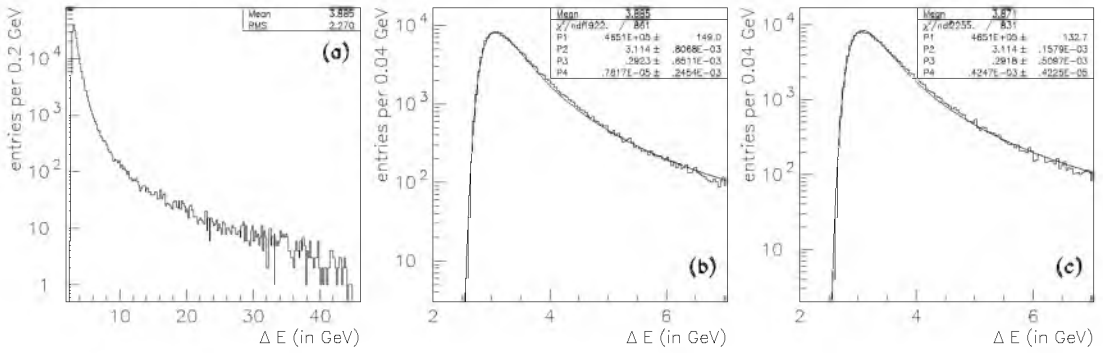

Figure 6.3: Energy loss of perfect muon tracks in the ATLAS detector (a & b) with and (c) without the generation of secondaries.

Figure 6.3(b,c) shows the energy loss distribution in both cases[3]. The graphs are definitely not symmetric, which implies that they are not defined by their mean and rms (root mean square or standard deviation). A simple, standard histogram comparison[71] gives a 93% conformance in distribution shape and normalization.

Davídek and Leitner[72] explain how these distributions can be defined by a normalization factor ($P1$), a most probable value (MOP $= P2 - 0.13054 \cdot P3$), a Gaussian smearing ($\sigma = P4$) and the full width at half maximum (FWHM $= 2\sqrt{2\ln 2} \cdot P3$). The values for these parameters follow from fitting a Landau distribution convoluted with a Gaussian to the energy loss distributions. In case of a full physics simulation we find: MOP $= 3.0754 \pm 0.0002$ GeV and FWHM $= 0.688 \pm 0.001$ GeV, while we find: MOP $= 3.0764 \pm 0.0002$ GeV and FWHM $= 0.687 \pm 0.001$ GeV without generation and simulation of secondaries. The two distributions differ, since the most probable values do not overlap within their error margins. However, the precision of the fit is extremely good compared to the error margins that we are normally[4] dealing with. So, the conclusion is that the results, concerning energy losses, in the remaining chapters are not affected by the choice of secondary generation.

However as already mentioned, all track parameters are influenced by the discrete random processes, and indeed this behaviour is found. In Fig. 6.4(a), the tracks show a spread of 6.4 mm (rms) in both perpendicular directions (with a track length of 14 m), or $\sigma = 5.3$ mm for the half-width of a Gaussian fitted to the central region of the curve, i.e. not taking into account the tails of the distribution. No difference in half-width was found between the two samples.

The smearing behaviour explains why the Landau distribution, which is the expected distribution, has to be convoluted with a Gaussian, in order to get a better fit quality. Only some muons stay very close to the straight track, namely those with the

[3] 200.000 muons were generated, and about 15 of them decayed before reaching the outside of the ATLAS detector, which is a realistic approximation of the decay probability as calculated in Sect. 2.2.

[4] The precision of the convoluted fit is better than 1 MeV while an energy difference of 100 MeV is normally not of importance to the studies in this thesis. Actually, from now on, the term energy loss will be used both for ΔE and Δp since the influence of the mass of the muon is negligible. This also means that momenta can be given in terms of GeV instead of GeV/c.

most probable energy loss. Muons undergoing multiple (different) discrete processes move away from the straight track, thus encountering slightly more or slightly less material. In fact, this is of importance when one makes the choice to correct for the average energy loss or the most probable energy loss.

Figure 6.4(b,c) shows the energy loss distribution when nearly straight tracks have been selected. One can determine from Fig. 6.4(b) that a Landau distribution does not describe the distribution correctly. Instead, a Moyal function[73] fits this cut distribution better for the bulk part of the distribution, see Fig. 6.4(c). The Moyal function represents an analytic approximation of the energy loss of a minimum ionizing particle (mip), i.e. it does not take into account the complexity of multiple discrete processes. So, the conclusion is that muons which stay close to the perfect track (parameters) are also the ones which are described best by the most probable energy loss.

As a last remark one should note that the MOP has not changed much in Figs. 6.3 and 6.4, while the mean, which is connected to the average energy loss, has changed appreciably due to the reduction of tails in the distribution.

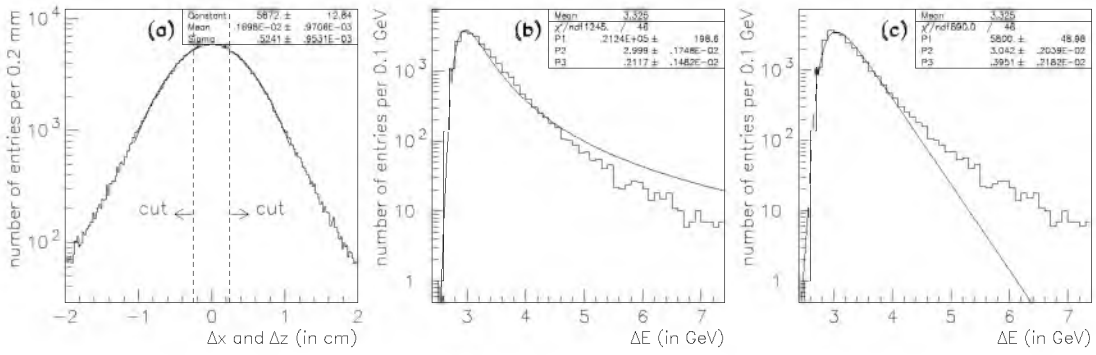

Figure 6.4: (a) Criterion for straight tracks, applied on energy loss calculation for (b) Landau distribution fit and (c) Moyal function fit.

The next data cards are there for debugging purposes and for signalling the actions of SLUG. The magnetic field data card (MFLD) loads the magnetic field map from an external file, for which version B-3D-O.1 (BmagAtlas02.data)[74] was used. The last data cards are used by the DICE package[75], with version tag 03-21-07, and define which detector elements need to be present. There is a division into four regions, namely a region for the beam pipe and shielding, an inner region for the inner detector, a central region for the calorimeters, and an outer region for the muon spectrometer. The precise definitions of these regions are important for this thesis, since it is on the boundaries of these regions that track parameters can be compared between the simulation and the reconstruction.

In order to do this properly, two changes to the production release code were needed. Firstly, the longitudinal boundary between the central and outer region was originally set at $|z| = 676$ cm. However, the geometry description of the muon subdetector (the Atlas Muon DataBase for simulation and reconstruction: Layout AT-640080PL version M, file AMDB_SIMREC.M2.8[76]) expects this boundary to be at

$|z| = 675$ cm. So, it was decided to change the definition in the subroutine ATLSGEO[77] accordingly.

Secondly, the subroutine GUSTEP[78] was changed such that the track information is not only available at the interaction point and at the first material-free location along the track inside the outer region. Instead, the information is made available at the interaction point, at the precisely defined boundaries between regions and at the first point of the track inside an MDT. Figure 6.5 shows the above defined points, together with the names of regions and boundaries for a sample of generated tracks.

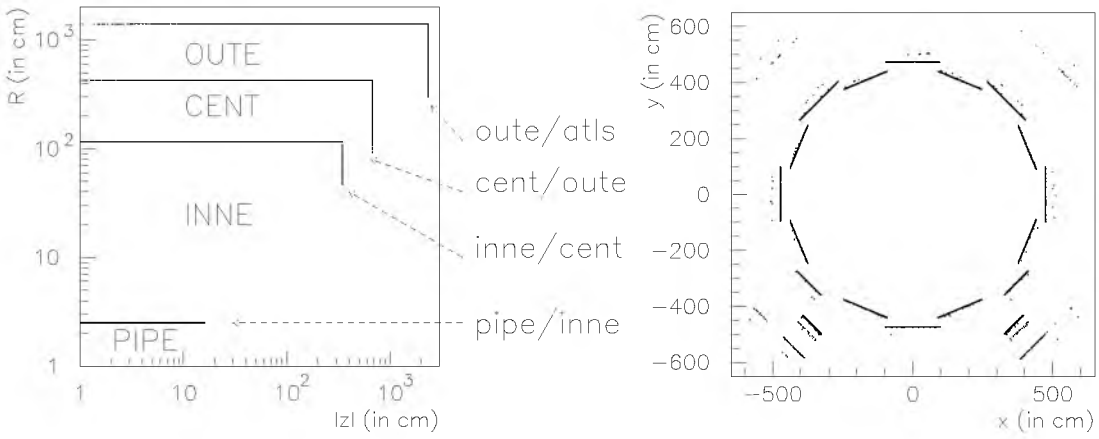

Figure 6.5: Definition of region names, boundaries and first detection point (along the track) in the muon spectrometer barrel.

Actually, the fact is that not DiceMain but AtreconMain[79], with version tag 00-00-15, is used for both simulation and reconstruction. This is possible because all simulation software packages are integrated into the reconstruction program, except for packages dealing with hadronic particles[80], as G-CALOR[81] with version tag 00-00-31, G-GHEISHA[82] and G-FLUKA[83] with version tag 21-08-33. The advantage is that only one executable program needs to be maintained, which helps in preventing mistakes. Simulation of hadronic particles is not needed for this thesis, since we are not interested in jets or calorimetric information. It has been checked that DiceMain and AtreconMain give exactly the same output, when using the same input data cards (and selecting HADR 0 or HADR 2). A few minor changes were made to ZEBCOM[84], PAWCOM[85], and AGSBEGM[86] to allow for much larger data storages.

6.2 Overview of reconstruction software

Starting point is the executable program AtreconMain, which takes a data card file as its primary input. Data flow through the executable program is presented in Fig. 6.6. The data cards influence the origin of data input and outcome of reconstruction and

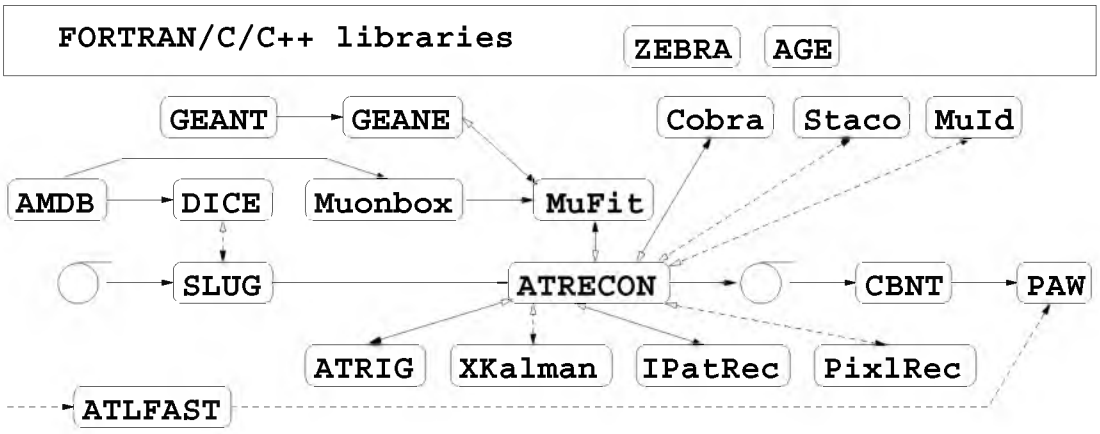

Figure 6.6: Data flow through various packages going from simulated detector data to reconstructed data entities. The dashed lines represent alternatives to the most general data flow which is denoted by solid lines, while the directions of major over minor data flows are given by solid and transparent arrowheads, respectively.

analysis packages. Table 6.2 gives a condensed summary of the data card file for a reconstruction job. Operational data cards for the number of events (TRIG), event selection (PICK, SKIP) and debugging purposes (TRAP, TIME, DEBUG) have been left out for clarity. The file differs in major aspects from the default data card file[87] proposed by the ATLAS software community.

The first data card (KINE -1) is still default and means that the event data are to be read from an external ZEBRA file. The data cards DIGITIZATION, RECONSTRUCTION, ANALYSIS, and OUTPUT also signify that we are performing standard reconstruction. The BKIO data cards define the data that can be found in the external file 'ZEBRA.P', namely: event headers, event kinematics, detector hits, and detector digits. These last two types of data are the output of the simulation run and represent the electronics data which come out of the ATLAS detector.

Part of the reconstruction program depends on GEANE for particle tracking. In order to be able to work with the GEANE package[88, 89], version tag 21-08-33, it is necessary to have the detector description functioning as in the simulation. A default solution would be to read in the geometry from tape, but several tests have shown that this simple approach does not work properly. Consequently, the geometry is generated again, by means of the SIMULATION data card. It was also necessary to make a small change to the initialization routine UGINIT[90] of SLUG. This change checks after the build-up of the geometry tree whether the reconstruction flag has been set, and if so, it assumes that the program needs to be a genuine reconstruction job, thereby resetting the simulation flag. It has been checked thoroughly that this solution gives exactly the expected behaviour in all cases. Namely, the geometry descriptions of both simulation and reconstruction match and GEANT/GEANE functions properly.

Then, a number of data cards follow that will be explained later-on. The left col-

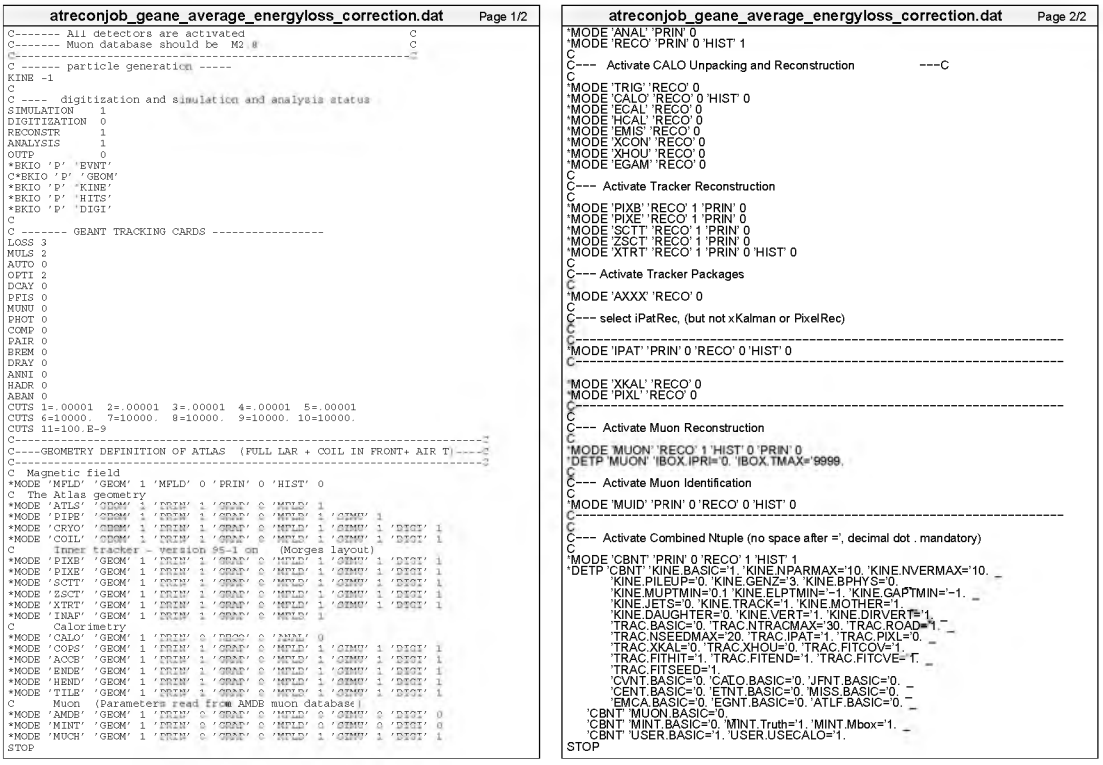

atreconjob_geane_average_energyloss_correction.dat Page 1/2

```
C------- All detectors are activated                                    C
C------- Muon database should be  M2.0                                  C
C-------------------------------------------------------------------C
C ------ particle generation -----
KINE -1
C
C ----  digitization and simulation and analysis status
SIMULATION    1
DIGITIZATION  0
RECONSTR      1
ANALYSIS      1
OUTP          0
*BKIO 'P' 'EVNT'
C*BKIO 'P' 'GEOM'
*BKIO 'P' 'KINE'
*BKIO 'P' 'HITS'
*BKIO 'P' 'DIGI'
C
C ------- GEANT TRACKING CARDS -----------------
LOSS 3
MULS 2
AUTO 0
OPTI 2
DCAY 0
PFIS 0
MUNU 0
PHOT 0
COMP 0
PAIR 0
BREM 0
DRAY 0
ANNI 0
HADR 0
ABAN 0
CUTS 1=.00001  2=.00001  3=.00001  4=.00001  5=.00001
CUTS 6=10000.  7=10000.  8=10000.  9=10000. 10=10000.
CUTS 11=100.E-9
C-------------------------------------------------------------------------7
C----GEOMETRY DEFINITION OF ATLAS  (FULL LAR + COIL IN FRONT+ AIR T)----2
C-------------------------------------------------------------------------2
C  Magnetic field
*MODE 'MFLD' 'GEOM' 1 'MFLD' 0 'PRIN' 0 'HIST' 0
C  The Atlas geometry
*MODE 'ATLS' 'GEOM' 1 'PRIN' 1 'GRAP' 0 'MFLD' 1
*MODE 'PIPE' 'GEOM' 1 'PRIN' 1 'GRAP' 0 'MFLD' 1 'GIMM' 1
*MODE 'CRYO' 'GEOM' 1 'PRIN' 1 'GRAP' 0 'MFLD' 1 'GIMM' 1 'DIGI' 1
*MODE 'COIL' 'GEOM' 1 'PRIN' 1 'GRAP' 0 'MFLD' 1 'GIMM' 1 'DIGI' 1
C     Inner tracker - version 95-1 on   (Morges layout)
*MODE 'PIXB' 'GEOM' 1 'PRIN' 1 'GRAP' 0 'MFLD' 1 'GIMM' 1 'DIGI' 1
*MODE 'PIXE' 'GEOM' 1 'PRIN' 1 'GRAP' 0 'MFLD' 1 'GIMM' 1 'DIGI' 1
*MODE 'SCTT' 'GEOM' 1 'PRIN' 1 'GRAP' 0 'MFLD' 1 'GIMM' 1 'DIGI' 1
*MODE 'ZSCT' 'GEOM' 1 'PRIN' 1 'GRAP' 0 'MFLD' 1 'GIMM' 1 'DIGI' 1
*MODE 'XTRT' 'GEOM' 1 'PRIN' 1 'GRAP' 0 'MFLD' 1 'GIMM' 1 'DIGI' 1
*MODE 'INAP' 'GEOM' 1 'PRIN' 1 'GRAP' 0 'MFLD' 1
C     Calorimetry
*MODE 'CALO' 'GEOM' 1 'PRIN' 0 'DEBG' 0 'ANAL' 0
*MODE 'COPS' 'GEOM' 1 'PRIN' 1 'GRAP' 0 'MFLD' 1 'GIMM' 1 'DIGI' 1
*MODE 'ACCS' 'GEOM' 1 'PRIN' 1 'GRAP' 0 'MFLD' 1 'GIMM' 1 'DIGI' 1
*MODE 'ENDC' 'GEOM' 1 'PRIN' 1 'GRAP' 0 'MFLD' 1 'GIMM' 1 'DIGI' 1
*MODE 'HEND' 'GEOM' 1 'PRIN' 1 'GRAP' 0 'MFLD' 1 'GIMM' 1 'DIGI' 1
*MODE 'TILE' 'GEOM' 1 'PRIN' 1 'GRAP' 0 'MFLD' 1 'GIMM' 1 'DIGI' 1
C     Muon  (Parameters read from AMDB muon database)
*MODE 'AMDB' 'GEOM' 1 'PRIN' 0 'GRAP' 0 'MFLD' 0 'GIMM' 0 'DIGI' 0
*MODE 'MINT' 'GEOM' 1 'PRIN' 0 'GRAP' 0 'MFLD' 0 'GIMM' 0 'DIGI' 0
*MODE 'MUCH' 'GEOM' 1 'PRIN' 0 'GRAP' 0 'MFLD' 1 'GIMM' 1 'DIGI' 1
STOP
```

atreconjob_geane_average_energyloss_correction.dat Page 2/2

```
*MODE 'ANAL' 'PRIN' 0
*MODE 'RECO' 'PRIN' 0 'HIST' 1
C
C---  Activate CALO Unpacking and Reconstruction              ---C
C
*MODE 'TRIG' 'RECO' 0
*MODE 'CALO' 'RECO' 0 'HIST' 0
*MODE 'ECAL' 'RECO' 0
*MODE 'HCAL' 'RECO' 0
*MODE 'EMIS' 'RECO' 0
*MODE 'XCON' 'RECO' 0
*MODE 'XHOU' 'RECO' 0
*MODE 'EGAM' 'RECO' 0
C
C---  Activate Tracker Reconstruction
C
*MODE 'PIXB' 'RECO' 1 'PRIN' 0
*MODE 'PIXE' 'RECO' 1 'PRIN' 0
*MODE 'SCTT' 'RECO' 1 'PRIN' 0
*MODE 'ZSCT' 'RECO' 1 'PRIN' 0
*MODE 'XTRT' 'RECO' 1 'PRIN' 0 'HIST' 0
C
C---  Activate Tracker Packages
C
*MODE 'AXXX' 'RECO' 0
C
C---  select iPatRec, (but not xKalman or PixelRec)
C
C-------------------------------------------------------------------------
*MODE 'IPAT' 'PRIN' 0 'RECO' 0 'HIST' 0
C-------------------------------------------------------------------------

*MODE 'XKAL' 'RECO' 0
*MODE 'PIXL' 'RECO' 0
C-------------------------------------------------------------------------
C
C---  Activate Muon Reconstruction
C
*MODE 'MUON' 'RECO' 1 'HIST' 0 'PRIN' 0
*DETP 'MUON' 'IBOX.IPRI=0. 'IBOX.TMAX=9999.
C
C---  Activate Muon Identification
C
*MODE 'MUID' 'PRIN' 0 'RECO' 0 'HIST' 0
C-------------------------------------------------------------------------
C
C---  Activate Combined Ntuple (no space after =', decimal dot . mandatory)
C
*MODE 'CBNT' 'PRIN' 0 'RECO' 1 'HIST' 1
*DETP 'CBNT' 'KINE.BASIC='1. 'KINE.NPARMAX='10. 'KINE.NVERMAX='10. _
        'KINE.PILEUP='0. 'KINE.GENZ='3. 'KINE.BPHYS='0. _
        'KINE.MUPTMIN='0.1 'KINE.ELPTMIN='-1. 'KINE.GAPTMIN='-1. _
        'KINE.JETS='0. 'KINE.TRACK='1. 'KINE.MOTHER='1. _
        'KINE.DAUGHTER='0. 'KINE.VERT='1. 'KINE.DIRVERT='1. _
        'TRAC.BASIC='0. 'TRAC.NTRACMAX='30. 'TRAC.ROAD='1. _
        'TRAC.NSEEDMAX='20. 'TRAC.IPAT='1. 'TRAC.PIXL='0. _
        'TRAC.XKAL='0. 'TRAC.XHOU='0. 'TRAC.FITCOV='1. _
        'TRAC.FITHIT='1. 'TRAC.FITEND='1. 'TRAC.FITCVE='1. _
        'TRAC.FITSEED='1. _
        'CVNT.BASIC='0. 'CALO.BASIC='0. 'JFNT.BASIC='0. _
        'CENT.BASIC='0. 'ETNT.BASIC='0. 'MISS.BASIC='0. _
        'EMCA.BASIC='0. 'EGNT.BASIC='0. 'ATLF.BASIC='0. _
    'CBNT' 'MUON.BASIC='0. _
    'CBNT' 'MINT.BASIC='0. 'MINT.Truth='1. 'MINT.Mbox='1. _
    'CBNT' 'USER.BASIC='1. 'USER.USECALO='1.
STOP
```

Table 6.2: Data cards of a typical AtreconMain job.

umn of Table 6.2 ends with the geometry description, already familiar from Table 6.1. The right column describes which software packages are to be used during the reconstruction phase. In general, SLUG is made such that it reads in the data cards in two goes: the first part deals mainly with simulation, the second part with reconstruction and analysis. Since the reconstruction part is not executed during the simulation run, Table 6.1 has two STOP data cards following one-another. Table 6.2 has two parts that are both fairly large, because the simulation phase is partly executed in a reconstruction run using the simulation part.

It can be seen from the reconstruction part that the calorimeter are not processed in any way (neither are any trigger data). The data cards ANAL(YSIS) and RECO(NSTRUCTION) are there for debugging purposes. The lower-level packages of reconstruction in the inner detector are, in principle, activated. However, AXXX is not activated in this example and the high-level packages IPAT(REC)[91], with version tag 00-00-33, XKAL(MAN)[92] and PIXL(REC)[93], both with version tag 01-42-26, are not executed either. This means that we are only interested in reconstructing muons when using these particular settings in the data card file.

The software package that performs the muon reconstruction is MUON(BOX)[94], with version tag 05-02-05. The next data card denotes that Muonbox should not output any information (IBOX.IPRI=0) and that it can take an (almost) infinite amount of time to find all tracks in the muon spectrometer (IBOX.TMAX=9999 seconds) per event. This might seem odd since the data cards in the simulation run were chosen such

that the quickest processing was obtained. However, we are interested in the highest possible reconstruction efficiency, which means that all tracks that are present should be found, no matter how long it takes. Figure 6.7 shows the number of seconds used by the muon reconstruction packages for reconstructing single muons in the lower part of the detector. The figure also shows the number of track candidates per single muon.

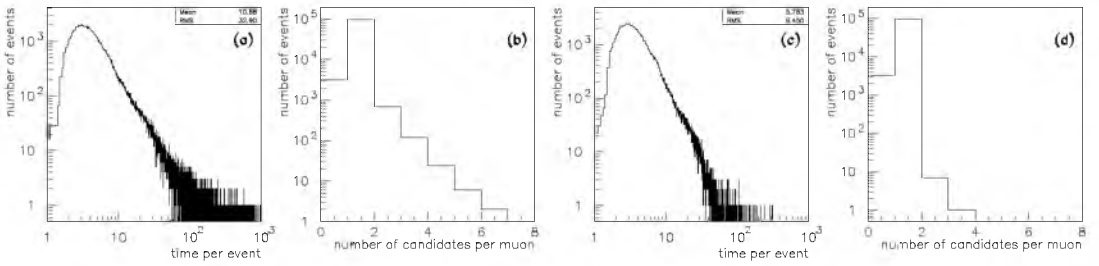

Figure 6.7: Two samples of 100,000 *single muons (a,b) with and (c,d) without incorporation of secondaries during simulation. (a & c) Time needed by muon reconstruction software per event. (b & d) Number of track candidates found per single muon track.*

A significant difference can be observed between the samples with and without generation of secondaries during the simulation run. It can be clearly seen from Fig. 6.7 that the muon reconstruction takes longer when secondaries are generated and simulated by GEANT during the simulation run. This is caused by the fact that more tubes have signals in them, e.g. because they were hit by a δ-electron, whereby more track candidates per event are considered valid by the pattern recognition. Some candidates can be properly removed using information from the other sub-detectors, but this is not taken into account in the studies reported here.

The Muonbox package is by far the most time-consuming package of all reconstruction codes, even though much effort has been put in optimizing the code. It is very advantageous for this reason to store the results of Muonbox in a separate file, which can be read in again afterwards for further processing. The subroutine 'MBox-Commons.cxx' was written to this purpose; it is based on an existing Muonbox subroutine 'MUONMOD'[95]. The subroutine reads or writes the Muonbox data structures IBOX, MBOX, VBOX, TBOX, DBOX, and SBOX as requested and does some additional initializations, which are normally done by Muonbox.

A large number of files needed to be changed to make this by-pass solution work properly. The changes to the MuonboxInterface package[96], with version tag 00-00-19, are: addition of a missing common block to COINTR.INC[97], construction of a C^{++} compliant COFIDR.INC[98] No changes were necessary to COMCAN.INC[99] and COSUPO.INC[100]. Some changes to the Muonbox package concern the files IBOX.INC[101], MBOX.INC[102], VBOX.INC[103], TBOX.INC[104], DBOX.INC [105], and SBOX.INC[106], which were made C^{++} compliant. The tool package AgeToCxx[107, 108], with version tag 01-00-01, was used to obtain the respective

'.cxx' and '.h' files. Also a number of bugs were found and corrected in it. Further testing showed that the data structures read in by MBoxCommons are exactly equivalent to those obtained directly from Muonbox. Small changes were made to 'RECOMU'[109], 'SUPOIN'[110], and 'WRICAN'[111] in order to allow for the necessary inclusion of super space-points into the data (which are disabled in the standard production release).

The main steering routine 'ARECON'[112] of the ATRECON package[113, 114], with version tag 01-42-26, needed to be changed in order to take into account several possibilities concerning muon reconstruction. These possibilities are: read Muonbox data and run MuFit, run Muonbox and run MuFit, run Muonbox and write data and run MuFit, run Muonbox and write data, use Monte Carlo information and run only GEANE. Two packages were written specially for the studies in this thesis, namely 'MuFit', which will be described in appendix B, and 'GEANETracking' which is used in the remainder of this chapter. The latter one uses Monte Carlo information only, provided by the simulation (GEANT), in order to be able to run GEANE and check its performance.

The next data card prevents the muon identification package[115], with version tag 00-00-22, from running since this tries to combine information from the three major sub-detectors. The last package is used for analysis and it combines all requested reconstruction data into one histogram file which is called the combined ntuple[116]. In the form presented, it provides access to the full event kinematics (KINE) and to user provided data (USER). Small changes were made to 'CBNT'[117], 'CBNTTrack'[118], 'CBNTKine'[119] and 'cbntMuid'[120]. 'CBNTUser'[121] was completely rewritten, in order to provide access to the MuFit package results. Also a small problem was discovered in the subroutine 'AgDATCAR'[122], which sometimes prevents certain data cards from being read in correctly. It has been checked that this problem did not occur anymore after the change of 'CBNT' and 'CBNTKine'.

We turn back to the data cards in Table 6.2 that were not dealt with up to now, namely those that are commented as *GEANT TRACKING CARDS*. It seems as if they may only apply to the simulation, but in fact they influence the behaviour of the GEANE package which is used during reconstruction. What happens is that GEANT is initialized in such a way that the geometry description is fully equal to the simulation run, but the parameters for the physics processes are chosen differently. These parameters influence internal GEANT tables which are used by GEANE.

One very important task of the GEANE package is to track particles through the detector. It performs this task in such a way that the track parameters do not change randomly from one step to the other. Instead, the track parameters change analytically and as such give an approximation of the original track parameters. Statistically seen, this means that the track parameters do not change due to multiple scattering, i.e. the MULS data card can have any value different from zero. Of course, the estimated errors on the track parameters do change due to the multiple scattering process. Discrete random processes (DCAY, PFIS, MUNU, PHOT, COMP, PAIR, BREM, DRAY, ANNI, HADR) can not be approximated at all. This means that their data card parameters are set to zero, or an estimation can be made of the energy loss they might induce,

in which case the data cards are set to one/two.

An important choice to be made is whether one wants GEANE to perform an average energy loss correction or a most probable energy loss correction[88, 89]. In the first case, it is necessary to set the CUTS data card to five times low (10^{-5}) and five times high (10^{5}), while the value for the LOSS data card does not matter as long as it is not zero. In the second case, it is necessary to set the CUTS data card to ten times low (10^{-5}) and the LOSS data card should be 2. The explanation comes from the GEANT manual[26]: the CUTS data cards 5 to 10 determine the cutoff energy value (in GeV) where the GEANT internal tables switch from continuous energy loss to full Landau fluctuations. The remaining data cards are needed for optimization purposes only.

The version tag 21-08-33 of the GEANE package suggests that it is adapted to the latest GEANT package that is used by the ATLAS software community. In fact, this is not true: the GEANT tracking routines have changed enormously in GEANT3.16 and GEANT3.21, while the tracking routines of GEANE are still based on GEANT3.15. This gives some incompatibilities. It was decided to correct the subroutines 'ERTRAK'[123], 'ERTRGO'[124], and 'ERTRCH'[125] in order to resemble precisely 'GTRACK'[126] and 'GTMUON'[127] again.

A detailed analysis was performed afterwards to check the compatibility of the two packages, i.e. the old version of GEANE and the corrected version of GEANE. They were found to agree on a step by step basis. It was also checked thoroughly whether both types of energy loss corrections show the behaviour wanted. The GEANETracking software was used on the two samples of Sect. 6.1 while the physics parameters were varied. No difference between the two samples was found during the tracking with GEANE. This obviously has to do with the fact that the tracking during a reconstruction run is independent of the tracking during a simulation run.

Furthermore, there is no dependence on the MULS data card of the tracking parameters at all. There is a small difference in energy loss correction when the discrete random processes are set or not. This difference amounts to about 0.029 GeV. In case the discrete random processes are set (data cards are 1 or 2), then a small amount of the energy is lost due to these processes, during simulation, and the GEANT internal tables are calculated accordingly. This yields a small energy correction deficit during reconstruction when only these tables are used. The CUTS parameters can be varied in a range[(5)] from 10^{-5} to 10^{5} GeV, but it is too hard to interpret any non-extreme value(s). Setting CUTS high yields an energy loss correction of 3.855 GeV, for any LOSS value different from zero, which is a bit less than the expected 3.88 GeV. Setting CUTS low gives a most probable energy loss correction of 3.49 GeV for LOSS$=2$ only, which is much more than the expected 3.08 GeV. It is possible to get the energy loss correction much lower using low CUTS values and LOSS$=1,3,4$ but the energy correction of 1.83 GeV obtained this way is too low. Table A.1 in appendix A has a complete list of energy loss correction values. Giving all data cards the same setting as during the simulation run, see Table 6.1, gives an intermediate energy correction of

[(5)]This statement is not entirely true: CUTS parameter number 10 has a lowest value of 2.04 GeV since GEANT does not permit to let it have a value below four times the electron mass.

2.35 GeV, which is not useful either. The impression might be that there could be a setting that reproduces the wanted 3.08 GeV energy loss, but it was decided not to try and tune the data card parameters in order to obtain this.

The conclusion seems to be that it is best to use the average energy loss correction settings, as shown in Table 6.2. This has been tested with the more realistic data sample, already presented in Fig. 6.2. The realistic data sample has a number of obvious advantages over the samples of one specific track, since the energy and angular ranges considered are much wider, i.e. a large energy range is sampled across the whole detector. The result is presented in Fig. 6.8, which shows the GEANE energy loss correction divided by the GEANT true energy loss during simulation, as a function of pseudo-rapidity.

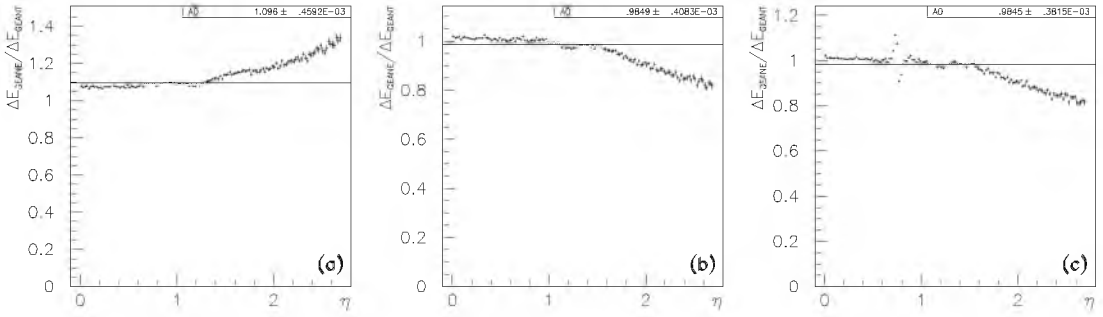

Figure 6.8: Energy loss correction of GEANE divided by true energy loss, (a) using average energy loss correction, or using most probable energy loss correction (b) with GEANETracking and (c) with MuFit.

A number of pronounced problems can be identified. For instance, the average energy loss correction is in fact not an average at all. If so, the ratio should be exactly unity for all angles and momenta, but Fig. 6.8(a) shows the ratio to be always above unity, with a rising tail. Plotting the ratio versus the muon momentum at the vertex, it also starts above unity and rises gradually, but this behaviour cannot be interpreted in a geometrical sense, i.e. no dependence on position or material composition has been found.

From Figs. 6.8(b) and (c), one can see that the ratio is almost unity for pseudo-rapidities up to $|\eta| < 1.56$ in case of most probable energy loss correction by GEANE. This is not as expected, since the most probable energy loss correction is always smaller than the average true energy loss and, hence, the ratio has to be smaller than one. In fact, the ratio should fall off rather slowly, because there are less and less muons that do not lose a significant part of their momentum. This effect is due to the amount of material encountered. It is possible to obtain a flat ratio over the entire momentum range by applying very tight cuts on the true energy loss. This situation would hold when the calorimeters would be well able to measure the energy lost by the muon, i.e. one does not expect GEANE to do the full correction for the energy loss anymore. Anyhow, the tail decreases too fast and too abruptly beyond the pseudo-rapidity $|\eta| > 1.56$. Plotting the ratio versus the muon momentum at the vertex, it

starts above unity and falls off gradually, but this behaviour cannot be interpreted in a geometrical sense, i.e. no noticeable dependence on position or materials.

A wiggle is clearly present in Fig. 6.8(c) in the pseudo-rapidity range $0.7 < |\eta| < 0.8$ which indicates that the detector geometry causes a tracking error. The difference Figs. 6.8(b) and (c) can be explained from the fact that GEANETracking uses exactly the same track parameters as in the simulation, while the track parameters are somewhat off after the fit performed by MuFit. So, the difference in track parameters explains a major difference in the amount of material seen in that region, which coincides with the crack between barrel and extended barrel tile calorimeter.

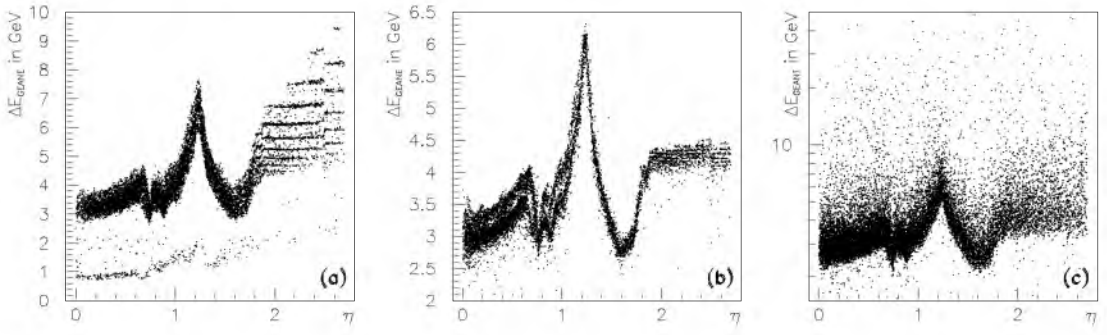

Figure 6.9: Energy correction of GEANE when doing (a) average or (b) most probable energy loss correction and (c) the true energy loss of GEANT.

Figure 6.9 shows possible reasons why the ratios presented in Fig. 6.8 behave unexpectedly. The problems clearly originate from the energy loss correction of GEANE. In case of average energy loss correction, a number of bands appear at high eta, while two bands appear at low eta, in case of most probable energy loss correction. It is very improbable that this should have happened since there is no trace of any kind of band structure in the true energy loss graph of Fig. 6.9(c). The simplest deduction would be that the new tracking routines are at error, but the fact is that the new tracking routines have been introduced precisely for this reason. That is to say: the old version of GEANE showed these band structures as well and it was hoped that the new tracking routines would have cured the problem. As this is not the case, a lot of effort has gone into isolating these effects, and this has been successful.

The eta-dependence of the band structures in the high eta region hints at a geometrical cause, but it was found that the dependence is on momentum rather than pseudo-rapidity, see Fig. 6.10(a). There has been success in separating the bands in the low eta region: a clear phi dependence is observed. This is shown in Fig. 6.10(b). It is possible that certain geometry description packages inside DICE have changed the GEANT parameters of physics processes, but it is not clear how that can explain the band structure observed. There is also a very peculiar band of points below 2.2 GeV in Fig. 6.9(a) which is not understood either. Figure 6.10(c) shows the geometrical distribution of these points with very low energy correction. It is clear again that there are some problems with the combination of the ATLAS detector geometry with the GEANE tracking software.

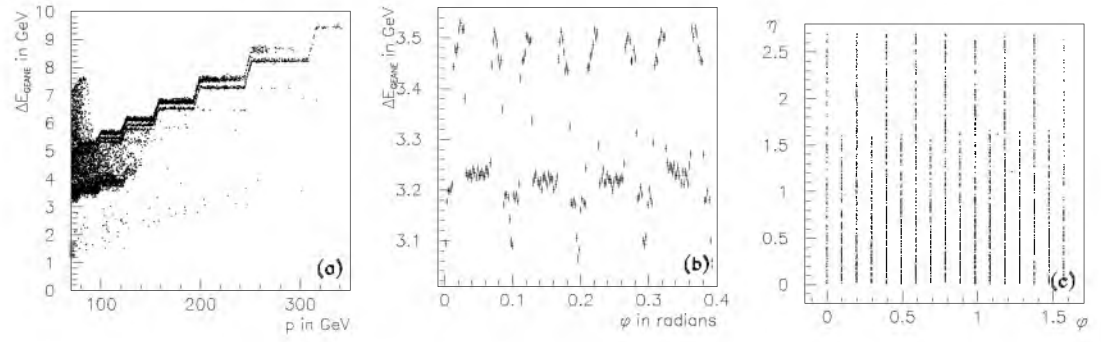

Figure 6.10: (a) Momentum dependence of band structures at high eta ($p >$ 70 GeV$/c$). (b) Phi dependence of bands at low eta ($|\eta| < 1.2$ and $2.6 < \Delta E <$ 4.1 GeV). (c) Eta and phi dependence of low energy loss band ($\Delta E <$ 2.4 GeV).

Anyhow, one concludes that the analysis of a single track is not to be trusted. Instead, a tuning of parameters is needed after all, thereby replacing the suggested parameter settings[88, 89]. The parameters of interest are: LOSS and CUTS (numbers 5 to 10), where the latter ones are more precisely identified as BCUTE/M, DCUTE/M and PPCUTM. If BCUTE/M is set high, then the discrete random process of Bremsstrahlung is accounted for as a continuous energy loss. The same applies for DCUTE/M in case of δ-ray creation and PPCUTM in case of electron-positron pair creation. Tables A.1 and A.2 in appendix A give the full dependence of two tracks on these parameters of interest. One observation of importance is that the PPCUTM has a reverse effect on the tail rise/decrease in the high eta region compared to BCUTM and DCUTM. Numerous tests have proven the combination LOSS 1-4, BCUTM 10^5, DCUTM 10^{-5}-10^5, PPCUTM 10^{-5} and discrete random processes switched on to give a decent ratio. The results are presented in Fig. 6.11. Since these results are good, it is for this reason that the settings, as defined above, have been accepted.

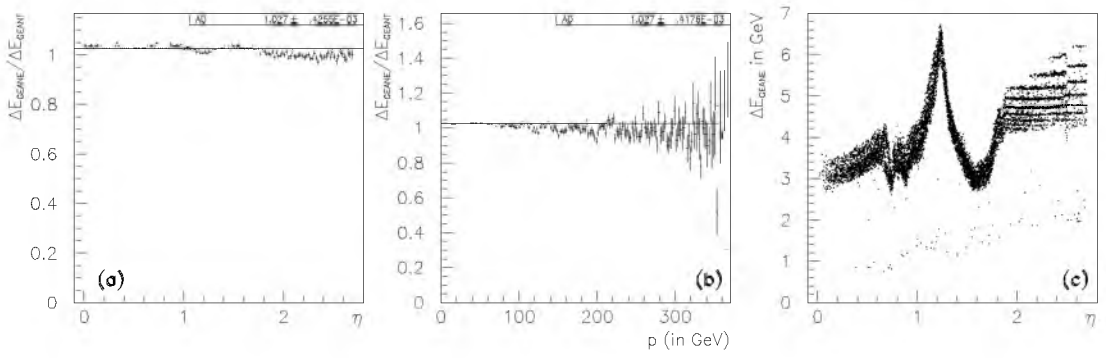

Figure 6.11: Ratio of energy loss correction, for the optimum set of tracking parameters, and true energy loss as function of (a) pseudo-rapidity and (b) momentum. (c) Energy loss correction as a function of pseudo-rapidity.

The other important tasks that are performed by GEANE, as error estimation (on

the track parameters) and error transportation, are not covered in this chapter but are delayed to Chapter 7, instead. It should be noted though that both ratios, in case of average as well as in case of most probable energy loss correction by GEANE, are compatible with unity within their spread (as shown in Fig. 7.16). The geometry and/or tracking problems do not seem to be severe using fitted tracks, compared to the straight tracks of GEANETracking, except for the wiggle at $0.7 < |\eta| < 0.8$.

6.3 Application of standard software

It is quite instructive to go into more detail when looking at the modularity of ATLAS software. Some of it has already been presented in the previous sections, where at least the major division into simulation and reconstruction software has become clear.

The simulation software is divided into two steps: event generation and detector response. In the first step, a generator, as PYTHIA[128], is instructed to sample a number of physics distributions of interest. That is to say: the generator simulates a selected process that can occur when the two particle beams collide in the centre of the detector. The result is kinematical data of the produced (semi-)stable elementary particles, i.e. resonance particles have already decayed by means of the strong interaction. See Chapter 8 for an explanation. The kinematical data consist of particle type and track parameters, see Chapter 2, including the common origins, which are called vertices, of particular tracks. In the second step, SLUG feeds GEANT these kinematical data and the detector description to obtain the detector response signals. They can be the so-called raw signals, from individual detector elements, or they can be so-called digitized, which means that the raw signals are transformed into (detector dependent) electronics data. The task of the simulation software ends here, because we have now obtained data that can be compared to data that comes directly from the ATLAS detector.

The task of the reconstruction software is to help in the analysis of the original physics process. In practice, this means that the underlying physics distributions are reconstructed for the process of interest. The idea behind the reconstruction software is to split up the task into a number of phases[129–131]. The proposed scheme is very elaborate, but the current realization in ATRECON does not follow it precisely, because some packages perform tasks of several phases in one go.

First, the data are moulded in a preprocessing phase, such that they can be easily used by the next reconstruction phases. In practice, this means that noisy or dead channels are flagged as the signals are unpacked. Also, calibration can be performed or background/noise can be added, if that has not already been done before. The preprocessing is different for every sub-detector and should result in the end in well defined (realistic) data. Then, another preprocessing phase is called namely the trigger phase, which is only applied on generated data, since the detector itself performs the triggering during operation. In this phase, it is checked whether all necessary thresholds have been exceeded in order for the data to have been registered in the first place. One would normally expect this to happen during digitization by the simulation software,

but doing it in this step makes it much easier to analyse the effect of certain thresholds. The triggering phase is rather special in the sense that it already performs a fast coarse reconstruction which is, however, not precise/good enough to be used by the next phases.

Phase 1 focuses on a reconstruction per sub-detector. Clusters of energy deposit are searched for and combined by the calorimetry packages. The muon packages search for track elements in the muon chambers and combine them to fitted tracks inside the muon spectrometer. Straight tracks, thus high energy particles, are possibly found and also fitted inside the inner detector.

Reconstruction phase 2 is characterized by the fact that the information from the sub-detectors is combined as much as possible. Tracks from the muon spectrometer are backtracked through the calorimeters and the inner detector towards the beam pipe. The calorimetric clusters also provide seeds for the inner detector to do a more refined track search. In essence, the notion is that the sub-detectors are combined in order to provide and improve track parameters over the full length of the particle track.

Phase 3 is defined as the particle identification phase. This means that every track obtained is checked whether it is compliant with a certain particle hypothesis. The third phase also associates tracks, either from jets or isolated particles, to vertices. As a result, one obtains a list of primary and secondary vertices and updated tracks which originate from these vertices.

The analysis software can be seen as performing the final phase, where it is checked whether the reconstruction objects conform to the physics event. Or, in how far do the reconstructed data match the generated physics distributions ?

6.3.1 Data samples

In the previous section, it has been noted that there are two means to obtain data for the reconstruction software. Since no detector has been built yet, so far only data can be obtained from the simulation software. This part of the thesis focuses on single muons, so that no physics generator is used yet to obtain the physics distributions. A number of data samples have already been used and discussed. Table 6.3 gives more or less just a summary[(6)].

6.3.2 Resolution studies

The complete muon spectrometer has now been described rather elaborately and the reasoning behind several solutions has been explained. Every decision had an impact on the performance, which is normally quantified by the momentum resolution. In fact, a resolution quantifies the match between reconstructed and generated physics

[(6)]The encoding of the physics row has the following meaning: 1 means that secondaries were generated and tracked, while 0 means that there was not any generation of secondary particles in the sample. The encoding of the remark row is as follows: m_H means that realistic distributions were used for the track parameters, as shown in Fig. 6.2, while 'mfld' signifies the absence of a magnetic field, thus resulting in straight muon tracks.

values. Quoted as a percentage of the true parameters, it gives the deviation of the reconstructed parameters. If the detector elements are accurate enough and the reconstruction software works well, then it is possible to have good resolutions such that the original physics process distributions can be extracted from the reconstructed data.

sample number	1	2	3	4	5	6
single tracks	200000	100000	400000	200000	200000	50000
charge	+/–	+/–	+/–	+/–	+/–	+/–
physics	0	1	0	0	1	0
$p_{\min}$(GeV/c)	20.0	20.0	10.0	45.0	45.0	45.0
$p_{\max}$(GeV/c)	448.4	448.4	373.7	45.0	45.0	45.0
$p_{\mathrm{T},\min}$(GeV/c)	20.0	20.0	10.0	44.8	44.8	11.0
$p_{\mathrm{T},\max}$(GeV/c)	60.0	60.0	50.0	44.8	44.8	11.0
$\varphi_{\min}$(radians)	3.32	3.32	0.00	1.48	1.48	1.48
$\varphi_{\max}$(radians)	6.11	6.11	6.28	1.48	1.48	1.48
$\varphi_{\min}$(degrees)	190.00	190.00	0.00	85.17	85.17	85.17
$\varphi_{\max}$(degrees)	350.00	350.00	360.00	85.17	85.17	85.17
$\eta_{\min}$	-2.70	-2.70	-2.70	0.09	0.09	2.09
$\eta_{\max}$	2.70	2.70	2.70	0.09	0.09	2.09
$\theta_{\min}$(radians)	3.01	3.01	3.01	1.49	1.49	0.25
$\theta_{\max}$(radians)	0.13	0.13	0.13	1.49	1.49	0.25
$\theta_{\min}$(degrees)	172.31	172.31	172.31	85.19	85.19	14.19
$\theta_{\max}$(degrees)	7.69	7.69	7.69	85.19	85.19	14.19
remark			m_H	mfld	mfld	mfld

Table 6.3: Description of single muon data samples.

Using models and parametrizations, it becomes possible to make theoretical predictions on the performance of the detector. Because of the extremely large number of parameters involved, it is clear that an exact solution cannot be given. Put differently: the complexity in correlations between parameters and variables is so overwhelming that the design of the spectrometer is based on lots of concessions which had to be made. This shortcoming will sometimes become apparent in results presented. As an example, Fig. 6.12 shows a theoretical prediction of the momentum resolution curve, averaged over the φ-angle, as a function of pseudo-rapidity for $p_{\mathrm{T}} = 100$ GeV/c.

Complicating items that have been taken into account are the three-dimensional magnetic field, the resolution on position measurements, the detailed chamber layout, and a simplified material distribution in order to take material effects into account. The multi-parametric nature of the problem signifies that, in order to get the final curves, several parameters have been averaged, for instance by means of a mathematical integration. Special emphasize has to be put on the η (track) parameter. It essentially denotes the polar angle between a plane perpendicular to the beam pipe, centred around

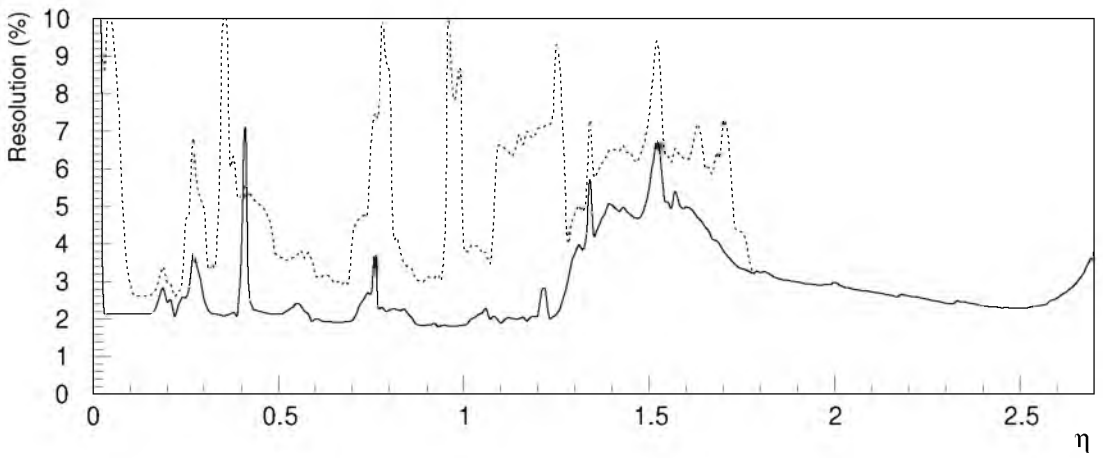

Figure 6.12: φ-averaged momentum resolution for $p_T = 100$ GeV/c muons. The dashed curve corresponds to the bottom sectors, which have a different chamber layout due to the support feet, while the solid curve corresponds to the standard sectors.

the interaction point, and the direction of the muon track. It can, therefore, be seen as a replacement of the more familiar angle θ, using:

$$\eta \equiv -\ln(\tan\theta/2) \ .$$

Inverting the equation gives θ in terms of η. If, in the expression $\tan\theta = R/z$, the angle θ is replaced by $2 \cdot \arctan(\exp -\eta)$ and a Taylor series is made, then it becomes clear that a small change in z results in a proportional change in η according to:

$$z = R/\tan(2 \cdot \arctan(e^{-\eta})) = R \cdot (\eta + \eta^3/6 + O(\eta^5)) \approx R \cdot \eta \ .$$

This relation is sometimes useful in order to get a first insight.

A detailed material distribution inside the spectrometer has been taken into account for the determination of the momentum resolution. The effects of multiple scattering in the magnet support structures stand out clearly from the curves. There is also the influence of the fluctuations in energy loss which occur mostly when the muon passes through the material of the calorimeters. The calculations were based on the principle that an energy loss of more than 5 GeV will be picked up correctly by the calorimeters, which means that there is no influence of catastrophic energy loss on the resolution curves. The alignment was taken into account by translating it into deviations on the chamber positions. All other possible influences on the position measurement were bundled together into one resolution per multilayer.

Care was taken to use the correct chamber layout. It needs to be remarked that some of the spikes in Fig. 6.12 are caused by inefficiencies in this chamber layout. Especially, the wall at $\eta \approx 0$ is due to the layout shown in Fig. 5.3. The effects of the muon trigger were not considered because we are not dealing with any kind of specific physics at this point.

The advantage of a semi-analytic evaluation of the muon momentum resolution is that the turn-around time is very short, i.e. changes in chamber layout and/or material distribution can be recalculated and compared very fast. Doing the same comparisons using the full software chain would yield an unacceptable turn-around time. However, a full simulation and reconstruction gives a better insight into the current state of the software.

However, there is another approach[132] which is more like an intermediate solution. It performs a full 3D tracking instead of using the integrated magnetic field along a straight line. This way, the material present along the track is picked up much more precisely. So, in effect, two simplified integrations, over magnetic field and material distribution, are now replaced by very detailed integrations. The result of this approach is shown in Fig. 6.13. It has the remarkable feature that the wall at $\eta \approx 0$ has virtually disappeared, which can be explained by the fact that the track curvature makes sure that at least three multilayers have been hit. Theoretically seen, it should be sufficient to do a track parameter estimation when three multilayers have been hit.

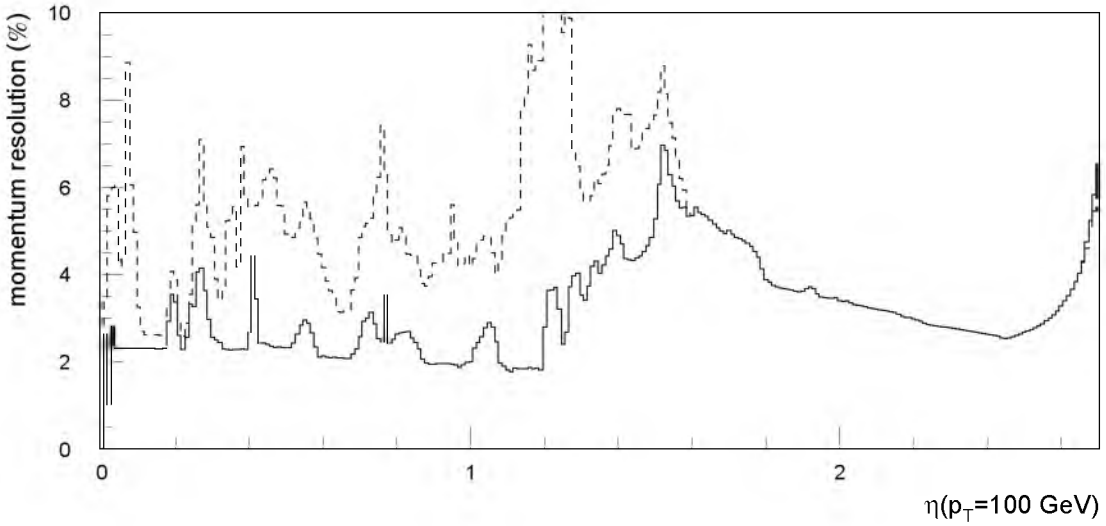

Figure 6.13: φ-averaged momentum resolution for $p_T = 100\,\mathrm{GeV}/c$ muons. Solid curve corresponds to the standard sectors, the dashed curve to the feet sectors.

6.3.3 Pattern Recognition

The theoretical calculations do not take pattern recognition inefficiencies into account. Full track reconstruction is more realistic in that sense, since it depends on the pattern recognition to select the hits belonging to the muon track from all other hits present in the muon detector. These other hits originate from background radiation mainly and are not (necessarily) correlated. Some hits may originate from δ-rays, and they spoil the real muon hit more often. This is also the case with noise from electronics. Correlated noise is not only caused by δ-rays but by punchthrough as well. The

punchthrough comes from pions decaying into muons, in the hadronic calorimeters, mainly. According to calculations[133–135] of the influence from photon and neutron background, the single tube occupancy will in general remain below 10% for the MDTs.

Thermal neutrons, i.e. with energies below 100 MeV, have a very small cross section, which allows them to travel a long distance through gas. These neutrons generate an abundance of low energy (< 10 MeV) photons that cause ionizations of the detector gas inside the MDTs. Since it would go too far to explain the origin of these backgrounds, one should keep in mind that they are of such complexity that it is hard to calculate the rates and occupancy levels in the muon system. Typical detector capture efficiencies for photons are lower than 1% and even lower than 0.1% for neutrons. However, the rates can be as high as 1 kHz/cm^2 for photons and 10 kHz/cm^2 for neutrons, respectively, inside the MDTs. While they are even a factor ten higher for the highest pseudo-rapidity, where the CSCs have taken over from the MDTs. Figure 6.14 shows the total counting rates, obtained by multiplying the background rates with the detector efficiencies, as a function of pseudo-rapidity.

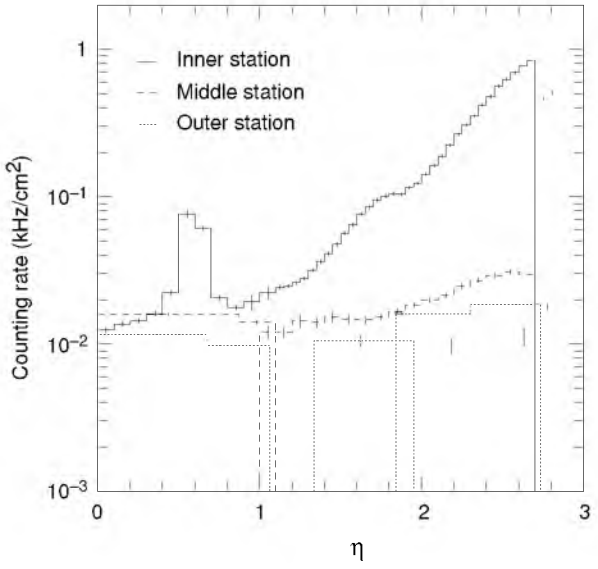

Figure 6.14: Total counting rates, in the three stations as a function of pseudo-rapidity, due to background radiation.

It should be remarked that it is also very hard to do a decent background simulation. For this reason, it has been decided to use an additional safety factor. The necessity for this follows from an example of a worst-case scenario. Consider a large chamber in the inner station at $\eta \approx 0.7$. It has a tube length of 2.7 m and can undergo a rate of 80 Hz/cm^2. At maximum drift time, this yields an occupancy of $500\ \text{ns} \times 80\ \text{Hz/cm}^2 \times 3\ \text{cm} \times 270\ \text{cm} \approx 3\%$. The effect of the background hits is that a muon track cannot be recognized or found by naked eye. This is shown in Fig. 6.15.

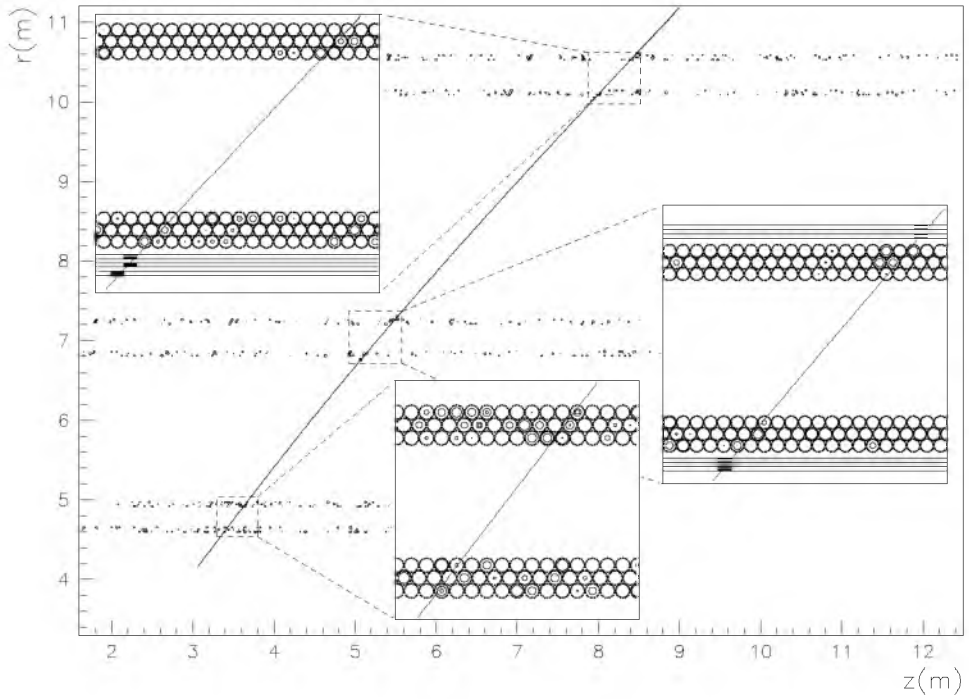

Figure 6.15: Recognition of a single track with magnifications of regions traversed by the muon. All other hits stem from background radiation.

Many algorithms exist[136] for performing pattern recognition, of which a number have been used by ATLAS[53, 94, 137–139]. The most important one is Muonbox[94], which is an implementation of the standard ATLAS software. It has been used already for many studies. The starting point is to combine hits using certain logic in the most outward chambers, because the occupancy is lowest there. This logic depends on a good knowledge of the *r*-*t* relation, see Fig. 3.19, to obtain a reasonable drift distance measurement from the measured drift times. Necessary corrections for the Lorentz angle and signal propagation time, along the wire, are inferred from the coarse second coordinate measurement and the corresponding magnetic field. The intricate interplay of track location and corrected drift time measurement calls forth additional iterations before the final track location is found.

Now, the profit from having separated the two multilayers or mattresses with a spacer structure becomes evident, since combining the two line-pieces (vectors) of the multilayers immediately rejects a very large part of the random background. Using the second coordinate, as measured by the trigger layers, makes it possible to reconstruct a track segment in the outermost measurement station. This strategy can be applied to the middle and inner stations as well, though it results in many more faulty segments caused by the higher occupancy. The momentum can now be estimated for every sensible set of three segments using for instance a Look-Up Table (LUT)[137]. Here, the task of second-level triggering ends[138]. Performing a more precise tracking now improves the error on the estimated momentum significantly. Spoiled hits, e.g. where

the drift time has been influenced by a δ-ray, and inefficient tubes are recognized at this stage.

It is also possible for the pattern recognition, i.e. Muonbox, to start constructing vectors in the middle station and combining them to segments. The association of these segments in the middle station to the segments in the outer station can be done already using precise tracking to obtain a good momentum estimate. This way, it becomes much easier to find the proper segment in the inner station, since this segment needs to have a good fit with the track obtained in the previous step.

As an example, Muonbox is able to find back at least 95% of the tracks simulated in the interval $-2.8 < \eta < 2.8$, with a chance of less than 0.1% of reconstructing a wrong[7] track. Figure 6.16 shows an example of entry points into the spectrometer of tracks that were not found by the pattern recognition. The presentation is deformed, because the samples used have tracks mainly in the two bottom sectors and because all points have been projected onto a quarter of the detector. The black areas correspond to the cutout around $z \approx 0$ m and to the support feet and rails.

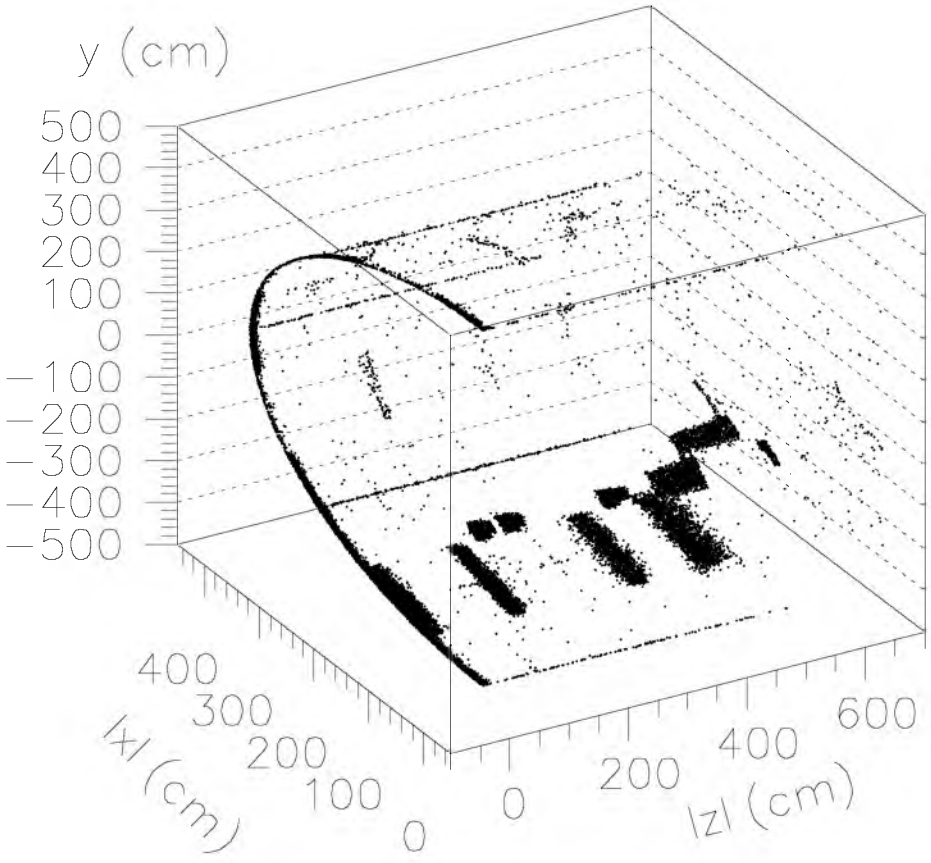

Figure 6.16: Spectrometer entry points of unrecognized tracks.

[7] Also called fake or ghost track.

6.3.4 The parameter fit

The pattern recognition delivers estimates of the track parameters at the innermost muon measurement station. However, in order to be able to do proper physics, it is necessary to know the track parameters and appropriate errors at the interaction point. The MuFit program was written to accomplish this task. It performs a separate fit of the track parameters in the spectrometer and does a backtracking[8] of them to the primary vertex. The materials present and the magnetic field inside the ATLAS detector are dealt with very concisely. MuFit uses the results of Muonbox in order to deliver the track parameters and error estimates at every point along the muon track, or likewise, at every desired location inside the ATLAS detector.

[8] The backtracking ensures a proper treatment of energy loss corrections because energy loss in the case of normal tracking becomes "energy gain" in the case of backtracking.

Chapter 7

Usage of MuFit

Now, that the chain of software has been described, it becomes important to check whether the quality of the fit procedure is sufficient to meet certain requirements. A number of tests are tackled to give a feeling of this quality. As the studies for this thesis have progressed during the years, one can also say that the understanding and, therefore, the quality of the software has increased during the years. A valid conclusion which results from this notion is that the quality and understanding will definitely still increase during the coming years. Actually, this statement proved to be right already, since the performance of the MuFit package (developed until June 1996) is less in comparison with Cobra[140], which has the best performance at present and still is in development. It is interesting to note that like MuFit the Cobra package is also based on GEANE. So, the aim of this thesis is not to show the ultimate performance, but only to show the state of affairs with the software as described previously. It is left to other scientists to perform additional studies to progress beyond this point.

In order to keep a good overview, it is necessary to say something about the MuFit internals, before going into a performance analysis. However, the reader is referred to appendix B for a detailed account on the programming structure of MuFit and its interaction with GEANE. MuFit needs a certain amount of input before it can start the fit procedure. The requirements on this input have been kept to a minimum with the profit to allow any pattern recognition code[(1)] to feed its output to MuFit. The input consists of a list of track candidates, where every candidate needs to be accompanied by a minimum of track information. This track information consists of the positions of the multilayers or mattresses, as defined in Sect. 3.5, and the positions therein, that have been hit, with an appropriate error estimate for every position. To speed up the fit procedure, it is useful to have a preferred sign of the charge and a momentum estimate, though this is not strictly necessary.

The information is transformed to a coordinate system used by GEANE. This yields the additional profit that every possible type of information is available in a well-defined reference framework. In this framework, a multilayer is essentially re-

[(1)] In practice, Muonbox is the only pattern recognition code for the muon spectrometer that has been developed by the ATLAS software community and it, currently, does a lot more than only the pattern recognition.

placed by a plane of infinite dimensions. The track angles are deduced from the two multilayers of the outermost station. GEANE tracks the muon from the most outside multilayer to the multilayer closest to the calorimeters. All previously defined planes are crossed this way and it is possible to compare the calculated track parameters with the pattern recognition information. Depending on the quality[2] of the pattern recognition information, the track will be pulled towards the preferred position, in every plane. If the initial momentum or charge estimate was completely off, then it takes more iterations before the final track parameters are obtained.

After all track candidates have been fitted, the second phase of muon reconstruction is started. Another coordinate system, or reference framework, is used, so that the track parameters are easily obtained at the volume boundaries of interest. The volumes and boundaries are defined in Fig. 6.5. In this second phase, MuFit can also perform a seed generation. A seed is defined at the boundary between inner detector and calorimeters, so that it can be used by inner detector pattern recognition codes. Sect. 7.4 deals with MuFit generated seeds in detail.

There has been no attempt to use MuFit for the third reconstruction phase, i.e. an overall refit of the muon track, as the design of MuFit is too rigid to make this possible. Part of the success of Cobra can be explained by the fact that it is flexible[141] enough to be used for the third phase.

7.1 Super space-points

The fit procedure of MuFit starts where the pattern recognition of Muonbox ends, namely at the point where it is more-or-less clear which muon detector elements constitute a track. Muonbox also has computed track parameters at the entrance to the muon spectrometer. However, what was[3] missing and is needed for physics studies, is the estimate of the errors on the track parameters. This is one of the main reasons why the MuFit package has been developed.

Instead of going back to the detector hits and trying to use them for the fit, it has been chosen to use an approach which is faster by making the simplistic assumption, in the first phase of the muon reconstruction, that the pattern recognition has found a valid track. During a later phase, the third one to be precise, the fit procedure can try to figure out whether the track is really valid and which hits should actually be used. The faster approach entails the use of part of the information already available. In each multilayer, a three-dimensional space-point has been calculated by Muonbox from the combined information of the detector hits in that multilayer or mattress. This point is called super space-point. It consists of three space coordinates, i.e. the location of the space-point, with an estimate on their respective errors.

[2] This quality or weight is proportional to the inverse of the squared error estimate.

[3] The version of Muonbox, with tag 05-02-05, included in the ATLAS software 1.0.1 production release does in fact have error estimates on the track parameters at several locations along the complete track, namely at the vertex, at the boundaries between inner detector, calorimeters and muon spectrometer. So, it is possible to make a direct comparison between Muonbox and MuFit.

Figure 7.1 shows the reference frames used by Muonbox, which differ from the Cartesian overall ATLAS coordinate system. The frame in the muon barrel differs from that in the muon endcap, because the MDT detector tubes have different orientations.

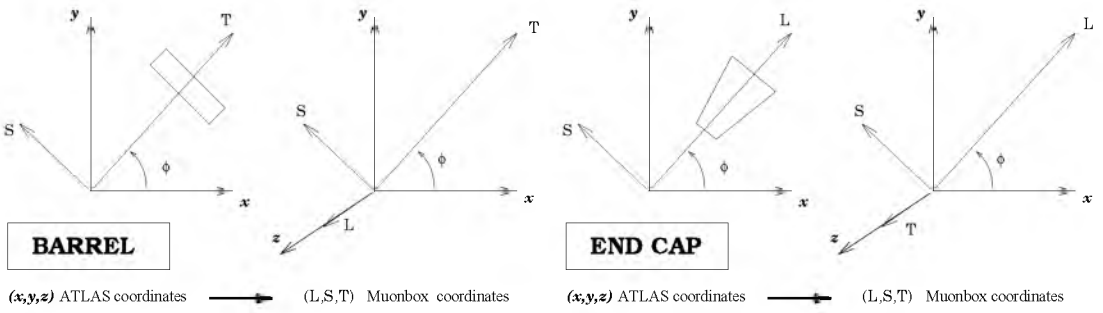

Figure 7.1: Two and three-dimensional comparison of ATLAS and Muonbox coordinate systems in the muon spectrometer barrel and endcaps. Cross sections of an MDT chamber are shown in the two-dimensional frames.

A super space-point consists of the set (L, S, T) with error estimates σL, σS and σT. Both for the barrel and the endcap, S stands for the distance of the hit along the tube wire to the middle of the tube, see Figs. 7.2 and 7.3. Figure 7.2 shows an arbitrary MDT multilayer in the spectrometer barrel with its corresponding (L, S, T) reference frame, while an MDT barrel chamber is shown in Fig. 7.3 along with the proper directions of L, S, and T. It might seem awkward, in first instance, to use the coordinate set (L, S, T), but in fact it is a natural choice.

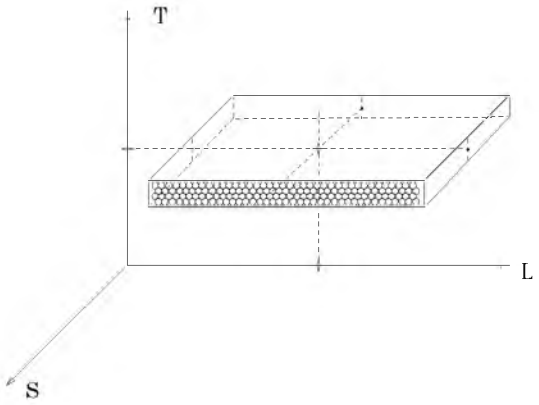

Figure 7.2: MDT multilayer placement in barrel-(L, S, T) frame.

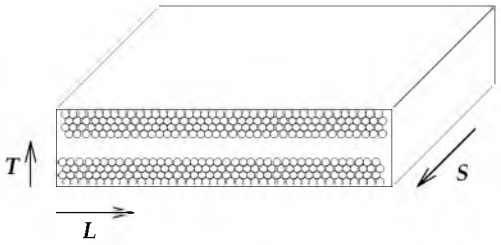

Figure 7.3: Definition of L, S, and T directions relative to an MDT barrel chamber.

The sign of S gives the direction along the wire as seen from the beam pipe in either clockwise(+) or anti-clockwise(–) sense. It is often called the non-bending parameter.

The bending parameter is denoted by L and stands for the distance of the hit to the centre (of gravity) of the station, measured along the tube layer and orthogonal to the

non-bending parameter. It can have a negative sign only in the muon barrel, where it defines which hemisphere of the barrel is concerned.

Finally, the parameter T stands for the distance between the centre of the ATLAS detector and the centre of the multilayer with the hit. It, in turn, is orthogonal to both the bending and the non-bending parameters. The parameter T can have a negative sign only in conjunction with a hit in one of the muon endcaps, where the sign distinguishes between the forward and the backward endcaps.

Since only distances are given and no directions, it is still necessary to have additional parameters defining the orientation of the reference system. For this purpose, Muonbox also provides the sector number of the multilayer and the information of whether it concerns the barrel or one of the endcaps.

To summarize the text above, one can compute the following transformation tables. For the muon barrel the table looks like:

$$\begin{aligned} z &= L \\ x &= T\cos\phi - S\sin\phi \\ y &= S\cos\phi + T\sin\phi \ , \end{aligned} \tag{7.1}$$

or

$$\begin{aligned} L &= z \\ S &= y\cos\phi - x\sin\phi \\ T &= y\sin\phi + x\cos\phi \ . \end{aligned} \tag{7.2}$$

For the muon endcaps it is as follows:

$$\begin{aligned} z &= \pm T \\ x &= L\cos\phi - S\sin\phi \\ y &= L\sin\phi + S\cos\phi \ , \end{aligned} \tag{7.3}$$

or

$$\begin{aligned} T &= |z| \\ L &= y\sin\phi + x\cos\phi \\ S &= y\cos\phi - x\sin\phi \ , \end{aligned} \tag{7.4}$$

where the plus or minus sign determines whether to use the forward (+) or the backward (–) endcap.

The idea behind the construction of the muon spectrometer is to have three concentric measurement stations around the beam interaction region. Ideally, each station should enclose the angular region defined by $0 < \varphi < 2\pi$ radians and $-2.7 < \eta < 2.7$. This would provide six super space-points in six multilayers for every muon track thus giving enough opportunity to perform a satisfactory pattern recognition and track fit. However, most stations do not cover the full angular region and there are overlaps between chambers inside a station. Figure 7.4(a) shows the number of super space-points

used by MuFit for the muon track. The majority of tracks has been fitted using six super space-points indeed. One track of this particular sample was lost during the fit as it has zero super space-points used.

The location of every muon chamber inside the spectrometer is well known. This is due to the fact that the chambers are precisely put in place, and because any chamber movement is registered by the alignment system. The accuracy of the alignment system is reflected in the parameter T, since it measures the distance between the centre of the beam pipe and the middle of the multilayer. According to [34], a typical accuracy of 20 μm is needed, so this is used as the error estimate (σT) on this measurement.

The bending parameter L is also known precisely, since it has a direct relation to the distances between the track and the wires, as can be seen from Fig. 7.3. Since this distance is known with a typical error of about 85 μm, the so-called single-wire resolution, the statistical average over the three layers is still better, with a typical resolution of 65 μm[34]. Sometimes, not enough layers have hits, so that the super space-point in that multilayer cannot be computed. This would result in a very large error estimate on the bending parameter in that particular multilayer. It is for this reason that Muonbox leaves out those multilayers.

Figure 7.4(b) shows the Muonbox provided measurement error estimate on the bending parameter L. This estimate is sometimes, misleadingly, called measurement resolution, or even resolution for short. The appearance of two distinct low value spikes can be traced back to the subroutine 'SUPOIN'[110] of Muonbox, which calculates the measurement error estimates on the super space-point coordinate values. It imposes a hard lower limit of 85 μm divided by $\sqrt{2.5}$ in case of a super space-point determined from a three tube multilayer, or divided by $\sqrt{3.5}$ in case of a four tube multilayer. The underlying reason is that a measurement in one multilayer only, cannot be better than these hard lower limits. So, the best possible measurement is 45 μm in the barrel inner stations, and 54 μm in all other stations.

As can be seen from Fig. 5.5, only part of the multilayers have trigger chambers fixed to them. Since the measurement of the non-bending parameter S can only come from these trigger chambers, this implies that an error estimate on S can only be derived in those cases. The segmentation of the trigger chambers varies throughout the spectrometer, so that the typical measurement error varies between 1 cm and 3 cm. However, the combined measurement is a bit better still. For those multilayers which do not have a measurement on the non-bending parameter, a large default error estimate (of 50 cm) is taken. Figure 7.4(c) shows the Muonbox provided measurement error estimate on S. The non-bending parameter is often called second coordinate measurement.

Again, a structure of spikes can be distinguished in this sub-figure. It is also caused by the 'SUPOIN'[110] subroutine of Muonbox. The pattern is too complex to allow an explanation for every spike, but it can be derived from three sets of numbers. The first set represents the segmentation of the RPCs. Here, we have three values: 3.07, 3.89, and 3.95 cm. They are to be combined with a second set consisting of the values: 2, 4, 6, $\sqrt{8}$, and $\sqrt{12}$. This second set represents the divisors for the first set that come from specific combinations of trigger chambers. The third set consists of the values 0.5 and

0.75 cm, which represent the hard lower limits used for the TGCs. It is of interest to note that the smallest measurement resolution possible, about 0.5 cm, is obtained both in the barrel and endcap middle stations.

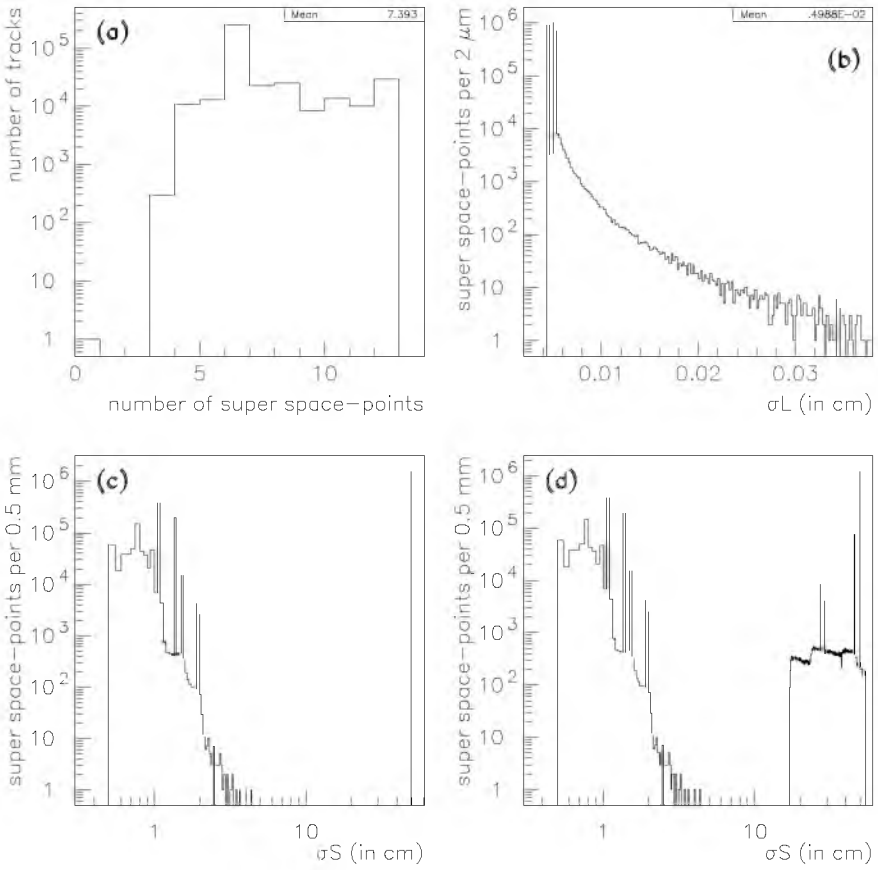

Figure 7.4: (a) Number of tracks with a given number of super space-points. Measurement error estimate (b) on L parameter and (c) on S parameter. (d) Improved measurement error estimate on S parameter.

Now, a possible strategy is to treat the super space-point information provided by Muonbox as is, i.e. MuFit performs a first phase track reconstruction without trying to use any additional information. However, there is another strategy proposed with respect to the large default error estimate on S. Statistically seen, a valid error estimate would also be the length of the MDT tubes divided by $\sqrt{12}$. This latter factor comes from the statistical variance/accuracy[(4)] of a uniform distribution[28]. Figure 7.4(d) gives the newly obtained measurement resolution on S. The spike at 50 cm has decreased a bit, thus giving rise to a plateau from about 20 cm upwards. However, as will be shown later on, the influence of this improvement on the reconstructed track parameters and fit quality is small.

[(4)] A uniform distribution has a probability density function: $f(x) = 1 \forall 0 \leq x \leq 1$, from which the variance is calculated as: $\sigma^2 = \int_0^1 x^2 dx - (\int_0^1 x dx)^2 \Rightarrow \sigma = 1/\sqrt{12}$.

Using the transformation tables, Eqs. (7.1) and (7.3), one can calculate the ATLAS coordinates of all super space-points. This has been done for many tracks, and the results are shown in Figs. 7.5 to 7.7. The structural layout of the spectrometer can be recognized, as well as the fact that two multilayers are separated by a space(r).

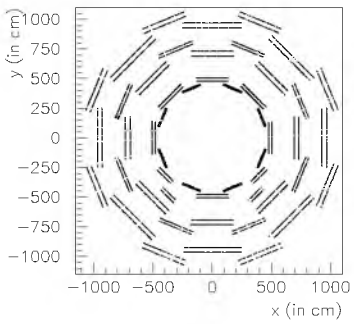

Figure 7.5:
Barrel super space-points in x-y projection.

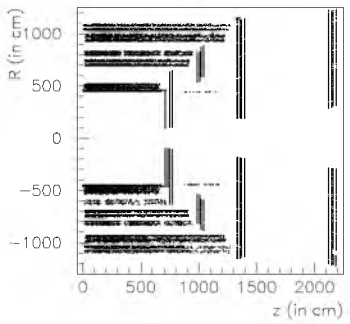

Figure 7.6:
Super space-points in R-z projection.

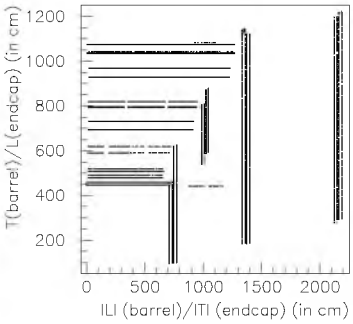

Figure 7.7:
Super space-points in L-T projection.

As can be envisaged from the previous, the success of the fit, performed by MuFit, depends heavily on the quality of the pattern recognition, as performed by Muonbox. So, if Muonbox does not find a particular track then it cannot be processed by MuFit either. Likewise, any ghost track found by Muonbox is presumed valid by MuFit and processed as such. The quality of the fit depends on the quality of the super space-points, i.e. the error estimates or weights on them. This means that MuFit cannot do better than Muonbox, provided the latter functions optimally. However, it has been shown[142] that Cobra obtains better results than Muonbox, since it uses more information. In fact, one should speak of an iterative, competitive process in which packages are constantly updated and improved, in order to overhaul weaknesses[(5)] and/or to gain an advantage over the other packages.

Figure 7.8 shows the track finding efficiency of the pattern recognition, without taking into account the quality of track parameters. It is clear that there are difficult areas, where only two measurement stations or even less are available. The presence of these problem regions has a direct influence on the recuperation possibilities of the physical processes, i.e. distributions, under study. Otherwise[(6)], the performance of Muonbox is excellent, with an average track finding efficiency of over 99.5%.

[(5)] An example: version 5.2.5 of Muonbox performs significantly weaker for very low energy muons, approximately 5 GeV/c and less, when compared to MuFit (and Cobra). The reason for this behaviour has been identified and, therefore, the newer releases of Muonbox do not show this weakness anymore.

[(6)] The track reconstruction efficiency is about 97% when averaged over the full detector, i.e. $|\eta| < 2.7$.

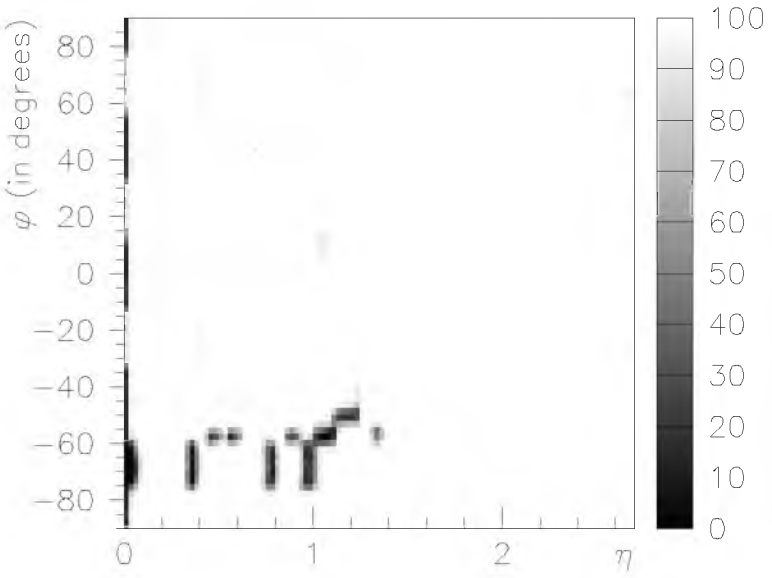

Figure 7.8: Tracks recognized by Muonbox as a percentage of the GEANT generated tracks, as a function of η *and* φ *for one quarter of the spectrometer.*

7.2 Consistency checks of MuFit

Experience over the years has proven that it is always necessary to perform a number of relatively simple tests. The chain of software is of such complexity that a lot of non-foreseen behaviour can occur (at rather surprising places sometimes). Especially, since many people have contributed to parts of the software chain, it has to be verified how one part can have unexpected effects on other parts. These tests should have been straightforward and easily performed, after each new release of the ATLAS software framework. In practice, it has often been necessary to check every part of the software chain, before the MuFit package, in order to solve problems encountered by the fit software. In Chapter 6, we have already described necessary changes, in detail. Here, only a number of tests will be presented which are essential to MuFit. These tests are based on the differences between Muonbox and MuFit, or put differently: the extra[7] functionality of MuFit forms the basis of the consistency checks.

Even though not much material is present in the spectrometer, it is necessary to take it into account and to correct the track parameters for it. If it is not possible to apply a correction, then at least the error estimates on the track parameters can be changed in such a way that they correctly reflect the effect. Since the GEANE software package, used by MuFit, makes use of the detailed geometry description of GEANT, i.e. the simulation, this implies that the distribution of material inside the spectrometer is precisely known.

[7] Actually, the extra functionality applies only to the situation of several years ago, when Muonbox did not do the backtracking (nor did Muonbox provide the error estimates on the track parameters).

The material distribution, as seen by infinite momentum muons[8], is shown in Figs. 7.9 and 7.10. Figure 7.9 shows a map of the average energy loss inside one quadrant of the spectrometer, as seen by the simulation. The measure used is the number of radiation lengths (X) encountered, divided by a specific gauge (X_0), which is the mean distance traversed by a high-energy electron before it has lost all but $1/e$ of its energy by bremsstrahlung. For aluminium(-equivalent): $X_0 = 24\ \mathrm{g/cm^2}$ with a corresponding mean distance of 8.9 cm.

Figure 7.10 shows the same map, but this time using the average energy loss, as calculated by the reconstruction software, for two quadrants of the spectrometer (corresponding to one quarter of its full size). The appropriate, corresponding gauge is now 57.6 MeV for a 40 GeV/c muon, which experiences a mean $\mathrm{d}E/\mathrm{d}x = 2.4\ \mathrm{MeVcm^2/g}$ in aluminium. One observes several structures, namely the barrel coils (at $\varphi = \pm 22.5^\circ$ and $\pm 67.5^\circ$), the endcap coils (at $\varphi = 0^\circ, \pm 90^\circ$ and $\pm 45^\circ$) and the support feet (at $\varphi = -71^\circ$ and -64°).

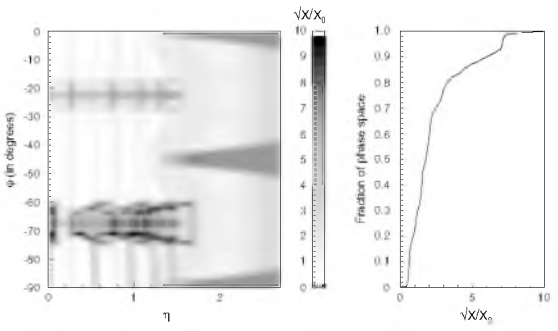

Figure 7.9: Map of square root of number of radiation lengths, inside the spectrometer, as a function of η *and* φ *(left). Fraction of phase space versus maximum number of radiation lengths (right).*

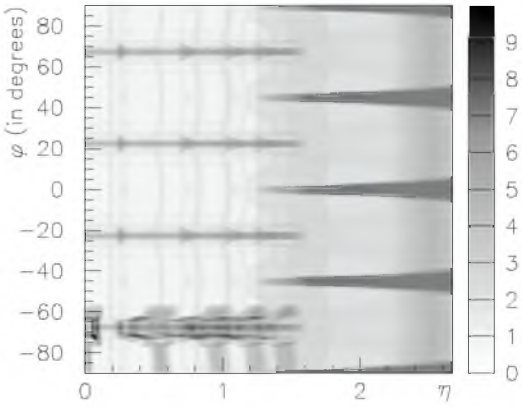

Figure 7.10: Map of square root of the average energy loss correction, divided by 57.6 MeV*, as a function of* η *and* φ*.*

7.2.1 of multiple scattering

The track following procedure of GEANE takes multiple scattering into account by increasing the error estimates on the track parameters. It cannot change the track parameters themselves, because multiple scattering induces an angle of deflection in a random direction with an unknown amplitude. Averaged over an infinite number of tracks, one would obtain zero nett deflection. Straight tracks have been used to produce Fig. 7.11, but multiple scattering effects were turned on during simulation, this time.

[8]These straight tracks cannot be simulated, nor do they exist in reality of course, but they can be approximated well by turning off the magnetic field, multiple scattering effects and energy losses (also those due to discrete random processes).

This means that samples 4 and 6 from Table 6.3 have been augmented[9]. At the vertex, the track parameters were taken from the simulation by GEANT. Figure 7.11 shows the differences between the GEANT location (L,S) of the track at the exit of the ATLAS detector and the expected location of the track if it were a completely straight line. Figure 7.11 also shows the deviation of the track angles (θ,φ) at the exit of the detector compared to those expected for a straight line. The bulk of the distributions is described by a Gaussian, while they all exhibit a non-Gaussian tail as explained in Sect. 2.1.3. The magnitude of the deviation of the two orthogonal track location parameters is the same, as the amount of material encountered is exactly equal for both. Any possible difference in these parameters is purely statistical.

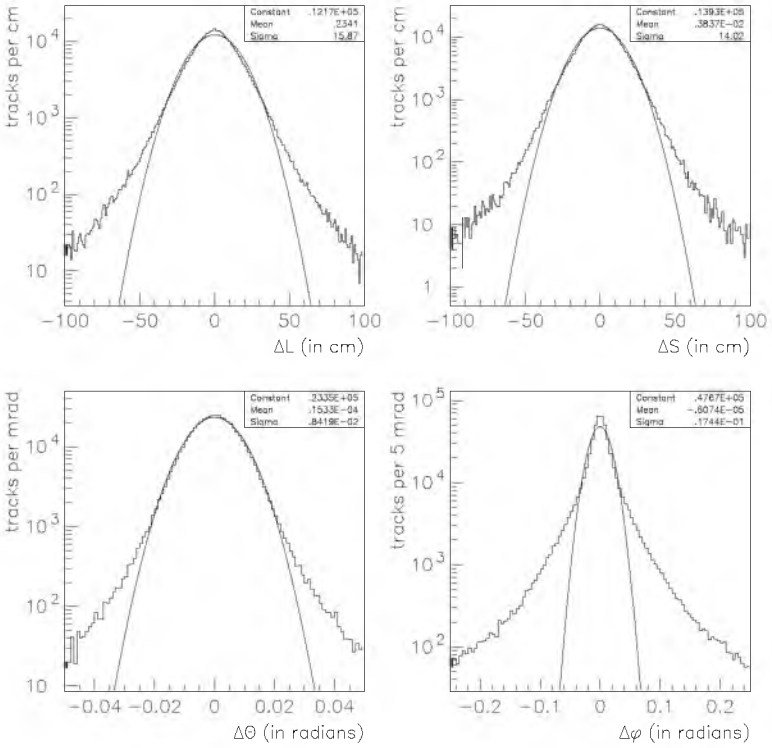

Figure 7.11: Deviation due to multiple scattering from a straight line of track parameters L, S, θ, and φ, computed after simulation by GEANT at the exit of the detector.

The same track parameters at the vertex have been fed into GEANE. This time, there is no deviation from a straight line, but the error estimates on the track parameters reflect the presumed deviation. These error estimates of the track parameters at the exit of the detector are plotted in Fig. 7.12. It should be noted that another modification to

[9]The augmentation alone is not of interest, since two sets of track parameters are concerned. The figures were produced using a sample of 500.000 tracks in the full detector, containing both μ^- and μ^+ with momentum 25 GeV/c, the magnetic field and all energy loss processes were turned off, thereby obtaining tracks affected by multiple scattering only.

the GEANE program-code had to be made, in order to obtain this result. Subroutine 'TRPROP'[143] is modified, entailing the change of a sign[(10)] in some of the matrix elements[141].

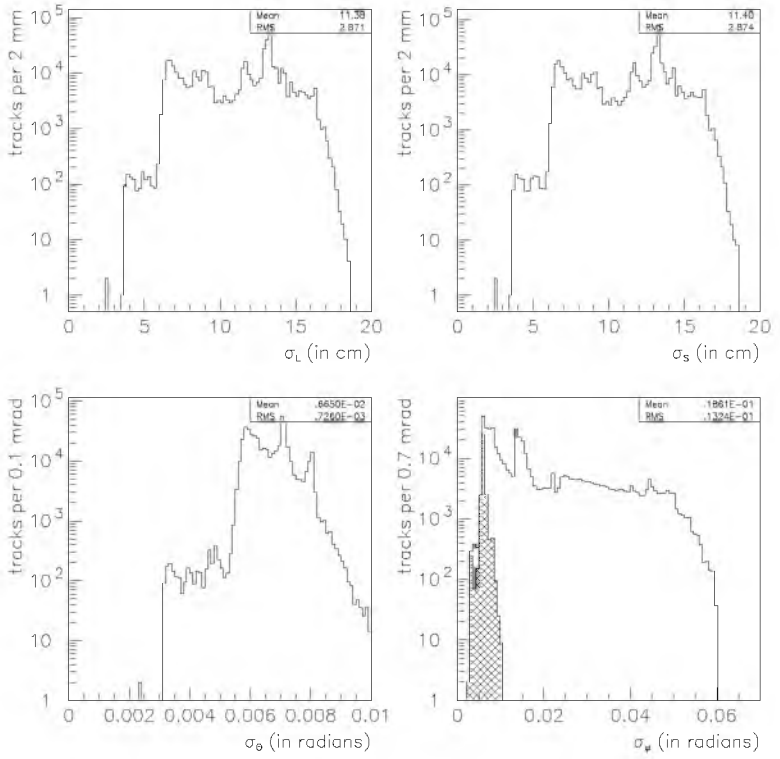

Figure 7.12: Reconstruction error estimate coming from multiple scattering only, for track parameters L, S, θ, and φ. The shaded area represents tracks isotropic in θ and φ.

Though it seems strange at first glance, it is actually natural that the error estimates on the track parameters L and S are similar. The underlying reason is that it is the amount of material seen, which determines the magnitude of the error estimate. This amount does not differ, of course, between L and S. On the other hand, the error estimate distributions on φ and θ differ, because the detector extends more in the direction of the latter. Put differently, the track generation is non-isotropic in θ and φ, which causes the difference in Fig. 7.12. In the plot of the error estimate σ_φ on φ, an area is shaded that represents those tracks that are isotropic, which is true for $|\eta| < 0.2$ only. It extends to 0.01 radians just like σ_θ. One observation, which does not follow from the figure, is that the error estimates correlate very well, i.e. $\sigma_{\theta,L} = \sigma_{L,\theta} = \sqrt{\sigma_{L,L}\sigma_{\theta,\theta}} = \sigma_L\sigma_\theta$ and $\sigma_{\varphi,S} = \sigma_{S,\varphi} = \sqrt{\sigma_{S,S}\sigma_{\varphi,\varphi}} = \sigma_S\sigma_\varphi$, while all other

[(10)] A coordinate transformation from a spherical coordinate system was used, instead of a transformation from a cylindrical coordinate system. As the transformation has to go from a natural multiple scattering coordinate system to the natural coordinate system of the magnetic field[144–146].

correlations remain zero. This means that the displacement of the track is indeed completely explained by the change of angles.

Finally, Fig. 7.13 shows that GEANE, on average, has an error estimate compatible with the real deviation, though it exhibits a consistent underestimation. The distributions are almost Gaussian with widths larger than one, where the tails can be attributed to rare large scatters. The conclusion which results from this is that multiple scattering is correctly taken into account during the fit procedure by an increase of the error estimates on the track parameters. However, the method used by GEANE to take the multiple scattering into account, is based on a classical approximation, which is not valid because of the small step size involved. Furthermore, as is noticed here, the Particle Data Group[68] states that the usage of this approximation method results in an underestimation of the multiple scattering effect.

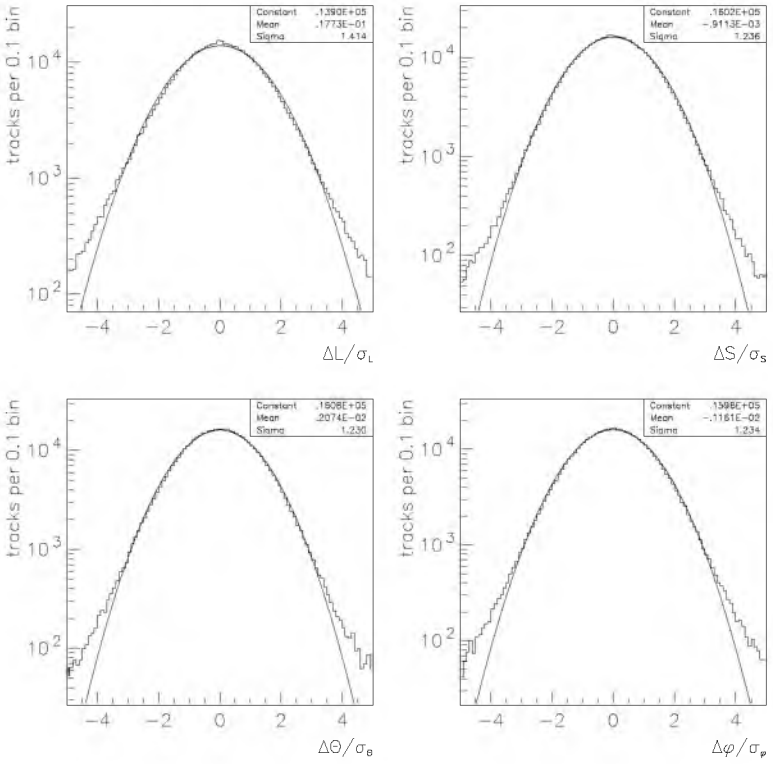

Figure 7.13: Real deviation of straight track divided by estimated deviation/error, for the multiple scattering effect only.

7.2.2 of energy loss

One important property of the fit procedure is that it can trace back the track to its point of origin. While doing this, the calorimeter is tracked through and since the calorimeter consists of a lot of material, a muon loses on average about 3.5 GeV of its energy in it. Although it should be possible to reconstruct this energy loss from the information

available inside the calorimeter, at least first studies have shown this to be a difficult task. However, in case of a large energy deposit such as catastrophic energy loss by the muon, it is expected that the calorimeter is able to signal such an event. Still, we want to keep the procedure as fast and simple as possible with the consequence that no information of other sub-detectors is used during the first phase of the muon track reconstruction. So, we rely completely on the ability of GEANE to correct the track parameters (and error estimates) for energy losses. In order to check this again (see also Sect. 6.2, Fig. 6.11), track parameters were compared at the entrance and exit of the calorimeters.

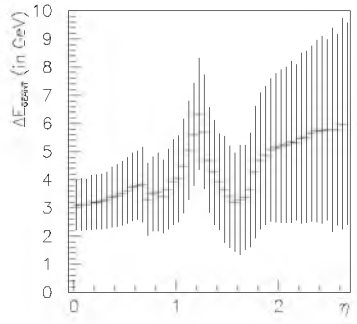

Figure 7.14: Spread on average energy loss, according to GEANT.

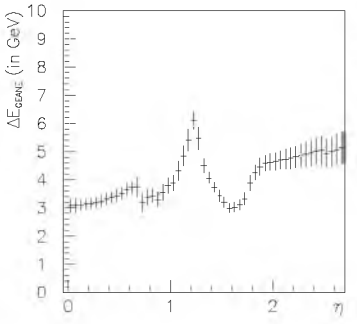

Figure 7.15: Spread on average energy correction, according to GEANE.

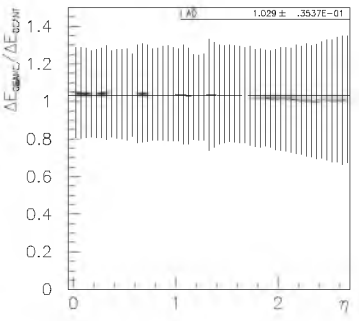

Figure 7.16: Spread on comparison of simulation and reconstruction.

In Fig. 7.14, the average energy loss of a muon during the simulation by GEANT is plotted, along with error bars showing the spread in energy loss. Cases of catastrophic energy loss have been cut out as not to deform the picture. A structure stands out clearly around $|\eta| \approx 1.3$. It is due to the material[(11)] of the extended barrel tile calorimeter[80].

Figure 7.15 uses the same tracks but the energy loss correction of GEANE is plotted. It shows a much smaller spread.

Finally, Fig. 7.16 shows the comparison of the energy loss during simulation with the energy recuperation by the reconstruction, again exhibiting the spread. This comparison is based on the division of the energy loss correction according to GEANE by the true energy loss according to GEANT. The average of the division is close enough to one as to conclude that the energy loss of a muon is correctly taken into account during the fit procedure (see also Sect. 6.2).

The spread on the average energy loss shown in Fig. 7.14 is not at all reproduced by Fig. 7.15. Still, it is important to have an indication of this effect, which is in fact reflected by the increase of the estimated error σ_E on the momentum (or energy) parameter, shown in Fig. 7.17. The appropriate comparison, in Fig. 7.18, leads to the

[(11)]Figure 1-4 of the ATLAS Calorimeter Performance TDR[80] shows the number of absorption lengths as a function of η. In general this number stays below 15 but has an (isolated) peak at $|\eta| \approx 1.3$.

conclusion that GEANE has a correct estimation of the energy loss fluctuations, as long as catastrophic energy losses are signalled by other means.

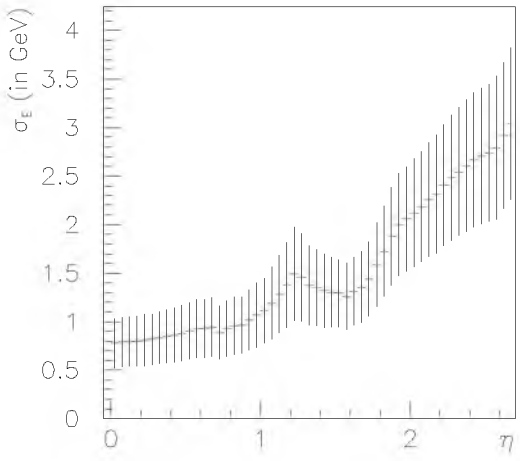

Figure 7.17: Spread on average energy loss fluctuation estimate.

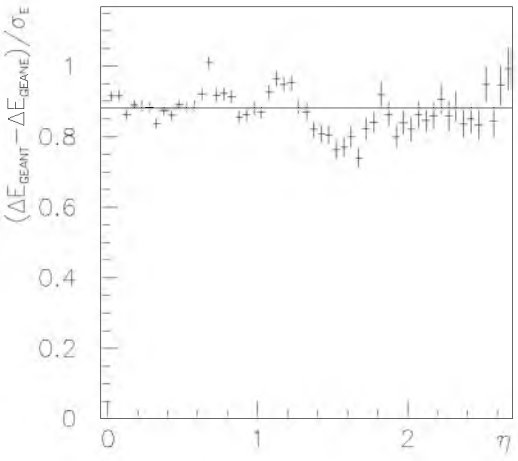

Figure 7.18: Comparison of real and estimated energy loss fluctuation.

7.2.3 of pull distributions

Another type of test is one which shows the validity of the fit procedure itself, i.e. whether the mathematics has been implemented correctly. A little trick is played in order to perform the fit in a controlled manner. This is done with the assumption that the result of the procedure has to be known if the input into it is known. So instead of using the measurements as made available by Muonbox, the whole pattern recognition is replaced by a toy model. It computes the super space-points and associated measurement error estimates, as well as the track parameters at the entrance of the spectrometer directly from the Monte-Carlo information of the simulation.

There is some difference between the error on a parameter and its error estimate, also often called error window. Suppose that the error on a measurement is known[(12)] to have a Gaussian distribution, then a typical value for the error estimate would be the width of that Gaussian. Likewise, a uniformly distributed error on a parameter has an associated error window of half of its half-width. In all cases the real error distribution divided by the error estimate has to result in a distribution with its mean at zero and width (RMS) at one, e.g. as in Fig. 7.20. In this case, we would be able to construct an optimal fit procedure[28] to the underlying distribution(s). The distribution of the absolute measurement error divided by the ideal measurement error window does not

[(12)] It is fundamentally impossible to obtain the error on a measurement, as this value could only have been obtained by another measurement, which results in a spiral dependence. In practice, an error estimate, or even a measurement error, is checked by a statistical combination of high precision measurements.

necessarily have its mean at one. It is at one for the uniform distribution, but not for the normal distribution, see Fig. 7.19.

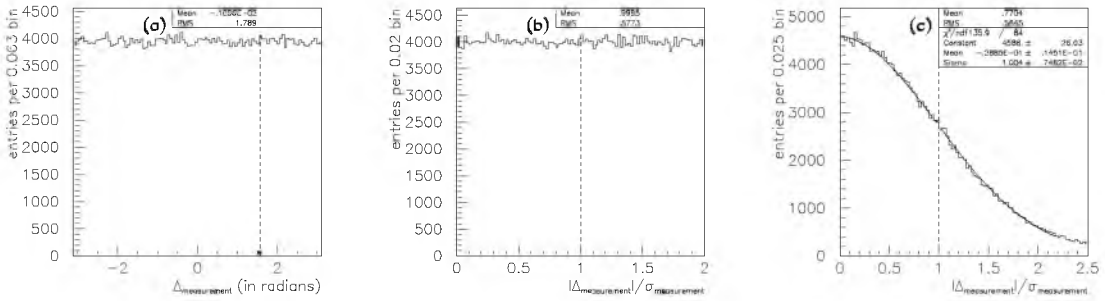

Figure 7.19: (a) Uniform distribution of 2π total width. Absolute errors divided by error window, for (b) uniform and (c) normal distributions. The error window, or error estimate, is represented by a dashed line in all three examples.

Errors on L, S, and T are taken randomly according to Gaussian distributions and imposed by shifting the obtained MC track locations. Since the error on T reflects more-or-less the error on the position of the chamber, it can be considered negligibly small compared to the others because the position is supposedly well known. The errors on L and S are chosen such that they become more comparable, instead of being several orders of magnitude apart as is the case with the super space-points obtained from Muonbox, see Fig. 7.4. This helps to check the stability of the fit procedure. Figure 7.20 shows the errors as imposed by the toy model. The appropriate (1σ) estimates of the measurement errors are shown by dashed lines, but the imposed estimates differ from them in order to study the behaviour of the fit procedure. The imposed estimates are: $\sigma_L(\text{before fit}) = 10$ cm and $\sigma_S(\text{before fit}) = 0.1$ cm, i.e. a large overestimation of the measurement error ΔL and a large underestimation of the measurement error ΔS, respectively.

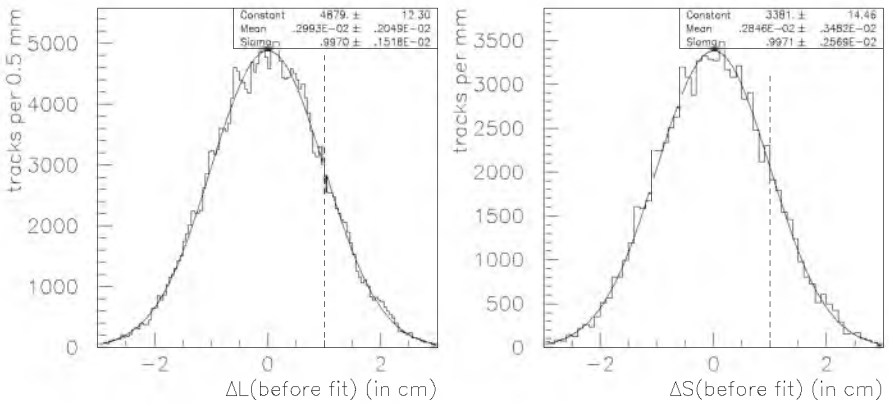

Figure 7.20: Errors imposed on the L and S coordinates, according to the toy model. The dashed lines represent the appropriate measurement error windows.

It is possible for MuFit to diminish the errors and error estimates on track measurements. At least, this possibility exists theoretically but is not easily attained in practice. Factually, only five (parameter) measurements are needed to calculate the track parameters. Since there are in general six super space-points[13] associated with a track, the conclusion follows that it is over determined (by a few parameter measurements). In practice, this means that the results of the fit procedure show a small improvement on the measurement errors and error estimates. For instance, if the error estimates inserted into the fit procedure are highly exaggerated, then the error estimates resulting from the fit can be much smaller and thus reflect the spread in errors on the measurements better. The argument goes likewise when the case is vice versa, i.e. when error estimates largely underestimate the errors, although this situation more often results in an unstable fit. The effect of MuFit on the measurement errors and error estimates is indeed an improvement.

From the sub-figures in Fig. 7.21, we can determine the following behaviour of the fit procedure. When looking at the L parameter in Fig. 7.21(a)-(c), it can be concluded that MuFit was able to improve it, compared to the toy model imposed values. The Gaussian width of the error on L has reduced from 9.97 ± 0.02 mm (in Fig. 7.20) to 7.87 ± 0.02 mm as shown in Fig. 7.21(a). This can only have been accomplished by changing the value of L, as is shown in Fig. 7.21(b). Most tracks were changed in a favourable way, see Fig. 7.21(c), since $\Delta L(\text{after fit})/\Delta L(\text{before fit}) < 1$ in a large number of cases.

The argument goes likewise for the S parameter, which is shown in Fig. 7.21(d)-(f). However, it needs to be remarked that the measurement error estimate imposed was apparently so small that the fit procedure could hardly change the value of S, which can be concluded from the peaks found in Figs. 7.21(e) and (f). The fact that it did change in most cases, has only become possible by increasing the error estimate/window from 0.1 cm to more appropriate values up to about 4 cm, shown in Fig. 7.21(h).

Also, one can see that the error estimate on L has been improved in Fig. 7.21(g), by about 2 to 4 cm, to $\sigma_L(\text{after fit}) = 8$ cm or less. In both cases though, the ideal error window of 1 cm is not obtained.

The most important plots, Figs. 7.22 and 7.23, show the real error on a parameter divided by its error estimate, which is called the pull distribution of a parameter. The error estimate under consideration is the one resulting from the fit procedure, while the real error is defined to be the difference between the generated track parameter, coming from the simulation, and the reconstructed track parameter, coming from MuFit. An optimal[28] fit procedure should give a Gaussian distribution around zero with width one. If the pull distribution comes out correctly for every track parameter, then the fit procedure can be trusted.

The fact that the error window on the S coordinate was set far too small, reflects itself in the pull distributions of the track parameters S and φ in Fig. 7.22. Firstly, they

[13] Six super space-point measurements as in Fig. 7.4(a) would give rise to twelve parameter measurements (leaving out the T parameter measurements), but not all super space-points have meaningful S parameter measurements, as shown in Fig. 7.4(d).

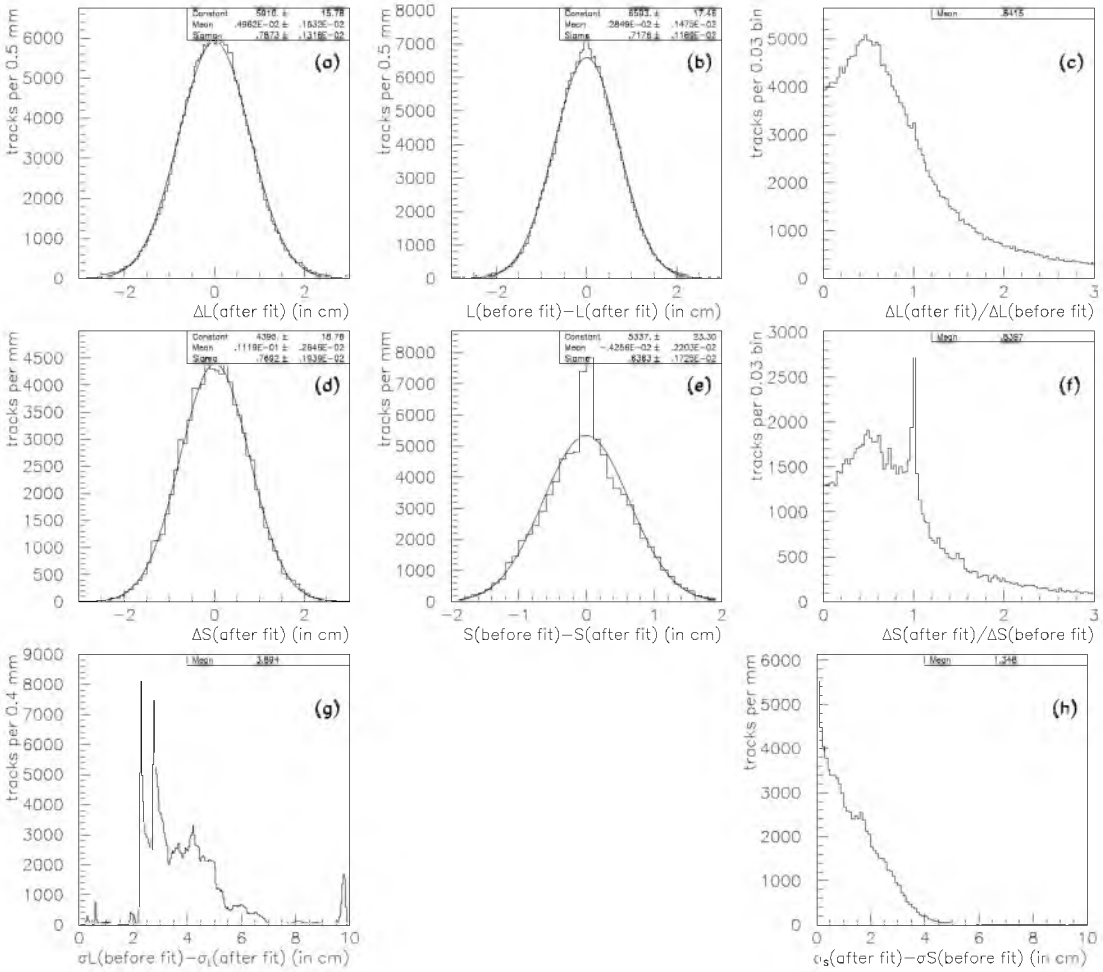

Figure 7.21: (a) Error on L parameter after the fit. (b) Change in value and (c) relative error on L parameter before and after the fit. (d-f) Same for S parameter. (g) Improvement on L parameter imposed error window of 10 cm *and (h) correction of S parameter imposed error window of* 0.1 cm, *where the peak of* 5.5% *unchanged tracks has been cut off.*

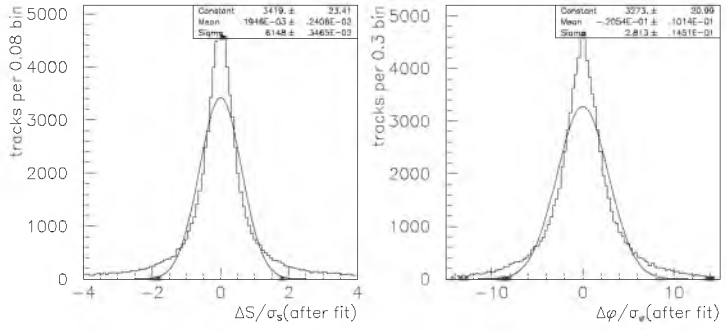

Figure 7.22: Pull distributions of track parameters S and φ.

do not look like proper Gaussians, which points at some instability of the fit procedure. Secondly, the width of the pull distribution of S comes out smaller than one because the mean error estimate, shown in Fig. 7.21(h), is larger than the optimum value, which is 7.69 ± 0.02 mm as shown in Fig. 7.21(d). Thirdly, the width of the pull distribution of φ is larger than one reflecting the underestimated error window in this direction.

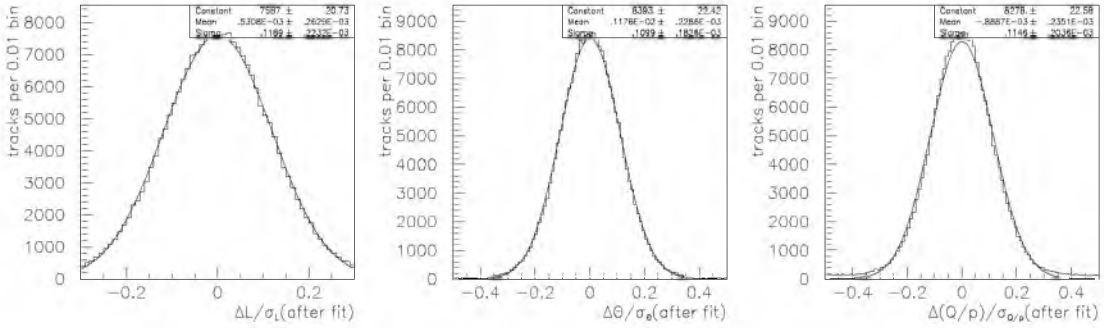

Figure 7.23: Pull distributions of track parameters L, θ, and $\frac{Q}{p}$.

Figure 7.23 shows the pull distributions of track parameters L, θ, and Q/p. They are Gaussian, so it can be argued that the fit procedure performs stable in this direction, given the poor input of the measurement error estimates. However, it is clear that the overestimation of the L coordinate is not overcome since the widths of the pull distributions are almost ten times too small. This is in agreement with Fig. 7.21(g) because not only the error window has decreased but also the real error, see Fig. 7.21(a). As expected, the pull distribution of the charged inverse momentum shows that the overestimated error on the L coordinate has a stronger impact on it than the underestimated error on the S coordinate.

We conclude that no major bugs are present in the MuFit software[14] package as its output can be understood. However, the observation that follows from this intermezzo using the toy model, is that the requirement on the quality of the output from the pattern recognition code(s) is rather strict. In order to obtain satisfying fit results, Muonbox needs to provide error estimates that agree well with the measurement errors made.

7.2.4 of robustness

The initial step of the fit procedure starts with a preliminary estimate of the track parameters. These estimates are provided by the pattern recognition, or alternatively by the toy model, which already come up with decent values. It was tested that the fit procedure is robust enough to perform a satisfactory fit even in the case that these parameters would be off. In order to test this, a simple default was taken for the initial track parameters, namely a track starting at the first super space-point and pointing straight to the last super space-point with random charge and random momentum.

[14] The existence of less clear software bugs is not excluded, since they could become apparent in more extreme situations as the toy model more-or-less only tests the ideal situation.

Figure 7.24 shows that the fit procedure recuperates from this detrimental situation. The number of iterations needed to perform a satisfactory fit increases however, with respect to the normal procedure. Also the number of tracks that causes difficulties to the fit procedure increases. In some cases certain super space-points were removed in order to make the fit possible, but the fit remained successful in more than 99.9% of all cases.

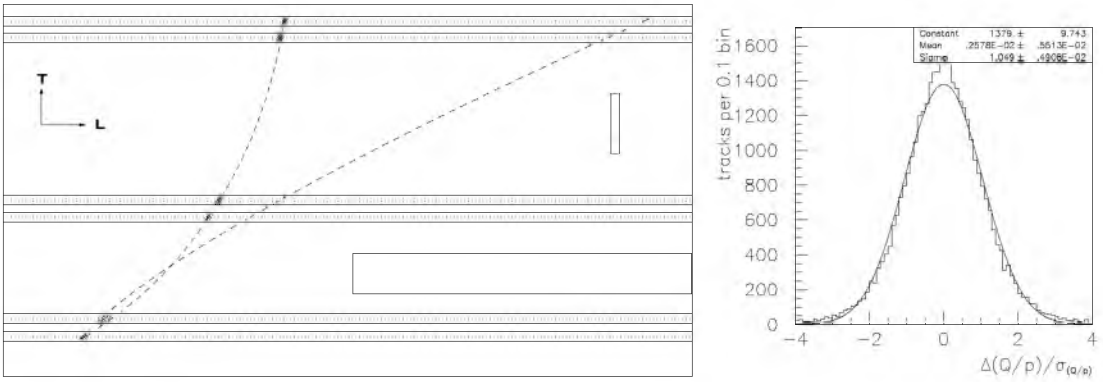

Figure 7.24: Cross section of an arbitrary segment of the spectrometer showing outlines of MDT chambers and two magnet structures. Dotted lines coincide with the planes of detection wires. The first and last iteration of a low momentum muon track fit are represented by the dashed curves and the true Monte Carlo hits by crosses, which proves recuperation from the false charge and momentum assignment. The good pull distribution confirms the robustness.

The pull distribution of the charged inverse momentum[(15)] demonstrates nicely that the fit works in this non-ideal case. Working with the inverse momentum has the advantage that tracks with a high momentum, which are virtually straight anyhow, do not deform the plot(s). Also the charge assignment is more difficult to make in case of highly energetic muons, which is nicely reflected in the fact that the values $1/p$ and $-1/p$ lie close to one-another for $p \gg 200$ GeV$/c$.

Figure 7.25 shows the χ^2 probability distribution for the toy model. The number of degrees of freedom (NDOF) is given by the number of super space-points times two measurements where applicable, i.e. there is a good S parameter measurement, minus the number of five track parameters, which needs to be fixed/fitted. A flat distribution reflects the fact that we adhere to the laws of statistics, but this would be an ideal situation. The non-flat distribution gives information on the quality of the measurements[136] and how they are treated by the fit procedure. Namely, an excess near zero signifies that the fit was over constrained, e.g. when the estimated measurement error windows have been set too small, or when a too large number of degrees of freedom are used. Likewise, an excess near unity points to evidence for an under constrained fit, e.g. when the error windows were overestimated by the pattern recognition, or when

[(15)] It is actually the charged inverse momentum (Q/p) that is used by both MuFit and Muonbox, as a replacement for the track parameters Q(charge) and p(momentum).

they are (still) too large after the fit procedure. So, from Fig. 7.25(a) we conclude that the error windows after the fit procedure are too large compared to the real difference in parameter values. Of course, this does not come as a surprise given the results in Sect. 7.2.3. It has also been checked that no hidden degrees of freedom exist, as Fig. 7.25(b) suggests the incorrect χ^2 probability behaviour opposite to Fig. 7.25(a).

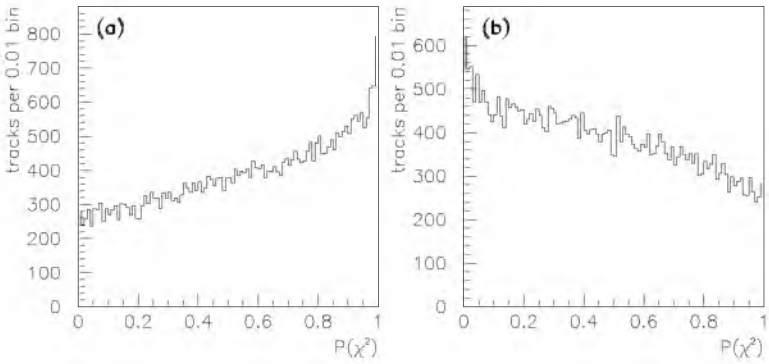

Figure 7.25: Probability distribution of χ^2 for the toy model. (a) Five fixed degrees of freedom, (b) and the hypothetical case of six fixed degrees.

7.3 Performance of fit procedure

All ingredients have been dealt with by now, i.e. every software package or component, that influences MuFit, has been identified and tested up to a certain extent. Furthermore, part of MuFit has been tested and proven to work successfully, even under nonideal circumstances.

As shown in Fig. 7.4, the input obtained from Muonbox, is not ideal. So, the tests described previously are now applied on this realistic input. The results are found in Fig. 7.27. They apply to sample 3 of Table 6.3. However, special measures had to be taken as not to deform the plots due to a large number of tracks, especially in the endcaps, where the fit procedure has failed.

The proof of this failure comes from Fig. 7.26(a), which shows the error estimate on the track parameter S, i.e. the non-bending coordinate. The resolution on this parameter goes up to 35 cm, while it is normally expected to be below 4 cm. This observation has been checked rigorously, whereby it was found that tracks with a small number of contributing super space-points, i.e. three, four or five, allow σ_S and σ_φ to become very large. Consequently, the error estimates on the other track parameters become under constrained too, which leads to very large values of σ_L and σ_θ. This is shown for the track parameter L, i.e. the bending coordinate, in Fig. 7.26(b) and only for tracks for which the fit procedure failed. The resolution on this parameter is expected to lie around 50 μm, while the values shown are much larger. Fig. 7.26(c) shows the percentage of successfully fitted tracks as a map, of η and φ, which has been

folded to one-sixteenth of its full size. From this figure, the conclusion follows that the fit procedure was unsuccessful mainly in those endcap regions where the muon chambers do not overlap. These tracks have in common that they yield only two second coordinate measurements lying close to one another in the middle station. This is not sufficient to constrain the direction of the track thereby giving error estimates which are much larger than the actual errors on the track parameters. This is considered to be a failure, or unstability, of MuFit which can only be circumvented using additional information.

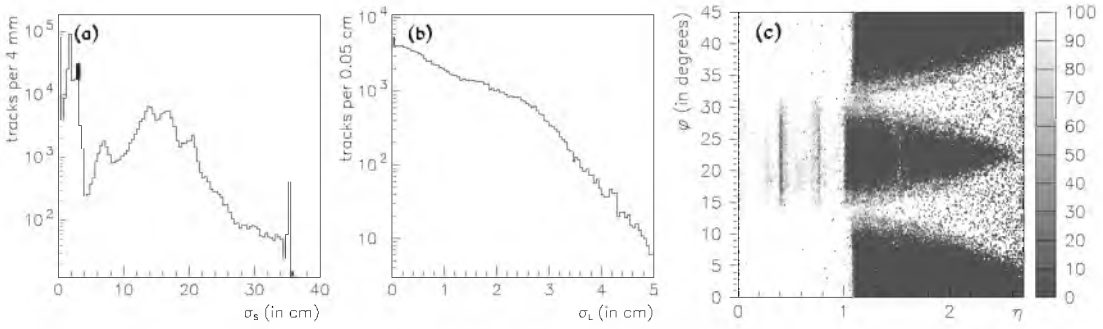

Figure 7.26: (a) Error estimate on second coordinate (after fit procedure), (b) Error estimate on precision coordinate for unsuccessfully fitted tracks only and (c) percentage of successfully fitted tracks as a function of η *and* φ *(for one-sixteenth of the muon spectrometer).*

It was decided to remove all tracks from the sample for which the fit procedure failed, i.e. $\sigma_S > 4$ cm. The χ^2 probability distribution and pull distributions on all track parameters of the successfully fitted tracks is shown in Fig. 7.27. It does not come as a surprise that the χ^2 probability distribution exhibits an excess near unity, as the default measurement error window on S clearly overestimates the real error on this coordinate measurement. The charged inverse momentum parameter comes out best, while σ_S and especially σ_φ seem somewhat overestimated, or under constrained. The pull distribution for the bending parameter L does not come out well at all, but this can be explained rather easily. Namely, the information of the simulation is obtained at the wall of the first tube hit in the muon spectrometer while the track parameters that come out of MuFit are given at the central plane of the first multilayer. This implies a little difference in the T parameters (see Figs. 7.2 and 7.3), which has the effect that the ΔL value cannot be computed accurately enough resulting in the non-Gaussian behaviour of its pull distribution. In the end, one concludes that the fit procedure behaves well enough to trust the track parameters and their error matrix for those tracks that were successfully fitted.

7.3.1 Quality considerations

Actually, the fact that the fit procedure works well, mathematically seen, does not necessarily mean that the results are of good quality, e.g. as is shown in Fig. 7.26.

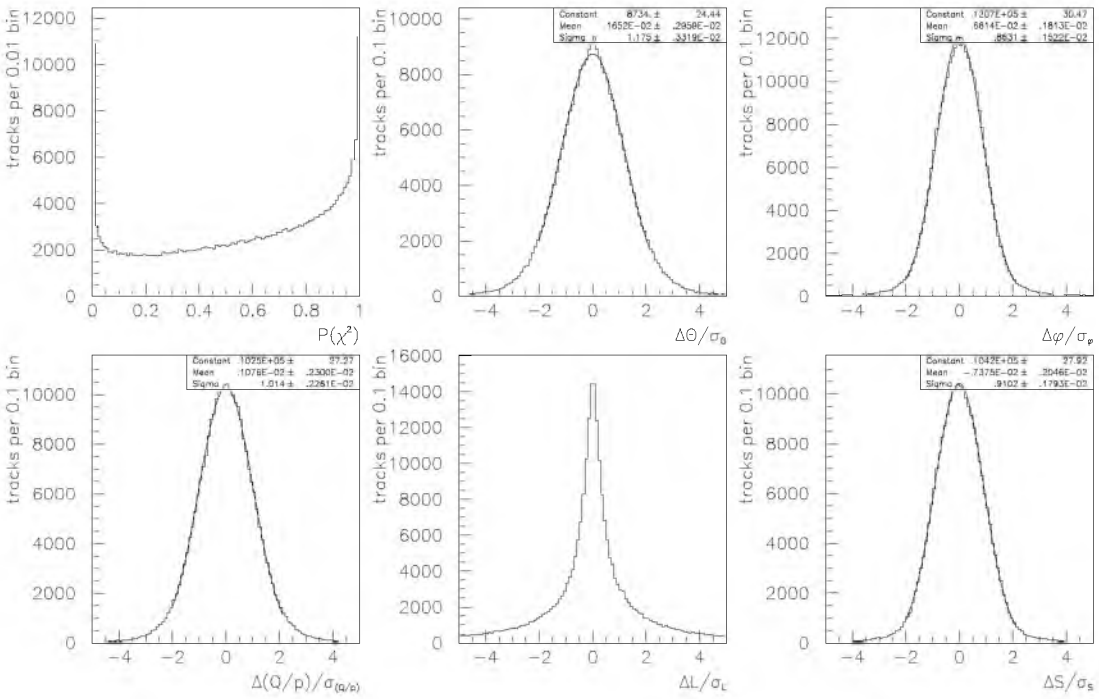

Figure 7.27: Probability distribution and track parameter pulls.

7.3.1.1 ATLAS defined quality requirements

A simplistic criterion to judge the quality of the fit output is to expect it to be the same as the generated input track parameters. This will never be the case, thus it is better to formulate a practical definition. The input to that comes from requirements specified in the ATLAS Muon Technical Design Report[34], which states (amongst others):
(for the pattern recognition:)

1. chamber positioning resolution should be better than 30 μm,
2. measurement accuracy of bending parameter has to be about 50 μm,
3. sufficient resolution on the second coordinate is 5 to 10 mm.

(for the fit procedure:)

4. transverse momentum resolution should be better than $10^{-4}\,p/\,\mathrm{GeV}/c$ for $p_\mathrm{T} > 300\,\mathrm{GeV}/c$,
5. transverse momentum resolution of a few percent is expected for transverse momenta of $p_\mathrm{T} < 300\,\mathrm{GeV}/c$.

(for combined muon reconstruction:)

6. momentum resolution should be about 1% for low momenta.

(for physics analysis:)

7. mass resolution needs to be about 1% for an intermediate Higgs mass (of $m_\mathrm{H} = 100$ to $200\,\mathrm{GeV}/c^2$).

Only some of these requirements pertain to the first phase of muon track reconstruction.

Figure 7.28 shows plots relevant for a comparison to the criteria above, where

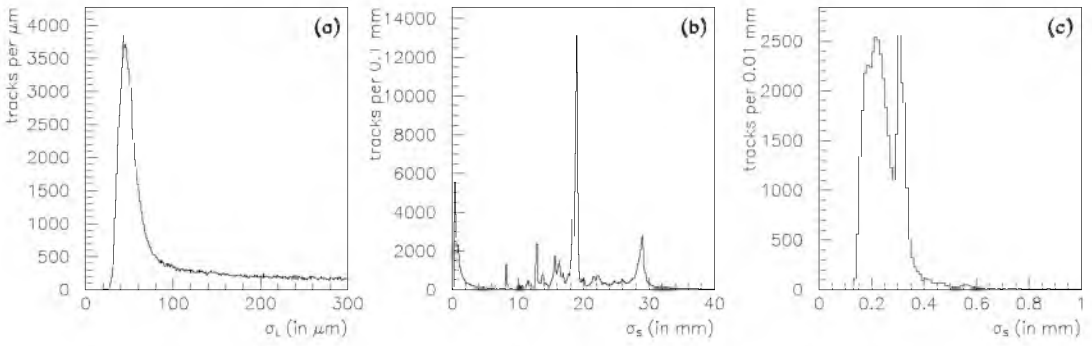

Figure 7.28: Resolution on (a) L parameter and S parameter in (b) barrel and (c) endcap.

successfully fitted tracks have been used only (see Fig. 7.26). It is obvious that the requirements for the pattern recognition cannot be used for the fit procedure without taking proper care. For instance, there is a peak just below $\sigma_L = 50$ μm, for the bending parameter L in Fig. 7.28(a). While this seems to be the behaviour wanted (for the second requirement), one also has to take into account the tail. It is this absurdly long tail, going up to 1000 μm, which spoils the fulfilment of the requirement. This tail is caused partly by those under constrained tracks for which the number of super space-points is too small. The second coordinate resolution does not seem to suffice in the barrel (in Fig. 7.28.b), according to the third requirement, but it is more than sufficient in the endcaps (in Fig. 7.28.c).

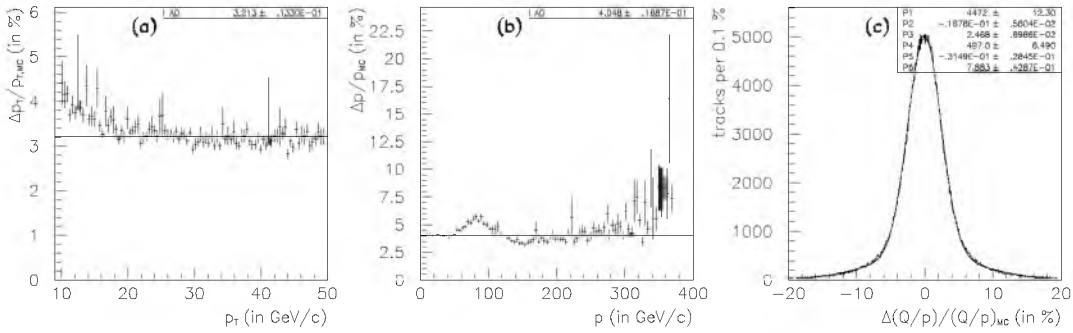

Figure 7.29: (a) Transverse momentum resolution versus transverse momentum, (b) momentum resolution versus momentum and (c) charged inverse momentum resolution. All resolutions are averaged over the full detector. Monte Carlo information used are the track parameters at the primary vertex. The horizontal lines in (a) and (b) represent the average transverse momentum and the average momentum resolutions.

The same can be said about the momentum resolution shown in Fig. 7.29, which is also not consistent with the required specification, i.e. the fifth requirement. However, this statement needs to be elaborated.

Firstly, it is possible to calculate the momentum resolution using the fitted momen-

tum track parameter. This can be done by comparing it with the GEANT information obtained at the first tube hit. Another strategy is to backtrack to the beam pipe first, as to obtain the track parameters close to the primary vertex. They can then be compared with the GEANT generated track parameters. In practice, it turns out that there is not much difference, since GEANE is well able to correct for the energy loss, in the calorimeters. So, this latter option has been used in order to produce Fig. 7.29.

Secondly, not much can be said about the fourth requirement, stated for the transverse momentum, since the sample used does not include muons with such high momenta. The transverse momentum resolution for low momenta is above 3%, see Fig. 7.29(a), which is at the high end of the few percent required in the fifth requirement.

Thirdly, the momentum resolution for low momenta in Fig. 7.29(b) stays well above the 1% stated in the sixth requirement. This leads to the conclusion that the stand-alone spectrometer is clearly no replacement for the combination of inner detector and spectrometer, as used by the combined muon reconstruction.

Lastly, the (transverse) momentum resolutions just discussed have been averaged over η and φ. This means that the structure of the spectrometer has not been taken into account. Since there are regions which yield a momentum resolution better than the stated 3%, there are also regions where the momentum resolution is much worse. The proof of this is shown in Fig. 7.29(c), which exhibits that the momentum resolution, averaged over η, φ, and p, consists of two components. These two components are inferred from the numbers in this figure, which define two Gaussian distributions on top of each other. The important/central component coincides with matter free regions, yielding a resolution of about 2.5% , while the other component denotes the influence of material in the spectrometer in the tails of the distribution, with an (average) resolution degradation to about 8%.

Figure 7.30 shows the momentum resolution as a function of φ and as a function of η. Clearly, the coils and support feet (see Fig. 7.10) give rise to a momentum resolution degradation in the corresponding φ regions. The presence of struts, voussoirs, and/or ribs (see Fig. 6.13) causes small resolution degradations at low η, but the degradation around $\eta \approx 1.5$ is primarily due to the transition region from barrel to endcaps (see Fig. 4.12).

In conclusion, it is better to define another, more workable set of requirements, on which to judge the quality of MuFit. To perform this redefinition, we go back to the basic duties of the muon spectrometer.

7.3.1.2 MuFit defined quality requirements

The muon spectrometer has to detect all muons in an η-range of -2.7 to 2.7 ($7.7^\circ < \theta < 172.3^\circ$). However, some muons decay before they reach the spectrometer and some other muons have a too low momentum. It is not expected that they should be detected by the muon spectrometer, so a practical lower limit is set at $p_T \approx 5$ GeV/c.

Upon detection, the muon reconstruction tries hard to calculate the track parameters, but it cannot do much better by itself than just described. For every muon detected,

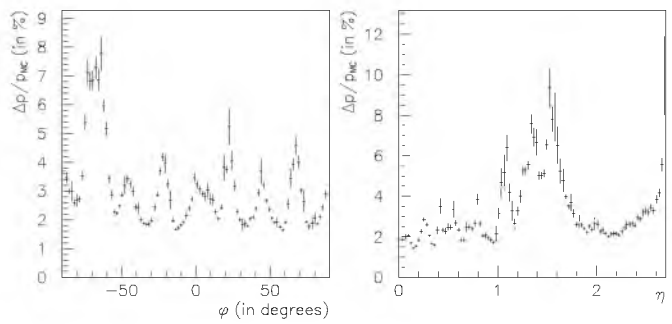

Figure 7.30: Charged inverse momentum resolution versus φ and versus η, showing degradation in areas with an excessive amount of material. Monte Carlo information obtained at first tube hit.

a path is specified, going through the calorimeters and inner detector towards the interaction region, along which the muon probably will have travelled. The spectrometer will be aided by the inner detector in pin-pointing this track, when the inner detector reconstruction software is able to find the proper hits belonging to the particular muon track. The match is most successful if the information from both subsystems can be combined, in order to provide more accurate track parameters. These considerations lead to a new set of requirements, which can even be made free of information from the track generation:
(for the pattern recognition:)
1. each muon, going through the spectrometer, should be detected and measured.

(for the fit procedure:)
2. every measured muon, which originates from the interaction region, should have fitted track parameters pointing back to the interaction region,
3. every backtracked muon candidate has to deliver a seed on the outer boundary/shell of the inner detector.

(for the combined muon reconstruction:)
4. every seed has to belong to a muon track segment, if the track candidate adheres to a genuine muon,
5. fake seeds should not give rise to fake muon track segments in the inner detector,
6. track parameters, to be combined, should be comparable within their (estimated) error windows.

Especially this last requirement makes sure that information is combined only when we are dealing with the same, genuine muon track in both sub-detectors. With this redefinition, it also becomes easier to compare MuFit and Muonbox.

The requirements are not easily enforced, since again a lot of information needs to be combined. The first three requirements do not pose a problem since they refer to the first phase of muon reconstruction. However, the remaining three requirements cannot be checked yet, since they apply to the second phase of muon reconstruction, which has not been dealt with yet. So, for now a slightly adapted requirement is used,

namely that the charged inverse momentum resolution should not exceed 100% for any single track. Another option would be that the absolute charged inverse momentum resolution should be below several times the (estimated) error window (multiplied by the momentum)[16], but it has been verified that this option gives worse results.

Concerning the first requirement, it is best to refer to Figs. 6.16 and 7.8 which show the areas where the muon spectrometer is not 100% efficient in detecting muons. Excluding these areas of difficulty, the track finding or detection and measurement efficiency is over 99.5%. For the full phi and rapidity range ($|\eta| < 2.7$), the average efficiency is 97%.

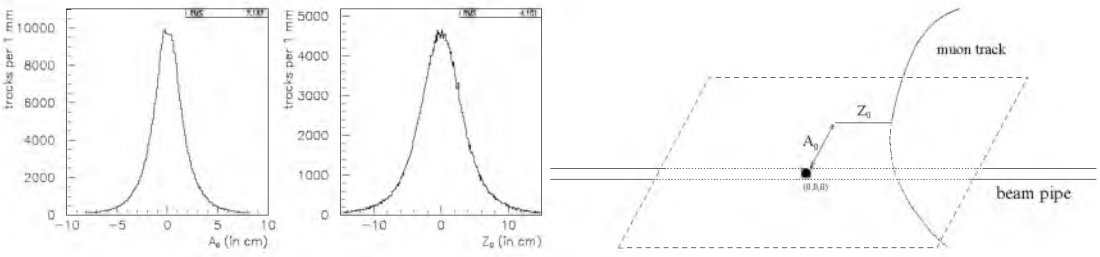

Figure 7.31: Longitudinal and transverse distances of closest approach between muon track candidates and the detector origin.

Some things can be said about the second and third requirements as well. By default, the version of Muonbox used performs an extrapolation of every candidate track to the interaction region. Figure 7.31 shows the longitudinal (Z_0) and transverse (A_0) distances of closest approach of the muon track candidates to the centre of the ATLAS detector, as well as their definition. The transverse/longitudinal distance of closest approach is often referred to as transverse/longitudinal impact parameter. The tails in Fig. 7.31, which reach up to ± 100 cm, are not shown in the plots, but they are not of importance since the pull distributions behave well. This in turn indicates that Muonbox is able to estimate the error windows well. It delivers a seed for every track, with an efficiency of 100%.

The situation is somewhat different when using MuFit, as this can operate in two distinct modes. The first mode, which has been solely used up till now, uses only the super space-points in the spectrometer to obtain the track parameters. It can happen that this information is not limiting enough to constrain the track parameters, as shown in Fig. 7.26. As a result, a small number of tracks do not cross the inner detector boundary at all. This situation is considered as a fit failure if the original track did indeed originate from the interaction region. The positive effect of this method is that it does not introduce a bias and as such can be used to reconstruct muon tracks

[16] The charged inverse momentum resolution can be compared with the estimated error window multiplied by the momentum as follows:

$$\left|\frac{\Delta Q/p}{Q_{MC}/p_{MC}}\right| = \left|\frac{p_{MC}}{p_{fit}}\frac{Q_{fit}}{Q_{MC}} - 1\right| \approx \left|\frac{p_{fit}}{p_{MC}}\frac{Q_{MC}}{Q_{fit}} - 1\right| = p_{fit}\left|\frac{Q_{MC}}{p_{MC}} - \frac{Q_{fit}}{p_{fit}}\right| \approx p_{fit}\sigma_{Q/p}$$

stemming from pion decays in the calorimeters, which should help reduce some of the background. The seed generation efficiency in this mode is over 99.5%.

There is a difference between MuFit and Muonbox in the way the distances are obtained that describe the closest approach of the muon track to the ATLAS detector origin. Muonbox calculates them for every track, as shown in Fig. 7.31. MuFit only takes those tracks into account that pass through the beam pipe, which has a radius of 2.5 cm near the interaction region. There are two reasons that help explain why a number of tracks do not cross the beam pipe during the backtracking phase.

Firstly, the accuracy of the second coordinate fit is of the order of several millimetres, which means that the φ angle parameter is not accurately determined either. During simulation, the muon has undergone multiple scattering where the precise Monte Carlo information, i.e. the location and magnitude of the angles of a scatter, is only known to the simulation itself. This precise information is unavailable during the fit and consequently the track parameters cannot be corrected for the random scatters. However, the error estimates on track positions (e.g. second coordinate) and angles (e.g. φ angle) are increased by the average contributions. On the other hand, the track momentum during reconstruction will be different from that of the simulation in order to fit the measured points. This is especially the case when single, large scatters have occurred, as is explained in appendix B. Effectively seen, the initial inaccuracy is augmented during the backtracking phase.

Secondly, the solenoidal magnetic field inside the inner detector causes a deflection of the muon track in the *x-y* plane, i.e. a change of the φ angle (parameter). This change is partly undone in the magnetic field of the return yoke, but not entirely since the muon momentum has decreased by an unknown amount, by then. So, during backtracking the φ angle changes as well, but by different amounts since the muon momentum is not known accurately. This gives an extra contribution on the initial inaccuracy.

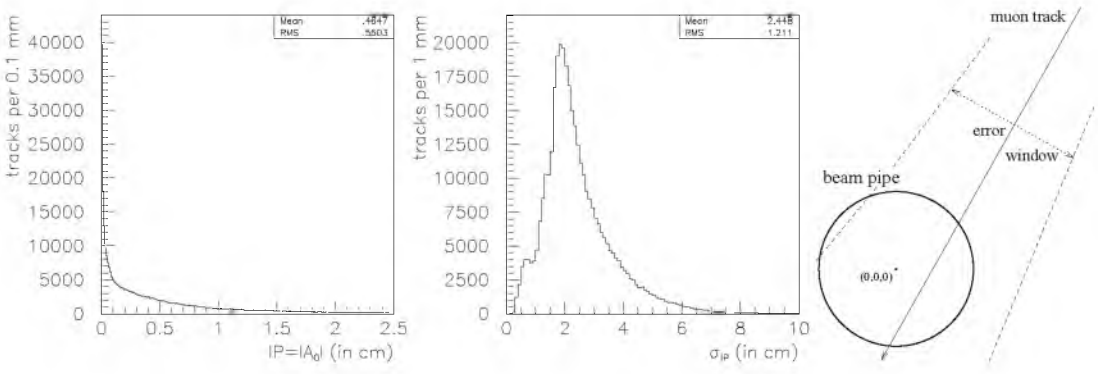

Figure 7.32: Transverse distance of closest approach and error window on transverse distance, obtained by MuFit for tracks crossing the beam pipe.

Even if the backtracked muon misses the beam pipe, this does not mean that the fitted track parameters are wrong. The reason is that the error windows on the backtracked parameters have become so large that the interaction region is still encompassed. Figure 7.32 shows an illustrative comparison. Only the transverse distance

(A_0) is shown in the figure, since the longitudinal distance (Z_0) does not differ much from what was already shown in Fig. 7.31. Another name for the transverse distance of closest approach or transverse impact parameter is just impact parameter (IP), which is very misleading of course. The pull distributions, of the distances of closest approach, do not behave well as σ_{IP} is largely overestimated and σ_Z somewhat underestimated. About 50% of the fitted muon tracks go through the beam pipe.

7.3.2 Using a vertex constraint

The second mode of MuFit includes the beam pipe as an additional super space-point. This method introduces a clear bias, because all muon tracks are expected to originate from the interaction region. The additional super space-point is obtained by imposing a measurement at the detector origin with measurement error estimates: $\sigma L = 60$ cm, $\sigma S = 1$ cm, $\sigma T = 0$ cm. This has profound consequences, which are mainly positive. For instance, all tracks are successfully refitted and the inner detector seed generation efficiency is 100%. There is an improvement on the χ^2-probability distribution, see Fig. 7.27 and Fig. 7.33(a). It has become flatter and the peak at 1 has decreased, which indicates that more information has been used successfully. Also, the resolution on the S parameter in the muon spectrometer barrel has improved drastically, compare Fig. 7.26(a) and Fig. 7.33(b) keeping in mind the difference in vertical scale. Finally, the seed definition has become better, but this subject is postponed till later.

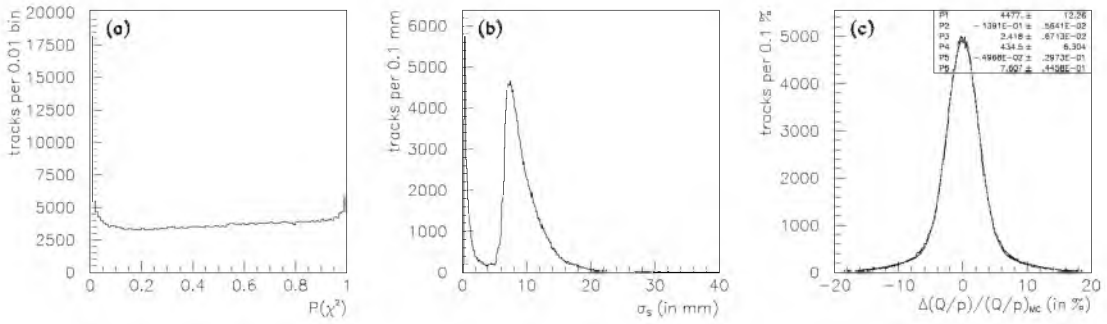

Figure 7.33: (a) Improved χ^2 probability, (b) S parameter error window and (c) charged inverse momentum resolution, due to MuFit beam pipe constraint.

As expected, there is not much improvement on the momentum resolution, or the L and η parameter resolutions, since they are constrained sufficiently already by the measurements inside the muon spectrometer. The pull distributions shown in Fig. 7.27 become better as can be seen from Fig. 7.34 for θ, φ, and S. An explanation could be that a different type of constraint has been introduced, namely a severe constraint on the S and φ parameters. This behaviour has been tested as a function of the constraint severity, using a measurement error estimate of $\sigma S = 5$ cm. As expected, the improvements just mentioned become less profound and the results are between those shown in Figs. 7.27, 7.28 and 7.33, 7.34. There seems to be a statistical 1σ (or 68%) effect, since the number of tracks reaching the beam pipe goes down to 83% (which equals

50% plus 68% of the remaining 50%), in this particular case. The muon tracks that miss the beam pipe come from the muon spectrometer barrel which is explained by the fact that the S parameter resolution exceeds 10 mm for those tracks.

It takes more time[17] to fit a single track using the beam pipe constraint, since the track length has become a lot longer and the muon encounters many more volumes. When using the more severe constraint of $\sigma S = 1$ cm, the number of tracks that crosses through the beam pipe increases to 93%. This percentage depends on the fraction of tracks in barrel and endcaps, as the latter ones always reach the beam pipe. It also depends on the transverse momentum, i.e. the percentage reaches almost 97% for muon tracks with $p_T > 40$ GeV/c.

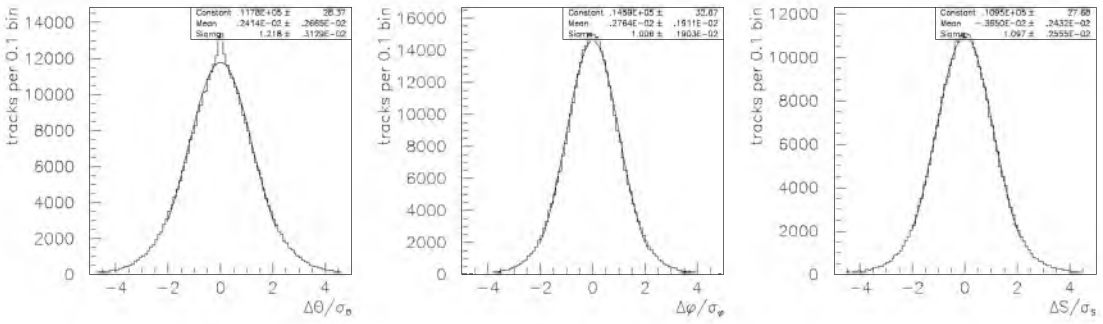

Figure 7.34: Improved pull distributions on track parameters of interest at the primary vertex, due to MuFit beam pipe constraint.

7.3.3 Stand-alone performance

One kind of benchmarking often looked at, is the muon spectrometer stand-alone performance. This means that all detector elements that constitute inner detector and calorimeters are treated as dead material. The explanation is that it could happen, during a very unlikely situation, that only the muon spectrometer functions[18]. This would also be the case if no information of the muon tracks could be isolated from calorimeters and inner detector. Figure 7.35 presents the stand-alone charged inverse momentum resolution, averaged over φ and p_T, as a function of pseudo-rapidity (η), using the beam pipe constraint, but leaving out the feet sectors. The resolution is calculated by fitting the entries in a particular eta-bin with a normal distribution, and taking the resulting half width at half maximum ($\equiv \sigma$). Comparing Fig. 7.35 with Fig. 6.13 one can conclude that MuFit performs according to the theoretical expectation. Especially when taking into account that the material of the RPCs was neglected by mistake[147] in producing the latter figure, it even seems that MuFit achieves a momentum resolution which is better than (theoretically) expected.

[17] One second per track is needed now, which is still about six times faster than the full pattern recognition, but is about two times slower than before.

[18] Though it can be argued that no-one would power up the detector when this disaster happens.

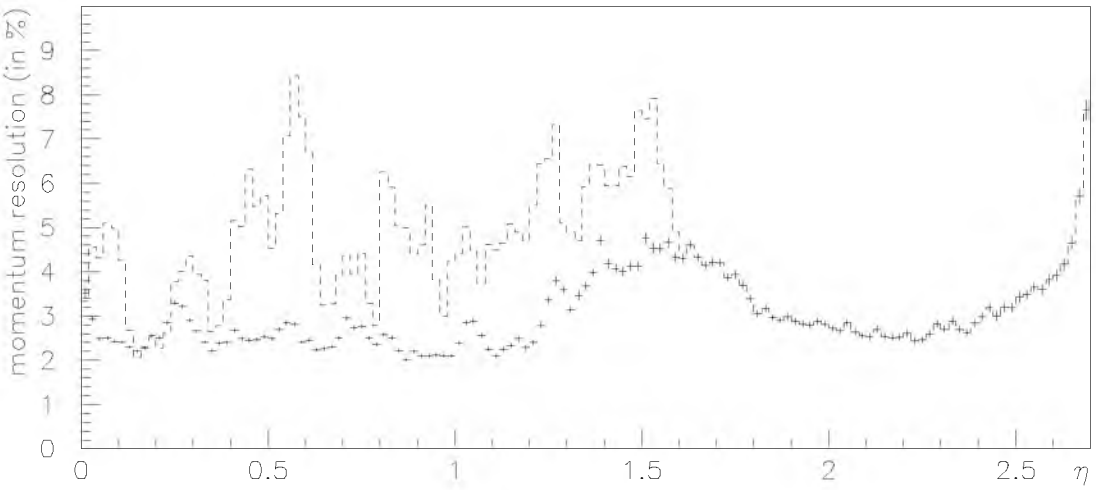

Figure 7.35: Stand-alone spectrometer muon momentum resolution (at vertex), averaged over φ and $5 < p_T < 120$ GeV/c using MuFit beam pipe constraint without feet sectors, as a function of η. The dashed line shows the resolution for the feet sectors only.

The performance would increase a lot when the full spectrometer would be matter free. As this is not the case, this essentially means that only part of the spectrometer performs according to the fifth requirement of Sect. 7.3.1.1. The impact on muon physics is large and can be expressed in a number that denotes the useful volume of the spectrometer. A map is used for this calculation, see Fig. 7.36, which shows the fraction of usefully fitted tracks per η-φ bin. The limit is set at twice the best possible charged inverse momentum resolution, which equals 3.5%, for every single muon track. The result obtained is that only two-thirds of the spectrometer volume could be used for physics analysis in stand-alone mode. Furthermore, no noticeable difference between MuFit and Muonbox was observed.

7.4 Muon seeds

The way out of the disastrous situation sketched in the previous section, is to make it possible to combine information from various sub-detectors. This feat is accomplished by giving a seed, at the outer boundary of the inner detector, to the inner detector pattern recognition software codes. XKalman[92] is used for this purpose, as it seems to be too difficult to make iPatRec[91] work with the software changes introduced in Chapter 6. The extra data cards[148] used are:

```
*MODE   'AXXX'   'RECO' 1
*MODE   'XKAL'   'PRIN' 0   'RECO' 1   'HIST' 0
*DETP   'XKAL'   'INRO='1.   'ONOFF='0.   'INRO='2.   'ONOFF='1.
                 'INRO='3.   'ONOFF='0.   'INRO='4.   'ONOFF='1.
                 'PDG1='13.   'PDG2='-13.   'PDG3='0.   'PDG4='0.
                 'INRO='5.   'ONOFF='0.
```

which means that seeds are constructed from tracks found by Muonbox, and from tracks generated at the vertex.

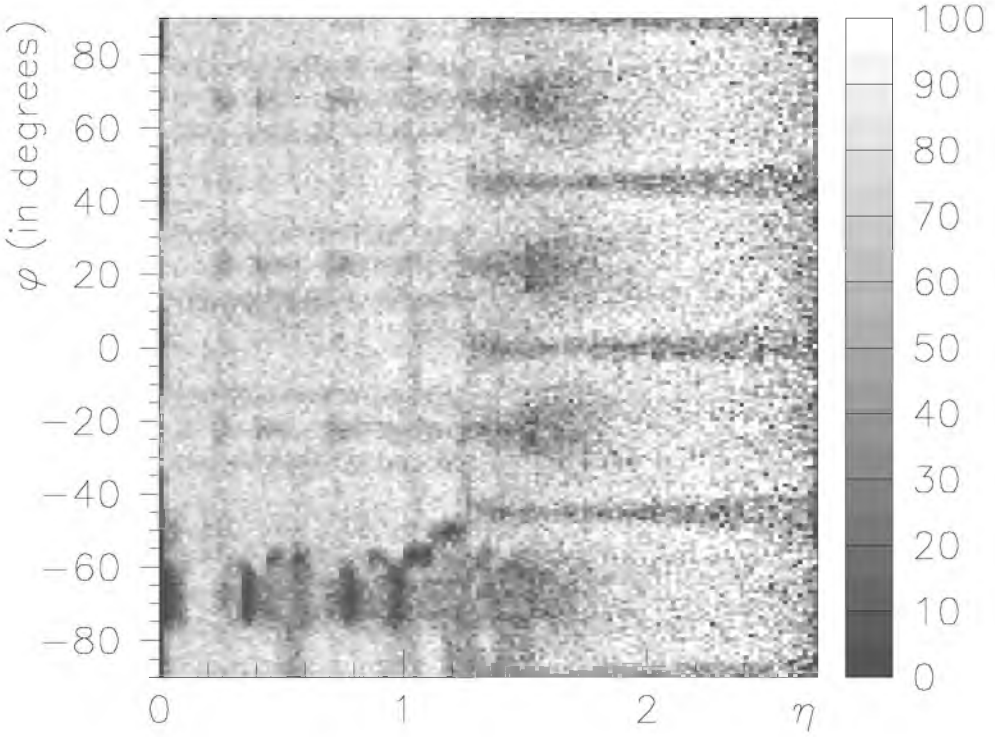

Figure 7.36: Percentage of fitted muon tracks with momentum resolution below 3.5%, averaged over $5 < p_T < 120$ GeV/c *as a function of* η *and* φ.

For Muonbox seeds, the η and φ values of the track intersection point with a cylinder of radius 105 cm and half-length 320 cm are used, see Fig. 7.37. The standard half-widths in η and φ, namely $\Delta\eta$ and $\Delta\varphi$, are set at 0.5 each which are also the XKalman defaults. This means that all tracks found within the window $(\eta - \Delta\eta, \eta + \Delta\eta) \times (\varphi - \Delta\varphi, \varphi - \Delta\varphi)$ are considered valid. The use of an $\eta \times \varphi$ window makes life easier for the inner detector pattern recognition code since the size of the window does not change along the track. It needs to be remarked though that this default window size is really large[(19)], thus making it more probable that false tracks will be found. For GEANT/Monte Carlo generated seeds, the argument goes likewise though the intersection points do now reside on a cylinder with radius 140 cm and half-length 360 cm.

[(19)] As a comparison: for $z = 0$ cm the window/box size around the intersection point equals 109 cm $\times$ 105 cm, increasing to 351 cm $\times$ 105 cm at $|z| = 320$ cm, and decreasing to 45 cm $\times$ 43 cm at the ends of the cylinder for $R = 43$ cm. Actually, the window boxes are asymmetric and highly influenced, i.e. exaggerated by the value of $\eta + \Delta\eta$. So, taking only the value of $\eta - \Delta\eta$ into account, one gets more sensible boxes of 269 cm $\times$ 105 cm and 34 cm $\times$ 43 cm.

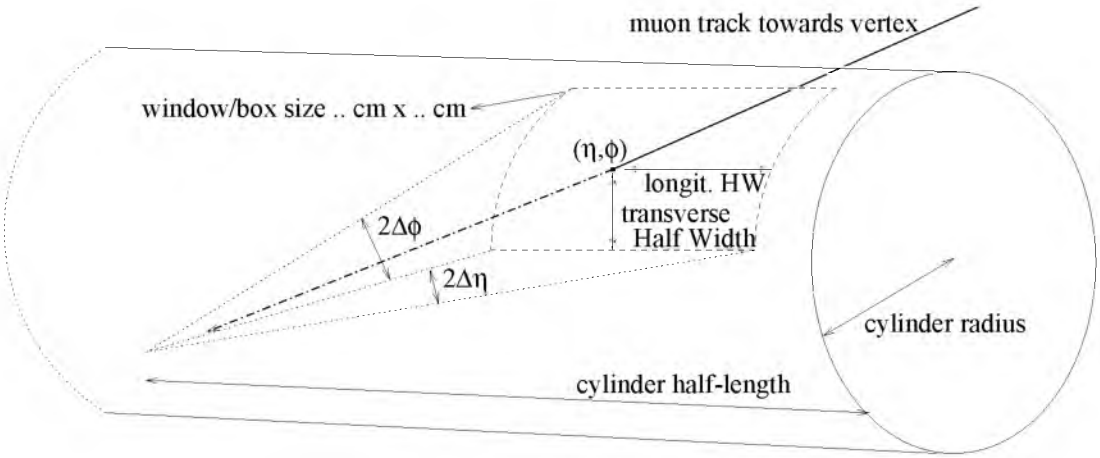

Figure 7.37: Concept of seed definition and quantities involved.

MuFit uses a different approach that was first proposed[149] many years ago. It utilizes the structure for ROAD banks[148], where a road half-width is defined in both transverse and longitudinal directions on a track-by-track basis. These quantities can be compared to the window box sizes. Figure 7.37 shows the definitions of all sizes involved. Since we are not dealing with planes anymore, but with cylinder surfaces, this implies that some definitions have changed slightly. For the curved barrel surface, the track parameters still are Q/p, η, φ, L, S, and T, but with the adapted definition that the distance T does not equal the radius (R) of the cylinder. Instead, we now use:

$$\begin{aligned} L &= z \\ T &= \sqrt{R^2 - S^2} \\ S &= R \cdot (\arctan\left(\frac{y}{x}\right) - \varphi) \quad , \end{aligned} \tag{7.5}$$

where φ equals the azimuthal track direction. This azimuth can be defined for the track point as well, thus giving $\phi_p = \arctan(y/x)$. Upon inspection, it is found that Eqs. (7.1), (7.2), and (7.5) on page 80 do not differ essentially. For the flat cylinder end-surfaces, the track parameters Q/p, η, φ, L, S, and T remain to be used. Again, the roles of L and T are interchanged, as was the case for the muon spectrometer endcaps, since T always measures the fixed distance to a point of reference. So,

$$\begin{aligned} T &= |z| \\ L &= \sqrt{R^2 - S^2} \\ S &= R \cdot (\arctan\left(\frac{y}{x}\right) - \varphi) \quad , \end{aligned} \tag{7.6}$$

in this case, which is equivalent to Eqs. (7.3) and (7.4).

The longitudinal and transverse half-widths of a seed are now defined as: $\Delta L_{HW} = 9 \cdot \sigma_L$ (for the longitudinal half-width), and $\Delta S_{HW} = 7 \cdot \sigma_S$ (for the transverse half-width), where σ_L and σ_S represent the error estimates obtained by MuFit. Multiplying

these estimates by the above factors ensures that over 99.5% of the seeds coincide with a valid track inside the inner detector. The remainder of tracks is assumed to have been misfitted. Figure 7.38 shows the seed half-widths used by MuFit as a function of pseudo-rapidity. For comparison, the transverse half-width is also shown when no vertex constraint would have been used.

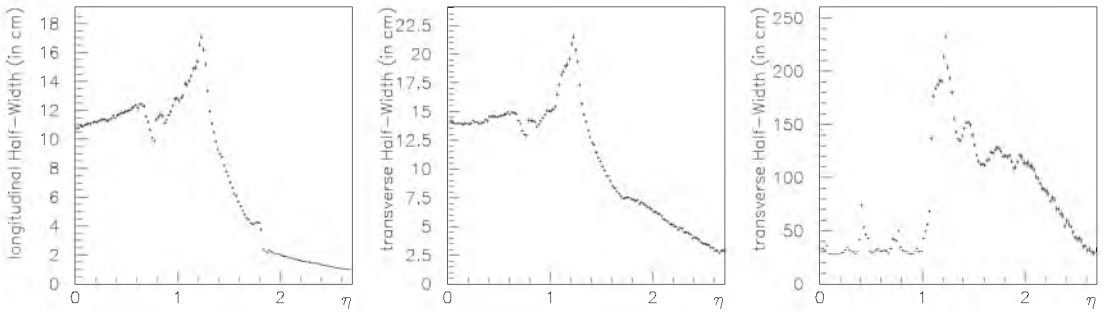

Figure 7.38: Longitudinal and transverse half-widths as a function of pseudo-rapidity using the MuFit beam pipe constraint, compared to the transverse half-width without constraint.

Taking into account the cylinder half-length of 345 cm and radius of 115 cm used by MuFit, it is possible to make a comparison with the default road definitions used by XKalman (and Muonbox). The window box sizes are roughly equal to $2 \cdot \Delta L_{HW} \times 2 \cdot \Delta S_{HW}$, which leads to a maximum average box size of 36 cm $\times$ 45 cm when using MuFit. Likewise, using the equations $\Delta\varphi = \Delta S_{HW}/R$ and $\Delta\eta = \ln(\tan(\frac{1}{2}\arctan(R/L + \Delta L_{HW}))) - \ln(\tan(\frac{1}{2}\arctan(R/L)))$, it is clear that the maximum window size is found at $|\eta| \approx 1.2$ where $\Delta\varphi \approx 0.2$ and $\Delta\eta \approx 0.1$ in average. The conclusion follows that it is well possible to use seeds on a track-by-track basis smaller than the default $\Delta\eta = \Delta\varphi = 0.5$ assumed by XKalman.

7.4.1 XKalman performance

Using the muon seeds, the inner detector pattern recognition code constructs a road, going from the seed to the beam pipe, in which all inner detector hits are sampled. Hereby, a new track segment is obtained inside the inner detector, which should be combined with the extrapolated track from MuFit. Two types of operation are available for the hit sampling of XKalman, namely it is possible to choose whether or not to use the interaction region[(20)] as the origin of the track. This beam constraint is clearly far more restrictive than that used by MuFit. On the other hand, the accuracy of the measurements in the pixels near the beam pipe is already such that tracks originating from the primary vertex also point back to it.

Figure 7.39 shows the results of the XKalman-fit procedure in comparison to the Monte Carlo / GEANT generated tracks parameters. Here, the parameters: Q/p_T,

[(20)]The interaction region is defined as the region in which the beams collide. It is defined by the Gaussian widths $\sigma_x = \sigma_y = 16$ μm and $\sigma_z = 5.6$ cm around the vertex $(0,0,0)$.

$1/\tan\theta$, φ, A_0, z_0 are used at the vertex to describe the muon track. One can see that these parameters are natural variables to use when the transverse momentum is used as reference, since most distributions are flat as a function of p_T. The reason to use the transverse momentum as reference seems strange but has to do with the magnetic field. Tracks having the same p_T experience a comparable amount of deflection by the magnetic field. This leads to comparable sagittas for those tracks, which is exactly the behaviour wanted as it is the sagitta that is measured by the detector. It has been found that the pull distributions do not behave very well, i.e. they are Gaussian but do not obey unity width.

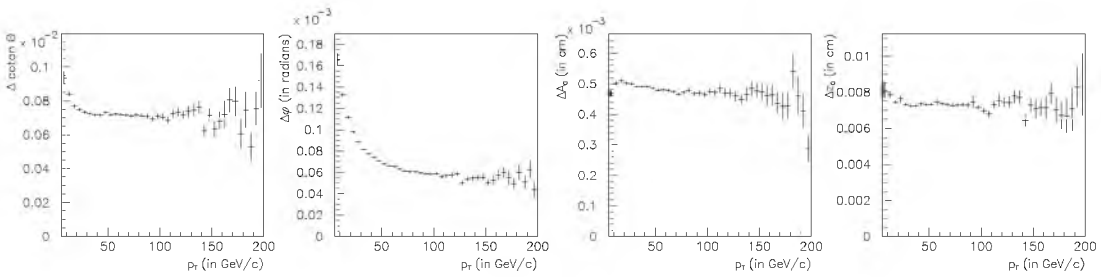

Figure 7.39: XKalman track parameters: $1/\tan\theta$, φ, A_0, and z_0 compared to GEANT track parameter values, as a function of p_T using the primary vertex constraint.

7.4.1.1 XKalman compared to MuFit

Average values for IP$\equiv \Delta$IP $= |\Delta A_0|$ and Δz_0 can be inferred from Fig. 7.39 and compared to those of the muon stand-alone reconstruction given in Figs. 7.31 and 7.32, already. It is no surprise that the former is orders of magnitude better, see Table 7.1. Likewise, the accuracy of the angles θ (or η) and φ is expressed in terms of micro-radians, while the accuracy of the muon reconstruction code is more-or-less in the order of milli-radians, which is again a difference of a few orders of magnitude. A valid conclusion is thus that there is no use in combining position and/or angle parameters of the reconstruction codes. Or, in other words, the positional and angular track parameters can be taken directly from the inner detector pattern recognition software.

	$1.0 < \lvert\eta\rvert < 1.2$			$2.5 < \lvert\eta\rvert < 2.7$		
average	MuFit	Muonbox	XKalman	MuFit	Muonbox	XKalman
ΔIP (μm)	$9 \cdot 10^2$	$1.24 \cdot 10^4$	5.91	$3.3 \cdot 10^3$	$4.11 \cdot 10^3$	5.8
Δz_0 (μm)	$2.50 \cdot 10^4$	$2.64 \cdot 10^4$	66.4	$2.46 \cdot 10^4$	$2.50 \cdot 10^4$	170
$\Delta\varphi$ (μrad)	$3.52 \cdot 10^3$	$4.08 \cdot 10^3$	94	$4.1 \cdot 10^3$	$4.8 \cdot 10^3$	125
$\Delta\theta$ (μrad)	$2.69 \cdot 10^3$	$2.99 \cdot 10^3$	227	$6.4 \cdot 10^2$	$7.3 \cdot 10^2$	76

Table 7.1: Average position and angle accuracy for track reconstruction codes. (Muonbox does not have a vertex constraint. Last digits are not significant.)

7.4.2 Combining track information

The situation is different regarding the momentum information of MuFit and XKalman, as this is comparable over a large range of p_T. Figure 7.40 shows the charged inverse momentum resolution obtained by MuFit at the vertex using the beam pipe constraint, as well as the error estimate on this track parameter as a percentage of the generated muon momentum. This is considered to be the best possible muon stand-alone performance. The same is done for the stand-alone inner detector using the muon seeds as its input. The result, in Fig. 7.41, shows the charged inverse transverse momentum resolution obtained by XKalman using the interaction region, and the error estimate on this track parameter as a percentage of the generated transverse momentum.

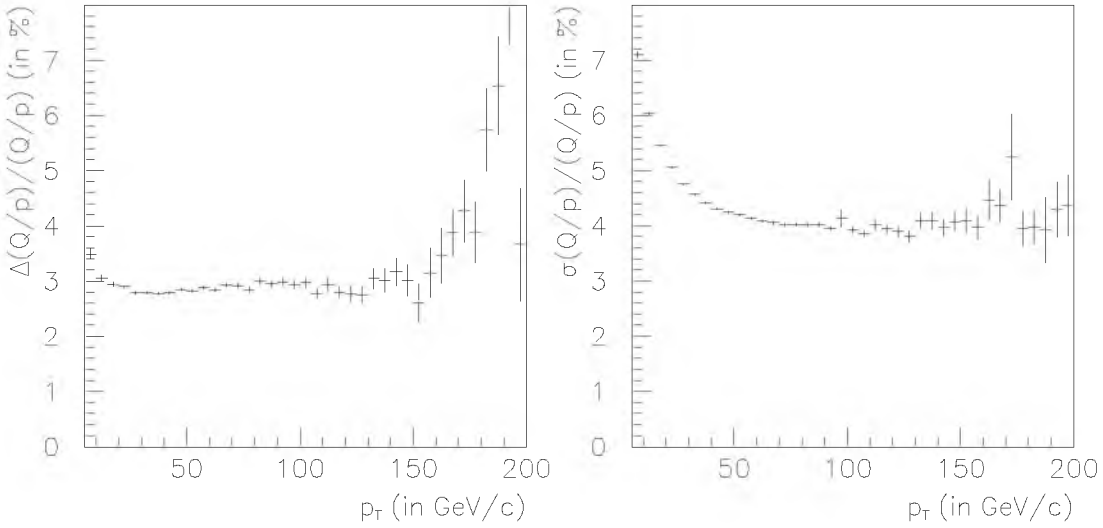

Figure 7.40: Muon stand-alone resolution for the charged inverse momentum track parameter, and its error estimate.

It can be debated whether to use the interaction region constraint for XKalman or not, as it becomes more and more effective at higher momenta, i.e. at $p_T = 100$ GeV/c the improvement has become a full percent on the momentum resolution. In any case, it seems valid to conclude that the stand-alone inner detector momentum resolution is better than the stand-alone muon spectrometer momentum resolution up to $p_T \approx 100$ GeV/c. The stand-alone muon spectrometer performance becomes crucial for higher values of p_T, which is of importance to physics[21] beyond the standard model.

We are dealing with statistical quantities here, which means that the combination has to be applied in a statistical manner. In practice, this implies that a factor $\sqrt{2}$ can be gained, at maximum when the two values and their weights are roughly equal.

[21] Part two of this thesis deals with several physics goals of ATLAS. When compared to CMS, the decision to choose for a well performing stand-alone muon system could prove advantageous, especially in the endcap regions where a toroid performs much better than a solenoid.

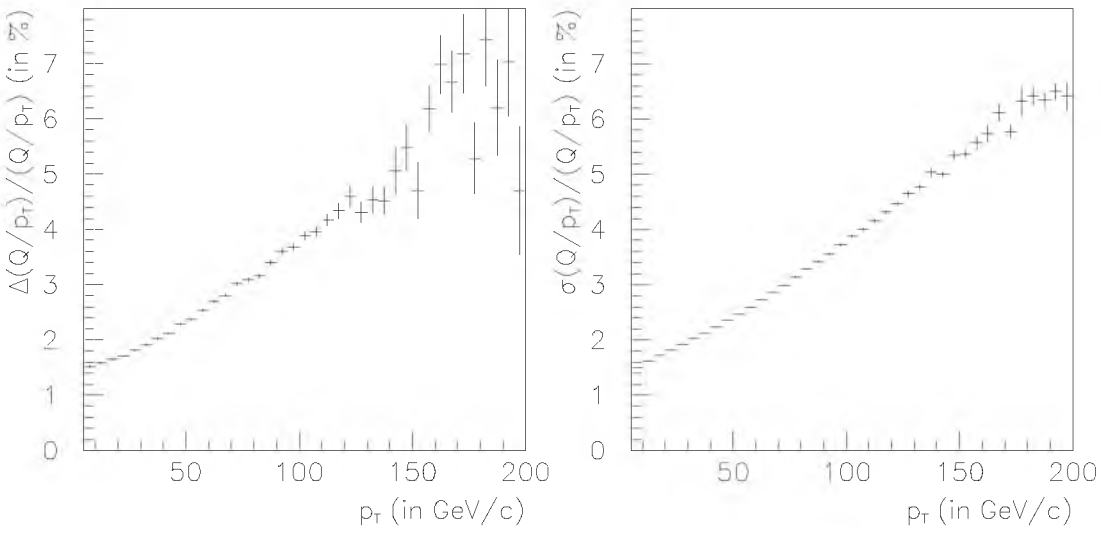

Figure 7.41: Inner detector resolution for the charged inverse transverse momentum track parameter, and its error estimate.

The combined result is presented in Fig. 7.42, which is explained in detail in the next section.

7.5 Combined performance

In order to perform the statistical combination in a mathematically correct way, it is necessary to first transform both sets of track parameters and their respective error estimates, i.e. covariance matrices, to a common set. This is done by means of a Jacobian transformation matrix, using the transformation $\zeta_M^a \equiv (Q/p, \frac{\pi}{2} - \theta, \varphi, S, L, (T)) \xrightarrow{J} \zeta_I^a \equiv (Q/p_T, 1/\tan\theta, \varphi, A_0, z_0)$. The covariance matrices are σ_M^{ab} and σ_I^{ab} for MuFit and XKalman, respectively. Now, the relation $p_T = p\sin\theta$ gives rise to the Jacobian element $J^{11} = 1/\sin\theta$. The only other element of interest is $J^{12} = Q\cos\theta/p\sin^2\theta$, since all others $J^{13} = J^{14} = J^{15} (= J^{16})$ remain zero. It is not of any importance to calculate every Jacobian matrix element, since only the ones mentioned previously play a role in combining the momentum information. Transforming MuFit results into the reference frame used by XKalman is done as follows: $\zeta_M^a \xrightarrow{J} \zeta'^a_M \equiv J^{ab}\zeta_M^b$ and $\sigma_M^{ab} \xrightarrow{J} \sigma'^{ab}_M \equiv J^{ac}\sigma_M^{cd}J^{db}$. Or, in a shorthand notation: $\zeta'_M = J\zeta_M$ and $\sigma'_M = J\sigma_M J^T$. Since $\sigma^{12} \equiv \sigma^{21}$ in general, we have now obtained that $\sigma'^{11}_M = \sigma_M^{11}/\sin^2\theta + 2(Q\cos\theta)\sigma_M^{12}/p\sin^3\theta + (\cos^2\theta)\sigma_M^{22}/p^2\sin^4\theta$, which happens to be the square of the error estimate on the new charged inverse transverse momentum (of MuFit).

Having the results of MuFit and XKalman in the same reference frame makes it possible to perform the actual combination. This is given, in general[88,89], as $\zeta_{\text{comb}} = (\sigma'^{-1}_M + \sigma_I^{-1})^{-1}(\sigma'^{-1}_M\zeta'_M + \sigma_I^{-1}\zeta_I)$ with covariance matrix $\sigma_{\text{comb}} = (\sigma'^{-1}_M + \sigma_I^{-1})^{-1}$. Since $\zeta^a_{\text{comb}} \equiv \zeta_I^a$ for $a = 2\ldots5$, it is only instructive to show $\zeta^1_{\text{comb}} = (Q/p_T)_{\text{comb}}$ and

$\sigma^{11}_{\text{comb}}$ which should be interpreted as the improved combined momentum and its error estimate. See Fig. 7.42 for a comparison with the original values coming from MuFit and XKalman, as were shown in Figs. 7.40 and 7.41.

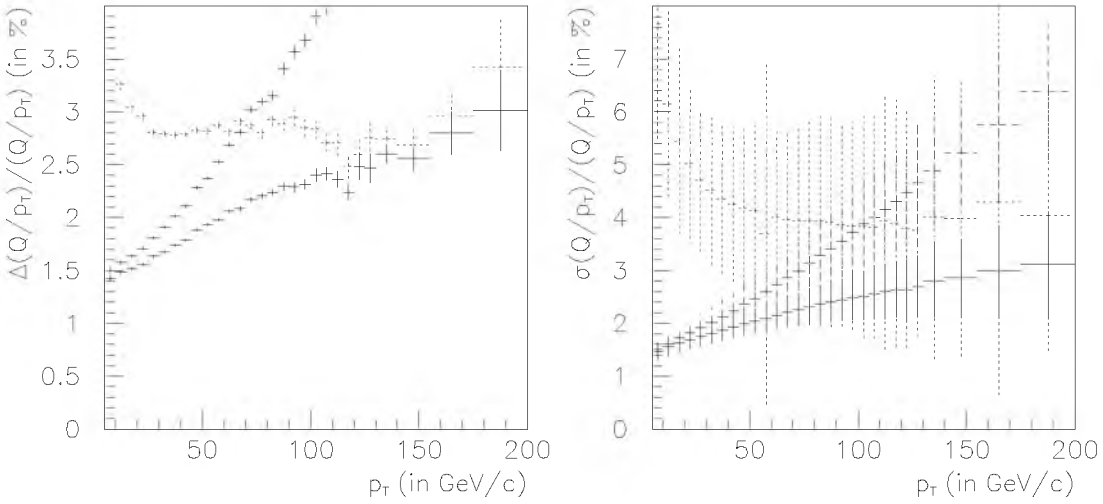

Figure 7.42: Improved charged inverse transverse momentum resolution (represented by full lines inside the left sub-figure), and its percentual error estimate (represented by full lines inside the right sub-figure), obtained through statistical combination of muon stand-alone (dotted lines) and inner detector (dashed lines) track segments.

Since the resolutions were obtained by fitting a normal distribution to the contents per bin, a test is to acquire a feeling[(22)] of the pull distribution $\Delta(Q/p_{\text{T}})/\sigma_{Q/p_{\text{T}}}$, which is trivially obtained as it evolves from dividing the values in the figures of interest on a bin-by-bin basis. Another test is to compare the results of Fig. 7.42 with results stemming from other approaches, like COBRA[142] and STACO[132]. It should be remarked that the procedure used by STACO is based on exactly the same mathematical formulas for the statistical combination as described above. Surprisingly enough, it is found that the simplistic approach used by MuFit yields the same results as its recent counterparts.

Several remarks need to be made though. Firstly, MuFit performs only the first phase of muon reconstruction, and prepares for the second phase. This means that it assumes that all tracks found by Muonbox are due to genuine muons originating from the event of interest. The other codes perform a combined fit, i.e. the second phase of muon reconstruction, in order to prepare for the third phase, where a muon (track) is uniquely identified. So, since they do not assume that a track comes from a genuine muon, their performance and efficiency is a bit different. Secondly, this also means that these codes do not utilize a primary vertex constraint, in general. Thirdly,

[(22)]This is not true for Fig. 7.40 because the central peak of the momentum resolution (in Fig. 7.33.c) is narrow compared to the width of the distribution. The momentum resolution comes from the central peak, and would be largely overestimated when taking the tails of the distribution into account.

the underlying data samples used to evaluate the performance are fundamentally different. MuFit uses a sample that resembles muons coming from Higgs decays, while performance comparisons between competing combined fit methods are based on distributions flat in η and φ, at a given value of p_T. The former has relatively more tracks inside the muon and inner detector barrels, where fit results happen to be better than in the endcaps. Direct comparisons of Fig. 7.42 to other results[150] may, therefore, be misleading.

Figure 7.43 shows the fraction/percentage of successfully combined tracks as a function of η and φ, averaged over the momentum range $5 < p_T < 200$ GeV/c. It is clear that the combined fit method fails in several regions, shown in dark in the figure. The overall success rate lies at 93%, for a total of 200.000 tracks. Detector and/or pattern recognition inefficiencies make up the largest part of the missing 7%. Namely, 3% of the tracks have not been found by Muonbox, most of them are located at $|\eta| \approx 0$ or in the feet sectors. Another 1.7% of all tracks is not found by XKalman, since the inner detector has a pseudo-rapidity coverage of $|\eta| < 2.5$, only. When trying to combine information, in 0.8% of all cases no inner detector track is found within the road defined by the provided seed. This percentage can be decreased by increasing the seed widths, at the risk of finding fake inner detector tracks. For the remaining 1.5% combining failures, the track momenta of the two track segments are too far off to be combined sensibly. There are three possible underlying reasons for this kinematical mismatch: either one of the track segments was misfitted or the error on the track momentum was by far underestimated, or the muon may have experienced a catastrophic energy loss inside the calorimeters. This percentage can also be decreased, e.g. by relaxing the requirement on the kinematics. No η, φ or p_T dependencies can be found in case of miscombined track segments.

Now that the tools of interest have been thoroughly analysed, it is time to look at an application of muon track reconstruction. The next part of this thesis deals with a case study.

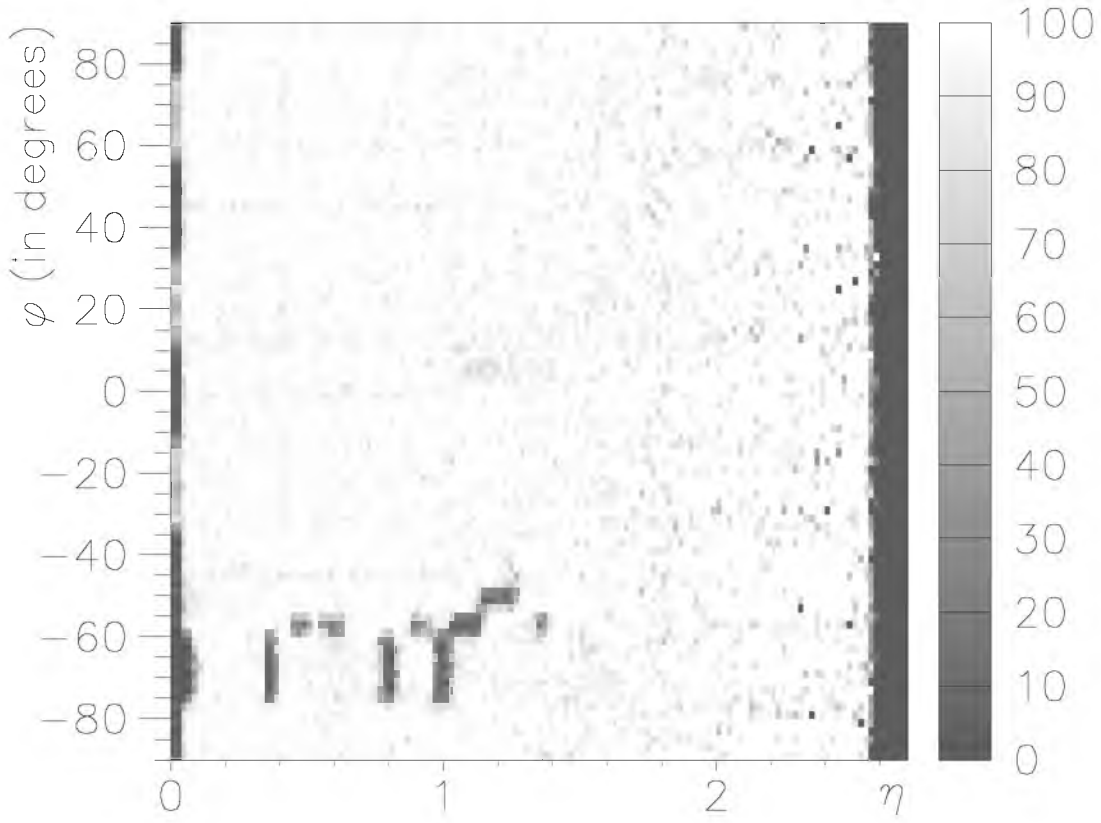

Figure 7.43: Percentage of successfully combined muon and inner detector track segments, averaged over $5 < p_{\mathrm{T}} < 200$ GeV$/c$*, as a function of* η *and* φ.

Part II

Multiple muons

Chapter 8

Introduction to the theory

A rather elaborate description was given in Part I how to obtain the track parameters of elementary particles, in particular muons, using the ATLAS detector. Then, of course, the question arises of what can be done with this knowledge. In order to be able to answer this question, it is necessary to first introduce several basic notions.

8.1 Constituents of nature

According to the ancient Greeks[(1)], everything around us consisted of four constituents, namely earth, fire, air, and water. Hidden herein lies an awesome thought which is usually unnoticed by modern man. The Greeks had been able to abstract the notion that it is possible to construct larger structures using existing building blocks, a clear example from everyday experience, into the notion that possibly all matter around us can be considered as larger structures built up of still smaller, but yet fully unknown, elements. This idea goes under the name of reductionism[152], a concept that is still constantly criticized, also because it implicitly entails an even more profound thought. This is the belief that the full structure can not be more than just an addition of the parts. Or put otherwise, the properties of a substance should follow completely from the properties of its constituents. In the light of this, it becomes obvious that earth, water, air, and fire stand for different, much more abstract, elements[(2)].

So, in short, it is not really the nomenclature that matters but more importantly how the basic notions are dealt with. In view of this, it becomes understandable why it took numerous centuries before this, as we see it, strange and limited worldview began to change. During the Middle Ages, attention was primarily paid to the (divine) entirety[155, 156], while reductionism became fashionable again in the Renaissance with the rise of art and science. The four ancient Greek elements did not fit any more into the new vision of the world and their place was gradually taken by many tens of chemi-

[(1)]Reference [151] states this to be the vision of a certain Empedocles (about 490-430 B.C.).

[(2)]It is questionable altogether in how far the vision of the ancient Greeks can be said to be reductionistic[153], though Democrites (about 460-370 B.C.) conceived the notion of finite divisibility of matter[154], which is also referred to as atomic theory.

cal elements[157]. The culmination of logic came in 1869, when Mendeleev[158] was able to draw up the periodic table[3] of elements. Every substance could now be described, using chemical formulae, by its constituents, the atoms that form the elements of the periodic table.

However, reductionism has gone further by explaining the logic behind the periodic table to describe every atom as a number of protons and neutrons, that comprise the atomic nucleus[159], around which circle a number of electrons[160]. It becomes now necessary to introduce the fundamental forces of nature also. But the description of matter has not been completely finished yet, since other constituents do exist, such as the muon, which has been found in (high energy) experiments in the middle of the twentieth century. Later experiments gave more insight and the current understanding is that three generations of quarks and leptons exist with their corresponding anti-particles. They are listed in Table 8.1 (from reference [68]).

family	symbol	electric charge (e)	mass (c^{-2})	symbol	electric charge (e)	mass (c^{-2})
1	d	$-1/3$	$3-9$ MeV	e	-1	511.0 keV
	u	$+2/3$	$1-5$ MeV	ν_e	$+0$	<3 eV
2	s	$-1/3$	$75-170$ MeV	μ	-1	105.7 MeV
	c	$+2/3$	$1.15-1.35$ GeV	ν_μ	$+0$	<0.19 MeV
3	b	$-1/3$	$4.0-4.4$ GeV	τ	-1	1777.0 ± 0.3 MeV
	t	$+2/3$	174 ± 5 GeV	ν_τ	$+0$	<18.2 MeV

Table 8.1: Quark and lepton families.

Only the members of the first generation are present in matter around us. The small cartoon in Fig. 8.1 more-or-less shows how.

8.2 (Fundamental) forces of nature

Sir Isaac Newton published his 'Principia' in 1687[161], where he introduced classical mechanics, a description of the laws of motion, on the basis of action by forces in nature. Well known is the apple falling from the tree, which is associated to the gravitational force. Furthermore, he showed the equivalence of force and motion, or better yet: acceleration. Newton's laws are a perfect description for what happens daily in our surroundings, but still they are only a good approximation. The validity of the laws depends on the scale at which the experiments are performed. When systems are measured that approach the speed of light more-and-more, then it becomes apparent that the deviation from Newton's laws becomes larger as well. The solution has been postulated by Albert Einstein in the form of special relativity[162](in 1905)

[3]The strength of logic lies in the fact that Mendeleev's table contained a number of open places and thus predicted the existence and characteristics of several more chemical elements which were actually found later on using this knowledge.

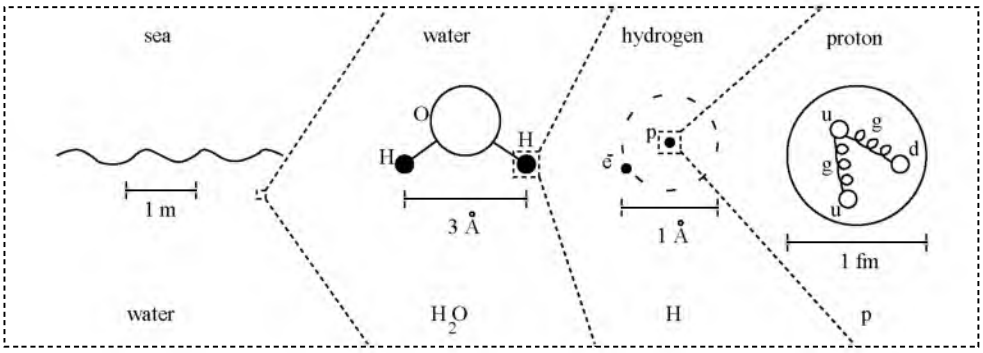

Figure 8.1: Magnification into increasingly smaller constituents of matter, i.e. from molecules via atoms to nucleons.

and general relativity[163](in 1916), which conform extremely well to these kinds of measurements.

Another example involves magnetism, electricity and the corresponding electromagnetic forces, i.e. meaning both magnetic and electric forces, which are all commonly encountered in every day life as well. It is very well possible to constitute a separate theory for both, but Maxwell was able in 1864 to unify the two phenomena into one theory. The strength of the theory of electromagnetism[164, 165] is not so much that it gives an adequate description of magnetic and electric forces, but what makes it special is the notion that these forces are actually two possible appearances of one unified electromagnetic force.

Same-signed charges experience a repulsion, according to Coulomb's law[166], and the smaller their mutual distance the larger the repulsion. This would mean that the positively charged protons cannot be brought together close enough to form the atomic nucleus. Still, it is known that they do, in conjunction with the neutrons. The strong nuclear force, better known as the strong interaction, acts on the various quarks and it is this force which is responsible for the stable atomic nucleus, since its attraction is so much stronger at short distances[(4)] than the electromagnetic repulsion.

Lastly, one other important force in nature which is subject to experiments is the weak nuclear force, better known as the weak interaction. The weak interaction is responsible for natural radioactivity of various elements, and also for the "slow" decay of elementary particles. Examples hereof are the decay of a neutron: $n \rightarrow p + e^- + \overline{\nu}_e$ and the decay of a muon: $\mu^- \rightarrow e^- + \overline{\nu}_e + \nu_\mu$. A model[167, 168] describing this interaction was introduced by Fermi in 1933, where he had to postulate[(5)] the existence of the (possibly) massless, neutrally charged neutrino. Furthermore, the model predicted the existence of a four-point interaction according to the scheme presented below.

Although the idea of the existence of the neutrino has proven to be very successful, that of the existence of a four-point interaction was not good enough. Further experi-

[(4)]The typical distance here is of the order of one femtometer.

[(5)]The postulate actually came from Pauli in 1930[169].

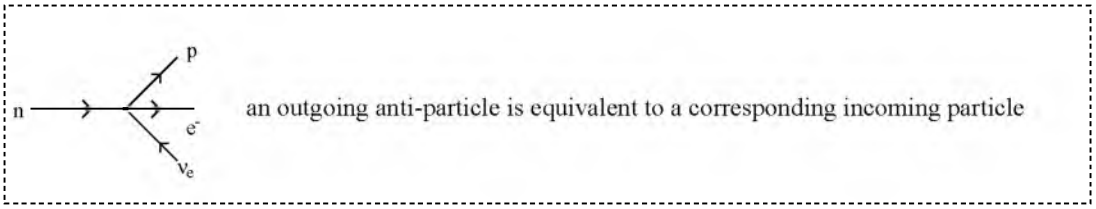

Figure 8.2: β-decay of a free neutron.

ments showed a clear disagreement with the model at higher energies. This behaviour has led to the improved Glashow-Weinberg-Salam model[170–172] where use is made of the exchange of virtual particles. Here, we deal with a very peculiar non-intuitive concept.

It is not uncommon in physics to bring forth counterintuitive theories. Through Newton's laws it has become known that force and acceleration are equivalent. Einstein's famous formula $E = mc^2$ puts mass and energy on the same footing, while, according to his theory of general relativity, space becomes curved under the presence of mass, c.q. influence of gravity. The atomic shell model of Bohr[160] shows that even the densest substance consists of almost nothing, even neglecting the interatomic space. Furthermore, quantum mechanics has taught us that the observation itself exercises an influence on the observed system. So to say, the above examples show that phenomena expose themselves depending on the way in which observations are being executed. This is called paradigm[6] cultivation.

Also for the other forces in nature, it is very well possible to build models in which they are described by virtual particle exchange. See Table 8.2 (taken from [174]).

name	symbol	mass (GeV/c^2)	type of interaction	strength	acts upon
gluon	g	0	strong	1	quarks, gluons
photon	γ	0	electroweak	10^{-2}	charged particles
vector-	Z^0	91.2	electroweak	10^{-13}	quarks, leptons
bosons	$W^{\pm}$	80.2	electroweak	10^{-13}	quarks, leptons
graviton	g	0	gravity	10^{-38}	massive particles

ps. the graviton has not been observed (yet) while both gluons and quarks have not been observed in isolation.

Table 8.2: Fundamental forces in nature, with corresponding virtual particles, interaction type and relative strength compared to the strong interaction at a distance of 10^{-15} m.

[6] An interesting example of a paradigm is the attempt to formulate physics in terms of music instead of the usual maths[173], which clearly demands a completely different way of performing observations.

8.3 History of the Standard Model

At the moment, experiments in the field of elementary particle physics are conducted within the framework of the so-called Standard Model. This theory is a combination of a theory for the strong interaction with that of the electroweak interaction, both working on the previously described constituents of matter. Gravity has not been taken into account, since it has virtually no influence on the processes[7] under consideration. The building blocks of the Standard Model, therefore, are given by Tables 8.1 and 8.2, while leaving out gravitons. Its description was complete around 1968, though a small extension of the original model by one full family proved to be necessary.

The success of the model is reflected in the fact that a large number of predictions could be made[175, 176] which all proved to be correct later on. In 1973[17] it became obvious that the Z^0-vector boson did indeed exist, although it took until 1983 before it was actually observed[177, 178], shortly after the discovery of the W^+- and W^--vector bosons[179, 180]. The τ^--lepton was found in 1975[181] and the matching generation of quarks a bit later, namely the b-quark in 1977[182] and the t-quark in 1995[183, 184].

To explain the phenomenon of mass, the Standard Model predicts the existence of a so-called Higgs-boson. This vital particle has not been observed by the existing experiments yet. The remainder of this thesis will concentrate on how to prove the existence of this particle. Before it is possible to continue, however, it is necessary first to introduce the essence of mass and the mathematics involved.

8.4 Concept of mass

It is important to ask oneself: what is mass, or: how do we experience the influence of mass when we cannot tell what mass is itself?

In fact, it turns out to be a deep philosophical question to be able to give the definition of mass. For this purpose[8], we concentrate on a ball and a boulder. These objects clearly exhibit the property mass; as they are said to be massive. According to Table 8.2 this must mean that these objects are under the influence of gravitational forces. Actually, it is precisely this property that tells us that these objects must possess mass. As everyday experience tells us that we can weigh massive objects, i.e. a ball weighs a bit and a boulder usually weighs a lot more.

What happens is that the earth's gravitational field pulls these objects towards the earth. The more mass an object has, the harder it is being pulled at by the earth, i.e. the more weight is shown on the balance. By the way, the objects pull the earth back just as hard[9], but the earth does not budge that easily. Gravitational forces are responsible

[7] The typical distance scale inside the atomic nucleus is of the order of one femtometer.

[8] The text of this paragraph has been fully inspired by the inaugural speech[185] of prof. dr. Sijbrand de Jong. This booklet also gives a very readable introduction to the field of high energy physics.

[9] As Newton's law states that action equals reaction.

for the solar system, though, where the earth orbits around the sun, and the moon around the earth.

Even though gravity does have a clear connection to mass, it has not been possible yet to incorporate gravity into the Standard Model. Put differently, it is not clear how to put a consistent mathematical description of gravity into the mathematical description of the Standard Model. In this thesis no attempt will be made to do so, or to describe any of the ongoing research. Furthermore, as has been said before, the processes under consideration throughout this thesis are practically uninfluenced by gravitational forces. The other fundamental forces of nature are much more of importance for the processes under study.

Now, it has become important to make the distinction between mass and weight. For this purpose we are going to exercise an equal force on both objects, for instance by kicking against them. The ball will roll away some distance and the boulder should move a bit, probably, but if it were larger the boulder stays on its spot completely. The conclusion from this experiment is that the heavier the object is the harder it is to make the bulk come to movement.

Our experience changes when we conduct the same experiment in space, where the gravitational forces and friction have reduced to practically nil. Again, an equal force is applied to the objects. The result will be, according to [185], that the ball will speed away from us. The boulder moves away as well but at a much lower pace. If the boulder were larger it should move still, but that would be hardly noticeable; there is more chance that we will have propelled ourselves into outer space. The conclusion is two-fold: firstly, objects in space are weightless, i.e. the balance shows zero weight, but not massless and secondly, the more mass the object has the slower it will move. It seems as if the mass of an object prohibits it attaining a certain velocity. The higher the velocity should become[(10)] the more the mass seems to resist[185].

Now of course the question comes up what it might be that causes this resistance to occur. Again, reference [185] is used to give an example. Try to move a treacle-pot along a perfectly smooth table without touching the pot itself. From childhood we know that this can be done by putting a spoon into the treacle and moving the spoon. The spoon will move a bit inside the treacle at first, but soon the whole pot moves as well. Then, when a specific velocity has been reached, the effort to sustain the movement becomes practically none. This is exactly what has happened with the massive objects.

The table represents space around us, the objects represent the treacle-pot, the equal force applied is the force applied on the spoon and so the spoon[(11)] stands for mass. But then: what is the treacle? The answer[185]: it is a background Higgs-field.

[(10)] Actually, the choice of words has been a bit sloppy till now. When kicking against the object a certain force has been applied during a certain time interval (Δt), thus giving the object a certain acceleration ($\vec{F} = m \cdot \vec{a}$) during that time interval (Δt) resulting in a specific velocity afterwards ($\vec{v} = \vec{a} \cdot \Delta t + \vec{v}_0$).

[(11)] Here, a small spoon corresponds to a large mass, because the small spoon will have moved a lot in the treacle before the pot starts to move, meaning that much force has to be applied before the object starts to move. Likewise, a small mass corresponds to a large spoon.

8.5 Vacuum, energy and particle creation

It seems strange that an object can have mass in space. This would mean that the vacuum is like the treacle, as described in the example of the previous paragraph, i.e. the vacuum of space would be filled with a background field of Higgs particles. Even though this seems a clear contradiction, it is in fact not. It is true that there are no particles in (a perfect) vacuum, but the Heisenberg uncertainty relation[186, 187] does allow for the existence of so-called virtual particles during a short[(12)] time-period. All particles one can possibly think of appear (together with their anti-particles) and immediately disappear spontaneously in space. The particles do not live long enough to be measured, but their influence can be measured as was done by Casimir in 1948[189], therefore they are virtual. The process of spontaneous creation and annihilation of particle anti-particle pairs is called vacuum fluctuation.

In Sect. 8.2, we already touched on the idea of the exchange of virtual particles (quanta) associated with particular types of interaction, see Table 8.2. Actually, the classical point of view, where an interaction at a distance is described in terms of a potential or a field due to the influence of one object upon another one, is equivalent on a macroscopic scale, to the quantum mechanical point of view where quanta are exchanged. Both concepts are just as fictitious[188] since neither fields nor virtual quanta can be observed directly. Their influence is in both cases the same, namely a resulting force is exercised and this is the measurable quantity. On a microscopic scale though, on the other hand, it has been found that propagating fields are quantized in the form of bosons.

In 1935, Yukawa was seeking a way to describe the short-range force between neutrons and protons in the atomic nucleus and he came up with the connection stated in the following sentence. The range of the static interaction depends on the mass of the free field quantum, because the time of existence of virtual particles (during vacuum fluctuations) is also restricted by their mass. This Yukawa theory[3] led to the hypothesis of the existence of a spinless quantum with mass $m \simeq 100$ GeV$/c^2$ given a range[(13)] of interaction of $R \simeq 10^{-18}$ m, where $R = \hbar/mc$.

Turning back to the original argument, one should say that the idea of a vacuum consisting of absolutely nothing is based on a misconception. And so, even though the spontaneously created particles exist for a very short period of time, the vacuum fluctuations have their influence. The influence of the Higgs particles is rather special as they give mass to all particles (see appendix C for details on this mechanism). With this notion the argument is concluded.

[(12)]The uncertainty principle states that $\Delta E \cdot \Delta t \leq \hbar$, meaning that a particle with mass 1 MeV$/c^2$ at rest ($E = mc^2$) could exist at most in the order of 10^{-21} s $= 10^{-6}$ fs[188].

[(13)]Page 23 of [188] states the range of the weak interaction to be in the order of 10^{-18} m, while the mediators of the weak interaction have masses in the order of $80 - 90$ GeV$/c^2$.

Chapter 9

Theory: the Standard Model

9.1 A mathematical base

Humankind has a predilection for symmetry, or phrased differently: everywhere around us we experience symmetries in nature. Mathematics, usually, is a very good instrument to describe symmetry. So, it seems a good idea to formulate nature in terms of maths. Actually, during the development of philosophy a sound mathematical base emerged as well. One can say that there is a basis to empiricism thanks to symmetry because it states that every experiment should be repeatable at a different location and time while giving the same outcome. This means that verifiability can only be achieved when the laws of nature are independent of place and time. This is called a global, external symmetry.

A sphere, which looks exactly the same from every point of view, has the highest possible degree of global, internal symmetry. An internal symmetry does not depend on the movement of the system under consideration. Group theory[(1)], which is the maths behind symmetries, states that the symmetry group of a global symmetry remains the same for every point in space-time[190]. Quite a number of properties of elementary particles can already be explained by this type of symmetry.

9.1.1 Global symmetry

The space-time transformations associated with special relativity are the Lorentz-transformations, along with the Lorentz-group. If translations are taken into account as well then we end-up with the Poincaré-group $(P(T))$. To be more precise: the group of all coordinate transformations T in Minkowski space-time of the form $x'_\mu = \Lambda_{\mu\nu}(T)x^\nu + t_\mu(T)$ with $x^\nu = (ct, x, y, z)$; $x_\mu = g_{\mu\nu}x^\nu$, where the 4×4 real matrices $\Lambda(T)$ satisfy the relation $\widetilde{\Lambda}_{\sigma\rho}(T)g^{\rho\mu}\Lambda(T)_{\mu\nu} = g_{\sigma\nu}$ with $g_{\mu\nu} = \left(\begin{smallmatrix} 1 & 0 \\ 0 & -\mathbb{I}_3 \end{smallmatrix}\right)$; $g_{\mu\rho}g^{\rho\nu} = \delta^\nu_\mu$ and $t(T)$ an arbi-

[(1)] An example of a textbook on group theory is J.F. Cornwell[190].

trary 4×1 real matrix. Now, for every physical system[(2)], described by the Lagrangian density $\mathcal{L}(x)$, the relationship $P(T)\mathcal{L}(x) = \mathcal{L}(x)$ must hold. This is the mathematical definition of a global, external symmetry. It is actually responsible for some very important kinematic conservation laws: energy conservation and momentum conservation.

An example of a Lagrangian density is that describing a freely moving electron: $\mathcal{L} = \overline{\Psi}(i\partial\!\!\!/ - m)\Psi$, where the typical standard notation[(3)] of quantum field theory is used. Writing things out more explicitly we get[190]:

$$\mathcal{L}_0^{\mathrm{f}}(x) = \Psi^\dagger(x)\gamma^4(i\hbar c\gamma^\mu\partial_\mu - mc^2)\Psi(x) \quad . \tag{9.1}$$

This expression is valid for every free fermion field, so it just stands for a free particle with intrinsic spin $\frac{1}{2}$ and rest mass m. The four-component spinor field $\Psi(x)$ is determined by this equation except for a fully arbitrary normalization, or gauge. Namely, every $\Psi'(x) = \mathrm{e}^{-i\alpha}\Psi(x)$, $\alpha \in \mathbb{R}$ fulfills the equation and gives rise to an identical Lagrangian density.

The transformation $\Psi(x) \to \Psi'(x) = U\Psi(x)$ with $U = \mathrm{e}^{-i\alpha}$, $\alpha \in \mathbb{R}$ is called a global gauge transformation and has a unique connection to a global internal symmetry[194]. Or, put in mathematical terms, the theory described above has a global gauge invariance under the group[(4)] U(1). The Noether theorem[195] states that a local conserved current exists which is connected to this invariance, i.e. symmetry. Integration of the current over the three space coordinates gives rise to a conserved quantity, i.e. charge, which can be physically measured.

Important quantum numbers, conserved quantities, or charges, as for instance L, B, Q, S, C label one-dimensional representations of mutually commuting groups which are isomorphic to U(1)[194]. So, one can write the following:

$$\begin{aligned}
&B: \Psi \to \mathrm{e}^{-i\alpha B}\Psi, && B = \text{baryon number of particle } \Psi \ \ (\text{quarks have } B = \tfrac{1}{3})\\
&Q: \Psi \to \mathrm{e}^{-i\beta Q}\Psi, && Q = \text{electric charge of particle } \Psi\\
&S: \Psi \to \mathrm{e}^{-i\gamma S}\Psi, && S = \text{strangeness of particle } \Psi \ \ (\text{s-quark has } S = -1)\\
&C: \Psi \to \mathrm{e}^{-i\delta C}\Psi, && C = \text{charm of particle } \Psi \ \ (\text{c-quark has } C = +1)\\
&L: \Psi \to \mathrm{e}^{-i\sigma L}\Psi, && L = \text{lepton number of particle } \Psi \ \ (\text{quarks have } L = 0\\
& && \text{and leptons have } L = 1),
\end{aligned}$$

where all of these quantum numbers stand for global internal symmetries of elementary particles.

When performing experiments, however, it turns out that not all of these quantities are exactly conserved. For example, strangeness and charm are not necessarily conserved under the weak interaction. This phenomenon is known by symmetry breaking.

---

(2) Textbooks dealing with descriptions of physical systems are for example: 'Classical Mechanics' by Goldstein[191], 'Quantum Field Theory' by Itzykson & Zuber[192], 'Relativistic Quantum Mechanics' by Bjorken & Drell[193].

(3) Usually so-called natural units are used, where the relation $\hbar = c = 1$ holds.

(4) The groups U(n) consist of all unitary (complex) $n \times n$ matrices U (they satisfy $U^\dagger U = UU^\dagger = \mathbb{I}_n$), where the group U(1) consists of every $\mathrm{e}^{-i\alpha}$ with $\alpha \in \mathbb{R}$.

Though it might seem artificial at the moment, the importance of symmetry breaking will become more clear when looking at local gauge invariance.

The last, and utterly important, example of a global internal symmetry is that of isospin. The existence of this type of symmetry has been suggested by Heisenberg [196–198] in 1932, when he remarked that the proton and neutron could be treated as two states of one type of particle: the nucleon. Likewise, $\pi^{\pm}$ and π^0 form the three isospin states of the pion.

Experiments confirm that isospin symmetry is conserved under strong interactions. This can be visualized by considering isospin to be an iso-spatial vector $\vec{I}$. The length (I) of this vector does not change under rotations in isospin-space, which is what counts during the strong interaction and thus no discrimination is made between the separate states of either nucleon or pion. The electroweak interaction, on the other hand, fixes the isospin. The I_3 (or I_z)-axis becomes fixed in isospin space and all states are projected onto it. This happens because the electromagnetic interaction couples to the electric charge of a particle. The latter has a direct association to I_3 according to the relation given in Eq. (9.2). It is possible to give the group representation of particles in isospin space; for the nucleons we write $|p\rangle = \left|\frac{1}{2},\frac{1}{2}\right\rangle$, $|n\rangle = \left|\frac{1}{2},-\frac{1}{2}\right\rangle$, and for the pions $|\pi^{\pm}\rangle = |1,\pm 1\rangle$, $|\pi^0\rangle = |1,0\rangle$. This is according to standard notation: the isospin $\vec{I}$ wave function becomes $|I,I_3\rangle$ with $I = |\vec{I}|$.

The symmetry group for the isospin of nucleons is SU(2). It leaves the norm I invariant (and accordingly that of the particle wave function). Actually, this underlying symmetry group is the only, and very misleading, connection to spin, as SU(2) is the typical symmetry group of spin-$\frac{1}{2}$ particles. The u- and d-quarks, given in Table 8.1, are grouped in an isospin doublet, while all other quarks belong to isospin singlets. After introduction of the hypercharge Y as $Y = B + S + C$, the empirical relation[5]:

$$Q = I_3 + Y/2 \tag{9.2}$$

seems to hold, as has been found by Nishijima[199] and Gell-Mann[200]. The importance of isospin symmetry is that it explains the build-up of all hadronic multiplets, which becomes apparent when placing known particles in a Y-I_3 plane[6] (and even more after adding an additional axis for the charm charge C).

Isospin is of importance for the weak interaction as well, though the value I_3 is replaced by T_3, which is called weak isospin (denoted by the symbol $\vec{T}$). As already mentioned, the quarks (u, d, s, c, b, and t) are not invariants under the weak interaction, i.e. they are not eigenstates of the weak interaction. Cabibbo[201, 202] found that certain linear combinations of quarks do become invariant under the weak interaction, though. In practice this means that the quarks (d, s, b) are replaced by (d', s', b'), which are eigenstates of the weak interaction. The leptons in Table 8.1 are eigenstates of the weak interaction, i.e. they are given as weak isospin doublets in the table.

[5] Physical constants like e and $\hbar$ have been left out from the equation since natural units have been used.

[6] This insight has led to the discovery of the Δ^{++} particle.

One striking observation is that the mass differences of quarks and leptons within one family can be really large. So, the weak isospin symmetry is a broken symmetry.

9.1.2 Local Symmetry

Having seen several manifestations of global symmetries in nature, it is now interesting to look a bit further into the details of local symmetries. Cornwell[190] states that a system has a local symmetry when it has an internal symmetry group $\mathcal{G}(x)$ at every point $x \equiv \underline{x} = (ct, \vec{x})$ in space-time and that all these groups $\mathcal{G}(x)$ have to be isomorphic to each other. The local symmetries correspond to gauge theories that can be of the Yang-Mills type[203] when $\mathcal{G}(x)$ is not abelian.

It is illustrative again to consider a free, charged fermion to demonstrate the power of a gauge field theory. However, this time the electric charge of the particle (field) is turned into a local U(1) symmetry, according to:

$$\Psi(x) \rightarrow \Psi'(x) = e^{i\theta(x)Q}\Psi(x) \quad .$$

Application of this transformation to Eq. (9.1) gives rise to the inequality[7] $\mathcal{L}'(x) \neq \mathcal{L}(x)$ whereby the U(1) symmetry seems to have disappeared. Thus, it becomes necessary to use a technique called gauge fixing where the derivative ∂_μ is exchanged by the covariant derivate $D_\mu = \partial_\mu + iqA_\mu$. This introduces the gauge field $A_\mu(x) \rightarrow A'_\mu(x) = A_\mu(x) + \partial_\mu\alpha(x)$. With the identification $\theta(x) = -e\alpha(x)$ we now do get the proper equality $\mathcal{L}'(x) = \mathcal{L}(x)$. Since Q stands for the electric charge quantum number, we derive that eQ stands for the electric charge q of the particle, which is the coupling constant[8] of this U(1) group. The vector field A_μ is the electromagnetic potential describing a massless, intrinsic spin 1 boson; the photon. The interesting part of the QED Lagrangian density is the interaction term:

$$\mathcal{L}_{\text{int}} = -q\overline{\Psi}\gamma^\mu A_\mu \Psi = -J^\mu A_\mu \tag{9.3}$$

with the electromagnetic current: $J^\mu = eQ\overline{\Psi}\gamma^\mu\Psi$. Though the argument looks rather artificial, one might conclude that when the Lagrangian density of free, charged fermions and the free, electromagnetic field[9] needs to be (gauge) invariant under the previously given (gauge) transformations, then this means that an interaction between fermions and photons exists through a coupling to the electric charge. However, though the coupling goes through the charge (of the group), this does not mean that there is an explanation why, for instance, protons, electrons, and muons have the same magnitude of the electric charge.

In 1949, Feynman[204] introduced a way to get more insight into field theoretical calculations. Through the technique of Feynman-diagrams, it becomes possible to

[7] To be more exhaustive: $\mathcal{L}'(x) = \mathcal{L}(x) - (\gamma^\mu\partial_\mu\theta(x))Q\overline{\Psi}(x)\Psi(x)$.

[8] The coupling constant is generally denoted by $g/\hbar c$ when using the proper units.

[9] This Lagrangian density has the general form $\mathcal{L}_0^{\nu}(\underline{x}) = -\frac{1}{4}F_{\mu\nu}F^{\mu\nu} + \frac{1}{2}M^2c^2/\hbar^2 A_\mu A^\mu$ with $F_{\mu\nu} = \partial_\mu A_\nu - \partial_\nu A_\mu$ where $A_\mu(\underline{x})$ is a four-vector which denotes a free particle of intrinsic spin 1 and rest mass M; so $M = 0$ for photons.

associate every term of the Lagrangian density with a schematic representation of it. Without giving the rules of the schematic representations, we conclude the example by just showing the Feynman-diagram of $\mathcal{L}_{\text{int}}$, i.e. Eq. (9.3), in Fig. 9.1.

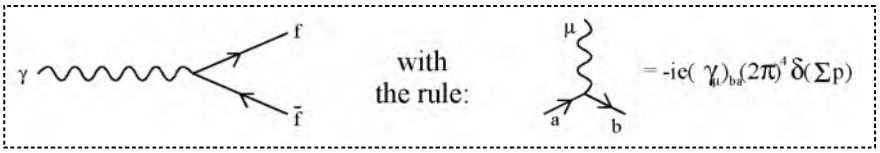

Figure 9.1: Feynman diagram and Feynman rule of electrodynamic interaction. a, b and μ stand for space-time, i.e. four-vector, components (of incoming, outgoing fermions and photon, respectively).

9.2 Symmetry within the Standard Model

The fermions in the Standard Model, that is: the leptons and the quarks, have another property which has not been discussed yet. It is called chirality and can be experimentally measured only by means of the so-called helicity[188, 205–207]. It has been shown that the four-component spinor $\Psi(x)$ describing the fermion (field) is actually a superposition of a fermion field with left-handed helicity and one with right-handed helicity. This helicity is the measure in how far the intrinsic spin of the fermion is aligned with its direction of flight. Now, the following holds: $\Psi(x) = \Psi_{\text{L}}(x) + \Psi_{\text{R}}(x) = \text{P}_{\text{L}}\Psi(x) + \text{P}_{\text{R}}\Psi(x) = \frac{1}{2}(1-\gamma_5)\Psi(x) + \frac{1}{2}(1+\gamma_5)\Psi(x)$ and with this the helicity projection operators: $\text{P}_{\text{L}} = \frac{1}{2}(1-\gamma_5)$ and $\text{P}_{\text{R}} = \frac{1}{2}(1+\gamma_5)$ can be defined.

Application of this relation to the free fermionic part of the QED Lagrangian density in Eq. (9.1) gives $\mathcal{L}_0^{\text{f}} = i\overline{\Psi}_{\text{L}}\gamma^\mu\partial_\mu\Psi_{\text{L}} + i\overline{\Psi}_{\text{R}}\gamma^\mu\partial_\mu\Psi_{\text{R}} - m\overline{\Psi}_{\text{R}}\Psi_{\text{L}} - m\overline{\Psi}_{\text{L}}\Psi_{\text{R}}$, from which one concludes that Ψ_{L} and Ψ_{R} can be considered as independent fields. The mass term induces transitions between the fields, as illustrated graphically in Fig. 9.2.

Figure 9.2: Helicity flips of (massive) electrons caused by the mass term(s) of the free fermionic Lagrangian density.

The concept of chirality goes back to 1956[208,209] when experiments on β-decay gave clear indications of parity violation. Namely, one can prove that four-vector couplings $(\overline{\Psi}\gamma^\mu\Psi)$ and axial four-vector couplings $(i\overline{\Psi}\gamma_5\gamma^\mu\Psi)$ conserve parity, while scalar $(\overline{\Psi}\Psi)$, pseudo-scalar $(\overline{\Psi}\gamma_5\Psi)$, and tensor couplings $(i\overline{\Psi}\gamma^\mu\gamma^\nu\Psi)$ do not. Just like

the scalar coupling $m\overline{\Psi}\Psi$, also the tensor coupling $i\overline{\Psi}\sigma_{\mu\nu}\Psi$ is responsible for a chirality flip. The electrons produced in β-decay (the process drawn in diagram 8.2) have been experimentally measured to be solely left-handed. In nature, also only left-handed neutrinos have been observed, which gives rise to the matrix element for this decay to be $(\overline{\Psi}_p\gamma_\mu(1+\gamma_5)\Psi_n)(\overline{\Psi}_e\gamma^\mu(1+\gamma_5)\Psi_\nu)$. This is an example of the so-called pure V-A interaction. Another example, namely the fermion-photon coupling, is presented in the diagrams in Fig. 9.3.

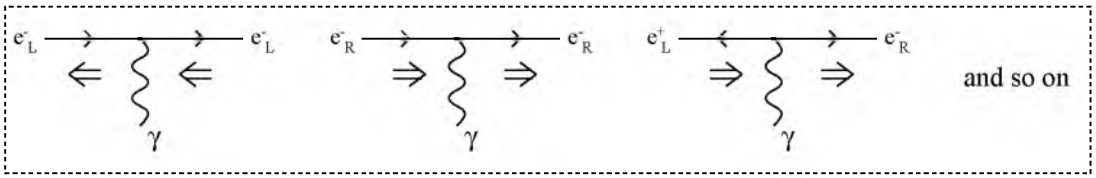

Figure 9.3: Examples of pure V-A interaction diagrams of the electrodynamic fermion-photon coupling.

Going back to the underlying SU(2) weak isospin symmetry group, one can say that the left- and right-handed components of fermions within the Standard Model correspond to different representations of this group. Namely, the left-handed components belong to doublets while the right-handed ones represent singlets. The scheme of Table 8.1 now has changed and is presented again in Table 9.1, along with appropriate quantum numbers.

	family				
$Q=q/e$	1	2	3	I_3	Y
-1	$\begin{pmatrix} e^- \\ \nu_e \end{pmatrix}_L$	$\begin{pmatrix} \mu^- \\ \nu_\mu \end{pmatrix}_L$	$\begin{pmatrix} \tau^- \\ \nu_\tau \end{pmatrix}_L$	$-1/2$	-1
$+0$				$+1/2$	-1
-1	e_R^-	μ_R^-	τ_R^-	0	-2
$-1/3$	$\begin{pmatrix} d \\ u \end{pmatrix}_L$	$\begin{pmatrix} s \\ c \end{pmatrix}_L$	$\begin{pmatrix} b \\ t \end{pmatrix}_L$	$-1/2$	$+1/3$
$+2/3$				$+1/2$	$+1/3$
$-1/3$	d_R	s_R	b_R	0	$-2/3$
$+2/3$	u_R	c_R	t_R	0	$+4/3$

Table 9.1: Quark and lepton families divided up into weak isospin doublets and singlets.

The symmetry group underlying the electroweak part[(10)] of the Standard Model is $SU(2)_W \otimes U(1)_Y$. Here, $SU(2)_W$ stands for the weak isospin symmetry. Sometimes, this is also written as $SU(2)_L$ to emphasize that the left-handed doublets transform under SU(2), while $U(1)_Y$ stands for the hypercharge symmetry.

[(10)] That is: the GWS-model[170–172].

In 1971, 't Hooft[210–212] was able to prove that this theory[11] is renormalizable. This means that calculated quantities can be given a physical interpretation, e.g. they can be measured. Before this statement becomes really true though, it is necessary to introduce a complex doublet field: the Higgs-field[213–215] which is written as a weak isospin doublet of complex scalar fields $\Phi = \begin{pmatrix} \phi^+ \\ \phi^0 \end{pmatrix}$. This field serves the purpose of generating masses for the particles in an elegant way.

To do this, a rather delicate construction is needed, because mass terms cannot be introduced into the Lagrangian density by hand anymore. According to Laterveer[216], the mass term in Eq. (9.1) gives rise to problems. The argument goes as follows: in the case that the mass of the fermions has been put into the Lagrangian density manually, this would mean that left- and right-handed fermions have to have the same coupling to vector gauge bosons in order to keep the theory gauge invariant. However, this immediately means that parity is conserved, which is in contradiction to experiment. Keeping the kinematic term of $\mathcal{L}_0^{\mathrm{f}}$, it is still possible to give a substitute for the mass term in the form of Yukawa-couplings $g_{\mathrm{f}}((\overline{\Psi}_{\mathrm{L}}\Phi)\Psi_{\mathrm{f_R}} + \mathrm{h.c.})$. With this, the theory remains gauge invariant because $\overline{\Psi}_{\mathrm{L}}\Phi$ transforms like the singlet $\Psi_{\mathrm{f_R}}$. Later on in this thesis, it will become clear from where the mass of the fermions originates.

The gauge transformation of the group $\mathrm{U}(1)_{\mathrm{Y}}$ is given by:

$$\Psi(x) \rightarrow \Psi'(x) = \mathrm{e}^{-ig_1\alpha_1(x)\cdot Y/2}\Psi(x) \quad ,$$

the gauge transformations of the group $\mathrm{SU}(2)_{\mathrm{W}}$ by:

$$\Psi_{\mathrm{L}}(x) \rightarrow \Psi'_{\mathrm{L}}(x) = \mathrm{e}^{-ig_2\vec{\alpha}_2(x)\cdot\vec{T}}\Psi_{\mathrm{L}}(x) \quad ; \quad \Psi_{\mathrm{R}}(x) \rightarrow \Psi'_{\mathrm{R}}(x) = \Psi_{\mathrm{R}}(x) \quad .$$

In this, Y and $\vec{T}$ are the so-called generators[12] of the groups, g_1 and g_2 are the accompanying coupling constants, while $\alpha_1(x)$ and $\vec{\alpha}_2(x)$ are fully arbitrary.

Again, it is necessary to perform gauge fixing. For this purpose the gauge fields B_μ and $\vec{W}_\mu$ are introduced. They transform simultaneously as: $B_\mu(x) \rightarrow B'_\mu(x) = B_\mu(x) + \partial_\mu\alpha_1(x)$ and as $\vec{W}_\mu(x) \rightarrow \vec{W}'_\mu(x) + \partial_\mu\vec{\alpha}_2(x) + g_2\vec{\alpha}_2(x) \times \vec{W}_\mu(x)$, where the very last term, i.e. the cross product, can also be written as $g_2\varepsilon_{jkl}\alpha_{2,k}(x)W_{\mu,l}(x)$. The covariant derivative[13] is now given by:

$$\partial_\mu \rightarrow D_\mu = \partial_\mu + ig_1B_\mu\cdot Y/2 + ig_2\vec{W}_\mu\cdot\vec{T} \tag{9.4}$$

for the left-handed spinors, while the last term logically becomes zero for the right-handed spinors. The resulting gauge invariance of $\mathcal{L}_0^{\mathrm{f}}$ can only be proven by going to the infinitesimal forms of the gauge transformations.

[11] We are dealing here with a spontaneously broken Yang-Mills gauge theory[203].

[12] The standard notation uses $Y/2$ and $\vec{T} = \vec{\sigma}/2$ with the Pauli matrices σ_j ($j = 1,2,3$).

[13] The hypercharge is different for left- and right-handed spinor fields, see also Table 9.1. This can be shown by considering the gauge invariance of the Yukawa interaction term $(\overline{\Psi}_{\mathrm{L}}\Phi)\Psi_{\mathrm{R}}$, because the gauge transformation $\Phi(x) \rightarrow \Phi'(x) = \exp(-ig_1\alpha_1(x)\cdot Y/2 - ig_2\vec{\alpha}_2(x)\cdot\vec{T})\Phi(x)$ gives rise to the identity $Y_{\mathrm{L}} - Y_\Phi - Y_{\mathrm{R}} = 0$[207].

9.3 Spontaneous symmetry breaking

It is most clarifying to study the properties of the Higgs-field in detail. The kinematic term inside the Lagrangian density is given by $|D_\mu \Phi(x)|^2$, with the covariant derivative as in Eq. (9.4) for a weak isospin doublet. The most general, non-trivial, renormalizable potential term is $V(\Phi(x)) = \mu^2|\Phi(x)|^2 + \lambda|\Phi(x)|^4 + \text{constant}$ and $\lambda > 0$. Because of the possibility to rotate freely in SU(2) weak isospin space, it becomes possible to consider just one component of $\Phi(x)$ only. The choice is to take the real part of $\phi^0(x)$ and denote it by $\phi(x)$. Different choices of μ^2 have their individual consequences, as sketched in Fig. 9.4 for the choices $\mu^2 < 0$ and $\mu^2 > 0$.

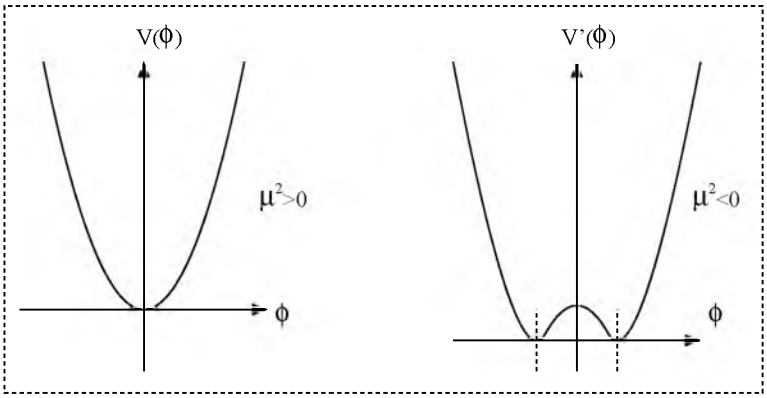

Figure 9.4: Two dimensional representations of the potential term $V(\phi(x)) = \mu^2|\phi(x)|^2 + \lambda|\phi(x)|^4$ with $\lambda > 0$, caused by the (rotated) Higgs field component $\phi(x)$.

In the first case of $\mu^2 > 0$, nothing special happens and the lower bound is found at $|\Phi(x)| = 0$. This state corresponds to the well known general vacuum. When $\mu^2 < 0$, i.e. the second case, we see that the lower bound lies below the usual symmetry point $\phi(x) = 0$ and is reached at $|\phi(x)|^2 = -\mu^2/2\lambda$. These two minimum values of ϕ correspond to a continuum of minimum values for $\phi^0(x)$, and therefore also for $\Phi(x)$.

A definition is to take the minimum at $v/\sqrt{2}$, which implies $v = \sqrt{-\mu^2/\lambda}$, thereby breaking weak isospin symmetry. This procedure is called spontaneous symmetry breaking[217,218], because the vacuum state has now been given a preferred direction in weak isospin space. Since the point $\phi(x) = 0$ has become manifestly instable, it is better to use an expansion around the vacuum[14]: $\phi(x) = \frac{1}{\sqrt{2}}(v + h(x))$.

Going back to the Lagrangian density of the Higgs-field and writing things out, we encounter various interesting terms. For instance, the term $(\frac{\mu^2}{2} + \frac{3\lambda v^2}{2})h^2(x) \equiv \frac{1}{2}m_H^2 h^2(x)$ shows that, by the principle of spontaneous symmetry breaking, a massive Higgs-particle has come into existence. Its mass $m_H^2 = 2\lambda v^2$ is fully unknown, since

[14]Many different notations are used here for the neutral scalar Higgs-field, eg. $\phi(x), H(x), \eta(x), \rho(x)$ instead of the $h(x)$ as used in the Higgs Hunter's Guide[219].

λ is unknown. The potential term also gives contributions proportional[15] to $h^3(x)$ and $h^4(x)$, which demonstrates that the Higgs-particle acquires its mass through self-interactions. Rather special is the fact that the masses of the three massive gauge bosons originate automatically from the kinematic term, while the fourth gauge boson remains massless[213–215]. Other kinematic terms of the Standard Model Lagrangian density give the interaction between fermions and gauge bosons, and between gauge bosons mutually. Corresponding calculations are to be found in appendix C.

One basic symmetry of the Standard Model still has not been taken into account yet. While the GWS-model deals only with the electroweak symmetry $\mathrm{SU(2)_W} \otimes \mathrm{U(1)_Y}$, the full symmetry of the Standard Model is $\mathrm{SU(3)_C} \otimes \mathrm{SU(2)_W} \otimes \mathrm{U(1)_Y}$. The group $\mathrm{SU(3)_C}$ houses the group theoretical base for the hadrons, which consist of quarks (and gluons), and the coinciding strong interaction. All other particles, which do not undergo strong interaction, are described by singlet representations of SU(3). The six different quark flavors (u, d, s, c, b, and t) themselves come in three varieties, denoted by colour, which corresponds to a fundamental triplet representation of SU(3).

Again, a gauge field theory can be constructed by making the SU(3) symmetry local. In complete analogy to the QED example, every generator acquires an accompanying gauge field. These gauge fields $\mathrm{G}^a_\mu(x)$ couple only to colour and are called gluons. There are eight of these gluons, since SU(3) is built up by eight generators[16]. The concept of colour is a fully abstract one, of course. There can be mention of real colour only in association with visible light, but the concept clarifies the underlying ideas quite well. An $\mathrm{SU(3)_C}$ singlet representation can be said to be colourless, or white, and it is possible to assign the triplet representation of the quarks to three additive base colours: red, yellow, and blue. Also, the gluons carry colour charge[17], which means that they can interact mutually. This can also be seen in a more mathematical way from the free QCD Lagrangian density $\mathcal{L}^{\mathrm{QCD}} = -\frac{1}{4}\mathrm{G}^a_{\mu\nu}(x)\mathrm{G}^{a,\mu\nu}(x)$, and $\mathrm{G}^a_{\mu\nu}(x) = \partial_\mu \mathrm{G}^a_\nu(x) - \partial_\nu \mathrm{G}^a_\mu(x) - g_s f^a_{bc} \mathrm{G}^b_\mu(x)\mathrm{G}^c_\nu(x)$, where the generators T_a of $\mathrm{SU(3)_C}$ satisfy the relation $[T_a, T_b] = i f^c_{ba} T_c$. It is clear from these expressions that three-gluon and four-gluon interactions have to be taken into account.

According to experiment, the baryons and mesons, together comprising the hadrons, are colourless. This can be attained only if either all three base colours are combined or one base colour is combined with its anti-colour[18]. The fact that only colourless particles have been found by experiment so far, has the profound consequence that it is fundamentally impossible to isolate free quarks or gluons. This principle is known as (colour) confinement.

The gluon self-interactions combined with the strength g_s of the coupling make it an arduous task to perform calculations in QCD. From now on, the strong interaction will not be taken into consideration any more, because of these difficulties and because

[15] See appendix C for detailed calculations.

[16] This can be compared with B_μ, which comes from the single generator of $\mathrm{U(1)_Y}$, and with $W_{\mu,i} (i = 1,2,3)$, which come from the three generators of $\mathrm{SU(2)_W}$.

[17] See page 395 of Perkins[188] for the precise assignments.

[18] Anti-red is green, i.e. the addition of yellow and blue. Anti-blue is cyan/orange, i.e. the addition of red and yellow. Anti-yellow is magenta/purple, i.e. the addition of blue and red.

of the fact that only the electroweak interaction is of concern when dealing with the Higgs-boson.

Chapter 10

Large Hadron Collider (LHC)

Einstein's law ($E = mc^2$) defining the equivalence of energy and mass has two profound consequences. Firstly, it states the possibility to transform mass, e.g. particles, into a concentration of energy. The easiest way to accomplish this is to let a particle collide with its counterpart: the anti-particle. Aside from technical details, this is what was done until recently inside the LEP-ring[220], where an electron(-beam) and a positron(-beam), i.e. anti-electron, were both accelerated to a kinetic energy of 103 GeV. In the collision, the particles annihilate one-another with the result that all potential and kinetic energies added up[(1)] are concentrated inside a small area.

The second consequence is that a given concentration of energy can be transformed into mass, i.e. particles can be created, or put differently: new particles will be pulled out of the vacuum[185]. The available energy is partly used for the creation of the new particle(s) (the potential energy part) and partly used to boost these particles if a number of them have been formed (the kinetic energy part). In the extreme situation, only one massive particle at rest is created. This has been the case during the LEP-I running, where Z^0-bosons of mass 90 GeV/c^2 were formed. Clearly, the higher the desired mass of the particle that is to be pulled from the vacuum, the more energy needs to be used. In practice, this means that the accelerator, which is used to build up the kinetic energies of the particles, needs to be sufficiently large.

Already in 1984, first studies were conducted on the idea to build a future large particle collider using (infra-)structures existing at CERN[221] (shown in Fig. 10.1). Especially the circular tunnel of 27 km length and 3.8 m diameter is of interest. The LEP accelerator, which occupied the tunnel until recently, reached centre-of-mass energies of slightly more than 200 GeV[222] using electrons and positrons moving in opposite directions. Current technology is not able to go far beyond this value, so that other solutions needed to be explored. The possibility of building an even larger tunnel has been ruled out because of the high costs. A more cost-effective solution is to accelerate particles which are more massive than the electron/positron. These particles

(1) The net energy concentration is 206 GeV which is twice the kinetic energy. Clearly, the potential energy 1 MeV of the two particles is not the main contribution to the total energy.

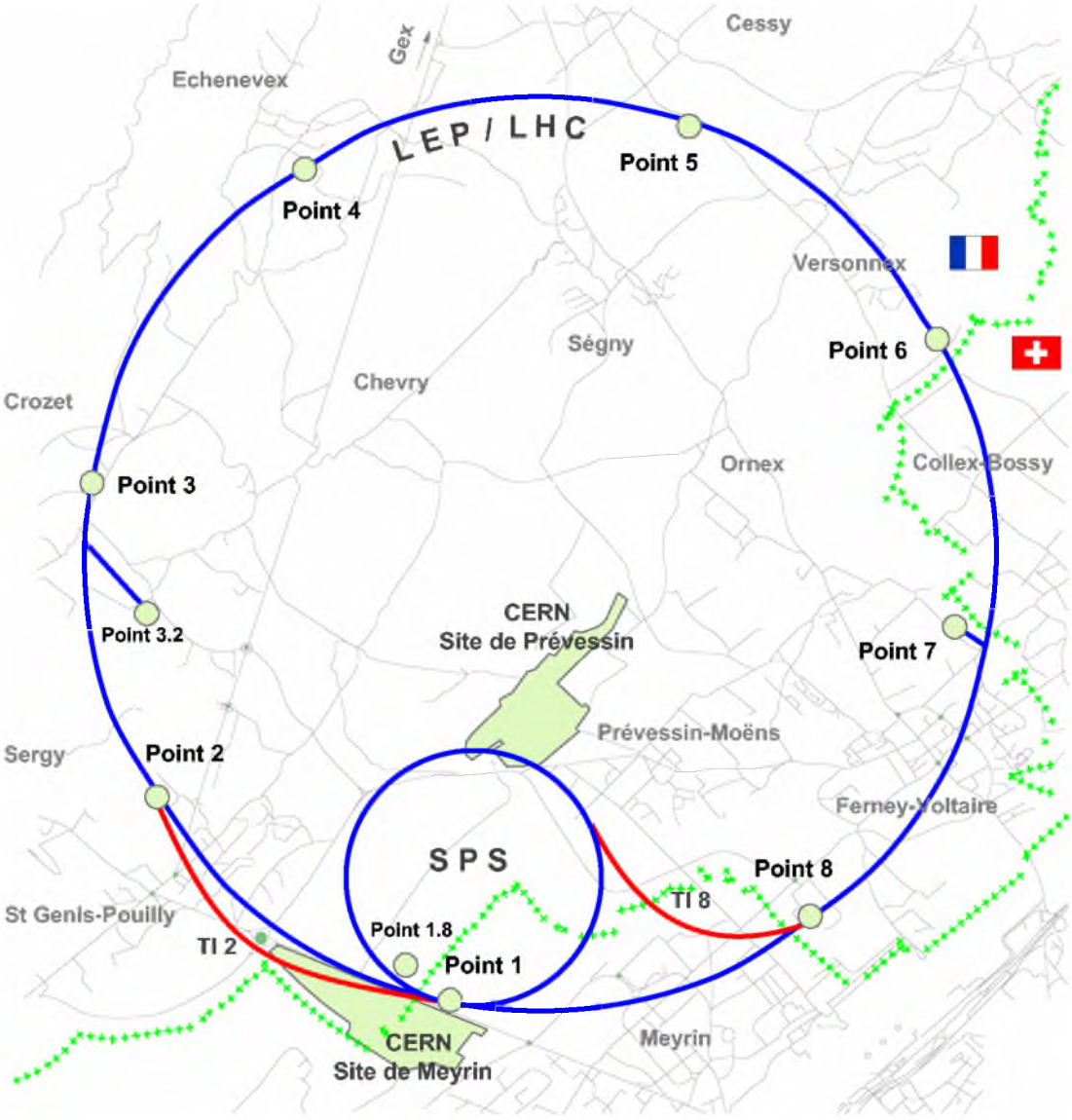

Figure 10.1: Location of CERN sites and LHC access points with respect to a map of Pays de Gex showing roads and villages. The ATLAS experiment is situated in Point 1, just outside of the CERN main site.

do not need a larger tunnel since they lose less energy due to synchrotron radiation[(2)] as compared to lighter particles. Another type of solution would be to use a linear accelerator where the particles do not suffer any synchrotron radiation. However, the drawback is that current technology again requires a very long, new, straight tunnel. In a circular accelerator all elements are reused every revolution, where bending magnets are needed to make the particles move in a circle. The heavier the particle is that needs to be accelerated, the stronger the bending magnets need to be to deflect the particle from a straight path.

This latter solution has been adopted for the LHC[9, 221, 224–228] where 1232 bending magnets will be used. Each magnet is 14.3 m long and needs to be superconducting in order to reach the necessary field strength of 8.33 T. It has a structure such that both particle beams can be housed using one magnet, as shown in Fig. 10.2.

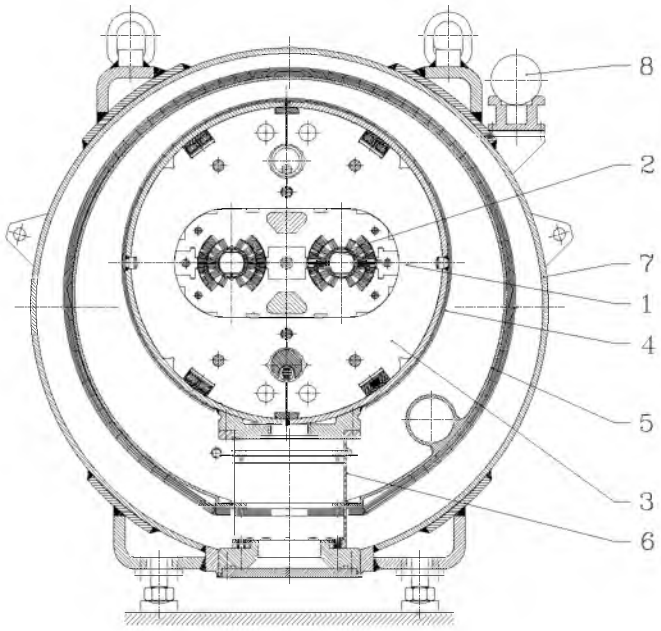

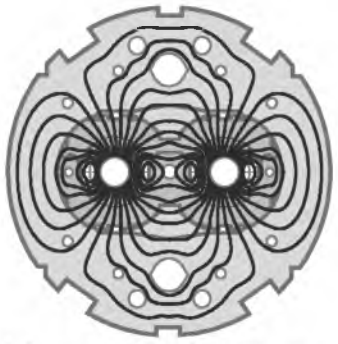

Magnetic field line configuration of two-in-one dipole magnets.

Figure 10.2: Cross section of the dipole magnets two-in-one structure. 1. Beam screen, 2. Cold bore, 3. Cold mass at 1.9 K, *4. Radiative insulation, 5. Thermal shield at* 55 *to* 75 K *6. Support post, 7. Vacuum vessel, 8. Alignment target.*

Three bending magnets are combined with several correction magnets, i.e. quadrupoles, sextupoles, octupoles and decapoles, to guide and collect the LHC beams resulting in so-called half cells of 53.45 m length, as shown in Fig. 10.3. The LHC will have eight arcs of 23 cells, each consisting of two half cells. This bending section clearly uses up most of the 26.66 km available length of the tunnel.

[(2)]Even an accelerator with a 200 km circumference would not help much, since a 500 GeV electron would lose more than 150 GeV per revolution[223]. The 1800 times heavier proton loses 10^{13} times less energy according to the formula $\Delta E = \frac{e^2\beta^3}{3\varepsilon_0 R}(\frac{E}{mc^2})^4$[24], where ΔE stands for the energy loss, E is the energy of the beam particles with mass m, charge e, and velocity $\beta = v/c$, R is the radius of curvature of the accelerator, c is the speed of light, and ε_0 the dielectric constant.

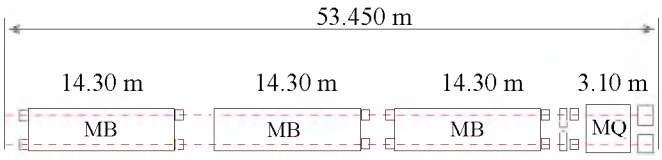

Figure 10.3: Half cell consisting of three main bending and many correction magnets. (MB: main bending magnet, MQ: main quadrupole magnet, and others up to decapole correcting magnets)

Protons will be accelerated from 450 GeV to an energy of 7 TeV by eight superconducting 400.8 MHz radio frequency cavities per beam operating at a maximum[3] voltage of 2 MV. This results in a centre-of-mass energy of 14 TeV. This is needed to produce particles with masses below 1 TeV/c^2, since protons are composite objects and the 7 TeV energy is divided over its constituents. In practice, this means that the effective energy for particle production is much lower since the protons do not collide as a whole but only via one of their constituents[229]. Figure 10.4 shows examples of possible interactions.

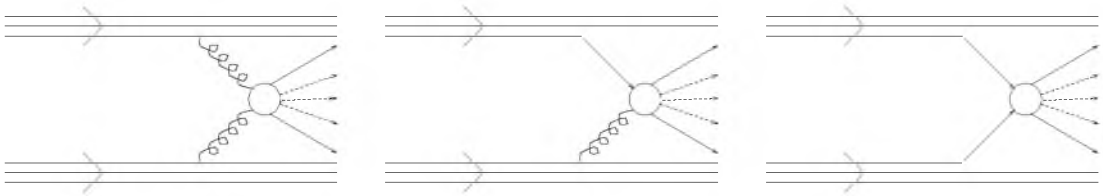

Figure 10.4: Common interaction types between proton beams: gluon-gluon, quark-gluon and quark-quark interaction, where the quarks can be valence type quarks or the quarks can stem from the quark sea, i.e. free quarks inside the proton coming from spontaneous quark-anti-quark pair creation.

The chance of two particles colliding with each other is extremely small. Even though the width of the beams will be focused within (a transverse radius of) 15.9 μm, this still is 16 milliard times larger than the size of a proton. Furthermore, even if a collision occurs, the chances to pull out a Higgs particle from the vacuum remain slim, as will be explained later on. The only way around these problems is to let many bunches of protons collide with another in a time as short as possible. Therefore, 2808 bunches of about $1.1 \cdot 10^{11}$ protons are injected into both beam pipes, where the detailed bunch structure is determined by the beam dump requirements[230] and injection sequence as shown in Fig. 10.5.

These beams are accelerated and used for physics purposes in the interaction regions of the experiments during ten hours. After that time the quality of the beams has deteriorated so much that it is better to dump the beams and start up the filling sequence again. However, the bending magnets cannot just be switched off to discard

[3]The resulting maximum radio frequency voltage per beam is 16 MV.

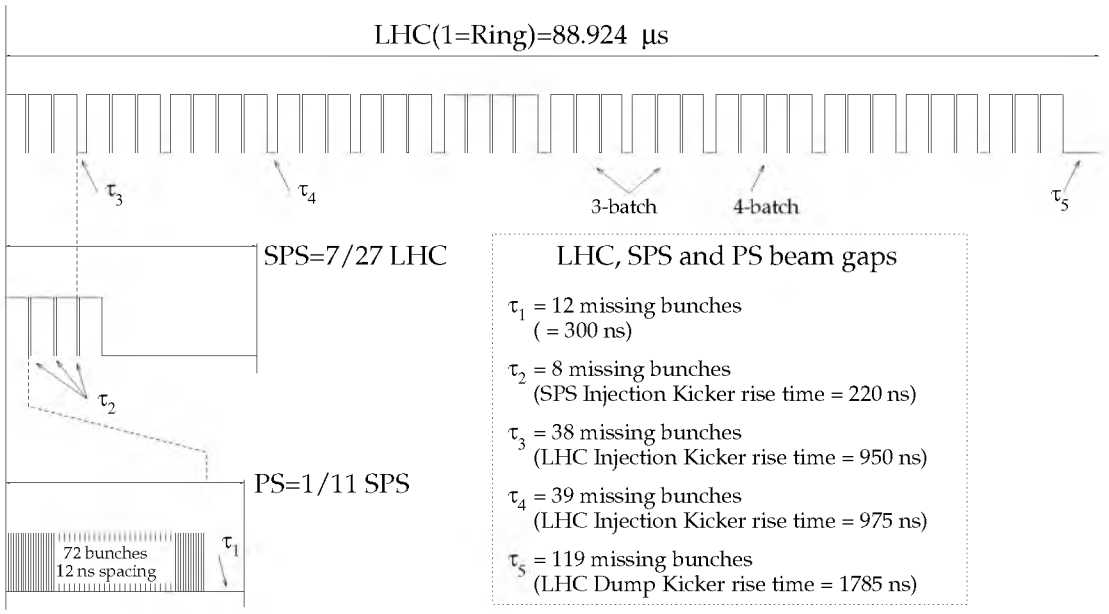

Figure 10.5: Detailed bunch scheme structure.

the beams since the energy stored is about 350 MJ, which would destroy[4] the LHC machinery immediately.

The length of each individual bunch is 7.7 cm. Owing to this length, the interaction region along the beam direction can be described best by a Gaussian of width 5.6 cm. Given these parameters, it is now possible to calculate the luminosity of LHC[229]:

$$\mathcal{L} = N_1 N_2 f/A \approx 10^{34} \ /\mathrm{cm}^2\mathrm{s} \ .$$

Here, N_1 and N_2 are the number of particles in each bunch crossing, f is the bunch-crossing frequency[5], and A is the overlap area of the bunches at the collision point. The overlap area is somewhat difficult to calculate so it is sometimes expressed in other parameters[68, 151]:

$$A = 4\pi\varepsilon_n\beta^*/\gamma \ ,$$

with β^* being the value of the betatron function at the interaction point, ε_n the emittance corresponding to the 1σ contour of the beam profile, and γ the Lorentz factor[227]. The importance of the luminosity is that it has a direct proportionality to the number of events one can expect in a certain physics channel:

$$N(t) = \sigma \int_0^t \mathcal{L}(t')\mathrm{d}t' \ .$$

[4]This amount of energy is equivalent to the power that is needed to stop at once a column of ninety 10 ton trucks driving at 100 km/h.

[5]The bunch-crossing frequency ($f = 1/24.95$ ns) can be replaced by the revolution frequency ($f_r = 1/88.9\ \mu\mathrm{s} \approx c/27$ km) times the number of bunches ($k = 2808$). This latter expression is actually more accurate since it takes beam gaps into account.

Here, $N(t)$ stands for the number of events after a time-period t, $\mathcal{L}(t')$ is the luminosity during that time-period, and σ is the cross-section of the physics channel. During the first few years of the LHC running period, it is expected that the luminosity will be 10^{33} /cm^{2}s due to the fact that the machine needs to be tested and commissioned. After this initial period the standard luminosity should become 10^{34} /cm^{2}s. An advantage is that the lower luminosity makes it easier to perform studies on B-physics for which high event rates can be expected[132]. Of course, all studies requiring a high luminosity in order to reach a significant amount of events will suffer.

Since the number of protons in each bunch is so high, one can expect several interactions to occur during a bunch crossing. Most of these interactions will be soft hadronic collisions, meaning that the participating partons/constituents i.e. quarks and/or gluons, carry a low fraction of the total energy of 7 TeV. Each interesting hard collision will, on average, be accompanied by 23 soft collisions. The detector is not able to distinguish between them and thus will always detect these collisions superimposed. This is called pile-up. If the detector were to register every bunch crossing, then it would mainly record soft collisions. These minimum-bias events added up give practically the full contribution to the total proton-proton collision cross section[(6)] of about 60 mb.

Furthermore, the time between bunches is 24.95 ns, which is shorter than the time needed for particles to fly through the detector; at essentially the speed of light they have travelled about 7 metres. This means that it is very important to know to which bunch crossing a particle belongs, since otherwise even more (fake) hits and/or tracks would incorrectly be associated with a certain event. As is the case now, about 3500 tracks[132] are present in the detector with each interesting event. This amount reflects the number of tracks that is incident on the calorimeters. However, very few tracks reach the muon spectrometer meaning that it does not suffer from minimum-bias. Also, the inner detector suffers less from minimum-bias tracks because of its smaller eta-coverage and insensitivity to neutrally charged tracks.

According to the current building schedule, it is foreseen that the LHC machine and detectors are finished before April 2007. This means that the first particle beams will circulate and collide then to produce physics events of interest to ATLAS. It is anticipated and hoped for that LHC will remain in operation for at least twenty years.

[(6)]Here, mb stands for millibarn (1 barn= 10^{-24} cm^2) so that $6 \cdot 10^8$ interactions per second are to be expected (at LHC). Though, this value is averaged because of the gaps in the bunch structure, see Fig. 10.5, and the limited lifetime of the beams.

Chapter 11

Higgs boson detection

The main purpose of the LHC machine is to provide interaction regions inside the LHC experiments: ATLAS, CMS, LHCb[231], and ALICE[232]. In these experiments, the energy densities are so high that massive particles can be pulled from the vacuum. The particle of most interest is the Higgs boson, of course, since it plays a central role in the theory but has not been discovered yet.

As the mass of the Higgs boson is unknown, it is also not known under which conditions it will be produced. That is to say: over the years, a number of searches[219] have been conducted already, resulting in the exclusion of the mass range up to about 114 GeV/c^2[233]. It has been possible to positively exclude Higgs bosons with a mass within this range by carefully comparing available production and decay channels to existing data. A 2.9 standard deviation has been reported for a Standard Model like Higgs boson at 115.6 GeV/c^2[233]. This possible evidence does not change anything to the mission of the LHC though, which is to confirm or to disprove this evidence and to measure a number of properties of the Higgs boson[234], e.g. mass, spin, parity, couplings, branching ratios and width. The most important property is the Higgs mass, since that determines the coupling to other particles.

It is interesting, and necessary, to comment on the possible evidence found at LEP, for Higgs bosons with a mass between 115 – 116 GeV/c^2. Firstly, the number of events concerned is so small that every single event has been studied in detail, resulting in a quantity denoting the events compatibility with an expected[(1)] Higgs event. However, a twist of fate cannot be ruled out due to this low number of events, i.e. statistically seen they might be caused by mere background fluctuations. Secondly, after an extended running time of one month[235], the CERN Council decided against running the LEP experiments for another year[236]. This decision was steered by the fact that no more Higgs candidate events were observed during the one-month extension. Furthermore, the LEP machinery has to make way in order to build the LHC machinery, with the latter being better equipped to study the Higgs sector, and thus to turn the first evidence into a confirmed observation.

[(1)]Typical signatures have been derived from Monte Carlo simulations which predict the possible event topologies.

Thirdly, the introduction of the isospin doublet Higgs-field described in Sect. 9.2 is merely the simplest way to incorporate mass into the theory. This theory is therefore called minimal Standard Model. However, studies over the years have not only yielded the limits of the minimal Standard Model[219, 237] but also probable inconsistencies within the theory[(2)]. Many extensions to the minimal Standard Model exist[219]. They will not be discussed here, since they lie beyond the scope of this thesis. It is important to note though that most of these extended models predict the existence of a Standard Model like Higgs boson. So, even when more proof is found against the validity of the minimal Standard Model, then the signal study of this chapter still remains essential. The extended models are spectacular though in that they predict a whole spectrum of new particles that are to be discovered by the LHC.

11.1 S.M. Higgs production

Figure 10.4 already showed examples of particle production diagrams. Using Feynman-diagrams, like Fig. 9.1, and Feynman-rules which follow from the calculations in appendix C, one can determine the processes of most importance for Higgs boson production by the LHC. Keeping in mind that the Higgs coupling to other particles depends on their mass, it is clear that the production processes should involve massive elementary particles. It also signifies that the cross sections of these processes depend on the Higgs boson mass. Concentrating on the interacting elementary particles only, it is determined that Higgs bosons will mainly be produced by the following processes[219], see Fig. 11.1: gluon fusion and massive vector boson fusion, the latter being of less importance.

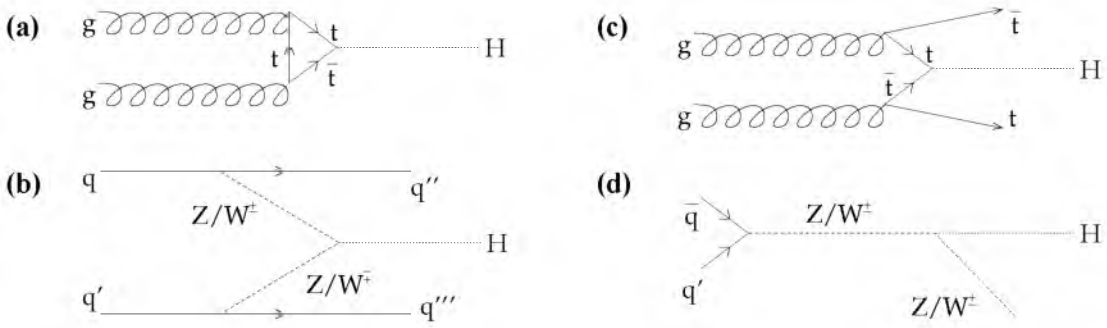

Figure 11.1: Feynman diagrams corresponding to typical Higgs production processes at the LHC. (a) gluon fusion, (b) vector boson fusion, (c) associated gluon fusion and (d) associated quark fusion. These associated fusion production processes are often referred to as Higgs strahlung or Higgs radiation.

The Higgs production cross sections used for Fig. 11.2 are obtained with the PYTHIA 6.2[128] program package, which is able to sample a large number of different pro-

[(2)] Calculations on this subject form the frontier of elementary particle physics today and are difficult to perform, in general, while experimental results supporting new theories remain to be virtually absent.

cesses. These calculations are of such complexity that the magnitudes of the cross sections shown are believed to be only first estimates of the real cross sections and production rates. Specialized calculations (and studies) on some of these production processes have yielded correction factors[238], originating from higher-order Feynman-diagrams, going up to $K = 1.9$, i.e. an increase of almost 100% compared to Fig. 11.2. Anyhow, given the large number of Higgs bosons produced during a years running, one can regard the LHC as a future Higgs factory(3).

Figure 11.2 shows that Higgs production through gluon fusion dominates over the full mass range. A small effect due to a real top-quark loop contribution (Fig. 11.1(a)) is visible as a shoulder above $m_H \approx 2m_t \approx 340$ GeV$/c^2$. Usually, all attention goes to the gluon fusion and massive vector boson fusion production processes only. However, it can be inferred from the right-hand scale of Fig. 11.2 that a non-negligible number of Higgs bosons are expected to be produced through other processes.

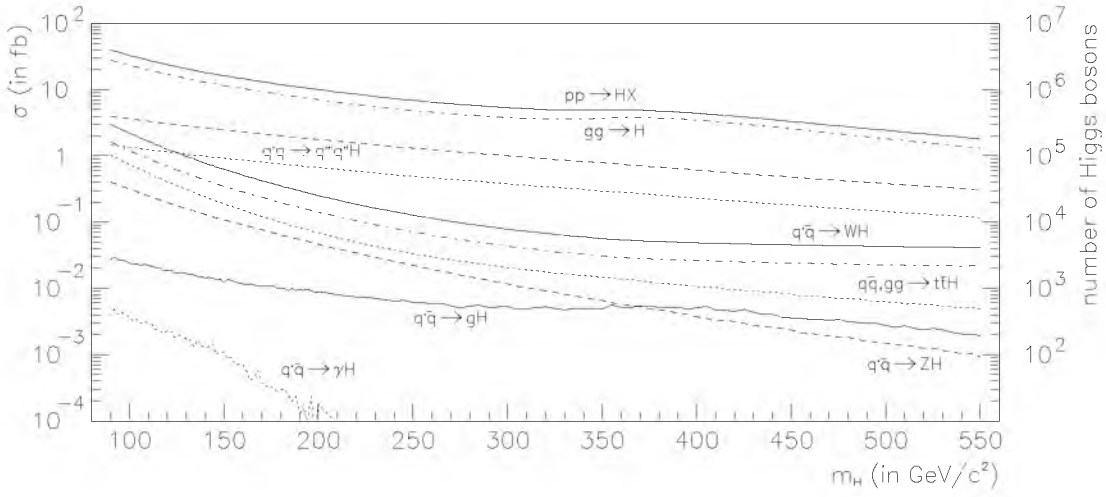

Figure 11.2: Cross sections of Standard Model Higgs production processes with respect to the nominal Higgs boson mass, without usage of K-factor corrections. The right-hand scale denotes the anticipated number of Higgs bosons produced during a running period of one year (10^7 seconds) at high luminosity (10^{34} /cm^{2}s), thus yielding 10^5 events per pb.

11.2 S.M. Higgs decays

Like most other elementary particles, the Higgs boson is not stable, which means that it will decay immediately after having been produced. Again, the largest coupling is to decay products with the highest possible mass. This is shown in Fig. 11.3, where the branching ratios to particular decay products are given as a function of the nominal Higgs mass.

(3)The LEP machine is often referred to as a Z factory.

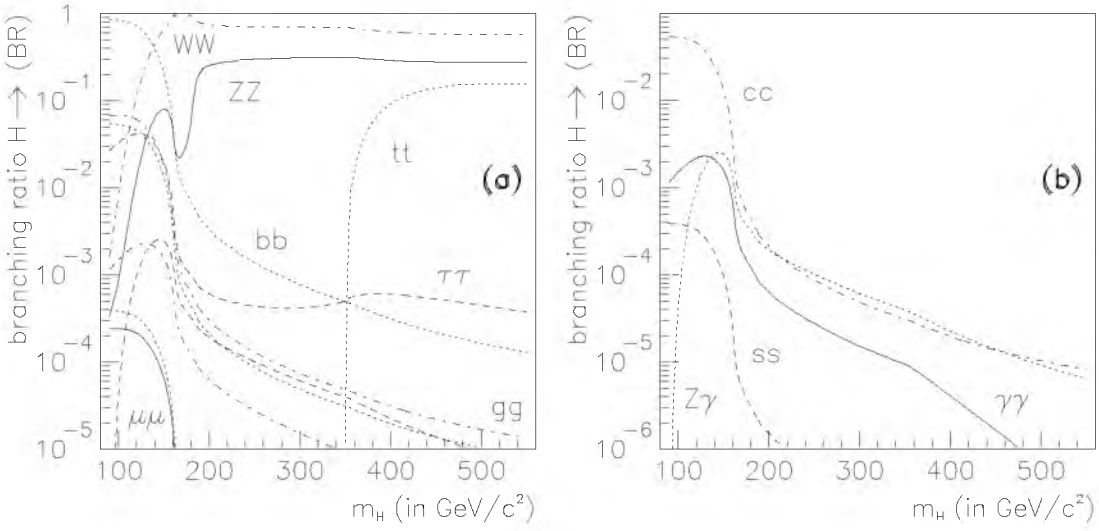

Figure 11.3: (a) Branching ratios of all possible Higgs decays in relation to its nominal mass. (b) Same as (a) but for those channels that were not labelled yet in sub-figure (a). Note the different scale of the sub-figures.

The decay $H \to b\bar{b}$ dominates up to $m_H \approx 140\ \mathrm{GeV}/c^2$, from where the decay $H \to W^+W^-$ is taking over to dominate up to the theoretical limit of $m_H \lesssim 1\ \mathrm{TeV}/c^2$. Other decays of importance, i.e. accounting for more than ten percent of the Higgs decay, are $H \to ZZ^{(*)}/\gamma^*$, especially when both Z bosons are real, and $H \to t\bar{t}$ as soon as the threshold $m_H \gtrsim 2m_t$ has been passed. Some decays can possibly lead to clear event topologies, i.e. decays into relatively stable particles that lead to easily recognizable event topologies. However, most of the decays lead to multiple jets of particles. These particle jets are caused by cascade decays, where a decay product almost immediately decays itself.

A particularly clear event topology is the "golden" Higgs decay channel: four high energy muons form two pairs originating from the decay of real Z bosons from the Higgs decay, i.e. $H \to ZZ \to \mu^+\mu^-\mu^+\mu^-$. The chance for this particular decay channel to occur is not very large, as three small branching ratios are involved: $\mathrm{BR}(H \to ZZ) \approx 30\%$ for $m_H > 200\ \mathrm{GeV}/c^2$ and $\mathrm{BR}(Z \to \mu^+\mu^-) = 3.36\%$ independently of m_H, which yields $\mathrm{BR}(H \to 4\mu^{\pm}) \approx 3.4 \cdot 10^{-4}$ for $m_H > 200\ \mathrm{GeV}/c^2$. Ironically enough, this is comparable to the direct decay probability $H \to \mu^+\mu^-$, which has a branching ratio of $\approx 2 \cdot 10^{-4}$ for $m_H < 125\ \mathrm{GeV}/c^2$. However, events with just two high energy muons do not provide a clear, or better yet, distinct enough event topology. There are too many QCD background processes in which two high energy muons are produced, e.g. $pp \to Z + X \to \mu^+\mu^- + X$ where the Z is produced directly.

The four-muon event topology is of interest as well when one of the Z bosons is not real. This happens when the Higgs mass is below the $2m_Z \approx 180\ \mathrm{GeV}/c^2$ threshold. The virtual Z or massive photon, denoted as γ^*/Z^* has the same properties as a real Z boson except for the lower mass. However, there are now other QCD processes that yield a comparable four-muon event topology. These processes will be dealt with in

greater detail in Sect. 11.4.

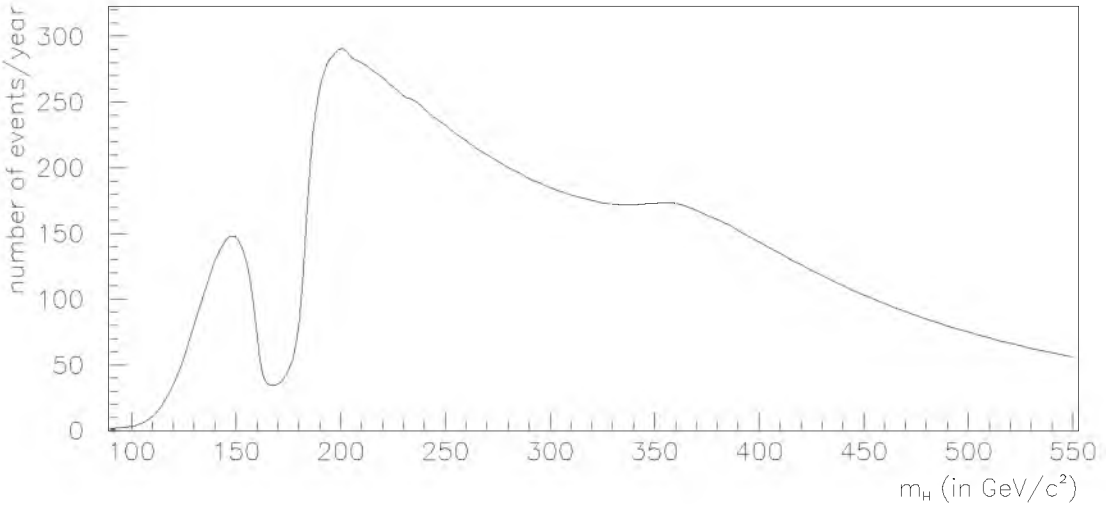

Figure 11.4: Number of events per year to be expected in the decay channel $pp \rightarrow H + X \rightarrow ZZ^{(*)} + X \rightarrow \mu^+\mu^-\mu^+\mu^- + X$ *as a function of the Higgs mass.*

Combining Figs. 11.2 and 11.3(a), leads to the number of events expected in the golden decay channel as a function of m_H during a one-year running period[(4)], as shown in Fig. 11.4. Table 11.1 gives a comparison between the results shown in Fig. 11.4, obtained from PYTHIA6.2, and those that were published previously[132, 239]. The former are multiplied by a factor four to reproduce the full $pp \rightarrow H + X \rightarrow ZZ^{(*)} + X \rightarrow 4l^{\pm} + X$ cross section used by the latter. Previous publications used PYTHIA5.7 and corrections on the branching ratios to obtain the best possible results[239]. These older results yielded a slightly lower cross section for Higgs masses below 150 GeV/c^2 and a clearly higher cross section for Higgs masses above 240 GeV/c^2.

120	130	150	170	180	200	240	280	320	360	400	500
1.41	3.22	5.88	1.42	3.24	11.6	9.78	8.01	7.01	6.90	5.74	3.00
1.29	2.97	5.53	1.40	3.26	12.4	11.2	9.59	8.90	8.65	6.76	3.15
1.36	3.12	5.73	1.44	3.33	12.4	11.2	9.59	8.90	8.65	6.76	3.15

Table 11.1: Higgs boson production cross section times branching ratio for the "golden" decay channel (in fb, *where* 1 fb *equals* 100 *events). Top row shows nominal Higgs mass in* GeV/c^2. *Production cross sections obtained in this thesis using* PYTHIA*6.2 are given in the second row. Results from the Detector and Physics Performance TDR and from ATLAS Internal Note Phys-NO-048 are presented for comparison in rows three and four, respectively.*

(4)Using the equality that one femtobarn (fb) corresponds to hundred events in one year.

11.3 Muon tracks from the Higgs signal

Chapter 6 already used single muon tracks that should typically resemble real muons originating from Higgs decays, with $m_{\mathrm{H}} = 150\ \mathrm{GeV}/c^2$. Here, using the PYTHIA6.2 program, a sample of 100.000 Higgs bosons has been generated which were forced to decay into four muons. The corresponding muon track parameter distributions are shown in Fig. 11.5. For comparison, see Fig. 6.2 for the single-muon sample used before. Though there is a resemblance between the two samples, as was intended of course, one can also see that the muons in Fig. 11.5 tend to have higher p_{T} and $|\eta|$ values.

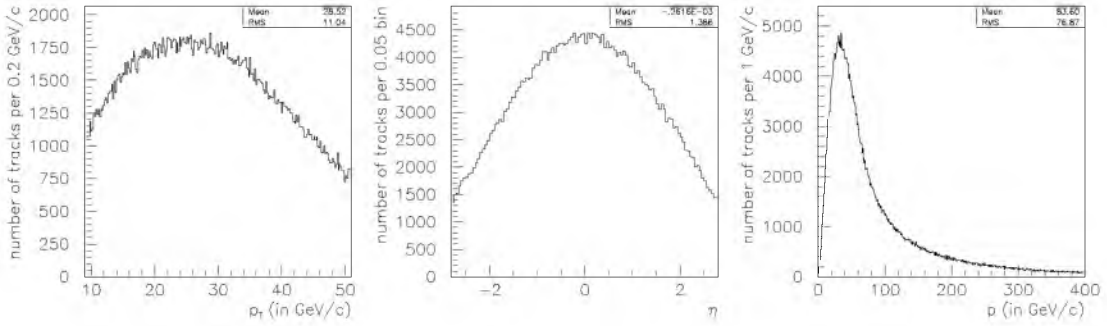

Figure 11.5: Track parameter distributions (p_{T}, p and η) of muons originating from the "golden" Higgs decay channel ($m_{\mathrm{H}} = 150\ \mathrm{GeV}/c^2$).

The higher p_{T} is advantageous as this makes it easier for the pattern recognition and reconstruction programs to successfully reconstruct the event. Still, many such Higgs decays will not be detected, as at least two muons with $p_{\mathrm{T}} > 20\ \mathrm{GeV}/c$ are required to trigger the data read-out of the ATLAS detector. The choice has been made that the other muons in the event should have at least a transverse momentum of $7\ \mathrm{GeV}/c$. This is for convenience of the muon reconstruction, which performs less well at lower transverse momenta.

The long tails of the η-distribution pose a problem, since these tails adhere to muons that stay close to the beam pipe where no detector elements reside. Therefore, an upper bound for the rapidity of $|\eta| \lesssim 2.5$ is used, which corresponds to the rapidity coverage of the inner detector. Together with the p_{T} cuts, these practical limits have the profound consequence that at a Higgs mass of $150\ \mathrm{GeV}/c^2$ only about $55 \pm 1\%$ of all Higgs-into-four-muon decays can be registered.

After removal of unregistrable events from the sample, it is found that the distributions shown in Fig. 11.5 have not changed drastically, see Fig. 11.6. Actually, the distributions of η and p are now somewhat more between those of Figs. 11.5 and 6.2. The same behaviour is found for samples of Higgs bosons with other masses. Table 11.2 lists the acceptance with which the ATLAS detector registers the "golden" Higgs decay at various nominal masses of the Higgs boson.

The ideal situation, i.e. at the Monte Carlo generator level, is summarized in row two of Table 11.2. However, reality can be far from ideal. To study this, the event sam-

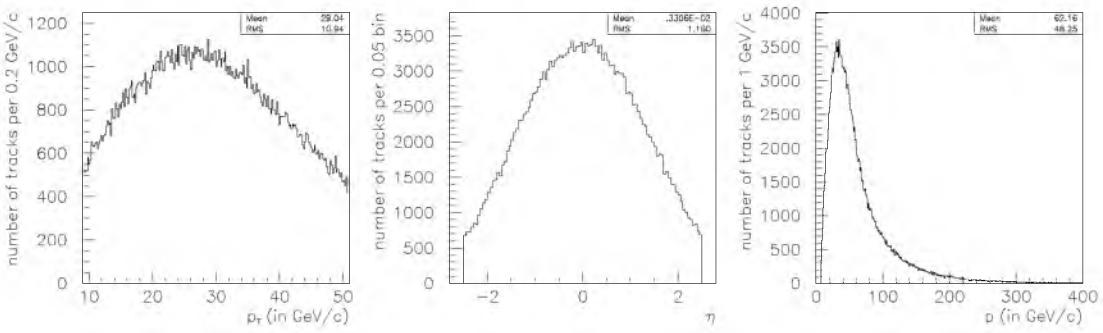

Figure 11.6: Track parameter distributions (p_T, p and η) of remaining muons, originating from the "golden" Higgs decay events ($m_H = 150$ GeV/c^2), after application of trigger and detector acceptance cuts.

ples have been used as input to the detector simulation program, described in Sect. 6.1. The resulting detector Monte Carlo output has then been fed into the reconstruction program, see Sect. 6.2. The output, i.e. fully reconstructed muon tracks, has been used to reevaluate a more realistic detector acceptance. Row four of Table 11.2 reviews the numbers of interest and one can conclude that another 20% of events is lost due to only partially reconstructed tracks.

m_H(GeV/c^2)	130	150	170	200	250	400
MC acceptance (%)	45	55	61	66	67	74
(at generator level)	(2225)	(2760)	(3047)	(3323)	(3354)	(3716)
full reco. eff. (%)	34	42	47	51	51	57
	(1705)	(2089)	(2360)	(2556)	(2539)	(2836)
rescued rec. eff. (%)	45	55	61	66	67	74
	(2227)	(2752)	(3040)	(3310)	(3343)	(3701)

Table 11.2: Percentage of events accepted after applying trigger and detection cuts on the Monte Carlo generator level (second row) and using a realistic detector simulation with fully reconstructed tracks (fourth row). When most partially reconstructed tracks can be rescued, i.e. measured with decent track parameters, we end up near the ideal situation (comparing second and sixth row). The numbers of events remaining, compared to the original 5000*, is shown between parentheses.*

The event loss is recuperated, however, once an attempt is made to rescue the partially reconstructed tracks. This rescue procedure entails the following ingredients: if track segments of the inner detector do not match those of the muon spectrometer, then only that segment with the better track parameters is used. The same applies when segments have not been found in either the inner detector or the muon spectrometer. It is possible though that the rescued track segments are of such poor quality that they cannot be used for the final event sample, i.e. their influence would deteriorate the results.

11.4 Background to the Higgs signal

It needs to be remarked that further cuts are needed, as there are other events that yield four high-energy muons. These events are considered to be background events with respect to the Higgs signal. This background consists of events that are accepted by the trigger, and therefore recorded by ATLAS, in first instance. However, a large part is already removed by the detector acceptance cuts, i.e. four muons with $p_T > 7$ GeV$/c$ need to be reconstructed successfully. The (remaining) background events are divided into two categories.

The first category consists of non-resonant or continuous background. This category has the characteristic property that some muons come from secondary vertices. It is also referred to as reducible background, because it can be easily reduced by imposing cuts on specific (track parameter) distributions. The largest contributions to the reducible background originate from $t\bar{t}$ and $Zb\bar{b}$ events. In these cases, two muons originate from b (cascade) decays, which means that they appear non-isolated in the detectors, i.e. such muons are accompanied by particle jets. These muons can also be subjected to an impact parameter cut, because their respective secondary vertices can be well separated from the primary vertex.

Even though reducible, the non-resonant background forms a potential problem, because it is produced copiously. Since the production cross section is around 3.3 nb, more than $3 \cdot 10^8$ $t\bar{t}$-pairs are produced per year. Using only the direct decays $t \to W^+b$; $W^+ \to \mu^+\nu_\mu$; $b \to l^\pm + X$ (and $\bar{t} \to W^-\bar{b}$; $W^- \to \mu^-\bar{\nu}_\mu$; $\bar{b} \to l^\pm + X$), underestimates the total branching ratio[240] of $t\bar{t} \to 4l^\pm + X$. Also the cascade decays need to be included, even though the latter are more suppressed by the detector acceptance cut $p_T > 7$ GeV$/c$. An invariant mass cut $|m_{12} - m_Z| < \Delta_{m_Z}$, which is to require a real Z to be part of the event, helps in reducing this particular background. Another further invariant mass cut, for the second muon pair, aids in removing the low energy part of the background. This cut requires the invariant mass of the second muon pair to exceed a given threshold, i.e. $m_{34} = m_{\gamma^*/Z^*} >$ threshold mass.

Clearly, the first invariant mass cut is not as selective against another reducible background from $Zb\bar{b}$ with $Z \to \mu^+\mu^-$ and $b, \bar{b} \to l^\pm + X$. However, this background is produced less abundantly. Its production cross section is only about 40 pb[241], corresponding to $4 \cdot 10^6$ events per year.

Given the large production rates and the high rejection factors, no attempt was made to simulate and reconstruct these backgrounds. It would simply take too much (computing) time to obtain satisfactory, trustworthy results. Despite the quantitative uncertainties, [132] claims that the remainder of these background events add up to a number similar to that of the signal events after application of trigger, detector acceptance and invariant mass cuts. A Higgs mass of 170 GeV$/c^2$ forms the exception, where the number of signal events only amounts to about half the number of reducible background events. However, one has to keep in mind that so far only acceptance and invariant mass cuts have been applied, and that the background has been integrated over a mass window of ± 5 GeV$/c^2$ around the nominal Higgs mass. In order to insure protection against uncertainties, it is necessary to further impose impact parameter and

isolation cuts (see Table 11.6 in Sect. 11.6 below). The reducible background is highly affected by these cuts, as an additional rejection factor[242] of one hundred can be achieved.

The second category, the irreducible background, differs from the reducible one in a number of aspects. Firstly, it has the same decay products as the Higgs signal. This is clear from the production processes: $q\overline{q} \rightarrow ZZ^{(*)}$ (quark fusion) and $gg \rightarrow ZZ^{(*)}$ (gluon fusion), which yield exactly the same intermediate state containing two Z bosons or one Z boson and one virtual photon γ^*/Z^*. Furthermore, this intermediate state is produced at the primary vertex. Also, the Z/Z^* bosons decay at this vertex. So, the $q\overline{q}, gg \rightarrow ZZ^{(*)} \rightarrow 4\mu^{\pm}$ channel does not differ from the "golden" Higgs decay channel regarding the event topology, i.e. four muons originating from the primary vertex. There is another difference, however, but that will be dealt with later.

Secondly, a major difference between the two categories of background is the magnitude of the production cross section. This is 11.07 ± 0.01 pb for $q\overline{q} \rightarrow ZZ^{(*)}$ plus another 30% for $gg \rightarrow ZZ^{(*)}$[242] giving a total production cross section of 14.4 ± 0.1 pb. There is more than one possibility again to arrive at a four-muon event topology. The most obvious way is the direct decay channel $ZZ^{(*)} \rightarrow 4\mu^{\pm}$, which has a production cross section times branching ratio of $\sigma \times BR = 22.9 \pm 0.2$ fb. Another possibility is through cascade decays, e.g. $Z^{(*)} \rightarrow b\overline{b}$; $b, \overline{b} \rightarrow l^{\pm} + X$ or $Z^{(*)} \rightarrow \tau^+\tau^-$; $\tau^- \rightarrow \mu^-\overline{\nu}_{\mu}\nu_{\tau}$ ($\tau^+ \rightarrow \mu^+\nu_{\mu}\overline{\nu}_{\tau}$), but even more channels exist. The direct decay channel is clearly irreducible, but it is questionable whether this holds for the four-muon final states of the cascade decays, since at least one muon will originate from a secondary vertex. When taking into account the easiest cascade decays only, one can estimate the cross section times branching ratio to be $\sigma(pp \rightarrow ZZ^{(*)}) * (BR(ZZ^{(*)} \rightarrow \mu^+\mu^- b\overline{b} \rightarrow 4\mu^{\pm}) + BR(ZZ^{(*)} \rightarrow \mu^+\mu^-\tau^+\tau^-)) \approx 4.8$ fb. This is already less than the direct decay channel. So, for now, we concentrate on the irreducible background: $pp \rightarrow ZZ^{(*)} + X \rightarrow 4\mu^{\pm} + X$.

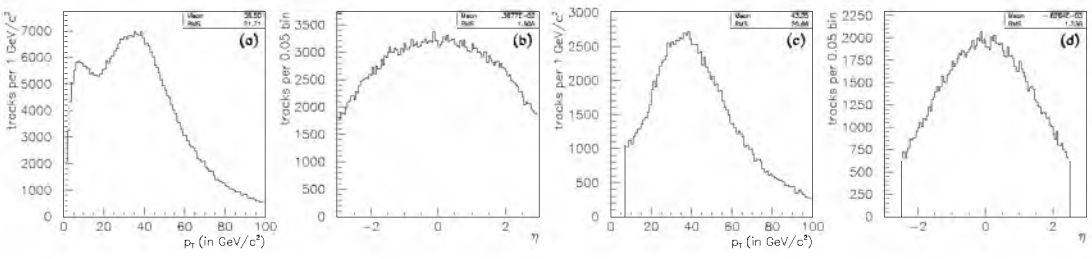

Figure 11.7: Track parameter distributions of muons originating from the irreducible background: $pp \rightarrow ZZ^{(*)} + X \rightarrow 4\mu^{\pm} + X$. *Transverse momentum (a) and pseudo-rapidity (b) distribution of muon tracks. Likewise for (c) and (d) after application of the detector acceptance cuts.*

The most characteristic track parameter distributions are shown in Figs. 11.7(a) and (b). There are striking differences when comparing these distributions with those

of the muons coming from the "golden" Higgs decay in Fig. 11.5. This means that also the response to the acceptance cuts differs, as can be seen from Figs. 11.7(c) and (d). Firstly, Fig. 11.7(c) shows that the abundant low p_T muons, which appear as a shoulder in Fig. 11.7(a), are removed from the sample, because these events do not pass the trigger. Secondly, Fig. 11.7(b) shows a very wide distribution in pseudo-rapidity, but only those events in which all muon tracks stay within the detector acceptance, i.e. $|\eta| \lesssim 2.5$, will pass the trigger and reconstruction program. The effect is that the distribution of remaining tracks is much more centralized, as shown in Fig. 11.7(d). In the end, of the 100,000 irreducible background events generated, not more than 36% (35,840 events) are accepted. Taking into account another 20% loss due to partially reconstructed tracks, one expects a reconstructed event efficiency of about 29%.

The reason for the difference between the two track-parameter distributions lies in the fact that the four-muon invariant mass distributions of Higgs signal and irreducible background do not resemble each other at all. Figure 11.8(a) shows the invariant mass distribution of the irreducible background, which should be compared with the pronounced resonance behaviour of the Higgs signal peak in Fig. 11.9(c). The resonance of the Higgs peak is absent of course in the background, but maxima appear just above the m_Z and $2m_Z$ thresholds. Fig. 11.8(b) shows the same invariant mass distribution after application of the detector acceptance cuts. The irreducible background below $2m_Z$ has been reduced by a factor of six, while the large peak around 200 GeV/c^2 has diminished to 50% of its previous height.

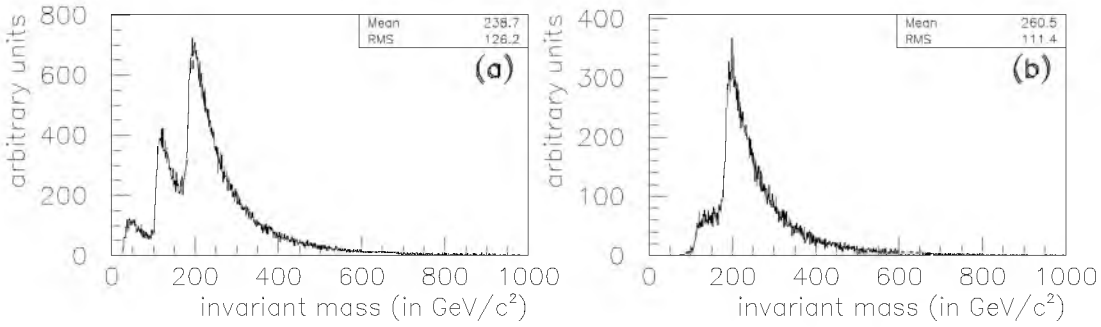

Figure 11.8: Four-muon invariant mass distribution of irreducible background (a) before and (b) after application of detector acceptance cuts.

11.5 Higgs signal selection

Various aspects of the signal selection will be dealt with in the following subsections. The behaviour of samples containing Higgs bosons with pre-selected nominal masses is studied. Though the main focus lies on determining the Higgs mass and its width, some discussion will also be on methods to increase the number of recorded events.

11.5.1 Default selection cuts

The additional invariant mass cuts which were introduced in the previous section, select one real Z boson which decays into one $\mu^+\mu^-$ pair, while the other $\mu^+\mu^-$ pair is required to have a two-muon invariant mass above a specific threshold. Both cuts were found to have maximal efficiency when they are made Higgs mass dependent. As an example, Fig. 11.9 shows the effect of the invariant mass cuts for a nominal Higgs mass of 150 GeV/c^2. Furthermore, knowledge of the Higgs mass could lead to an additional cut on the four-muon invariant mass, which would then be required to be close to the nominal Higgs mass.

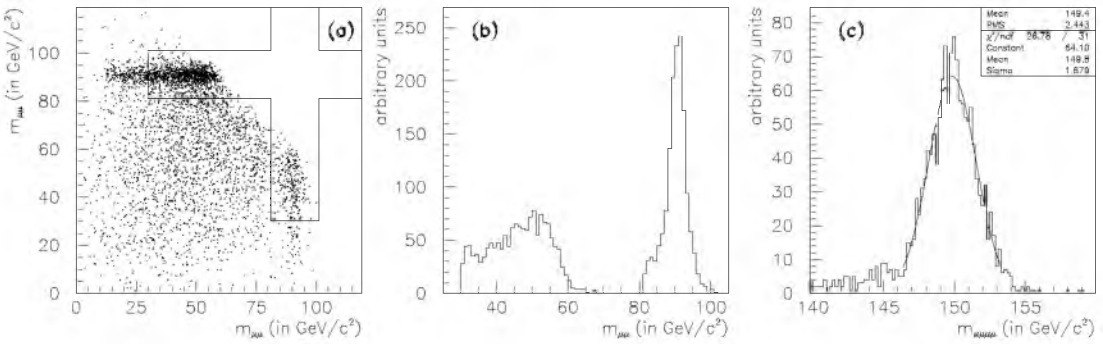

Figure 11.9: (a) Scatter plot of all possible $\mu^+\mu^-$-$\mu^+\mu^-$ pairs before application of the invariant mass cuts. (b) $\mu^-\mu^+$ pairs remaining after cut application, showing the Z^0 peak on the right and the γ^*/Z^* on the left. (c) Signal peak with an overlaid 2σ fit, for $m_H = 150$ GeV/c^2.

One might conjecture that cut windows around the Z and Higgs boson masses affect the background only. However, this is not entirely true since signal events get smeared and possibly lost due to three reasons. Firstly, the measuring inaccuracy of the track parameters can be such that they are too far off to give the proper invariant mass. Secondly, and more importantly, the muons can undergo final-state radiation. Both initial-state and final-state radiation are processes that change track parameters of decay products through QED and/or QCD interactions. The initial-state radiation is of no importance since it does not influence the Higgs mass measured, but final-state radiation does. It reduces the momentum of outgoing decay products, i.e. muons in our case, thus providing a four-muon invariant mass which is too low.

The third reason is that events get cut out due to the natural width of the Z and Higgs boson resonances. The lineshape of the former is well known, as it has been measured by LEP[243]. The resonance width of the Higgs boson around its nominal mass is fully dependent on the Higgs mass, according to the third-order law: $\sigma_m \sim \frac{1}{2} m_H^3$ (both σ_m and m_H in units of TeV/c^2) for high Higgs masses, but of a much more complex form for lower masses. See Fig. 11.10 for the full mass dependence[244].

In order to interpret Fig. 11.10 correctly, one has to keep in mind that the width is given as the full width where the resonance distribution reaches its half maximum. This distribution is usually described by a Breit-Wigner (also called Cauchy) probability

distribution function[28]. It resembles the Gaussian (also called normal) distribution but has much longer tails. Both distributions have the problematic artifact, though, that they are symmetric around their mean, which means that radiative corrections are not taken into account. Therefore, the choice is made to use a Gaussian to fit only the bulk of the distribution. In an ideal situation, the feature of importance of both distributions, i.e. the width denoted by Γ for the Breit-Wigner and by the standard deviation σ for the Gaussian distribution, is related according to Γ (FWHM) $= 2.355\sigma$ (SD).

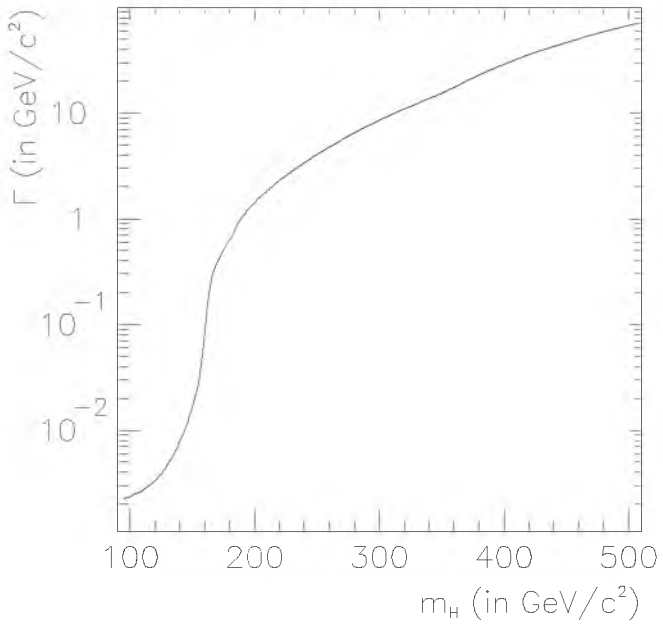

Figure 11.10: Natural width of Higgs boson resonance in relation to its nominal mass, where Γ stands for the full width at half maximum (FWHM).

Again, reality is far from ideal. Especially at lower Higgs masses, i.e. $m_{\mathrm{H}} < 200$ GeV$/c^2$, is the reconstructed width of the resonance peak dominated by the performance of the reconstruction program, see Chapter 7. Table 11.3 gives various numbers of interest related to the invariant mass cuts and the measured Higgs resonance width.

The second and third rows of Table 11.3 show the cut values on the invariant masses of the Z and γ^*/Z^*. These values have been chosen such that a decent efficiency remains for the genuine Higgs events, while rejecting the majority of background events (shown in Table 11.6). An efficiency of 70% is maintained for Higgs masses below the ZZ-threshold, i.e. about 183 GeV$/c^2$. Above this threshold, it becomes possible to demand two real Z^0 bosons, which is reflected in the high cut value of 80 GeV$/c^2$ for the minimal invariant mass of the second muon pair given in row three. Row four gives several theoretical values of $\sigma_{m_{\mathrm{H}}}$ which were derived from Fig. 11.10, according to the relation $\sigma \equiv \sigma_{m_{\mathrm{H}}} = \Gamma/2.355$.

Contrary to the case of the detector acceptance, which differed for the simulated/reconstructed samples and MC generator level samples, as shown in Table 11.2, the fifth

and ninth row prove that both samples behave the same when subjected to the mass cuts. Shown here, between parenthesis again, is the number of events remaining after the detector acceptance cuts and after the invariant mass cuts. As the last digits are not significant, one should read the number of events as ± 5 and the efficiencies as $\pm 0.5\%$, e.g. $70.0 \pm 0.5\%$. The σ_{m_H} of row eight is obtained from a two-sigma peak fit to the four-muon invariant mass distribution of the generated muon tracks, after application of detector acceptance and invariant mass cuts. This fit method is described in Sect. 11.5.3. Reconstructed tracks were used to obtain the σ_{m_H} of row twelve, again after application of detector acceptance and invariant mass cuts.

m_H (in GeV/c^2)	130	150	170	200	250	400
Δ_{m_Z} (in GeV/c^2)[132]	15	10	6	6	6	6
min m_{γ^*} (in GeV/c^2)[132]	20	30	45	80	80	80
theoretical σ_{m_H} (in GeV/c^2)[244]	0.002	0.007	0.16	0.61	1.7	12
MC cut efficiency (in %)	70	72	70	80	85	85
(at generator level)	(2225→	(2760→	(3047→	(3323→	(3354→	(3716→
	1558)	1992)	2119)	2657)	2855)	3164)
σ_{m_H} of MC events (in GeV/c^2)	0.0043	0.010	0.20	0.76	2.5	15
MuFit cut efficiency (in %)	69	72	69	79	84	84
(full track reconstruction)	(1705→	(2089→	(2360→	(2556→	(2539→	(2836→
	1184)	1509)	1632)	2020)	2143)	2389)
σ_{m_H} of MuFit (in GeV/c^2)	1.50	1.68	2.11	2.71	5.03	17.8
σ_{m_H}/m_H of MuFit (in %)	1.15	1.12	1.24	1.36	2.01	4.45

Table 11.3: See text for an explanation. Last digits given are not significant. Δ_{m_Z} denotes maximum allowed deviation from m_Z for first muon pair, while minγ^* *refers to the minimal invariant mass allowed for the second muon pair.*

The σ_{m_H} of rows eight and twelve of Table 11.3 can be compared, but a number of additional remarks need to be made. Firstly, the events have been simulated with secondaries included. However, as was discussed in Sect. 6.1, this does not have a large effect on σ_{m_H}. The effect was measured to lie within the error window of ± 0.05 GeV/c^2. Secondly, the option of including the vertex with XKalman (see Sect. 7.4.1) was not used. This would not have a large effect on σ_{m_H}, but would bias the tracks to come from the primary vertex, while background events with cascade decays have muon tracks coming from secondary vertices as well. Actually, the largest effect on σ_{m_H} of row twelve comes from the vertex spread of the primary vertex.

Above a mass of 200 GeV/c^2, the natural width of the Higgs boson (in row eight) can be found from the measured width of the resonance peak (in row twelve), when taking into account the momentum resolution of the reconstruction program. The resulting effect of the momentum resolution on the mass resolution is 1.5 GeV/c^2 at $m_H = 130$ GeV/c^2 and increases to 2.8 GeV/c^2 at $m_H = 400$ GeV/c^2. This is in accordance with Fig. 7.42, as it shows that the momentum resolution deteriorates at higher p_T values. See also appendix D for the p_T distributions of Higgses with masses

other than 150 GeV/c^2.

The last row, i.e. row thirteen, has to do with a requirement, stated in Sect. 7.3.1.1, which had not been dealt with yet. This requirement is: the mass resolution needs to be about 1% for an intermediate Higgs mass. From row four of Table 11.3 and Fig. 11.10, we can now understand that this requirement can only concern Higgs boson masses below 200 GeV/c^2, since the natural width of the Higgs boson does not play an important role in the reconstructed width. The reconstructed mass resolution comes close to the requirement, i.e. for $m_{\mathrm{H}} = 150$ GeV/c^2 the minimum resolution of 1.12 ± 0.05 is reached.

11.5.2 Improvement of signal selection

The question arises if and how it might be possible to further improve the results of Table 11.3. A comparison of these numbers with [132] shows that the values of $\sigma_{m_{\mathrm{H}}}$, and therefore of the mass resolution as well, are equal within their error windows. Also the acceptances coincide, see Table 11.2. Comparing with Lavrijsen[245], again yields a comparable mass resolution. However, the acceptance of Table 11.2 times the efficiency of Table 11.3 is much lower than the total efficiencies quoted in [245]. Therefore, a valid conclusion seems to be that an improvement is possible.

If there is a need for a higher efficiency, i.e. a larger number of events passing all cuts, then it is necessary to include as many partially reconstructed tracks as possible. However, caution should be taken as only additional segments from the inner detector should be used. This is because it should be clear whether a track(segment) comes from the primary vertex or not. It is impossible to tell this for track(segment)s from the muon spectrometer. Trying to operate the ATLAS detector without a working inner detector is very academic therefore, as it is not possible to tell Higgs events from background when looking only at the interaction region.

Rows one to nine of Table 11.4 show results corresponding to Table 11.3 but after rescuing partially reconstructed tracks. Several additional comments should help in understanding this first part of the table. Firstly, the acceptances in row two and the corresponding numbers of successfully reconstructed/rescued events in row four are lower than the values quoted in Table 11.2. The reason is that the first part of Table 11.4 uses only the rescued events of the inner detector, while Table 11.2 used the rescued events of the muon spectrometer as well. Secondly, the number of generated events in the sample is given in row three, which means that the acceptances of row two are obtained by dividing the numbers in row four with those of row three. The same applies to rows five, six and seven, i.e. the efficiencies in row five come from the division of the numbers in row seven by the numbers in row six. These efficiencies should be compared to row five of Table 11.3, which leads to the conclusion that the behaviour of the accepted events is unaltered with respect to the invariant mass cuts. Thirdly, rows eight and nine of Table 11.4 give values of the reconstructed/measured Higgs resonance width and the mass resolution which are just slightly larger than the previous results, i.e. rows twelve and thirteen in Table 11.3. So, it seems fair to conclude that the additionally rescued tracks, and thus events, are in fact of only slightly inferior

m_H (in GeV/c^2)	130	150	170	200	250	400
acceptance (in %)	44	54	60	66	66	73
including partially	(5000→	(5000→	(5000→	(5000→	(5000→	(5000→
reconstructed tracks	2201)	2723)	3022)	3276)	3307)	3666)
cut efficiency (in %)	70	72	69	80	85	84
	(2201→	(2723→	(3022→	(3276→	(3307→	(3666→
	1534)	1961)	2084)	2608)	2806)	3096)
σ_{m_H} with segments (in GeV/c^2)	1.51	1.73	2.11	2.81	5.02	18.0
σ_{m_H}/m_H (in %)	1.16	1.15	1.24	1.41	2.01	4.50
σ_{m_H} with vertex (in GeV/c^2)	1.46	1.67	1.93	2.77	4.90	17.5
σ_{m_H}/m_H (in %)	1.12	1.11	1.14	1.39	1.96	4.38
σ_{m_H} with vertex (in GeV/c^2)	1.45	1.57	1.88	2.75	4.83	17.4
σ_{m_H}/m_H (in %)	1.12	1.05	1.11	1.38	1.93	4.35

Table 11.4: Using rescue procedure for inner detector track segments and/or using the XKalman vertex constraint. See text for a further explanation. Last digits given are not significant.

quality than the non-rescued ones.

After application of all cuts, the remaining events are considered to be Higgs bosons, having decayed into four muons at the primary vertex. It is possible to use this sample and refit all tracks using the XKalman vertex constraint. This gives a slight improvement on the mass resolution, but should not be used to further cut away any events (with outliers). The second and third parts of Table 11.4 give the relevant numbers using partially or only fully reconstructed tracks, i.e. the tenth and eleventh, or twelfth and thirteenth rows, respectively. So, rows twelve and thirteen of Table 11.4 can be compared directly to rows twelve and thirteen of Table 11.3, thus showing that the former, constrained values are indeed somewhat better than the latter, unconstrained values. It is not so certain actually, that usage of the XKalman vertex constraint will lead to a better mass resolution. The numbers in Table 11.4 are based on a clean sample containing genuine Higgs decays only. In reality, however, the sample will also contain some background events. This might spoil the possibility of obtaining a better mass resolution after the refit, because these events are more randomly distributed than the Higgs resonance peak. Furthermore, the differences between Tables 11.3 and 11.4 show the improvement not to be really significant.

Furthermore, better knowledge of the exact location of the primary vertex within the interaction region has been tested to lead to the ultimate resolution of $\sigma_{m_H} \approx 1.0 - 1.1\%$ of m_H for $m_H < 170$ GeV/c^2.

11.5.3 Method used to fit signal peak

To conclude this section, a bit more needs to be said about the width of the resonance peak. This width, denoted by σ_{m_H}, is obtained from a so-called two-sigma fit.

Figure 11.9(c) shows that the resonance peak has one completely non-Gaussian tail, which is due to final-state radiation. Taking this tail into account during the fit of the resonance peak would therefore be misleading. The way out is to use only part of the Gaussian fitting curve, namely two sigma both at the left and the right of its mean.

A few iterations are needed before the least significant digit is obtained. In general, the convergence proceeds well and quite fast. However, there were some cases in which the fit did not converge to one unique minimum, so the arithmetic mean was used instead. The convergence went particularly bad when using the XKalman vertex constraint with a 200 GeV/c^2 mass Higgs, which results in the relatively small improvement.

Normally, if it were to approach a perfect Gaussian, one would expect about 84% of the events to be contained within this two-sigma curve. Table 11.5 shows the percentages corresponding to the σ_{m_H} values of Table 11.3 for various Higgs masses. The percentage for $m_H = 130$ GeV/c^2 can be compared directly with [132], where this value is suggested to be $83.7 \pm 0.6\%$, which is significantly different from the value $88 \pm 1\%$ obtained here. This might be caused by the better momentum resolution of MuFit, see Sect. 7.3.3.

m_H (in GeV/c^2)	130	150	170	200	250	400
acceptance of mass cut (in %)	88 (1184–1046)	86 (1509–1304)	88 (1632–1430)	83 (2020–1678)	83 (2143–1785)	82 (2389–1961)
number of events	16.8	38.3	10.2	97.6	82.8	56.2

Table 11.5: Percentage of genuine Higgs events within the mass peak ($m_H - 2\sigma_{m_H}$, $m_H + 2\sigma_{m_H}$) and the expected number of events detected after running one year at high luminosity, for various values of the nominal Higgs mass. Last digits given are not significant.

The number of events expected to be found by the ATLAS detector during a one-year running period at high luminosity is also given in Table 11.5. It can be assumed that the luminosity of the first three low luminosity years added up will be equivalent to one year running at high luminosity.

11.6 Significance of Higgs signal

The previous sections have introduced the ingredients necessary for this section. The Higgs signal has been described quantitatively, i.e. Tables 11.2 and 11.3, while several aspects of the background were covered qualitatively.

11.6.1 Results obtained using PYTHIA6.2 and MuFit

Looking at Fig. 11.8, it is valid to say that the behaviour of the irreducible background with respect to the acceptance cuts depends on the mass (window) under consideration. Therefore, it was decided to generate, simulate and reconstruct samples of $10,000$ irreducible background events within certain mass windows. Table 11.6 shows how each sample behaves under the detector acceptance and invariant mass cuts.

The mass window under consideration has been chosen as $\pm 3\sigma$, with σ the width of the corresponding Higgs peak as calculated in row twelve of Table 11.3. A mass window of $\pm 2\sigma$ was considered to be too optimistic, given the small number of events inside the peak, e.g. see Table 11.5. Taking a fixed value, as done in reference [132], is not a viable choice either, as this does not take the varying shape of the Higgs peak into account. The number of background events left is derived from the production cross section, with the help of Fig. 11.8(b) to estimate the percentage of events inside the specific mass window. Using this knowledge and taking into account the effect of impact parameter and isolation cuts, one finally obtains the significance of the signal over background, after one year running at high luminosity.

m_H (in GeV/c^2)	130	150	170	200	250	400
σ_{m_H} (in GeV/c^2)	1.50	1.68	2.11	2.71	5.03	17.8
events in $6\sigma_{m_H}$ window (in %)	6.15	5.08	6.64	20.9	22.3	17.2
	(10000)	(10000)	(10000)	(10000)	(10000)	(10000)
events in $3\sigma_{m_H}$ window (in fb)	0.71	0.58	0.70	2.51	2.46	1.68
	(5017)	(4953)	(4616)	(5239)	(4809)	(4263)
detector acceptance (in %)	14	20	27	36	36	32
	(688)	(997)	(1255)	(1909)	(1728)	(1377)
Δ_{m_Z} (in GeV/c^2)[132]	15	10	6	6	6	6
min m_{γ^*} (in GeV/c^2)[132]	20	30	45	80	80	80
cut efficiency (in %)	57	48	53	79	82	84
	(392)	(481)	(669)	(1507)	(1423)	(1153)
signal efficiency (in %) after impact par. and isolation cuts	58	58	58	58	58	100
number of signal events (S)	11	26	6.8	68	58	69
irreducible background events	3.2	3.2	5.9	42	42	45
other background events (10%)	0.3	0.3	0.6	4.2	4.2	0
significance ($S/\sqrt{B}$)	5.9	14	2.7	10	8.5	10
significance ($2\sqrt{S+B}-2\sqrt{B}$)	3.9	7.1	2.2	7.8	6.8	7.9

Table 11.6: See text for an explanation. Last digits given are not significant. Δ_{m_Z} denotes maximum allowed deviation from m_Z for first muon pair, while minγ^* *refers to the minimal invariant mass allowed for the second muon pair. The number of signal events is denoted by S, while the total number of background events is referred to as B.*

Table 11.6 does not give the errors on the tabulated values, but the general rule is that the last digit given is never significant. The results in Table 11.6 need to be elaborated. Firstly, every row is described in detail. The first row gives the mean invariant mass of each particular sample, denoted by the corresponding nominal Higgs mass. The one-sigma width of the signal peak, denoted by σ_{m_H}, is taken from Table 11.3 and shown in row two. Row three gives the percentage of events, with respect to the total irreducible background, in a mass window of $6\sigma_{m_H}$. This mass window of $6\sigma_{m_H}$ was chosen as to allow for reconstruction inefficiencies, such that an event that was generated outside the $3\sigma_{m_H}$ window can fall inside it after the full event reconstruction. For every Higgs mass, a sample of 10,000 events was generated in the corresponding mass window (which is the number shown in parenthesis). In the fifth row, the corresponding production cross section was calculated, along with the number of events inside the $3\sigma_{m_H}$ window. Shown in the seventh row are the percentages of events that were accepted for the various samples after simulation and reconstruction. Comparison with the fourth row of Table 11.2 confirms the fact that muons originating from (irreducible) background events, in general, have lower transverse momentum and are closer to the beam line. The assumption that a 20% event loss is caused by partially reconstructed muon tracks, was also tested and found to be valid.

Rows nine and ten are a repetition of the invariant mass cuts belonging to that particular nominal mass[132], see also Table 11.3. The effect of these cuts is represented in row eleven, where the efficiency is given as a percentage of the fully reconstructed events. A comparison between Tables 11.3 and 11.6 shows these percentages to be smaller in Table 11.6 than in Table 11.3 below the ZZ threshold of about 183 GeV/c^2. This is again due to the lower transverse momenta of muons originating from the (irreducible) background. Also not surprising is that the percentages are about equal in Tables 11.3 and 11.6 in case of two real Z bosons, i.e. above 183 GeV/c^2.

In row fourteen, a number of percentages are given denoting the expected efficiency for the Higgs signal under the isolation and impact parameter cuts[242]. These cuts have a significant influence on the Higgs signal, which is reduced by almost a factor two up to 250 GeV/c^2. This efficiency has been kept rather low to insure a safe rejection against reducible backgrounds. However, the choice of a lower rejection factor (see Sect. 11.4) results in a smaller loss of signal events[242]. At higher masses, the opinion[132] is that isolation and impact parameter cuts are not needed anymore, as virtually no reducible background events survive the detector acceptance mass cuts. Applying these efficiencies on the number of signal events, see Tables 11.1 and 11.3, gives the remaining signal events in row fifteen, which need not necessarily belong to the two-sigma peak. The number in the 2σ peak can be calculated as well, but an additional fraction of about 0.85 would need to be used, see Table 11.5 for the exact numbers per nominal Higgs mass.

Application of all quoted percentages on the production cross section, yields the expected number of irreducible background events in a $3\sigma_{m_H}$ window, in row sixteen. Here, a multiplication factor is used of 100 events/fb, which corresponds to one high-luminosity LHC year per experiment. Since the first three years running at low luminosity yield results that are comparable to running one year at high luminosity,

no attempt has been made to perform the analysis for a low luminosity year. Not all background events originate from the irreducible background, so the total contribution due to the reducible background has been estimated. The 10% contribution (relative to the irreducible background) seems to be a safe estimate, when compared to the number of events quoted in other references[132]. Though, one has to keep in mind that the reducible background is difficult to analyse due to the large production cross sections and the high number of possible decay channels involved. Row seventeen presents the number of events remaining after application of all cuts for all reducible background channels.

Finally, rows eighteen and nineteen present the significance of the signal over the background, using $S/\sqrt{B}$, with S and B the number of signal and background events, respectively. This definition is based on an approximation, which is valid only if the uncertainties on S and B are small while the numbers of events themselves need to be sufficiently large[246, 247]. The approximation and definition are typical for a real experiment[248] that has delivered a number of observed events ($n_{\text{obs}} = S + B$), while an expected number of background events is obtained through Monte Carlo simulation. Subsequently, the number of signal events is derived by subtracting the MC background from the observed events. Using the Gaussian (or normal) distribution $N(x,\mu,\sigma) = \exp\left(-(x-\mu)^2/2\sigma^2\right)/\sqrt{2\pi}\sigma$[28], one can calculate the probability β to measure at least n_{obs} events[28], i.e. $\beta = \mathrm{P}(n \geq n_{\text{obs}})$. Knowledge of this probability allows for the derivation of the associated number of standard deviations or sigmas, which is given by $\int_s^\infty N(x;\mu=0,\sigma=1)\mathrm{d}x = \beta$ in the Gaussian sense or interpretation of standard deviation[249]. The significance s is just another name for the calculated number of standard deviations. Usually, the number of events is Poisson distributed in time, leading to $P(r;\lambda) = r^\lambda \exp(-\lambda)/r!$ with variance λ[28], so that $\beta = \mathrm{P}(n \geq n_{\text{obs}}) = \sum_{r=n_{\text{obs}}}^\infty P(r;\lambda = B)$ which can be approximated by $\beta = \mathrm{P}(n \geq n_{\text{obs}}) \approx \int_{n_{\text{obs}}}^\infty N(r;\mu=\lambda,\sigma=\sqrt{\lambda})\mathrm{d}r$[247]. Substituting $x = (r-B)/\sqrt{B}$, using $\lambda = B$, leads to $\beta = \mathrm{P}(n \geq n_{\text{obs}}) \approx \int_{S/\sqrt{B}}^\infty \exp\left(-x^2/2\right)/\sqrt{2\pi}\mathrm{d}x$ from which the identity $s \approx S/\sqrt{B}$ follows[248]. This significance, i.e. $s = S/\sqrt{B}$, is a measure of how many standard deviations(/sigmas) the background should fluctuate[(5)] in order to obtain the number of events of signal and background added together. However, the approximation made is particularly bad when the numbers of events are small[246], as is the case according to rows fifteen and sixteen of Table 11.6. So, another approximation is used, namely $s = 2(\sqrt{S+B} - \sqrt{B})$ as suggested by Bityukov and Krasnikov[247]. Like the other approximation, this approximation also has the advantageous feature that it can be used with non-integer numbers of signal and background events while the expression[249] $\int_s^\infty N(x;\mu=0,\sigma=1)\mathrm{d}x = \sum_{r=S+B}^\infty P(r;\lambda=B)$ is approximated much more accurately. Row nineteen provides the realistic significances, therefore.

[(5)] In particle physics, a significance of three sigma is considered evidence, while the limit is set at five sigma for a discovery (or confirmed measurement). It is for this reason that the potential Higgs events found by LEP[233] are said to be a 2.9 standard-deviation fluctuation of the background.

11.6.2 Comparison to earlier results

It is possible now to compare this analysis, using PYTHIA6.2 and MuFit, to previous results [132] and [242]. These references agree with each other on the number of signal events. However, the number of background events differs between them, which is of particular importance for the irreducible background. This difference can be traced back to the size of the mass window that is considered. Reference [242] uses a variable mass window of $1.4\sigma_{m_H}$, which is too narrow as compared to the more realistic width of $3\sigma_{m_H}$. So, [132] should be used to compare with the results of this thesis. In order to make the comparison, it is necessary first to divide the number of signal and background events by four, because [132] considers four types of event topology, i.e. $4l^{\pm}$ instead of $4\mu^{\pm}$. The simplistic variant of the significance in [132] should therefore be divided by two. Even then, it remains a difficult task to make a general comparison.

Looking first at nominal Higgs masses below $2m_Z$, it is found that more signal events remain in this analysis than in [132]. This rate growth amounts to about 15% to 20%, which is a very advantageous result, given the small rates involved. Furthermore, the reducible background event rates are found to be comparable. However, there is a prominent difference between the irreducible background event rates. In [132], a rather constant rate is found of 1.8 ± 0.2 events. This is two times lower than the results tabulated in Table 11.6 and even three times lower for $m_H = 170$ GeV/c^2. The different sizes of the mass windows cannot explain the factor of two difference. A likely explanation is that the irreducible background suffers more from the isolation and the impact parameter cuts, i.e. a 42% rejection might be too pessimistic. This has not been checked though. In the end, the significances remain comparable, except for $m_H = 150$ GeV/c^2 where a better significance is found here.

The situation is different for higher Higgs masses, since [132] uses the detector acceptance cuts only, i.e. the invariant mass, isolation and/or impact parameter cuts are not used at all for nominal Higgs masses above $2m_Z$. This is rather surprising as Linossier and Poggioli[242] still show substantial reducible background rates for these masses, i.e. about 200 events at $m_H = 200$ GeV/c^2 and about 100 events at $m_H = 250$ GeV/c^2. Therefore, the results quoted in [132] are considered to be too optimistic. It has been found that the mass windows, over which the background is integrated, differ a lot as well. In [132], the following numbers have been used for the mass windows: ± 6.6 GeV/c^2, ± 8.7 GeV/c^2 and ± 24 GeV/c^2 for $m_H = 200$, 250 and 400 GeV/c^2, respectively. They are clearly much smaller than those used for Table 11.6, i.e. 20%-55% less wide. So, it seems that [132] is too optimistic in this aspect as well.

The number of signal events cannot be compared easily either. Firstly, [132] expects 90% of the signal peak to lie within the mass windows just quoted. This assumption is not realistic if we compare to Table 11.5, which finds about 83% of the signal events within the mass windows ± 5.4 GeV/c^2, ± 10 GeV/c^2 and ± 36 GeV/c^2 for $m_H = 200$, 250 and 400 GeV/c^2, respectively. On the other hand, the effect of the detector acceptance cuts is approached from a negative point of view. A 90% reconstruction efficiency per track is used for every track that is detected by the ATLAS

detector. This means that the MC acceptance percentages, i.e. row two of Table 11.2, are convoluted with an additional factor of $(0.9)^4 = 65.6\%$. However, an additional loss of only 20% has been observed, i.e. the convolution factor using MuFit becomes $80\% = (0.95)^4$, which can even be undone almost completely when rescuing partially reconstructed tracks. Finally, the production cross sections were found to differ, i.e. Table 11.1 shows much smaller cross sections obtained using PYTHIA6.2. In the end, the number of signal events used by [132] within their mass windows is 487, 436 and 297 events, for $m_{\mathrm{H}} = 200$, 250 and 400 GeV/c^2, respectively. The number of background events is 247, 180 and 97, respectively, which corresponds to significances of about 30 in all three cases. This is without using any further cuts.

These numbers can be obtained from Table 11.6 if we abandon the invariant mass, isolation and impact parameter cuts. The number of signal events yielded is 149, 118 and 81, for $m_{\mathrm{H}} = 200$, 250 and 400 GeV/c^2, respectively. Here, only the final state with four muons is used. Since [132] treats muons and electrons on the same footing, this means that there is a factor four difference between the number of events. Lavrijsen[245] has recently performed a signal study using both muon and electron channels, which shows actually that these two types of leptons cannot be treated equally (that easily). Taking into account now both reducible and irreducible backgrounds, we find the number of background events to be 142, 113 and 54, respectively. The corresponding significances are: 12.5, 11.1 and 11.0. They are lower than 15 because of the higher, more realistic background rates, even though the signal rates have increased as well.

The conclusion is that the significances quoted in [132], which are based on several assumptions, are too optimistic for Higgs masses above the $2m_{\mathrm{Z}}$ threshold.

11.6.3 Limits of the golden Higgs decay channel

There are limits to the use of the golden Higgs decay channel: $\mathrm{H} \rightarrow \mathrm{ZZ}^{(*)} \rightarrow 4\mathrm{l}^{\pm}$. These limits are related to the number of signal or background events. The significance is a useful measure for these event rates, but it should not be followed blindly. Figure 11.11(a) helps in understanding this precaution. It shows an example, i.e. a statistically possible situation of the invariant mass spectrum of a 150 GeV/c^2 mass Higgs boson, measured after one year, including all four background events. The significance is very high, even for the four-muon decay only, but one cannot expect to extract many physical parameters from such a small sample. From the variety of interesting parameters, it would seem that just a few can be measured, and then only with large statistical errors.

Though Fig. 11.11(a) shows only the events inside the $m_{\mathrm{H}} \pm 3\sigma_{m_{\mathrm{H}}}$ mass window, one can safely assume that a peak will be visible in the full mass range. So, the first and most important observation will be that a Standard Model like Higgs boson does exist. Furthermore, from a Gaussian fit of Fig. 11.11(a) it follows that a mass between 149 and 151 GeV/c^2 will be measured, and a width around 0.5 to 4 GeV/c^2. Including the other leptonic decay channels and the other LHC detector, i.e. CMS[45], would already improve the statistics considerably. Though, a few years will be needed before

spin, parity and other properties can be measured meaningfully.

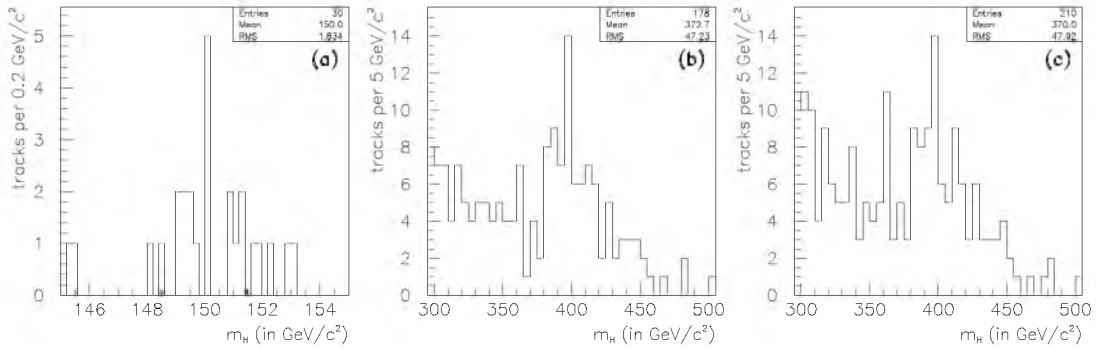

Figure 11.11: Invariant mass spectra obtained after one year running at high luminosity. All signal and background events included. (a) Higgs mass of 150 GeV/c^2 *in a* $3\sigma_{m_H}$ *window. (b) Higgs mass of* 400 GeV/c^2 *in a* $6\sigma_{m_H}$ *window and (c) likewise, but without using invariant mass cuts.*

A critical issue has been mentioned briefly, namely which strategy is to be used to find the Higgs peak. This is an issue because the invariant mass cuts are Higgs mass dependent, while they are also crucial for removing the reducible background. A strategy would be to try several settings for these cuts and to check whether a peak becomes visible over the remaining background. This is easy above the $2m_Z$ threshold, since one setting can be used throughout, i.e. $\Delta m_Z = |m_{12} - m_Z| < 6$ GeV/c^2 and $m_{34} = m_{\gamma^*} > 80$ GeV/c^2. However, the settings need to be adjusted below this threshold, where a scanning of m_H in steps of say 5 GeV/c^2 is necessary.

One question is: looking at the significances and signal rates, how far down can we get in Higgs mass? What is measured if the Higgs mass would turn out to be 116 GeV/c^2 after all. Table 11.6 shows that a Higgs boson of mass 130 GeV/c^2 will be detected using the golden decay channel, though it might not show up as a clear peak above the background that easily, due to the small number of signal events. However, such a Higgs boson should not prove impossible to be detected in combination with the other lepton decays and the CMS detector. Such a combination is certainly necessary for Higgs masses around 170 GeV/c^2, which is found to be a cumbersome region. So, using the information of various sources, one can conclude that the intermediate mass region is covered from $2m_Z \approx 183$ GeV/c^2 down to at least 130 GeV/c^2.

Using PYTHIA6.2 to obtain a production cross section times branching ratio of 0.228 fb, the expectation is that 23 Higgs bosons will be produced in ATLAS in the "golden" decay channel per year for a nominal mass of 116 GeV/c^2. The detector and reconstruction software acceptance is only 27%, while the efficiency against the invariant mass cuts is 60%. The invariant mass cuts have been adapted to this particular mass[132] and were set at $\Delta m_Z < 20$ GeV/c^2 and $\min m_{\gamma^*} > 15$ GeV/c^2, respectively. It is expected that a higher rejection factor is needed against the reducible backgrounds, which are more abundant at lower four-muon invariant mass. This has the effect that the signal efficiency due to the application of isolation and impact parameter cuts will

be lower. A value of 40% has been chosen, therefore, leading to (a meagre) 1.5 signal events per year, after application of all analysis cuts.

In order to evaluate the number of background events, a window of 4.5 GeV/c^2 has been used, even though this is larger than three times the reconstructed signal width at 116 GeV/c^2. This has to do with the small number of signal events from which a sensible width cannot be extracted. Just over 3% of the total irreducible background is produced inside this window around 116 GeV/c^2. The detector and reconstruction software acceptance is slightly below 10% for these background events, while the efficiency after application of the invariant mass and rejection cuts (isolation and impact parameter cuts) is 75% and 40%, respectively. This leaves a total of 2.2 irreducible background events per year. It seems reasonable to add another 0.3 events to this amount, due to the reducible backgrounds. So, in the end, the 1.5 signal events should be compared to the 2.5 background events, which leads to the conclusion that it will take many years before a Higgs boson with a nominal mass of 116 GeV/c^2 can be detected in the "golden" decay channel.

Can the "golden" Higgs decay channel be utilized to detect heavier Higgs bosons, e.g. can the theoretical limit ($m_{\mathrm{H}} < 1$ TeV/c^2) be reached? This question can also be answered best in a qualitative way. Figure 11.4 shows a gradual decrease, with increasing nominal Higgs mass, for the number of events to be expected per year. The reducible background has disappeared above 300 GeV/c^2, which implies that the invariant mass cuts need not be changed from the defaults $\Delta m_{\mathrm{Z}} = |m_{12} - m_{\mathrm{Z}}| < 6$ GeV/c^2 and $m_{34} = m_{\gamma^*} > 80$ GeV/c^2. These cuts have a moderate effect on the signal, so that an 85% signal efficiency seems likely (see Table 11.3). The detector and reconstruction software acceptance is also quite good for higher masses, as Table 11.2 indicates that a signal acceptance of almost 60% is reached.

At first sight, the situation looks favourable with respect to the irreducible background as well. Figure 11.8 shows that the production cross section of this background decreases with increasing four-muon invariant masses. However, it needs to be integrated over a mass window, around the nominal Higgs mass, which equals three times the width of the signal peak. This window determines the number of background events. The importance of the Higgs width, i.e. the integration window, is already apparent at $m_{\mathrm{H}} = 400$ GeV/c^2, as illustrated in Fig. 11.11(b). Here, the four-muon invariant mass spectrum is shown of signal and background events that are successfully reconstructed and survive the invariant mass cuts. A 6σ-window is used to illustrate the role of the background. It is asymmetric and contributes a majority of events at lower masses. Since the signal width is rather large, the signal does not stand out as a clear peak.

At higher nominal Higgs masses, the situation becomes even worse due to two reasons. Firstly, the signal width increases rapidly (recalling the third-order power law of Fig. 11.10). Secondly, the measured width increases even more due to the performance of the reconstruction software. As the muons originating from the decay (vertex) obtain higher transverse momenta, thus reflecting the higher invariant mass, the momentum resolution becomes worse according to Fig. 7.42. For example, a nominal Higgs mass of 500 GeV/c^2 has a corresponding mass window that stretches from

about 400 to 600 GeV/c^2. Reference [132] sets the limit at $m_H = 800$ GeV/c^2, though a remark is made that the signal rate might be too low already for $m_H = 700$ GeV/c^2. This latter Higgs mass has a corresponding mass window of about 400 GeV/c^2 to 1 TeV/c^2. It is doubtful that a signal peak, which has eighty percent of its small number of events spread between 600 and 800 GeV/c^2, can be detected within such a large range. Trying to increase the rate, as is shown in Fig. 11.11(c) by removing the invariant mass cuts, does not improve the picture. A safe conclusion is to assume that a heavy Higgs boson can be detected, deploying the "golden" decay channel, from $m_H = 2m_Z \approx 183$ GeV/c^2 up to about 550 GeV/c^2.

Chapter 12

Discussion and conclusions

Chapters 6, 7 and 11 prove very explicitly that it is crucial to understand the tools that are being used in order to understand the outcome of an analysis. It is the aim of this concluding chapter to interpret the results of the two parts of this thesis.

on standard software

It seems to be an inherent feature of software that it will never be perfect. Even packages that seem to work well are always subject to extensions and/or are found to have flaws in them, which influence their stability and reliability. Chapter 6 has been devoted to these issues of reliability regarding the standard software tools provided by ATLAS. Every functional aspect provided by the software tools is in at least some sense crucial to subsequent analyses, which is why several functional aspects have been studied intensively.

To be able to evaluate the ATLAS detector performance implies to have an accurate description of its geometry. One potential problem has been identified here already, as it was found that the calorimetric volumes have a tiny bit of empty space between them, see also Fig. 6.10(c). However, the muon tracks are bent so that the effect is smeared and thus turns out not to have a negative influence on the analysis.

on detector layout

The performance of the ATLAS detector is cost limited, because the toroidal field is not strong enough to bend the tracks of the highest energy muons. Cost limitations also prevent the detector from becoming larger, which has a strong influence on the muon chamber positioning. The lever arm of the muon track cannot be increased, which results in a degradation of the momentum resolution that is visible[(1)] in Figs. 12.1(a) and (e) and starts at $p_{\mathrm{T}} \gtrsim 150$ GeV/c. Also Muonbox, the muon pattern recognition software, is limited by some necessarily unfavourable chamber positions. It cannot provide enough super space-points for $\eta \approx 0$ and for the feet sectors, where space is taken up by cables, services and support structures, which results in tracks either badly fitted or completely lost in these regions, see Figs. 7.35 and 7.43. Though, it needs to

[(1)]Figure 12.1 is actually Fig. 7.42 but now with the individual momentum resolution figures split up. Refer to Sect. 7.4.2 and Sect. 7.5 for a precise description of the figures.

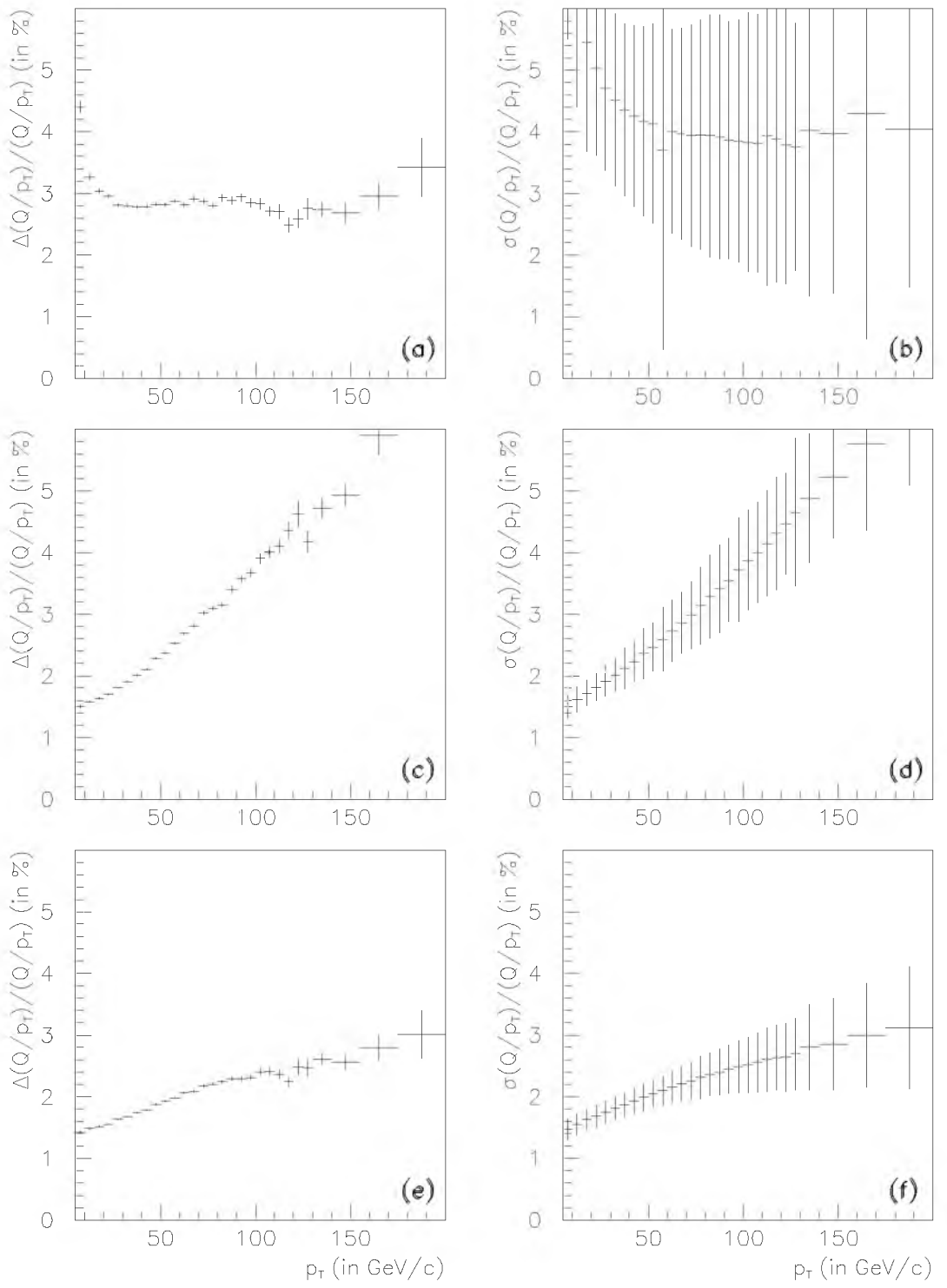

Figure 12.1: (a) Muon spectrometer resolution for the charged inverse momentum as a function of transverse momentum, and (b) its error estimate. (c) Inner detector resolution for the charged inverse transverse momentum, and (d) its error estimate. (e) Charged inverse transverse momentum resolution, i.e. performance, of the combined muon spectrometer and inner detector, and (f) its error estimate.

be noted that the detector layout has been highly optimized in order to reduce the size and influence of unfavourable regions as much as possible.

on physics simulation

In Chapter 6 the influence of secondaries, which are generated by the passage of the muon, on the energy loss recuperation of GEANE has been analysed. It was found to be smaller than the statistical errors involved and therefore secondaries were not considered. However, the influence is expected to be much larger when all types of background are correctly simulated.

The fact that minimum-bias, pile-up, electronic noise, dead detector elements and uncorrelated (background) hits have been left out in the simulation as well, implies that the pattern recognition tasks have been largely simplified. Nevertheless, tracks were lost when trying to combine their spectrometer and inner detector segments, because of momentum or position mismatches. The authors of the pattern recognition packages claim that their software is robust, so that this number of mismatches should not increase and the performance should not degrade too much in the presence of these backgrounds. If true, this means that the momentum resolution figures presented here, see Fig. 12.1, and by others, e.g. Lavrijsen[245], are feasible for the real ATLAS detector. This situation will definitely change for $p_{\mathrm{T}} > 300$ GeV$/c$, however, due to muon induced electromagnetic showers.

on muon seed usage

Two improvements are possible that should help in accomplishing the best possible momentum resolution figures as shown in Fig. 12.1. Firstly, Sect. 7.4 together with Fig. 7.38 shows that the seeds provided by the muon reconstruction can become much smaller than the default values. This helps greatly in combining the spectrometer and inner detector track segments, especially in the presence of the backgrounds mentioned previously. Secondly, Muonbox should not restrict its pattern recognition to the muon spectrometer only, as muons that pass through problematic regions are not likely to be found. Instead, it should try to match track candidates to inner detector track segments immediately, for instance using muon seeds. The gain of this procedure is expected to be large, i.e. it can be compared to the difference in performance when MuFit uses the beam pipe constraint or not, and will also lead to an early recognition of tracks not originating from the interaction region.

on fitting software

The GEANE software tool contains flaws. The energy loss recuperation had to be tuned in another way than suggested by the manual. It exhibits a strange discrete behaviour even then, see Fig. 6.10(a), which is still not understood. Furthermore, a sign error was identified, found and corrected in one of its subroutines by Lavrijsen[141]. The treatment of multiple scattering is incorrect as it is based on a wrong approximation. However, Lavrijsen[245] tested other methods but did not find any significant changes. This insensitivity is due to the existence of a very wide range of values approximately corresponding to the optimal results.

The track fitting method used was found to be insensitive to all problems in the tracking software, i.e. it was able to bend the track and fit it to the position coordinates without the need to change the track momentum parameter drastically. So, the conclusion is that the fitting method is very robust. However, two remarks are in order. Firstly, using super space-points only, implies that MuFit cannot do better than Muonbox if no additional information is used. Secondly, the fitting method allows the track to assume a new direction at every fit point. The magnitude of this change is primarily influenced by its neighbouring fit points. This explains the robustness but does not take physics implied limits into account. In other words, the change in angles at every fit point should conform to the multiple scattering distributions, see Fig. 7.11.

Furthermore, it came as a complete surprise and is very interesting to see that this relatively old fitting method, used by MuFit, gives results that are comparable within the statistical errors to the recently developed fitting methods, e.g. Cobra[245]. It is, therefore, a useful and complementary addition to the other methods. In conclusion, given the huge benefit of the knowledge of the origin of a muon track, the main advice is to find and use this origin as early as possible.

on Higgs signal

Part II of the thesis uses MuFit to reconstruct the tracks of muons originating from a specific type of Higgs boson decay. The analysis of this decay channel and the background channels with comparable event topologies has yielded very interesting results. Again MuFit proves its strength here, since the resulting number of signal events and the reconstructed resonance width are comparable within the statistical errors to previous studies. This is surprising to some extent as intermediate results were found to differ. One reason for this difference is that a recent version of PYTHIA6.2 was used to obtain samples of Higgs bosons and samples of irreducible background. This yields a production cross section for Higgs boson masses below the $2m_Z$ threshold, higher than that of PYTHIA5.7, which was used for previous studies. On the other hand, a lower production cross section is found above this threshold.

Another reason that accounts for the differences in analyses, is that very pessimistic reconstruction efficiencies were assumed in previous studies[132]. The analysis in this thesis gives a consistent 20% loss for four muon tracks in all cases, instead of the earlier assumed 34%. Lavrijsen[245] uses a different reconstruction method resulting in an even smaller loss. A prescription has been given in Sect. 11.3 how to increase the track reconstruction efficiency. Care should be taken, however, since the quality of the track parameters of these rescued tracks has to be comparable to the quality of the bulk of the events. Otherwise, most of these rescued events will end up in the tails of the four-muon invariant mass distribution thus effectively augmenting the background.

on stand-alone spectrometer operation

Consider the following illustrative example of an extreme situation. Suppose that the track segments of inner detector and muon spectrometer cannot be combined, for some

reason or other. All muon tracks, as found by Muonbox, will then be used by the analysis, since no distinction can be made between badly and well fitted muon tracks. Momentum and/or position mismatches are not noticed because no combination is made. Furthermore, there is no knowledge of the primary vertex, so that the impact parameter cut cannot be used. Referring to Sect. 11.4, this implies that the number of reducible background events equals the number of signal events. Concentrating on a given nominal Higgs mass, it is possible then to calculate the influence of this dramatic situation on the reconstructed Higgs resonance width, on the numbers of signal and background events and, therefore, on the significance.

At a nominal Higgs mass of 150 GeV/c^2, about 48% of the generated signal events are successfully reconstructed by the muon spectrometer. That is to say: 2395 out of 5000 events are comprised of four muons that pass the muon trigger (two muons with $p_T > 20$ GeV/c) and the acceptance cuts ($p_T > 7$ GeV/c and $|\eta| \lesssim 2.5$ for every muon). This acceptance is slightly higher of course than that quoted in row four of Table 11.2, because no tracks and therefore no events are lost due to mismatches between track segments in the muon spectrometer and the inner detector. However, the efficiency with respect to the invariant mass cuts has become about 68% (1630 out of 2395 events). This is slightly lower than the efficiency quoted in row nine of Table 11.3, because the muon track parameters can only be determined less accurately, thus resulting in a larger spread on the distributions of interest.

The reconstructed signal width suffers in particular from the spread, i.e. measurement inaccuracy, almost becoming twice as large, namely $\sigma_{m_H} = 3.09$ GeV/c^2 instead of 1.68 GeV/c^2 (see row twelve of Table 11.3). As a result, the background to be considered has become overwhelming. For the irreducible background, the detector acceptance of 19% is somewhat lower than in row seven of Table 11.6, namely 1746 out of 9160 events, while the invariant mass cut efficiency of 48%, namely 837 out of 1746 events, has remained the same (compared to row eleven of Table 11.6). The similarity of the percentages is due to the uniformity of the background.

Using the proper conversions, i.e. one year running at high luminosity, the number of irreducible background events becomes 9.7 per year. Likewise, the number of signal events is 48. These numbers will certainly become less when track isolation cuts are applied, which are needed to reject the reducible background. Reference [132] states that about 106 events per year, in a mass window of ± 5 GeV/c^2 around $m_H = 150$ GeV/c^2, are due to reducible background. The more realistic 3σ window is almost twice as large, so application of isolation cuts is necessary whereby the reducible background is rejected by a factor 20 while keeping 80% of the signal[132] (and irreducible background) events. In the end, a significance ($S/\sqrt{B}$) of about 9 seems feasible, using $S \approx 38.4$ and $B \approx 7.8 + 9.8$ events.

The situation is even more favourable for $m_H = 400$ GeV/c^2, where the reducible background does not contribute anymore, while the signal width has increased from 17.8 GeV/c^2 to only 19.4 GeV/c^2, because the inner detector does not play an important role at such high momenta. This leads to the conclusion that it is still possible to perform physics studies using the stand-alone muon spectrometer (in cases of emergency).

on cross sections

A misleading way that, at first sight, seems to drastically increase the number of signal events has already been mentioned briefly in Sect. 11.1 and involves the usage of K-factors to correct for higher-order QCD corrections. Spira[238] has calculated K-factors, which are in fact a function of the nominal Higgs mass, for the most important Higgs production processes. The increase in signal events is large, as is found when using the proper branching ratios (see Fig. 12.2). The reason why it is misleading and why it has been decided to use PYTHIA6.2 instead of these results is mainly that such detailed calculations do not exist for the background processes. Using K-factors for the signal but not for the background introduces a strong bias, even though K-factor corrections provide a better approximation of the cross section. Further studies would therefore benefit greatly when K-factors become available also for the background processes, regardless of whether the significance increases or not.

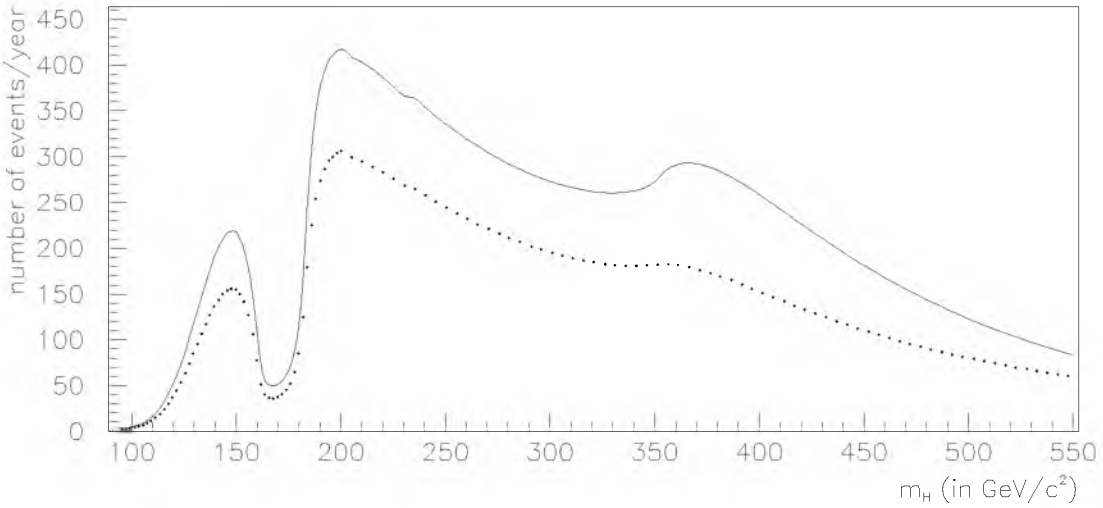

Figure 12.2: Number of events per year to be expected in the decay channel $pp \rightarrow H + X \rightarrow ZZ^{(*)} + X \rightarrow \mu^+\mu^-\mu^+\mu^- + X$ *for various Higgs masses using higher order QCD corrections (solid line) in comparison to* PYTHIA*6.2 results (points).*

on four-muon background

Returning to the interesting results of this thesis means to concentrate on the numbers of background events. These numbers were found to differ significantly from previous studies. Sect. 11.6.2 has been devoted to a comparison of methods used to obtain the numbers of background events. Several causes for this difference were found. The most important factor is the size of the integration window, i.e. the range of masses over which the background needs to be integrated. It was argued to use an integration window of $\pm 3\sigma_{m_H}$, i.e. a mass range of $m_H - 3\sigma_{m_H}$ to $m_H + 3\sigma_{m_H}$, because it takes the signal shape into account. The analysis indicated that even this window might be too small, since a well defined signal width cannot be extracted from the small number of

signal events involved. Previous studies have used smaller integration windows, thus resulting in a smaller number of background events.

It was also argued that the reducible background has not always been taken properly into account in the past. Reference [132] ignores it completely for four-muon invariant masses above 200 GeV/c^2, while Linossier and Poggioli[242] prove this treatment to be too optimistic. However, taking the reducible background into account properly is very difficult due to two reasons. Firstly, the production cross sections are not well known. Secondly, all possible decay channels should be taken into account, including the cascade decays which are hard to evaluate. Large safety margins have been built into the default analysis method to make the resulting significances independent of the reducible background. A better knowledge of this type of background could, therefore, be of great benefit to the analysis.

on observability

Another way to increase the number of signal events, and thus to increase the Higgs boson observability, is to combine the results of both general-purpose LHC detectors and of other leptonic decay channels. This is important, not only for an early discovery of the Higgs boson, but even more for extracting physical parameters of interest. Lavrijsen[245] has done that for the Higgs boson signal and came to the conclusion that care should be taken as all leptonic decay channels should be treated separately.

Care should be taken, however, of using the proper approximation of the significance of signal over background. The default approximation $s \approx S/\sqrt{B}$ is not as good as the suggested[247] approximation $s \approx 2(\sqrt{S+B} - \sqrt{B})$ for low numbers of signal and/or background events[246]. Since the number of events involved is small indeed, the latter significance has been given wherever applicable.

on discovery outlook

In the end it seems valid to conclude that future studies will be most interesting if all types of background are treated fully. This includes the usage of K-factors, of all possible decay channels and of the proper mass integration windows. K-factors for the signal can then be used, which in combination with other results should lead to well recognizable signal peaks.

m_H (in GeV/c^2)	116	130	150	170	200	250	400
Significance ($s = 2\sqrt{S+B} - 2\sqrt{B}$)	0.84	3.9	7.1	2.2	7.8	6.8	7.9
Years to measure before discovery	38	3.7	1.5	7.2	1.2	1.6	1.2

Table 12.1: Significance of the Higgs signal over a four-muon background expected for ATLAS after one LHC year running at high luminosity using the significance definition for future, planned experiments. Expected number of years needed to run the LHC experiment before reaching the 5σ-discovery limit assuming low luminosity runs for the first three years. Last digits given are not significant.

The studies in this thesis have shown that the ATLAS detector is well suited to the part of the LHC physics program that deals with the "golden" Higgs decay channel. Even the stand-alone muon spectrometer delivers a reasonable Higgs discovery potential. Results for the decay into four muons are summarized[(2)] in the concluding Table 12.1.

[(2)]Refer to Table 11.6 in Sect. 11.6 for the complete table.

Appendix A

ΔE of GEANE dependencies

In this appendix, it is shown how the energy correction of GEANE depends on specified parameters. As discussed in Chapter 6, the CUTS settings 6 to 10 and the settings of LOSS, DCAY, PFIS, MUNU, PHOT, COMP, PAIR, BREM, DRAY, and ANNI influence this energy correction. The dependence on the last set of parameters is so small that they are not looked at any further, except for the LOSS parameter which is of importance. The five CUTS parameters can be grouped, namely CUTS 6 (DCUTE) and 7 (DCUTM) have the same meaning, as well as CUTS 8 (BCUTE) and 9 (BCUTM).

The following tables show that the choice of BCUTE/M is of importance, as it has to have a high value, i.e. 10^5. Or, in case it does not, then LOSS 2 needs to be inferred. Otherwise, the value of LOSS is not of importance. It seems as if the DCUTE/M and PPCUTM (CUTS 10) parameters strengthen each-other, namely the lowest energy correction is obtained when both are low, i.e. 10^{-5}, while the highest energy correction follows when both are set to high values, i.e. 10^5. Table A.1 shows the energy dependence for sample four of Table 6.3, see also Fig. 6.3. And Table A.2 does the same for the sixth sample of Table 6.3.

LOSS	DCUTM	BCUTM	PPCUTM	ΔE (GEANE) (in GeV)
1	low	low	low	1.8293
2	low	low	low	3.4929
3	low	low	low	1.8293
4	low	low	low	1.8293
1	low	low	high	2.0366
2	low	low	high	3.7001
3	low	low	high	2.0366
4	low	low	high	2.0366
1	low	high	low	3.4929
2	low	high	low	3.4929
3	low	high	low	3.4929
4	low	high	low	3.4929
1	low	high	high	3.7001
2	low	high	high	3.7001
3	low	high	high	3.7001
4	low	high	high	3.7001
1	high	low	low	1.9843
2	high	low	low	3.6479
3	high	low	low	1.9843
4	high	low	low	1.9843
1	high	low	high	2.1914
2	high	low	high	3.8551
3	high	low	high	2.1914
4	high	low	high	2.1914
1	high	high	low	3.6479
2	high	high	low	3.6479
3	high	high	low	3.6479
4	high	high	low	3.6479
1	high	high	high	3.8551
2	high	high	high	3.8551
3	high	high	high	3.8551
4	high	high	high	3.8551

Table A.1: Track parameters: $p = 45$ GeV, $\eta = 0.084$, $\varphi = 1.4865$ *radians. Sample containing both* μ^+ and μ^-, *without the presence of a magnetic field. Specification of energy loss distribution:* mean $= 3.885$ GeV *and* MOP $= 3.076$ GeV.

LOSS	DCUTM	BCUTM	PPCUTM	ΔE (GEANE) (in GeV)
1	low	low	low	2.2600
2	low	low	low	4.3266
3	low	low	low	2.2600
4	low	low	low	2.2600
1	low	low	high	2.5370
2	low	low	high	4.6038
3	low	low	high	2.5370
4	low	low	high	2.5370
1	low	high	low	4.3266
2	low	high	low	4.3266
3	low	high	low	4.3266
4	low	high	low	4.3266
1	low	high	high	4.6038
2	low	high	high	4.6038
3	low	high	high	4.6038
4	low	high	high	4.6038
1	high	low	low	2.4670
2	high	low	low	4.5335
3	high	low	low	2.4670
4	high	low	low	2.4670
1	high	low	high	2.7438
2	high	low	high	4.8107
3	high	low	high	2.7438
4	high	low	high	2.7438
1	high	high	low	4.5335
2	high	high	low	4.5335
3	high	high	low	4.5335
4	high	high	low	4.5335
1	high	high	high	4.8107
2	high	high	high	4.8107
3	high	high	high	4.8107
4	high	high	high	4.8107

Table A.2: Track parameters: $p = 45$ GeV, $\eta = 2.084$, $\varphi = 1.4865$ *radians. Sample containing both* μ^+ and μ^-, *without the presence of a magnetic field. Specification of energy loss distribution:* mean $= 4.816$ GeV *and* MOP $= 3.934$ GeV.

Appendix B

MuFit internals

This appendix describes the program and data flow inside the MuFit subroutines and, where necessary, inside the GEANE subroutines. Figure B.1 shows the program flow chart, seen from the general ATRECON[113] steering routine ARECON[112].

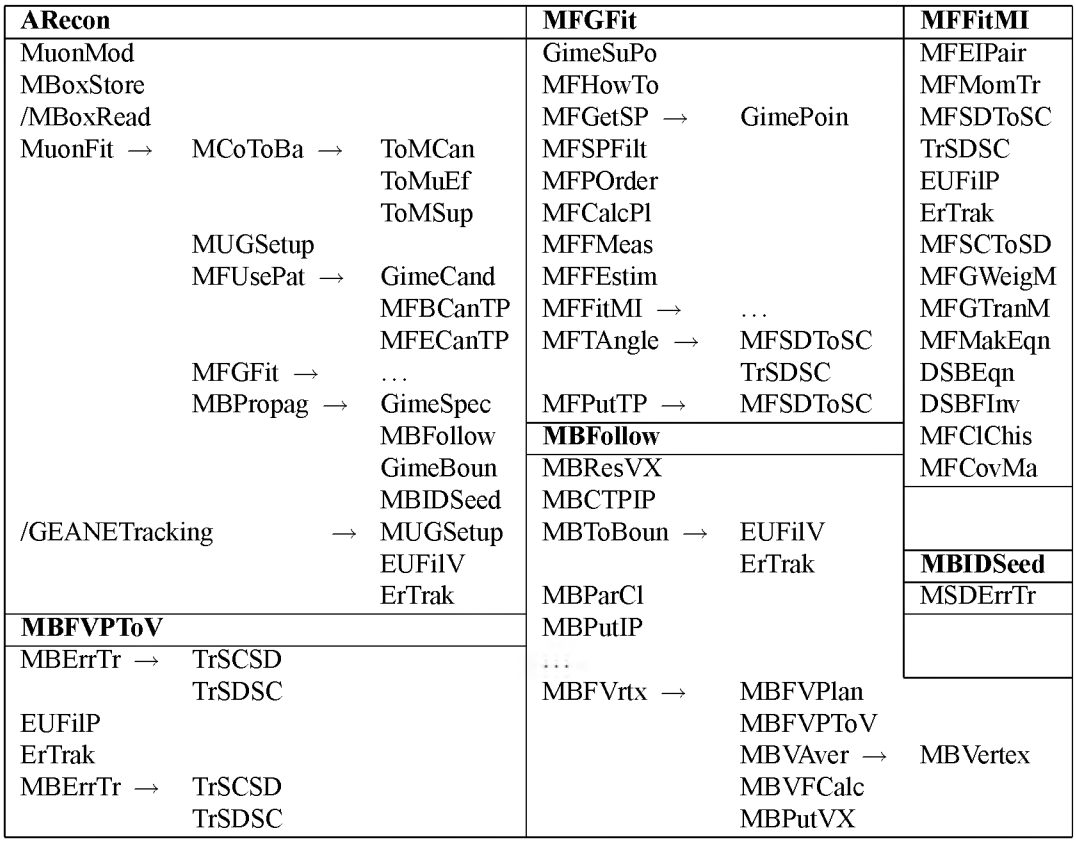

Figure B.1: Flowchart of MuFit program subroutines.

Though most subroutines should be considered internal to MuFit, there are several that were made specially for external users. These subroutines are the ones that do

not adhere to the ATLAS proposed naming scheme[250], i.e. they do not start with a capital M. In general, these subroutines provide access to data and should be understood as: give me something. They are used to retrieve certain pieces of information in a sequential way, i.e. the first subroutine argument whether the first data bank needs to be fetched or the next one. The second subroutine argument denotes the success of the operation and is, therefore, used to check if the end of the sequential chain has been reached. Table B.1 shows an example of typical FORTRAN[251] code using this method.

```
* retrieve parameters of all fitted muon tracks at the vertex
      Call GimeVrtx(.TRUE., okay)          ! first track
10    If (okay) Then                       ! past last track?
            :                              ! process data
         Call GimeVrtx(.FALSE., okay)      ! subsequent track(s)
         Goto 10
      Endif
```

Table B.1: Typical piece of FORTRAN code using 'give me something' user interface.

The subroutines that adhere to this scheme are:
GIMECAND - to retrieve candidate track information of Muonbox,
GIMESUPO - to obtain super space-point header information on each Muonbox track,
GIMESPEC - to retrieve fitted track information of MuFit, inside the spectrometer,
GIMEBOUN - to retrieve backtracked track information of MuFit, at a specified boundary[(1)],
GIMEVRTX - to retrieve backtracked track information of MuFit at the vertex.
Two routines do not obey this scheme. They help in obtaining additional information on an already specified track. GIMEMUEF holds Monte Carlo information on the GEANT hits, from which the single tube efficiency can be inferred. GIMEPOIN is used to obtain further information on every single super space-point. Using separate utility subroutines, in order to get access to window common block[252], is an outdated procedure; it is currently superseded by the USE-operator of AGE[108]. Figure B.1 shows that MuFit uses these external subroutines internally as an interface to the data coming from Muonbox.

Starting at the steering routine, it is now possible to understand the data flow by following the program flow. In the steering routine, the decision is made to perform the pattern recognition, using MUONMOD, and to store the results, or to skip this but to read in previously stored Muonbox common blocks instead. The track fit is selected by invoking MuFit. For some studies in chapter 6, Muonbox and MuFit are skipped

[(1)]This boundary is specified by two additional subroutine arguments, namely the name of the volume that needs to be entered and the name of the volume that will be left. These names can be: PIPE, INNE, CENT, and OUTE, as shown in Fig. 6.5.

altogether and their functionality is replaced by GEANETRACKING, which performs the track propagation using Monte Carlo information.

The first thing that MuFit does, is to prepare Muonbox data to be used by the utility subroutines, i.e. it builds ZEBRA banks[253] out of Muonbox internal common blocks. MCOTOBA is meant to mean: Muonbox Commons to (ZEBRA) Banks. Then, TOMCAN is used to prepare the MCAN-bank for GIMECAND, and TOMUEF prepares the MUEF-bank for GIMEMUEF, while TOMSUP prepares both MSUP- and MSPP-banks to be used by GIMESUPO and GIMEPOIN. MUGSETUP performs the user-defined setup of MuFit and GEANE taking pre-defined settings, e.g. for the maximum number of iterations, which can be changed by data cards. This is the only MuFit subroutine that is used by GEANETRACKING as well.

In order to prevent tracks from disappearing, it is necessary to have a back up in case of fit failures. MFUSEPAT goes along all Muonbox track candidates, see Table B.1, and fills in the fit result bank M1TP (for muon reconstruction phase 1 track reference point/parameters), which is used later on for track propagation by GIMESPEC. Barrel and endcap tracks need to be treated differently, i.e. MFBCANTP and MFECANTP. The M1TP-bank is overwritten when the track fit turns out to be successful.

Necessary preparations for GEANE and the mathematics of the fit procedure are performed by subroutine calls inside MFGFIT. It makes a loop on all tracks, using GIMESUPO, by gathering information on the super space-points belonging to that particular track only. MFHOWTO determines the maximum number of iterations, whether or not to use the beam pipe as an additional super space-point, and the direction of tracking, i.e. whether to go from the outer stations to the inner stations or vice versa. These prescriptions come from MUGSETUP, which already took them from default set values, or overriding data cards. Every super space-point is actually gathered sequentially by MFGETSP using GIMEPOIN. The possibility exists to filter out unwanted super space-points, i.e. bad information, or any other type of operation using the function MFSPFILT. After this step, the decision is made to continue with this track, when enough super space-points contribute, or not. The points are ordered, by MFPORDER, to insure the right sequence to be used by the fit procedure. The planes describing the multilayer or mattress to which a point belongs are calculated by MFCALCPL, and measurement errors are turned into proper weights, by MFFMEAS. The initial track parameters are inferred/guessed from the set of super space-points, in MFFESTIM. Now, the data has been prepared enough to conduct the track fit using GEANE. MFFITMI takes care of this, but we will look at it in detail later.

There are situations in which MFFITMI will fail to produce an adequate fit. This situation most often occurs when two super space-points lie very close to one another, as this can lead to an unstable situation in which the plane of the furthest super space-point is already passed before the closest one is reached. MFFITMI misses the furthest super space-point in that case and reports a failure back to MFGFIT. Now, the strategy has been adopted to try the fit in the opposite direction first, before selectively starting to drop points from the track. Super space-points should not be dropped, but it is very important to fit every track, no matter how, so it is tried then to perform the fit without using the super space-point which had the largest measurement error estimates on it. If

the fit fails again, the next worse super space-point is left out and so on until MFFITMI reports a successful fit. In any case, not more than one super space-point is removed from the track which is only a severe operation if the number of super space-points was six, or less.

GEANE makes use of three types of reference frames[89], in which to represent the track parameters. Two of these frames are actually used by MuFit, namely the standard representation: $(Q/p, \frac{\pi}{2} - \theta, \varphi, L, S)$, which is called[(2)] SC and can be seen as the overall reference frame. It is used for backtracking purposes, and is also the convenient representation for external users of the MuFit results. The actual fit is performed in a local detector plane frame, called SD. Consider v and w to be vectors spanning the detector plane, and u to be orthonormal to this plane, then the track parameter representation becomes: $(Q/p, v', w', v, w)$, where $v' = \frac{dv}{du}$ and $w' = \frac{dw}{du}$.

MFTANGLE uses the GEANE external subroutine TRSDSC to convert the fit results from the local detector plane system into the overall system, i.e. from SD to SC. These fit results comprise of five track parameters, the plane distance T and the covariance matrix, i.e. error estimates, of the track parameters. For ease of use, Cartesian coordinates of a point of reference on the track are provided as well, as obtained from MFSDTOSC. The final fit results are stored into the M1TP-bank by MFPUTTP.

Now that a proper description of the muon track parameters, and inaccuracies thereon, has become available, it is possible to finish the first phase of muon track reconstruction by propagating the track information towards the interaction region. MBPROPAG is responsible for this task. What is does is to loop over all tracks to obtain the tracks' point of reference, from the fit, using GIMESPEC. This point lies inside the muon spectrometer, on a multilayer which is closest to the interaction region. The backtracking, performed by MBFOLLOW, goes towards the interaction region thereby encountering several volume boundaries of interest. First however, the M1VX-bank is reset, by MBRESVX, just in case that the track passes the beam pipe, and the M1IP-bank is initiated, by MBCTPIP. Then, the backtracking is stopped at the first boundary encountered, which is the transition of OUTE to CENT, see Fig. 6.5. MBTOBOUN uses the external GEANE subroutines EUFILV, to define the volume boundary, and ERTRAK, to perform the actual backtracking, to this purpose. Track parameters are calculated and stored into the M1IP-bank for intermediate track reference points, by MBPARCL and MBPUTIP respectively. This procedure is repeated for the CENT/INNE and INNE/PIPE boundaries, where the latter happens to be the boundary closest to the interaction region. Figure B.2 shows, schematically, how the closest approach to the interaction region is constructed.

MBFVRTX steers the necessary steps. First, it makes sure that two planes are defined, by MBFVPLAN, which are parallel to the z-axis and orthogonal to the transverse track directions, i.e. azimuthal angle of the track. Then, MBFVPTOV changes the track from SC to SD representation, using MBERRTR and TRSCSD, places the vertex plane

[(2)]The terms SC, SD and SP come from EMC software[144–146], where SC denotes Streamer Chamber, which was identified with the overall system, SD means System of Detection, and SP comes from spline. The latter being a convenient mathematical description of a track in a fixed target experiment with successive parallel detector planes.

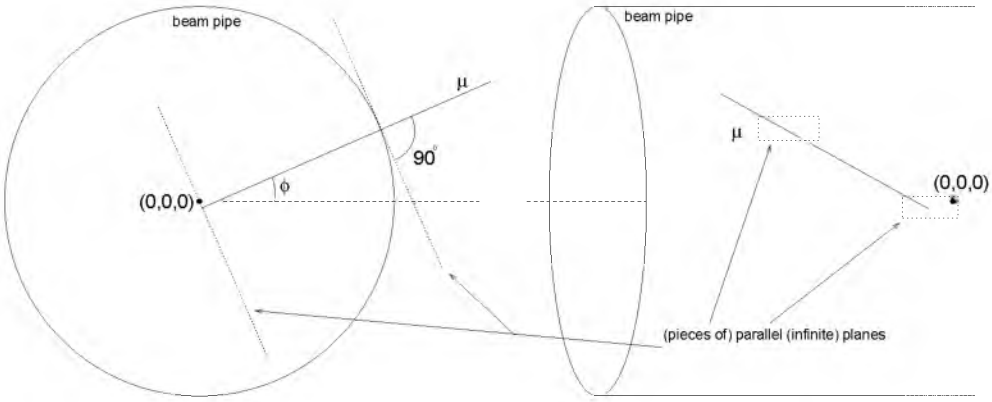

Figure B.2: Transverse and longitudinal representation of beam pipe and interaction region showing definition of closest approach for backtracked muon using two parallel planes perpendicular to the azimuthal track direction. The distance is measured in the parallel plane from the closest approach of the muon track to the event origin, i.e. vertex.

and backtracks to it, using the external GEANE subroutines EUFILP and ERTRAK. The new set of track parameters, at closest approach to the vertex, is transformed from SD to SC representation, by MBERRTR and TRSDSC, to be used for further processing, e.g. by MBVAVER. Here, it is possible to combine the vertex reference point with the real primary vertex, defined by MBVERTEX[3], in a statistical manner. This introduces a bias on the vertex position, though, which changes the muon momentum as well, hence the decision is made not to incorporate this feature into a standard MuFit application. Additional vertex parameters are calculated, by MBVFCALC, and the result is stored into the M1VX-bank by MBPUTVX.

The muon track parameters have been made available now at every point of the track, in principle. This feat makes it possible for MBPROPAG to loop along all tracks in the event, using GIMEBOUN to retrieve the track information on the outer boundary of the inner detector. The proper Jacobian transformation matrix is calculated by MBIDSEED and, afterwards, used by MSDERRTR to perform the transformation of track parameters and covariance matrix from the MuFit representation to the inner detector pattern recognition software representation. The result is stored into the MISD-bank. This ends the first phase of muon reconstruction.

MFFITMI is the heart of MuFit as it steers the subroutines that take care of track and error propagation, and others that solve mathematical equations. It consists of two loops. One which loops continuously over all super space-points to create a track segment. The other loops as long as certain convergence prescriptions are not met. However, before going into the loops, the elements of the covariance matrix, belonging to the point of reference near the inner surface of the muon spectrometer, are identified

[3]The real primary vertex is located at $x, y, z = (0,0,0)$ approximately, with an inaccuracy given by the Gaussian widths $\sigma_x = \sigma_y = 16$ μm, $\sigma_z = 5.6$ cm.

by MFEIPAIR. Then, the loops are entered taking the track information at the first super space-point and preparing the track information propagation. This information is needed in Cartesian form, so MFMOMTR, MFSDTOSC, and TRSDSC are used to go from the local detector to the overall system. A plane is placed at the next super space-point, by EUFILP, and the tracking is taken care of by ERTRAK, which delivers part of its results in SD form. The remainder is transformed by MFSCTOSD. See Fig. B.3 for this first step of the track fitting process.

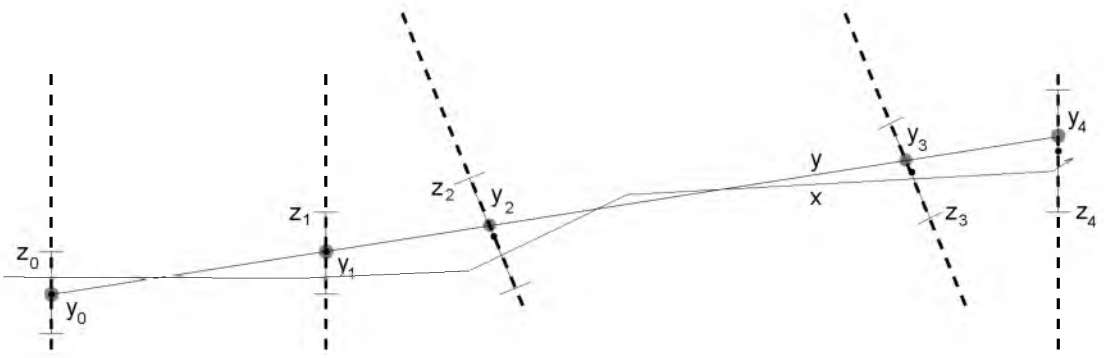

Figure B.3: Detector planes with measured track points (z_i). Real muon track (solid line x) and prediction of first iteration (dotted line y with predicted track points y_i).

The error matrix is transformed into a weight matrix, by MFGWEIGM, and stored along with the transport matrix, which describes the change of parameters from one plane to the other. It is processed by MFGTRANM. The predicted track parameters are used in the next iteration of the loop, which continues until all planes have been reached. Figure B.3 shows the procedure for subsequent planes as well, though it should be kept in mind that this figure is valid for the first iteration, as only the first plane has estimated track parameters associated to it, during the first iteration.

The information that is available at the moment is a set of planes with measured (z_i) and predicted track points (y_i) on them. Predicted track parameters (y_i) exist on every plane at the predicted track point (y_i) and these describe a hypothetical track (y) which fits more-or-less to the measured track points (z_i). The objective, however, is to reconstruct the true track parameters (x), i.e. the measured track points (z_i) form the best known approximation of the true track (point) (x_i). The quality of the current track (y) is described by the chi-square equation: $\chi^2 = (z-x)V(z-x) + (y-x)W(y-x)$, where V represents the $5N \times 5N$ weight matrix of the measurement errors, and W represents the $5N \times 5N$ covariance matrix on the tracking errors, with N the number of planes. The GEANE manual[88] describes how an improved estimate of x can be calculated from this equation. It is also proven that the given equations behave equivalent to the Kalman track filtering procedure[254], to first order in $1/p$. Compatibility to the Kalman filter is of importance, because it is the optimal linear filter[28]. It is even the best filter when the underlying error distributions are Gaussian in nature. MFMAKEQN prepares a linear set of equations, which is used as the linearized solution to

the chi-square equation. This linear set is solved by standard methods in the subroutines DSBEQN and DSBFINV, which are provided with GEANE. These subroutines are special in that they treat the problem in N blocks of 5×5 sub-matrices, instead of the full $5N \times 5N$ matrix. The reason is that the latter would provide a continuous solution, and thus, a smooth track. This is not the behaviour wanted as it is known that multiple scattering occurs along the track. So, it should be allowed to have kinks, which is made possible by the block banded method. The effect is that the track points (y_i) of the predicted track (y) are pulled towards the measured points (x_i). However, this is done in such a way that the influence of neighbouring planes is taken into account, i.e. an interplay between planes is created. Figure B.4 shows the result after this filtering step.

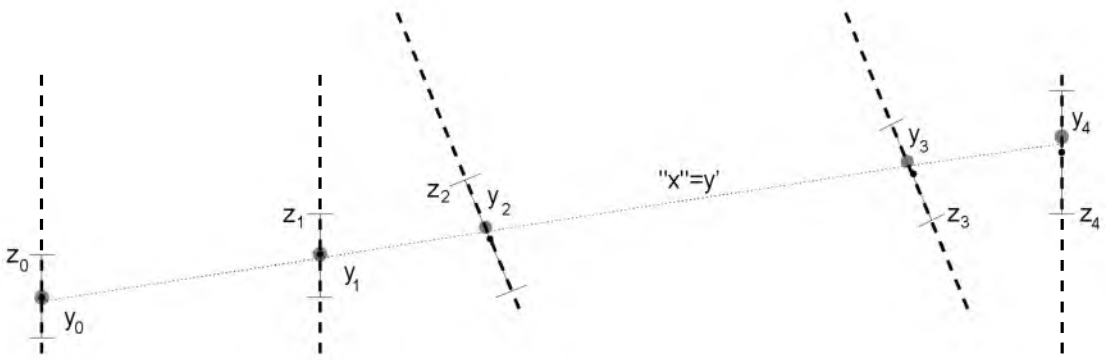

Figure B.4: Detector planes with measured (z_i) and predicted (y_i) track points. Fitted track (y') becomes true track ("x") at end of fit procedure.

The new chi-square of this track is calculated, by MFCLCHIS, and compared to previous chi-square values in order to determine the convergence behaviour. When it is found that the chi-square values exhibit a continuously decreasing behaviour, then the fit procedure is terminated as soon as the values would increase. Otherwise, if an oscillating behaviour is noticed, the fit procedure stops as soon as a new local minimum has been reached. A third condition, namely when the maximum number of iterations has been reached, is never met but incorporated for testing purposes and to guarantee the termination of MFFITMI. The fit procedure is ended by accepting the last predicted track (parameters) as the true track (parameters). MFCOVMA prepares the covariance matrix of this track at the reference point for the user, so that it can be stored into the M1TP-bank.

When necessary, the fit procedure is repeated for the next iteration. It starts at the first plane again and follows the track to the next one. However, this time the track information at that plane is used instead of continuing the track from the previous plane. As already noted, this behaviour is contrary to that of the first iteration. This is, however, the best way to propagate information of multiple scattering (centres) along the track, both upstream and downstream. So, in essence we can conclude with Fig. B.5, which is a replacement of Fig. B.3 for the general case of the MuFit/GEANE fit procedure.

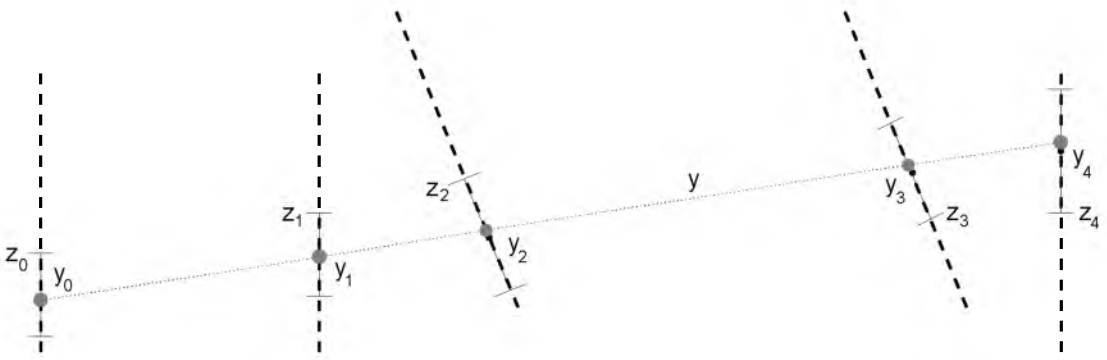

Figure B.5: Detector planes with measured (z_i) and newly predicted (y_i) track points for the next iteration.

Appendix C

$\mathcal{L}^{\mathrm{SM}}$

This appendix deals with various terms of the Lagrangian density associated with the electroweak part of the Standard Model. The expression:

$$\mathcal{L}_{\mathrm{SM}} = i\bar{\Psi}\gamma^{\mu}D_{\mu}\Psi + |D_{\mu}\Phi|^2 - V(\Phi) - \frac{1}{4}B_{\mu\nu}B^{\mu\nu} - \frac{1}{4}W_{\mu\nu,j}W_j^{\mu\nu} - \mathcal{L}_{\mathrm{yuk}}$$

is gauge invariant. Here, $\mathcal{L}_{\mathrm{yuk}}$ depends on the fermion(s) under consideration (see below), and $V(\Phi) = \mu^2|\Phi(x)|^2 + \lambda|\Phi(x)|^4 + \textit{constant}$. The different terms provide us automatically with the interactions and the matching Feynman-diagrams, along with important relations.

Huang[194] proves that it is always possible to go to the so-called unitary gauge, while Anselm[206] more-or-less shows how. Namely, consider that $\Phi(x) = \begin{pmatrix}\phi^+(x)\\ \phi^0(x)\end{pmatrix} = U^0(x)\begin{pmatrix}0\\ 1/\sqrt{2}(v+h(x))\end{pmatrix}$ with $U^0(x) = \mathrm{e}^{iT_j\theta_j(x)/2}$, then this expression is immediately fixed using Eq. (9.4) with the choice $\theta_j(x) = \alpha_{2,j}(x)$, or put differently: the symmetry is spontaneously broken with this choice.

Firstly, the Higgs-potential $V(\Phi)$ leads to the following calculations:

$$\begin{aligned}|\Phi(x)|^2 &= \left(0,\ \tfrac{1}{\sqrt{2}}(v+h(x))\right) U^{0\dagger}(x)U^0(x)\begin{pmatrix}0\\ \frac{1}{\sqrt{2}}(v+h(x))\end{pmatrix}\\ &= \frac{1}{2}v^2 + vh(x) + \frac{1}{2}h^2(x)\end{aligned}$$

and thus

$$|\Phi(x)|^4 = \frac{1}{4}v^4 + v^3h(x) + \frac{3}{2}v^2h^2(x) + vh^3(x) + \frac{1}{4}h^4(x)$$

which together gives:

$$V(\Phi) = -\mu^2h^2(x) - \frac{\mu^2}{v}h^3(x) - \frac{\mu^2}{4v^2}h^4(x) \quad .$$

Taking $m_{\mathrm{H}}^2 = -2\mu^2 = 2\lambda v^2$ finally leads to

$$V(\Phi) = \frac{1}{2}m_{\mathrm{H}}^2h^2(x) + \frac{m_{\mathrm{H}}^2}{2v}h^3(x) + \frac{m_{\mathrm{H}}^2}{8v^2}h^4(x) \quad .$$

From this, one can conclude that the Higgs-potential term gives rise to the mass term of the Higgs-boson, as well as to self-interactions. The strength of these self-interactions is unknown since the Higgs mass is unknown, and $v \approx 246$ GeV[219]. It is quite striking that the strength of the coupling is proportional to the mass of the Higgs-boson.

The next term is the kinematic term $|D_\mu\Phi|^2$ of the Higgs-field

$$D_\mu\Phi = \frac{1}{2\sqrt{2}} \begin{pmatrix} ig_1 B_\mu + ig_2 W_{\mu,3} + \partial_\mu & ig_2 W_{\mu,1} + g_2 W_{\mu,2} \\ ig_2 W_{\mu,1} - g_2 W_{\mu,2} & ig_1 B_\mu - ig_2 W_{\mu,3} + \partial_\mu \end{pmatrix} \begin{pmatrix} 0 \\ v + h(x) \end{pmatrix}$$

and

$$(D_\mu\Phi)^\dagger (D_\mu\Phi) = \frac{g_2^2}{8}\Big(v + h(x)\Big)^2 (W_{\mu,1}^2 + W_{\mu,2}^2) + \frac{1}{8}\Big(v + h(x)\Big)^2 (g_1 B_\mu - g_2 W_{\mu,3})^2 + \frac{1}{2}\Big(\partial_\mu h(x)\Big)^2 .$$

Application of the definitions:

$$T^\pm = \tfrac{1}{\sqrt{2}}(T_1 \pm iT_2)$$

$$\begin{aligned} Z_\mu &= -\tfrac{g_1}{g_Z} B_\mu + \tfrac{g_2}{g_Z} W_{\mu,3} && \text{and } W_\mu^\pm = \tfrac{1}{\sqrt{2}}(W_{\mu,1} \mp iW_{\mu,2}) \\ &\equiv -\sin\theta_W B_\mu + \cos\theta_W W_{\mu,3} && \text{and } g_Z \text{ (or } \overline{g}) = \sqrt{g_1^2 + g_2^2} \end{aligned}$$

leads to

$$\begin{aligned} |D_\mu\Phi|^2 = {} & \frac{1}{2}\Big(\partial_\mu h(x)\partial^\mu h(x)\Big) + \frac{g^{\mu\nu}}{2} m_W^2 (W_\mu^+ W_\nu^- + W_\mu^- W_\nu^+) + \frac{1}{2} m_Z^2 Z_\mu Z^\mu + \\ & + \frac{m_W^2}{v} h(x) g^{\mu\nu} (W_\mu^+ W_\nu^- + W_\mu^- W_\nu^+) + \frac{m_Z^2}{v} h(x) Z_\mu Z^\mu + \\ & + \frac{m_W^2}{2v^2} h^2(x) g^{\mu\nu} (W_\mu^+ W_\nu^- + W_\mu^- W_\nu^+) + \frac{m_Z^2}{2v^2} h^2(x) Z_\mu Z^\mu \end{aligned}$$

with[(1)] $m_W^2 = \frac{1}{4} g_2^2 v^2$ and $m_Z^2 = \frac{1}{4} g_Z^2 v^2$. From this one can conclude that the gauge bosons acquire their mass from the Higgs-field, factually by absorbing three of its four components[213]. On the other hand, the combination

$$A_\mu \equiv \cos\theta_W B_\mu + \sin\theta_W W_{\mu,3} \tag{C.1}$$

with $\cos\theta_W = \frac{g_2}{g_Z}$, $\sin\theta_W = \frac{g_1}{g_Z}$ remains massless and therefore represents the photon. Furthermore, the Higgs-boson couples to the massive gauge bosons with a coupling strength which is, this time, proportional to the mass of the gauge bosons.

The fermions do not acquire their mass in the manner described above. To accomplish this purpose, it has been necessary to introduce a different type of term in the

(1) Expressions like $g^{\mu\nu}(W_\mu^+ W_\nu^- + W_\mu^- W_\nu^+)$ are written like that only for an aesthetical reason, i.e. it shows the symmetry between W^+ and W^-. They can be written as $2W_\mu^+ W^{-,\mu}$ also, of course.

Lagrangian density, namely the Yukawa-interaction. This $\mathcal{L}_{\text{yuk}}$ depends on the type of fermion considered, since fermions can have different positions in the isospin doublet. For the leptons we have:

$$\begin{aligned}\mathcal{L}_{\text{yuk}} &= g_{\text{f}}\left((\overline{\Psi}_{\text{L}}\Phi)\Psi_{\text{f}_{\text{R}}} + \overline{\Psi}_{\text{f}_{\text{R}}}(\Phi^{\dagger}\Psi_{\text{L}})\right) \\ &= \frac{g_{\text{f}}}{\sqrt{2}}\left(\overline{\Psi}_{\text{f}_{\text{L}}}(v+h(x))\Psi_{\text{f}_{\text{R}}} + \overline{\Psi}_{\text{f}_{\text{R}}}(v+h(x))\Psi_{\text{f}_{\text{L}}}\right) \\ &= m_{\text{f}}\overline{\Psi}_{\text{f}}\Psi_{\text{f}} + \frac{m_{\text{f}}}{v}\overline{\Psi}_{\text{f}}h(x)\Psi_{\text{f}}\end{aligned}$$

with $\Psi_{\text{L}} = \begin{pmatrix}\Psi_{\nu_{\text{f}}} \\ \Psi_{\text{f}_{\text{L}}}\end{pmatrix}$ and $m_{\text{f}} = g_{\text{f}}v/\sqrt{2}$. Likewise, for the down-type quarks:

$$\mathcal{L}_{\text{yuk}} = g_{\text{d}}\left((\overline{\Psi}_{\text{L}}\Phi)\Psi_{\text{d}_{\text{R}}} + \text{h.c.}\right) = \overline{\Psi}_{\text{d}}\left(m_{\text{d}} + \frac{m_{\text{d}}}{v}h(x)\right)\Psi_{\text{d}}$$

with $\Psi_{\text{L}} = \begin{pmatrix}\Psi_{\text{u}_{\text{L}}} \\ \Psi_{\text{d}_{\text{L}}}\end{pmatrix}$. On the other hand, it is necessary to go to the conjugate representation for the up-type quarks, using $\overline{\Phi}$ (or $\tilde{\Phi}$, or Φ^{c})$\equiv i\sigma_2\Phi^*$. So, when $\Phi = \begin{pmatrix}\phi^+ \\ \phi^0\end{pmatrix}$, it then follows that $\overline{\Phi} = \begin{pmatrix}\phi^{0^*} \\ -\phi^-\end{pmatrix}$ with $\phi^- = \phi^{+^*}$ and thus

$$\mathcal{L}_{\text{yuk}} = g_{\text{u}}\left((\overline{\Psi}_{\text{L}}\overline{\Phi})\Psi_{\text{u}_{\text{R}}} + \overline{\Psi}_{\text{u}_{\text{R}}}(\overline{\Phi}^{\dagger}\Psi_{\text{L}})\right) = m_{\text{u}}\overline{\Psi}_{\text{u}}\Psi_{\text{u}} + \frac{m_{\text{u}}}{v}\overline{\Psi}_{\text{u}}h(x)\Psi_{\text{u}} \ .$$

Not only has a mass term appeared in the Lagrangian density for the fermions, but also an interaction term with the Higgs boson. Again, the coupling is proportional to the mass, of the fermion this time, so it seems valid to say that massive particles acquire their masses through an interaction with the Higgs field. Since the magnitudes of the Yukawa couplings are unknown, this also implies that the theory does not predict the masses of the fermions. A curious detail is that one obtains the prediction $m_{\text{t}} = 174$ GeV for the choice $g_{\text{t}} = 1$, which in fact could purport a deeper meaning.

All mass terms of the Lagrangian density have now passed in review. So, it is time to see what other information can be obtained from the remaining terms, like:

$$i\overline{\Psi}\gamma^{\mu}D_{\mu}\Psi = i\overline{\Psi}\gamma^{\mu}\partial_{\mu}\Psi + i\overline{\Psi}\gamma^{\mu}\left(ig_1B_{\mu}\frac{Y}{2} + ig_2W_{\mu,j}T_j\right)\Psi \ ,$$

where T_j $(j = 1,2,3)$ does not have an effect on the right-handed component Ψ_{R} (of $\Psi = \Psi_{\text{L}} + \Psi_{\text{R}}$). Inversion of the definitions in Eq. (C.1) and application thereof to the expression between brackets gives, amongst others the two following terms:

$$i\frac{1}{\sqrt{g_1^2+g_2^2}}Z_{\mu}\left(-g_1^2\frac{Y}{2} + g_2^2T_3\right) + i\frac{g_1g_2}{\sqrt{g_1^2+g_2^2}}A_{\mu}\left(\frac{Y}{2} + T_3\right) \ .$$

Because of the relation $Q = T_3 + \frac{Y}{2}$, one can make the identification $e = g_1 g_2 / \sqrt{g_1^2 + g_2^2}$ from which follows $\cos\theta_W = \frac{e}{g_1}$, $\sin\theta_W = \frac{e}{g_2}$, $g_Z = \frac{e}{\sin\theta_W \cos\theta_W}$, and $\tan\theta_W = \frac{g_1}{g_2}$. Use of this knowledge leads to:

$$ieQA_\mu + i\frac{e}{\sin\theta_W \cos\theta_W}\left(\cos^2\theta_W T_3 - \sin^2\theta_W \frac{Y}{2}\right) .$$

Since T_3 does only work on Ψ_{L}, it is often written as $T_{3,\mathrm{L}}$. Taking the Lagrangian density into account, we have now obtained the terms:

$$-e\overline{\Psi}\gamma^\mu Q\Psi A_\mu - g_Z\overline{\Psi}\gamma^\mu(T_{3,\mathrm{L}} - Q\sin^2\theta_W)\Psi Z_\mu .$$

For completeness, it needs to be remarked that $ig_2 W_{\mu,1} T_1 + ig_2 W_{\mu,2} T_2$ becomes $ig_2(W_\mu^+ T_{\mathrm{L}}^+ + W_\mu^- T_{\mathrm{L}}^-)$, or in full:

$$-g_2\overline{\Psi}\gamma^\mu T_{\mathrm{L}}^{\pm}\Psi W_\mu^{\pm} .$$

It is common practice to define currents to which Noether's theorem[195] applies. They are

$$J_{\mathrm{EM}}^\mu = e\overline{\Psi}\gamma^\mu Q\Psi$$

for the electromagnetic current,

$$J_{\mathrm{NC}}^\mu = g_Z\overline{\Psi}\gamma^\mu(T_{3,\mathrm{L}} - \sin^2\theta_W Q)\Psi$$

for the neutral weak current, and

$$J_{\mathrm{CC}}^{\mu,\pm} = g_2\overline{\Psi}\gamma^\mu T_{\mathrm{L}}^{\pm}$$

for the charged weak current. This part of the Lagrangian density can, therefore, be rewritten as:

$$-J_{\mathrm{EM}}^\mu A_\mu - J_{\mathrm{NC}}^\mu Z_\mu - J_{\mathrm{CC}}^{+\mu} W_\mu^+ - J_{\mathrm{CC}}^{-\mu} W_\mu^- .$$

A last remark about this is that the neutral weak current can be written as a V-A interaction, namely by a projection onto the chiral states, i.e.:

$$\begin{aligned} J_{\mathrm{NC}}^\mu &= g_Z\overline{\Psi}\gamma^\mu(T_{3,\mathrm{L}} - \sin^2\theta_W Q)\frac{1-\gamma_5}{2}\Psi + g_Z\overline{\Psi}\gamma^\mu(-\sin^2\theta_W Q)\frac{1+\gamma_5}{2}\Psi \\ &= \frac{g_2}{2\cos\theta_W}\overline{\Psi}(g_{\mathrm{v}}\gamma^\mu - g_{\mathrm{a}}\gamma^\mu\gamma_5)\Psi \end{aligned}$$

with $g_{\mathrm{a}} = T_{3,\mathrm{L}}$ and $g_{\mathrm{v}} = T_{3,\mathrm{L}} - 2\sin^2\theta_W Q$, or:

$$J_{\mathrm{NC}}^\mu = \overline{\Psi}\gamma^\mu(g_{\mathrm{V}} - g_{\mathrm{A}}\gamma_5)\Psi$$

with

$$g_{\mathrm{V}} = \frac{e}{2\sin\theta_W\cos\theta_W}(T_{3,\mathrm{L}} - 2\sin^2\theta_W Q)$$

and

$$g_{\mathrm{A}} = \frac{e}{2\sin\theta_W \cos\theta_W} T_{3,\mathrm{L}} \ .$$

It is clear that this is not a pure V-A interaction since $g_{\mathrm{V}} \neq g_{\mathrm{A}}$.

Lastly, only two terms of the Standard Model Lagrangian density dealing with the free gauge-boson fields remain:

$$-\frac{1}{4} B_{\mu\nu} B^{\mu\nu} - \frac{1}{4} W_{\mu\nu,j} W_j^{\mu\nu} \ ,$$

where the notation $B_{\mu\nu} = \partial_\mu B_\nu - \partial_\nu B_\mu$ and $W_{\mu\nu,j} = \partial_\mu W_{\nu,j} - \partial_\nu W_{\mu,j} + g_2 \varepsilon_{jkl} W_{\mu,k} W_{\nu,l}$ has been adopted. A lot of rewriting and a transition to the fields A_μ, Z_μ and $W_\mu^\pm$ in the end leads to the following expression[194] for the Lagrangian density:

$$\mathcal{L}_{\mathrm{V}} \equiv -\frac{1}{4} B_{\mu\nu} B^{\mu\nu} - \frac{1}{4} W_{\mu\nu,j} W_j^{\mu\nu} \equiv \mathcal{L}'_{\mathrm{free,V}} + \mathcal{L}_{3\mathrm{V}} + \mathcal{L}_{4\mathrm{V}}$$

with $\mathcal{L}'_{\mathrm{free,V}}$ denoting part of the free vector-boson Lagrangian ($\mathcal{L}_{\mathrm{free,V}}$), while $\mathcal{L}_{3\mathrm{V}}$ and $\mathcal{L}_{4\mathrm{V}}$ contain three- and four-vector-boson interactions, respectively. Now,

$$\begin{aligned}
\mathcal{L}'_{\mathrm{free,V}} &= \\
&= -\frac{1}{4}(\partial_\mu B_\nu - \partial_\nu B_\mu)(\partial^\mu B^\nu - \partial^\nu B^\mu) - \frac{1}{4}\sum_{j=1}^{3}(\partial_\mu W_{\nu,j} - \partial_\nu W_{\mu,j})(\partial^\mu W_j^\nu - \partial_\nu W_j^\mu) \\
&= -\frac{1}{4} F_{\mu\nu} F^{\mu\nu} - \frac{1}{4} Z_{\mu\nu} Z^{\mu\nu} - \frac{1}{4} g^{\mu\rho} g^{\nu\sigma} (W^+_{\mu\nu} W^-_{\rho\sigma} + W^-_{\mu\nu} W^+_{\rho\sigma})
\end{aligned}$$

such that

$$\mathcal{L}_{\mathrm{free,V}} = -\frac{1}{4} Z_{\mu\nu} Z^{\mu\nu} - \frac{1}{2} m_Z^2 Z_\mu Z^\mu - \frac{1}{2} W^+_{\mu\nu} W^{-,\mu\nu} - m_W^2 W^+_\mu W^{-,\mu} \ ,$$

where the symmetry between W^+ and W^- has either been shown explicitly or not. In order to build $\mathcal{L}_{\mathrm{free,V}}$, it was necessary to borrow several terms of $|D_\mu \Phi|^2$ and most terms of $\mathcal{L}'_{\mathrm{free,V}}$. Furthermore, the notations $Z_{\mu\nu} = \partial_\mu Z_\nu - \partial_\nu Z_\mu$ and $W^\pm_{\mu\nu} = \partial_\mu W^\pm_\nu - \partial_\nu W^\pm_\mu$ have been adopted in analogy with the familiar electromagnetic field tensor ($F_{\mu\nu} = \partial_\mu A_\nu - \partial_\nu A_\mu$). Lastly, the three- and four-vector-boson interactions become:

$$\begin{aligned}
\mathcal{L}_{3V} = &\frac{ie}{2}(W^+_\mu W^-_\nu - W^+_\nu W^-_\mu)\left(F^{\mu\nu} + \frac{\cos\theta_W}{\sin\theta_W} Z^{\mu\nu}\right) \\
&+ ie(W^+_{\mu\nu} W^{-,\mu} - W^-_{\mu\nu} W^{+,\mu})\left(A^\nu + \frac{\cos\theta_W}{\sin\theta_W} Z^\nu\right)
\end{aligned}$$

and

$$\begin{aligned}
\mathcal{L}_{4V} = e^2 (g^{\mu\rho} g^{\nu\sigma} - g^{\mu\nu} g^{\rho\sigma}) \Bigg(&\frac{1}{2\sin^2\theta_W} W^+_\mu W^-_\nu W^+_\rho W^-_\sigma \\
&+ \left(A_\mu + \frac{\cos\theta_W}{\sin\theta_W} Z_\mu\right)\left(A_\nu + \frac{\cos\theta_W}{\sin\theta_W} Z_\nu\right) W^+_\rho W^-_\sigma \Bigg) \ ,
\end{aligned}$$

which exhibit the surprising artefact that no interactions exist involving the neutral Z^0-bosons and/or neutral photons only.

Appendix D

Muon distributions from the "golden" Higgs decay channel

The figures (Figs. D.1 to D.6) in this appendix serve the purpose of providing a specific insight into (the track parameters of) the muons that originate from the "golden" Higgs decay channel. This decay channel has been analysed in Chapter 11, where Figs. 11.5 and 11.9 already have shown examples of distributions obtained from muon track parameters. In Figs. D.1 to D.6, four distributions are shown for nominal Higgs masses (m_{H}) of 130, 150, 170, 200, 250 and 400 GeV/c^2, respectively. Tables 11.2 and 11.3 present the numbers that correspond to these figures, e.g. how many events are used (for the four-muon invariant mass distribution) of the original sample of 5000 events, for each nominal Higgs mass.

The first distribution of interest is that of the transverse momenta of all muons in the event (shown in the first column of sub-figures in Figs. D.1 to D.6). Since we are studying the Higgs signal only, this implies that four tracks per event should appear in the distribution. However, for every sample of 5.000 events less than 20.000 tracks were used for the distributions shown, because of a minimum transverse momentum cut (at $p_{\mathrm{T}} > 7$ GeV/c) and a cutoff at $p_{\mathrm{T}} < 150$ GeV/c used for convenience.

It is no surprise that the average transverse momentum of a muon increases with an increasingly higher nominal mass of the Higgs bosons. From the distributions, a rough analysis yields the relation: $\langle p_{\mathrm{T}} \rangle \approx c \cdot m_{\mathrm{H}}/5$, with c the speed of light and m_{H} the nominal Higgs boson mass. This relation is very convenient, as it should be used together with the combined muon reconstruction performance shown in Fig. 7.42. Using this information, the following remarks can be made. Firstly, up to about $m_{\mathrm{H}} = 150$ GeV/c^2, the muon reconstruction relies fully on the inner detector. Secondly, given the width of the transverse momentum distributions in the first column of sub-figures, it should be concluded that the combined muon reconstruction plays a role for all Higgs boson masses. It is of particular importance for the mass range $m_{\mathrm{H}} = 150$ – 250 GeV/c^2. Thirdly, the muon spectrometer stand-alone performance becomes crucial at high Higgs boson masses, i.e. about 400 GeV/c^2 and onwards.

The second distribution is presented in a scatter plot (in the second column of sub-figures in Figs. D.1 to D.6). Muons are combined into neutrally charged pairs to

obtain two-muon invariant masses. The mass of one muon pair is then plotted against the mass of the other muon pair. Events are selected whenever a combination of muon pairs passes the invariant mass cuts. This is shown in the scatter plot by a closed contour (or "cross"). Any point inside the contour belongs to a combination of muon pairs that is used to obtain the nominal Higgs mass.

The third distribution is again a representation of two-muon invariant masses (and shown in the third column of sub-figures in Figs. D.1 to D.6), though this time only of those muon pair combinations that were selected by the invariant mass cuts. A resonance peak at about 92 GeV/c^2 is present in all cases, which is due to the on-shell Z boson in the intermediate state, as required by one of the invariant mass cuts. Another bump is found for a nominal Higgs boson mass below the $2m_Z \approx 183$ GeV/c^2 threshold. It is due to the virtual photon γ^*/Z^*. The lower bump has a very sharp lower cutoff, which is caused by the minimum invariant mass cut. There is no fundamental difference between the two-muon invariant mass distributions for Higgs bosons with masses above the $2m_Z$ threshold, since the distributions merely represent the Z resonance peak.

Finally, the fourth distribution (in the fourth column of sub-figures in Figs. D.1 to D.6) corresponds to the four-muon invariant mass of the selected events. It represents the reconstructed Higgs boson mass. The reconstructed width of the resonance peak can be extracted from this distribution when a sufficient amount of Higgs bosons has been detected. Care should be taken while doing this, because the reconstructed distribution exhibits large tails that are due to the reconstruction performance. Part of the low mass tail is also caused by final-state radiation, see Sect. 11.5.1. So, it seems best to apply a Gaussian fit to the bulk of the distribution only. In practice, this means that two standard deviations ($2\sigma_{m_H}$) are taken into account on both sides of the resonance peak, see Sect. 11.5.3. A number of iterations are needed before the measured value of σ_{m_H}, i.e. the reconstructed width, has converged. These values are used for the twelfth row Table 11.3. The plots of the four-muon invariant mass distributions, which are shown in a window of $\pm 6\sigma_{m_H}$ around the nominal mass, are overlaid by a curve that represents the Gaussian fit. This curve is cut off beyond $\pm 2\sigma_{m_H}$. The conclusion is that the tails of the distribution fall outside this curve, indeed.

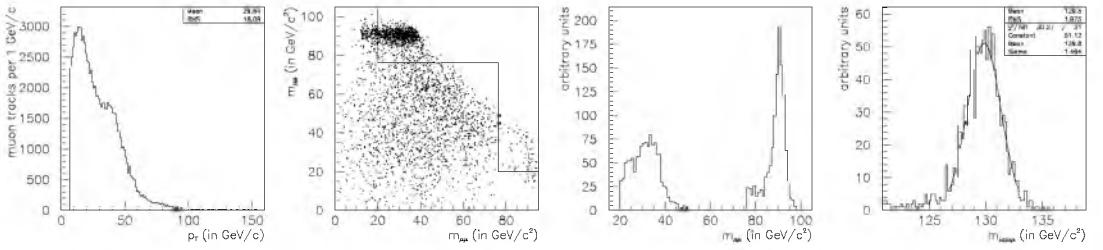

Figure D.1: Transverse momentum, two-muon versus two-muon, two-muon and four-muon invariant mass distributions for a nominal Higgs boson mass of 130 GeV/c^2. *See text for further explanation.*

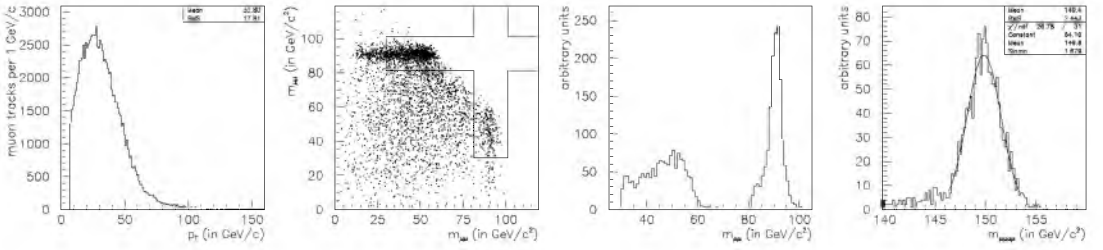

Figure D.2: Same as previous figure, but for a nominal Higgs boson mass of 150 GeV/c^2.

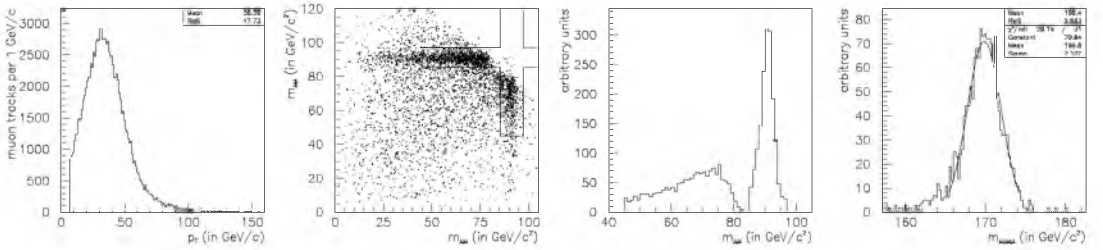

Figure D.3: Same as previous figure, but for a nominal Higgs boson mass of 170 GeV/c^2.

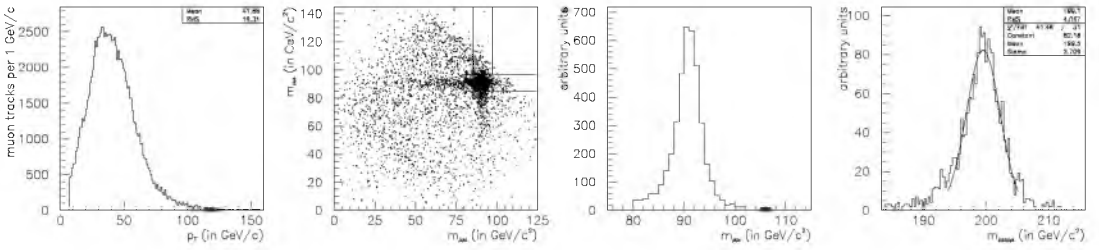

Figure D.4: Same as previous figure, but for a nominal Higgs boson mass of 200 GeV/c^2.

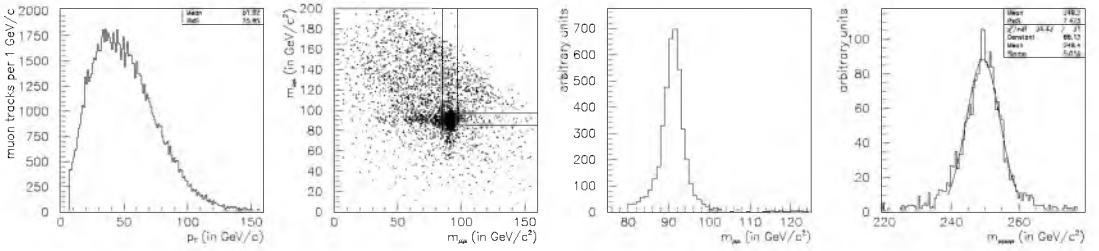

Figure D.5: Same as previous figure, but for a nominal Higgs boson mass of 250 GeV/c^2.

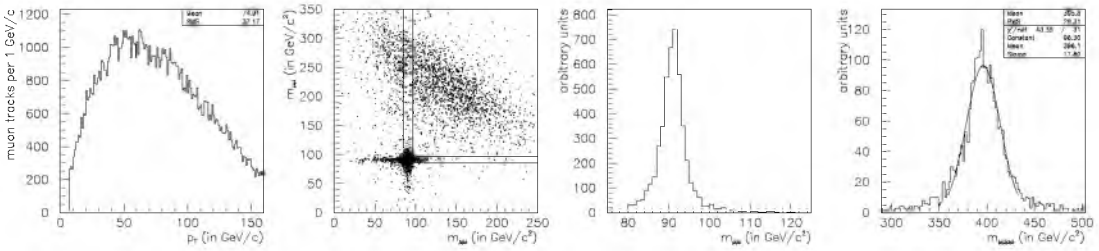

Figure D.6: Same as previous figure, but for a nominal Higgs boson mass of 400 GeV/c^2.

Appendix E

Glossary

ABAN	**Aban**don flag; control of stopping electron treatment (GEANT data card)
AgDATCAR	**Ag**e **dat**a **car**d input; AGE internal subroutine
AGE	**A**TLAS **GE**ANT language; specialized FORTRAN (dialect) interface to GEANT
AgeToCxx	**Age to C**++; C++ generator for AGE structures
AGSBEGM	**Ag**e **s**et **beg**in of **m**odule; AGE internal subroutine
ALICE	**A** **l**arge **i**on **c**ollider **e**xperiment; dedicated detector for heavy-ion collisions at the LHC
ALUMAN	**Alu**minium **man**ganese alloy; by Swiss nomenclature
AMDB	**A**TLAS **m**uon **d**ata**b**ase; text file containing the geometrical description of the muon spectrometer
ANALYSIS	**Analysis**; SLUG data card to control analysis phase (also part of MODE data card)
ANNI	**Anni**hilation flag; control of positron annihilation process (GEANT data card)
ARECON	**A**TLAS **recon**struction; ATRECON steering subroutine to the sub-packages
ATLAS	**A** **t**oroidal **L**HC **a**pparatu**s**; general-purpose detector for the LHC
ATLSGEO	**ATLAS geo**metry; overall volume containing PIPE, INNE, CENT and OUTE (DICE internal module)
ATRECON	**AT**LAS **recon**struction; package containing all ATLAS reconstruction sub-packages
AtreconMain	**ATRECON main** program; name of executable program for ATLAS reconstruction
AXXX	Uniform interface of sub-detector digitized hits to all inner detector pattern recognition tools
BCUTE	**B**remsstrahlung kinetic energy **cut** threshold for **e**lectron; GEANT data card (CUTS 6 data card)

BCUTM	**B**remsstrahlung kinetic energy **cut** threshold for **m**uon; GEANT data card (CUTS 7 data card)
BE	**B**arrel **e**xtra; extension to inner station of muon spectrometer barrel
BEE	**B**arrel **e**xtra **e**ndcap; special chambers in BE station
BI	**B**arrel **i**nner; inner station of muon spectrometer barrel
BIL	**B**arrel **i**nner **l**arge; standard large chambers in BI station
BIR	**B**arrel **i**nner **r**ails; special rails chambers in BI station
BIS	**B**arrel **i**nner **s**mall; standard small chambers in BI station
BKIO	**B**oo**k** **I/O**; to read or write specified bank (SLUG data card)
BM	**B**arrel **m**iddle; middle station of muon spectrometer barrel
BmagAtlas	**B-mag**netic field **ATLAS**; magnetic field information
BMF	**B**arrel **m**iddle **f**oot; special feet chambers in BM station
BML	**B**arrel **m**iddle **l**arge; standard large chambers in BM station
BMS	**B**arrel **m**iddle **s**mall; standard small chambers in BM station
BO	**B**arrel **o**uter; outer station of muon spectrometer barrel
BOF	**B**arrel **o**uter **f**oot; special feet chambers in BO station
BOG	**B**arrel **o**uter **g**-foot; special feet chambers in BO station
BOH	**B**arrel **o**uter **h**-foot; special feet chambers in BO station
BOL	**B**arrel **o**uter **l**arge; standard large chambers in BO station
BOS	**B**arrel **o**uter **s**mall; standard small chambers in BO station
BR	**B**ranching **r**atio; fraction of decays in a certain channel
BREM	**Brem**sstrahlung flag; control of Bremsstrahlung process (GEANT data card)
C++	**C** **p**lus-**p**lus; algorithm inclined, object oriented computer programming language
CBNT	**C**om**b**ined physics **N**-**t**uple; (combined) information of all sub-detectors for use by PAW
CBNTKine	**CBNT kine**matical information; CBNT/ATRECON internal subroutine
cbntMuid	**CBNT Mu**on **id**entification; CBNT/MuID internal subroutine
CBNTTrack	**CBNT track** information; CBNT/ATRECON internal subroutine
CBNTUser	**CBNT user** information and definitions; CBNT/ATRECON external subroutine
CENT	**Cent**ral volume; DICE geometry definition containing all GEANT elements of the calorimeters (also data card)
CERN	**C**onseil **E**uropéen pour la **r**echerche **n**ucléaire; European laboratory for particle physics in Geneva
CERNLIB	**CERN** program **lib**rary; collection of general purpose programs and modules
CMS	**C**ompact **m**uon **s**olenoid; general-purpose detector for the LHC

Cobra	**Co**mbined muon **r**econstruction for **A**TLAS; tool for track fitting during muon reconstruction phases 1 and 2
COFIDR	**Com**mon with segment **fi**t can**di**date **tr**acks; Muonbox internal data structure
COINTR	**Co**mmon with unassociated **in**ner station **tr**ack segments; Muonbox internal data structure
COMCAN	**Com**mon with track **can**didates; Muonbox internal data structure
COMP	**Comp**ton scattering flag; control of Compton scattering process (GEANT data card)
COSUPO	**Co**mmon with reconstructed **su**per **po**ints; Muonbox internal data structure
CSC	**C**athode **s**trip **c**hamber; detection technique used within the ATLAS muon spectrometer
CUTELE	Kinetic energy **cut** threshold for **ele**ctron; GEANT data card (CUTS 2 data card)
CUTGAM	Kinetic energy **cut** threshold for **gam**ma; GEANT data card (CUTS 1 data card)
CUTHAD	Kinetic energy **cut** threshold for charged **had**rons; GEANT data card (CUTS 4 data card)
CUTMUO	Kinetic energy **cut** threshold for **muo**n; GEANT data card (CUTS 5 data card)
CUTNEU	Kinetic energy **cut** threshold for **neu**tral hadrons; GEANT data card (CUTS 3 data card)
CUTS	Container for 10 energy cut thresholds: CUTGAM, CUTELE, CUTNEU, CUTHAD, CUTMUO, BCUTE, BCUTM, DCUTE, DCUTM, and PPCUTM (GEANT data card)
DBOX	Can**di**date tracks of Muon**box** from segment fit; Muonbox external data bank
DCAY	**Decay** flag; control of decays in flight (GEANT data card)
DCUTE	**D**elta ray kinetic energy **cut** threshold for **e**lectron; GEANT data card (CUTS 8 data card)
DCUTM	**D**elta ray kinetic energy **cut** threshold for **m**uon; GEANT data card (CUTS 9 data card)
DEBUG	**Debug**; GEANT data card to control first, last and frequency of events to debug (also part of MODE data card)
DETP	**Det**ector **p**arameter; sets parameters for specified detector (SLUG data card)
DICE	A **d**etector **i**ntegration **c**od**e**; package containing all ATLAS (sub-)detector geometry descriptions
DiceMain	**DICE main** program; name of executable program for ATLAS simulation
DIGI	**Digi**tizations; GEANT data bank for event related information: detector response

DIGITIZATION	**Digitization**; SLUG data card to control digitization phase (also part of MODE data card)
DRAY	**D**elta **ray** flag; control of δ-ray production (GEANT data card)
DSBEqn	Finds **d**ouble precision **s**olution of **b**anded linear **equation**s; GEANE external subroutine (see appendix)
DSBFInv	**D**ouble precision **s**olved **b**anded **f**actorized **inv**erse; GEANE external subroutine (see appendix)
EE	**E**ndcap **e**xtra; external extra station of muon spectrometer endcap (between EI and EM)
EEL	**E**xternal **e**xtra **l**arge; special large chambers in EE station
EES	**E**xternal **e**xtra **s**mall; special small chambers in EE station
EI	**E**ndcap **i**nner; external inner station of muon spectrometer endcap
EIL	**E**xternal **i**nner **l**arge; standard large chambers in EI station
EM	**E**ndcap **m**iddle; external middle station of muon spectrometer endcap
EMC	**E**uropean **m**uon **c**ollaboration; experiment providing the track propagation subroutines of GEANE
EML	**E**xternal **m**iddle **l**arge; standard large chambers in EM station
EMS	**E**xternal **m**iddle **s**mall; standard small chambers in EM station
EO	**E**ndcap **o**uter; external outer station of muon spectrometer endcap
EOL	**E**xternal **o**uter **l**arge; standard large chambers in EO station
EOS	**E**xternal **o**uter **s**mall; standard small chambers in EO station
ErTrak	GEANT **Er**ror propagation: **trak** propagation; GEANE external subroutine (see appendix)
ErTrCh	GEANT **Er**ror propagation: **tr**ack **ch**arged particle; GEANE internal subroutine
ErTrGo	GEANT **Er**ror propagation: **tr**ack propagation **go**; GEANE internal subroutine
EUFilP	GEANT **E**rror propagation: **u**ser **fil**ter for **p**lanes; GEANE external subroutine (see appendix)
EUFilV	GEANT **E**rror propagation: **u**ser **fil**ter for **v**olumes; GEANE external subroutine (see appendix)
EVNT	**Event**; GEANT data bank for event related information: track parameters and vertices
FI	**F**orward/endcap **i**nner; forward inner station of muon spectrometer endcap
FIL	**F**orward **i**nner **l**arge; standard large chambers in FI station
FIS	**F**orward **i**nner **s**mall; standard small chambers in FI station

FM	**F**orward/endcap **m**iddle; forward middle station of muon spectrometer endcap
FML	**F**orward **m**iddle **l**arge; standard large chambers in FM station
FMS	**F**orward **m**iddle **s**mall; standard small chambers in FM station
FO	**F**orward/endcap **o**uter; forward outer station of muon spectrometer endcap
FOL	**F**orward **o**uter **l**arge; standard large chambers in FO station
FORTRAN	**For**mula **tran**slation; mathematically inclined, algorithm based computer programming language
FOS	**F**orward **o**uter **s**mall; standard small chambers in FO station
FWHM	**F**ull **w**idth at **h**alf **m**aximum; measure of curve width
FZLIMIT	**F**ile si**z**e **limit**; controls maximum file size on permanent media (SLUG data card)
G-CALOR	**G**EANT-Monte Carlo program package for the design and analysis of **calor**imeter systems; package for hadronic shower development in GEANT
G-FLUKA	**G**EANT-**Flu**ctuating **ca**scade; package for hadronic shower development in GEANT
G-GHEISHA	**G**EANT-**Geisha** detector simulation program; package for hadronic shower development in GEANT
GEANE	**GEAN**T **e**rror propagation; package for trajectory estimation and error propagation using GEANT
GEANETracking	MuFit external subroutine replacing Muonbox and MuFit functionality using Monte Carlo information (see appendix)
GEANT	**Ge**ometry (or **G**eneration of **e**vents) **an**d **t**racking; detector description and simulation tool
GimeBoun	**Gi**ve **me** MuFit track at **boun**dary; MuFit external subroutine (see appendix)
GimeCand	**Gi**ve **me** Muonbox **cand**idate; MuFit external subroutine (see appendix)
GimeMuEf	**Gi**ve **me** **Mu**onbox **ef**ficiencies; MuFit external subroutine (see appendix)
GimePoin	**Gi**ve **me** super space-**poin**t; MuFit external subroutine (see appendix)
GimeSpec	**Gi**ve **me** MuFit track inside **spec**trometer; MuFit external subroutine (see appendix)
GimeSuPo	**Gi**ve **me** **su**per space-**po**int header information; MuFit external subroutine (see appendix)
GimeVrtx	**Gi**ve **me** MuFit track at **vertex**; MuFit external subroutine (see appendix)
GTMUON	**G**EANT **t**rack **m**uon; GEANT internal subroutine
GTRACK	**G**EANT **track** particle; GEANT internal subroutine
GUSTEP	**G**EANT **u**ser tracking **step**; GEANT external subroutine

GWS	**G**lashow-**W**einberg-**S**alam model; precursor to the minimal Standard Model
HADR	**Hadr**onic process flag; control of hadronic interactions (GEANT data card)
HIGZ	**H**igh-level **i**nterface to **g**raphics and **Z**EBRA;
HIST	**Hist**ogram; controls per detector histogramming (part of MODE data card)
HITS	Detector **hits**; GEANT data bank for event related information: detector intersections
I/O	**I**nput/**o**utput; data storage and retrieval to and from permanent media
IBOX	**I**nput data for Muon**box**; Muonbox external data bank
INNE	**Inne**r volume; DICE geometry definition containing all GEANT elements of the inner detector (also data card)
IPAT	**iPat**Rec definitions; data card for passing parameters to iPatRec
iPatRec	**I**nner detector **pat**tern **rec**ognition; tool for charged track reconstruction in inner detector during phase 1
KINE	Event **kine**matics; GEANT data card and data bank to control event (user) kinematics (also SLUG data card)
LEP	**L**arge **e**lectron **p**ositron collider
LHC	**L**arge **h**adron **c**ollider
LHCb	**LHC b**eauty experiment; dedicated detector for B-physics at the LHC
LOSS	Energy **loss** flag; control of energy loss process (GEANT data card)
LUT	**L**ook-**U**p **T**able; fast and convenient way to correlate results to reference values
M1IP	**M**uon reconstruction phase **1** **i**ntermediate **p**oints; MuFit external data bank (see appendix)
M1TP	**M**uon reconstruction phase **1** **t**rack **p**arameters; MuFit external data bank (see appendix)
M1VX	**M**uon reconstruction phase **1** track parameters at **vertex**; MuFit external data bank (see appendix)
MBCTPIP	**M**uFit **b**acktracking: **c**opy M1**TP** into M1**IP** data bank; MuFit internal subroutine (see appendix)
MBErrTr	**M**uFit **b**acktracking: **err**or matrix **tr**ansformation; MuFit internal subroutine (see appendix)
MBFollow	**M**uFit **b**acktracking: **follow** track; MuFit internal subroutine (see appendix)
MBFVPlan	**M**uFit **b**acktracking: **f**it **v**ertex **plan**es; MuFit internal subroutine (see appendix)
MBFVPToV	**M**uFit **b**acktracking: **f**it **v**ertex from **p**lane **to** **v**ertex; MuFit internal subroutine (see appendix)

MBFVrtx	**M**uFit **b**acktracking: **f**it **vertex**; MuFit internal subroutine (see appendix)
MBIDSeed	**M**uFit **b**acktracking: **i**nner **d**etector **seed**; MuFit internal subroutine (see appendix)
MBOX	**M**uon global track list of Muon**box**; Muonbox external data bank
MBoxCommons	**Muonbox commons**; I/O package for Muonbox common blocks
MBoxRead	**Muonbox read**; MBoxCommons external subroutine
MBoxStore	**Muonbox store**; MBoxCommons external subroutine
MBParCl	**M**uFit **b**acktracking: **par**ameter **cal**culation; MuFit internal subroutine (see appendix)
MBPropag	**M**uFit **b**acktracking: **propag**ate; MuFit internal subroutine (see appendix)
MBPutIP	**M**uFit **b**acktracking: **put** into M1**IP** data bank; MuFit internal subroutine (see appendix)
MBPutVX	**M**uFit **b**acktracking: **put** into M1**VX** data bank; MuFit internal subroutine (see appendix)
MBResVX	**M**uFit **b**acktracking: **res**et M1**VX** data bank; MuFit internal subroutine (see appendix)
MBToBoun	**M**uFit **b**acktracking: **to boun**dary; MuFit internal subroutine (see appendix)
MBVAver	**M**uFit **b**acktracking: **v**ertices **aver**age; MuFit internal subroutine (see appendix)
MBVertex	**M**uFit **b**acktracking: **vertex** definition; MuFit internal subroutine (see appendix)
MBVFCalc	**M**uFit **b**acktracking: **v**ertex **f**it parameters **calc**ulation; MuFit internal subroutine (see appendix)
MC	**M**onte **C**arlo; method to sample distributions randomly
MCAN	Muon reconstruction phase 1 **M**uonbox track **can**didate; MuFit external data bank (see appendix)
MCoToBa	**M**uonbox **co**mmons to **ba**nks; MuFit internal subroutine (see appendix)
MDT	**M**onitored **d**rift **t**ube; detection technique used within the ATLAS muon spectrometer
MFBCanTP	**M**uFit track **f**it: **b**arrel **can**didate **t**rack **p**arameters; MuFit internal subroutine (see appendix)
MFCalcPl	**M**uFit track **f**it: **calc**ulate **pl**anes; MuFit internal subroutine (see appendix)
MFClChis	**M**uFit track **f**it: **c**alculate **chi-s**quare; MuFit internal subroutine (see appendix)
MFCovMa	**M**uFit track **f**it: **cov**ariance **ma**trix; MuFit internal subroutine (see appendix)

MFECanTP	**M**uFit track **f**it: **e**ndcap **can**didate **t**rack **p**arameters; MuFit internal subroutine (see appendix)
MFEIPair	**M**uFit track **f**it: **e**rror matrix **i**ndex **pair**s; MuFit internal subroutine (see appendix)
MFFEstim	**M**uFit track **f**it: **f**it **estim**ate track parameters; MuFit internal subroutine (see appendix)
MFFitMI	**M**uFit track **f**it: **fit** using **m**atrix **i**nversion; MuFit internal subroutine (see appendix)
MFFMeas	**M**uFit track **f**it: **f**it **meas**urements to weights; MuFit internal subroutine (see appendix)
MFGetSP	**M**uFit track **f**it: **get** super **s**pace-**p**oints; MuFit internal subroutine (see appendix)
MFGFit	**M**uFit track **f**it: **G**EANE **fit**; MuFit internal subroutine (see appendix)
MFGTranM	**M**uFit track **f**it: **get tran**sport **m**atrix; MuFit internal subroutine (see appendix)
MFGWeigM	**M**uFit track **f**it: **get weig**ht **m**atrix; MuFit internal subroutine (see appendix)
MFHowTo	**M**uFit track **f**it: **how to** fit; MuFit internal subroutine (see appendix)
MFLD	**M**agnetic **fi**e**ld**; DICE definition of magnetic field strengths (also part of MODE data card)
MFMakEqn	**M**uFit track **f**it: **mak**e **eq**uatio**n**; MuFit internal subroutine (see appendix)
MFMomTr	**M**uFit track **f**it: **mom**entum **tr**ansformation; MuFit internal subroutine (see appendix)
MFPOrder	**M**uFit track **f**it: **p**lanes **order**; MuFit internal subroutine (see appendix)
MFPutTP	**M**uFit track **f**it: **put** into M1**TP** data bank; MuFit internal subroutine (see appendix)
MFSCToSD	**M**uFit track **f**it: from **SC** to **SD**; MuFit internal subroutine (see appendix)
MFSDToSC	**M**uFit track **f**it: from **SD** to **SC**; MuFit internal subroutine (see appendix)
MFSPFilt	**M**uFit track **f**it: **s**pace-**p**oints **filt**er; MuFit internal subroutine (see appendix)
MFTAngle	**M**uFit track **f**it: **t**ransform to **angle**s; MuFit internal subroutine (see appendix)
MFUsePat	**M**uFit track **f**it: **use pat**tern recognition information; MuFit internal subroutine (see appendix)
MISD	**M**uon reconstruction phase 1 **i**nner detector **seed**; MuFit external data bank (see appendix)
Mod.Phys.Lett. A	**Mod**ern **Phys**ics **Lett**ers A: Gravitation, Cosmology, Nuclear Physics, and Particles and Fields

MODE	Detector **mode**; controls specified per (sub-)detector flags: e.g. PRIN, DEBU(G), GEOM, HIST, SIMU(LATION), DIGI(TIZATION), RECO(NSTRUCTION), ANAL(YSIS), and MFLD (SLUG data card)
MOP	**Mo**st **p**robable value; parametrization of most probable energy loss
MSDErrTr	**Mu**Fit **b**acktracking: **see**d **err**or matrix **tr**ansformation; MuFit internal subroutine (see appendix)
MSPP	**M**uon reconstruction phase 1 super **sp**ace-**p**oint; MuFit external data bank (see appendix)
MSUP	**M**uon reconstruction phase 1 **sup**er space-point header information; MuFit external data bank (see appendix)
MUEF	Muon reconstruction phase 1 **M**uonbox **ef**ficiencies; MuFit external data bank (see appendix)
MuFit	**Mu**on **fit**; tool for track fitting during muon reconstruction phase 1 (see appendix)
MUGSetup	**Mu**Fit and **G**EANE **Setup**; MuFit internal subroutine (see appendix)
MuID	**Mu**on **id**entification; tool for track fitting during muon reconstruction phase 2
MULS	**Mul**tiple **s**cattering flag; control of multiple scattering process (GEANT data card)
MUNU	**Mu**on **nu**clear flag; control of muon nuclear interactions (GEANT data card)
Muonbox	**Muon** black **box**; tool for pattern recognition during muon reconstruction phase 1
MuonboxInterface	**Muonbox interface**; C++ wrapper around Muonbox output, i.e. internal data structures
MuonFit	**Muon** track **fit**; MuFit external subroutine (see appendix)
MuonMod	**Muon**box **mod**ule; interface from AGE to Muonbox
NDOF	**N**umber of **d**egrees **o**f **f**reedom; opposite of number of constraints used for statistics
NOMEX®	DuPont registered trademarked material
ntuple	**N-T**uple; set of many elements used for analysis/histogramming
Nucl.Instr.&Meth.	**Nucl**ear **Instr**uments and **Methods** in Physics Research
Nucl.Instr.&Meth.A	**Nucl**ear **Instr**uments and **Methods** in Physics Research Section A: Accelerators, Spectrometers, Detectors and Associated Equipment
Nucl.Phys.B	**Nucl**ear **Phys**ics B: Particle Physics, Field Theory and Statistical Systems, Physical Mathematics
OPAL	**O**mni **p**urpose **a**pparatus for **L**EP; general-purpose detector for LEP

OPTI	**Opti**mize; automatic optimization of geometry (GEANT data card)
OUTE	**Oute**r volume; DICE geometry definition containing all GEANT elements of the muon spectrometer (also data card)
OUTPUT	**Output**; control for writing event data to permanent media (SLUG data card)
PAIR	**Pair** production flag; control of e^-/e^+ pair production process (GEANT data card)
PAW	**P**hysics **a**nalysis **w**orkstation
PAWCOM	**PAW com**mon; storage space for PAW histograms and ntuples
PDG	**P**article **d**ata **g**roup; international collaboration that reviews particle physics
PET	**P**oly**e**thylene-**t**erephthalate; type of plastic
PFIS	**P**hoto**fis**sion flag; control of γ-induced nuclear fission process (GEANT data card)
Phil.Mag.	**Phil**osophical **Mag**azine
Phil.Trans.Roy.Soc.	**Phil**osophical **Trans**actions of the **Roy**al **Soc**iety of London Series A: Mathematical, Physical and Engineering Sciences
PHOT	**Phot**oelectric effect flag; control of photoelectric effect process (GEANT data card)
Phys.Lett.B	**Phys**ics **Lett**ers **B**: Nuclear Physics and Particle Physics
Phys.Rev.	**Phys**ical **Rev**iew of the American Physical Society
Phys.Rev.D	**Phys**ical **Rev**iew **D**: Particles, Fields, Gravitation, and Cosmology
Phys.Rev.Lett.	**Phys**ical **Rev**iew **Lett**ers of the American Physical Society
PIPE	**Pipe** volume; DICE geometry definition containing all GEANT elements of the beam pipe (also data card)
PIXL	**PIXL**Rec definitions; data card for passing parameters to PIXLRec
PIXLRec	**Pixel** steered pattern **rec**ognition; tool for charged track reconstruction in inner detector during phase 1
PPCUTM	**P**air **p**roduction energy **cut** threshold for **m**uon; GEANT data card (CUTS 10 data card)
PRIN	**Prin**t; GEANT data card to control printing (also part of MODE data card)
Proc.Phys.-Math.Soc.	**Proc**eedings of the **Phys**ical-**Math**ematical **Soc**iety of Japan
Proc.Roy.Soc.	**Proc**eedings of the **Roy**al **Soc**iety of London Series A: Mathematical, Physical and Engineering Sciences
PYTHIA	MC generator for multiparticle states induced by hadron interactions ("Priestess' of the Oracle of Delphi in Greece)
QCD	**Q**uantum **c**hromo**d**ynamics
QED	**Q**uantum **e**lectro**d**ynamics

RASNIK	**R**ed **a**lignment **s**ystem **NIK**HEF; relative alignment system using infrared LEDs, special masks and CMOS sensors/CCD cameras
RECOMU	Pattern recognition and **reco**nstruction of **mu**ons; Muonbox internal subroutine
RECONSTRUCTION	**Reconstruction**; SLUG data card to reconstruction phase (also part of MODE data card)
RMS	**R**oot **m**ean **s**quare; measure of curve width (also method to add individual error contributions)
RNDM	**Rand**o**m**; initial random number seed (GEANT data card)
ROAD	**Road** definition; internal data bank for use by all inner detector pattern recognition tools
RPC	**R**esistive **p**late **c**hamber; detection technique used within the ATLAS muon spectrometer
SBOX	Inner station track **s**egments of Muon**box**; Muonbox external data bank
SC	**S**treamer **c**hamber; MuFit internal reference system (see appendix)
SD	**S**ystem of **d**etection; MuFit internal reference system (see appendix)
SIMULATION	**Simulation**; SLUG data card to control simulation in GEANT (also part of MODE data card)
SLBEAM	**SL**UG **beam** interaction; SLUG internal subroutine
SLUG	**S**imulations for **L**HC **u**sing **G**EANT; package around GEANT for managing sub-detector geometries and event formats
SP	**Sp**line; GEANE internal reference system (see appendix)
STACO	**Sta**tistical **co**mbination; tool for track fitting during muon reconstruction phase 2
STOP	**Stop**; data card to stop reading further data cards
SUPOIN	**Super** space-**poin**t calculation; Muonbox internal subroutine
TBOX	**T**rack parameters of Muon**box** along full track; Muonbox external data bank
TDR	**T**echnical **d**esign **r**eport
TGC	**T**hin **g**ap **c**hamber; detection technique used within the ATLAS muon spectrometer
TIME	**Time** information; initialization and termination times (GEANT data card)
ToMCan	Muonbox data banks **to MCAN**; MuFit internal subroutine (see appendix)
ToMSup	Muonbox data banks **to MSUP** and MSPP; MuFit internal subroutine (see appendix)
ToMuEf	Muonbox data banks **to MUEF**; MuFit internal subroutine (see appendix)

TP	**T**echnical **p**roposal
TRAP	**Trap**; controls program behaviour when arithmetic traps occur (SLUG data card)
TRIG	**Trig**ger; total number of events to process (GEANT data card)
TrProp	**Tr**ack **prop**agation for GEANE; EMC external subroutine (see appendix)
TrSCSD	**Tr**ansform from **SC** to **SD**; EMC external subroutine (see appendix)
TrSDSC	**Tr**ansform from **SD** to **SC**; EMC external subroutine (see appendix)
UGINIT	**U**ser defined **G**EANT **init**ialization; SLUG internal subroutine
USE	**Use** data bank; AGE operator for accessing data structures
USER	CBNT **user** definitions; data card for passing parameters to CBNTUser
VBOX	**F**itted track parameters of Muon**box** inside muon spectrometer; Muonbox external data bank
WRICAN	**Wri**te out COM**CAN** information; Muonbox internal subroutine
XKAL	**XKal**man definitions; data card for passing parameters to XKalman
XKalman	E**x**tended **Kalman** filter; tool for charged track reconstruction in inner detector during phase 1
ZEBCOM	**ZEB**RA **com**mon; storage space for ZEBRA structures
ZEBRA	**ZB**OOK+HYD**RA**; data structure management system

Bibliography

[1] C.D. Anderson & S.H. Neddermeyer, *Note on the Nature of Cosmic-Ray Particles*, Phys. Rev. **51**, 884–886 (1937).

[2] C.D. Anderson, *The Positive Electron*, Phys. Rev. **43**, 491–494 (1933).

[3] H. Yukawa, *On the Interaction of Elementary Particles. I*, Proc. Phys.-Math. Soc. Japan **17**, 48–57 (1935).

[4] C.M.G. Lattes, G.P.S. Occhialini & C.F. Powell, *Observations on the Tracks of Slow Mesons in Photographic Emulsions*, Nature **160**, 453–456 & 486–492 (1947).

[5] C.T.R. Wilson, *Condensation of Water Vapour in the Presence of Dust-Free Air and other Gases*, Phil. Trans. Roy. Soc. **A189**, 265–307 (1897).

[6] C.T.R. Wilson, *On an Expansion Apparatus for Making Visible the Tracks of Ionising Particles in Gases and Some Results Obtained by its Use*, Proc. Roy. Soc. **A87**, 277–292 (1912).

[7] J.G. Wilson, *The Principles of Cloud-Chamber Technique*, Cambridge University Press, 1951.

[8] ATLAS Collaboration, *ATLAS Technical Proposal for a General-Purpose pp Experiment at the Large Hadron Collider at CERN*, Technical Report CERN/LHCC/94-43, CERN, Geneva, 15 December 1994.

[9] The LHC Study Group, *Large Hadron Collider, Conceptual design*, Technical Report CERN/AC 95-05, CERN, Geneva, 20 October 1995.

[10] R.P. Shutt (editor), *Bubble and Spark Chambers: Principles and Use*, volume **1**, Academic Press, New York, 1967.

[11] T.J. Ferbel, *Experimental Techniques in High Energy Physics*, volume **64** of *Frontiers in Physics*, Addison-Wesley Publishing Company Inc, Menlo Park, California, 1987.

[12] N. Armenise et al., CHORUS collaboration, *A new search for* $\nu_\mu - \nu_\tau$ *oscillations*, SPSC P254, CERN-SPSC/90-42, Geneva, 15 December 1990.

[13] D.A. Glaser, *Some Effects of Ionizing Radiation on the Formation of Bubbles in Liquids*, Phys. Rev. **87**, 665 (1952).

[14] D.A. Glaser, *Bubble Chamber Tracks of Penetrating Cosmic-Ray Particles*, Phys. Rev. **91**, 762–763 (1953).

[15] D.A. Glaser, *The Bubble Chamber*, in *Handbuch der Physik*, edited by S. Flügge, volume **45**, page 314, Springer-Verlag, Berlin, 1958.

[16] M. Ohayon & P. Petiau, *The Large Heavy Liquid Bubble Chamber "Gargamelle"*, in *Proceedings of the 1966 International Conference on Instrumentation for High Energy Physics*, pages 100–101, (Stanford Linear Accelerator Center, 9-10 September 1966), Stanford University, California, 1966.

[17] Gargamelle Neutrino Collaboration, F.J. Hasert et al., *Observation of Neutrino-like Interactions without Muon or Electron in the Gargamelle Neutrino Experiment*, Phys. Lett. **B46**, 138–140 (1973).

[18] J.W. Keuffel, *Parallel-Plate Counters and the Measurement of Very Small Time Intervals*, in *Minutes of the Meeting at the University of California, Los Angeles, California, 2-3 January 1948 (Proceedings of the American Physical Society)*, Phys. Rev. **73**, 530–542 (1948).

[19] J.W. Keuffel, *Parallel-Plate Counters*, Rev. Sci. Instr. **20**, 202 (1949).

[20] R.W. Pidd & L. Madansky, *Some Properties of the Parallel Plate Spark Counter I*, Phys. Rev. **75**, 1175–1180 (1949).

[21] F. Sauli, *Principles of operation of multiwire proportional and drift chambers (Lectures given in the Academic Training Programme of CERN 1975-1976)*, Technical Report CERN/77-09, CERN, Geneva, 3 May 1977.

[22] J.B. Birks, *The theory and practice of scintillation counting*, volume **27** of *International series of monographs on electronics and instrumentation*, Pergamon Press, Oxford, 1964.

[23] R.C. Fernow, *Introduction to experimental particle physics*, Cambridge University Press, New York, 1986.

[24] J.D. Jackson, *Classical Electrodynamics (Second Edition)*, John Wiley & Sons, New York, 1975.

[25] D.E. Groom et al., Particle Data Group, *Particle Physics Booklet (Extracted from the Review of Particle Physics)*, Springer, July 2000.

[26] Application Software Group, *GEANT, Detector Description and Simulation Tool (CERN Program Library Long Writeup W5013)*, CERN, Geneva Switzerland, march 1995 edition, 1993.

[27] A.P. Colijn, *Measurement of the Tau Lepton Lifetime*, PhD thesis, University of Amsterdam, 30 June 1999.

[28] W.J. Metzger, *Statistical Methods in Data Analysis (A course given in the Spring semester of 1991 and 1992)*, Technical Report HEN-343, University of Nijmegen, The Netherlands, 9 December 1992.

[29] H.P.T. Tolsma, *The Honeycomb Strip Chamber: A two coordinate and high precision muon detector*, PhD thesis, University of Twente, 19 April 1996.

[30] G. Viehhauser, *Detector Physics of the ATLAS precision muon chambers*, PhD thesis, Vienna University of Technology, February 1996.

[31] R. Santonico & R. Cardarelli, *Development of Resistive Plate Counters*, Nucl. Instr. & Meth. **187**, 377-380 (1981).

[32] I. Crotty et al., *The non spark mode and high rate operation of Resistive Parallel Plate Chambers*, Technical Report CERN PPE 93-180, CERN, Geneva, 13 September 1993.

[33] I. Crotty et al., *Further studies of avalanche mode operation of Resistive Parallel Plate Chambers*, Technical Report CERN PPE 94-39, CERN, Geneva, 4 February 1994.

[34] ATLAS Muon Collaboration, *ATLAS Muon Spectrometer Technical Design Report*, Technical Report CERN/LHCC 97-22, CERN, Geneva, 5 June 1997.

[35] S. Majewski et al., *A Thin Multiwire Chamber operating in the high multiplication mode*, Nucl. Instr. & Meth. **217**, 265-271 (1983).

[36] Y. Arai et al., *Timing optimization of Thin Gap Chambers for use in the ATLAS muon endcap trigger*, Nucl. Instr. & Meth. **A367**, 398-401 (1995).

[37] OPAL Collaboration, *The OPAL detector, Technical Proposal*, Technical Report CERN/LEPC/83-4, CERN, Geneva, 16 May 1983.

[38] G. Bencze et al., *Position and timing resolution of interpolating cathode strip chambers in a test beam*, Nucl. Instr. & Meth. **A357**, 40-54 (1995).

[39] E.I. du Pont de Nemours and Company, NOMEX® *is a DuPont registered trademark*, www.dupont.com/nomex

[40] ATLAS Muon Group, *Monitored Drift Tubes Chambers for Muon Spectroscopy in ATLAS*, ATLAS Internal Note MUON-NO-44, CERN, Geneva, 28 June 1994.

[41] M. Livan, *Monitored Drift Tubes in ATLAS*, ATLAS Internal Note MUON-NO-129, Università di Pavia, Italia, 9 September 1996.

[42] HPDT Working Group, *High Pressure Drift Tubes for ATLAS*, ATLAS Internal Note MUON-NO-29, CERN, Geneva, 28 October 1993.

[43] JCC Working Group, *ATLAS Muon detection using Jet Cells*, ATLAS Internal Note MUON-NO-32, CERN, Geneva, 16 February 1994.

[44] HCSC Working Group, *Honeycomb Strip Chambers for the ATLAS Muon Spectrometer*, ATLAS Internal Note MUON-NO-35, CERN, Geneva, 19 January 1994.

[45] CMS Collaboration, *CMS, The Compact Muon Solenoid Technical Proposal*, Technical Report CERN/LHCC/94-38, CERN, Geneva, 15 December 1994.

[46] K. Pretzl, *Summary of the LHCC-Magnet Panel-ATLAS Meeting, December 1, 1992 at CERN*, ATLAS Internal Note TECH-NO-7, CERN, Geneva, 7 December 1992.

[47] C. Daum et al., *Recommendations of the ATLAS Magnet Panel*, ATLAS Internal Note GEN-NO-2, CERN, Geneva, 18 March 1993.

[48] D. Froidevaux & R.St. Denis, *Summary of Physics Comparisons for Various Toroid Options*, ATLAS Internal Note PHYS-NO-013, CERN, Geneva, 21 December 1992.

[49] ATLAS Magnet Project Collaboration/Barrel Toroid Group, *ATLAS Magnet Project TDR Volume 2: ATLAS Barrel Toroid Technical Design Report*, Technical Report CERN/LHCC/97-19, CERN, Geneva, 30 April 1997.

[50] ATLAS Magnet Project Collaboration/End-Cap Toroid Group, *ATLAS Magnet Project TDR Volume 3: ATLAS End-Cap Toroids Technical Design Report*, Technical Report CERN/LHCC/97-20, CERN, Geneva, 30 April 1997.

[51] ATLAS Magnet Project Collaboration/Central Solenoid Group, *ATLAS Magnet Project TDR Volume 4: ATLAS Central Solenoid Technical Design Report*, Technical Report CERN/LHCC/97-21, CERN, Geneva, 30 April 1997.

[52] ATLAS Magnet Project Collaboration/CERN-ATLAS Team, *ATLAS Magnet Project TDR Volume 1: ATLAS Magnet System Technical Design Report*, Technical Report CERN/LHCC/97-18, CERN, Geneva, 30 April 1997.

[53] Boston Muon Consortium, *Pattern Recognition with MDT Chambers*, ATLAS Internal Note MUON-NO-150, Boston University, Boston, 16 April 1997.

[54] ATLAS Level-1 Trigger Group, *ATLAS First-Level Trigger Technical Design Report*, Technical Report CERN/LHCC 98-14, CERN, Geneva, 30 June 1998.

[55] C. Guyot, *The alignment procedure of the chambers of the ATLAS muon spectrometer*, ATLAS Internal Note MUON-NO-45, Saclay, Paris, 28 June 1994.

[56] W. Blum et al., *Development of an Optical Alignment Monitoring System for the ATLAS Muon Spectrometer - Update -*, ATLAS Internal Note MUON-NO-47, Max-Planck-Institut für Physik, Munich, 12 July 1994.

[57] H. Groenstege et al., *The RASNIK/CCD 3D alignment system*, ATLAS Internal Note MUON-NO-63, NIKHEF, Amsterdam, 15 December 1994.

[58] ATLAS Collaboration, *ATLAS Computing Technical Proposal*, Technical Report CERN/LHCC 96-43, CERN, Geneva, 15 December 1996.

[59] M. Stavrianakou, *Production Release 1.0.1*, www.cern.ch/Atlas/GROUPS /SOFTWARE/OO/dist/1.0.1/ReleaseLog

[60] Application Software Group, *ZEBRA, Overview of the ZEBRA System (CERN Program Library Long Writeups Q100/Q101)*, CERN, Geneva Switzerland, February 1995 edition, 1992.

[61] Application Software Group, *HIGZ, High Level Interface to Graphics and Zebra, HPLOT, User's Guide (CERN Program Library Long Writeups Q120 and Y251)*, CERN, Geneva Switzerland, June 1995 edition, 1994.

[62] Application Software Group, *CERNLIB, CERN Program Library Short Writeups*, CERN, Geneva Switzerland, June 1996 edition, 1996.

[63] R.S. DeWolf, *SLUG, Simulations for LHC Using GEANT*, Version 1.07 (outdated) edition, 7 April 1993.

[64] Information Technology Division, *PAW, Physics Analysis Workstation (CERN Program Library Long Writeup Q121*, CERN, Geneva Switzerland, January 1999 edition, 1992.

[65] www.cern.ch/Atlas/GROUPS/SOFTWARE/OO/dist/1.0.1/Applications /DiceMain/src/

[66] www.cern.ch/Atlas/GROUPS/SOFTWARE/OO/dist/1.0.1/Applications /DiceMain/datacard/README

[67] www.cern.ch/Atlas/GROUPS/SOFTWARE/OO/dist/1.0.1/slug/slugcore /slbeam.F

[68] Particle Data Group, *Monte Carlo Particle Numbering Scheme*, pdg.lbl.gov /mc_particle_id_contents.html

[69] G.Z. Molière, *Theorie der Streuung schneller geladener Teilchen I: Einzelstreuung am abgeschirmten Coulomb-Feld*, Z. Naturforsch. **2a**, 133–145 (1947).

[70] G.Z. Molière, *Theorie der Streuung schneller geladener Teilchen II: Merfach- und Vielfachstreuung*, Z. Naturforsch. **3a**, 78–97 (1948).

[71] Information Technology Division, *HBOOK, Statistical Analysis and Histogramming (CERN Program Library Long Writeup Y250)*, CERN, Geneva Switzerland, August 1998 edition, 1995.

[72] T. Davídek & R. Leitner, *Parametrization of the Muon Response in the Tile Calorimeter*, ATLAS Internal Note TILECAL-NO-114, Charles University, Prague, 10 April 1997.

[73] J.E. Moyal, *Theory of Ionization Fluctuations*, Phil. Mag. **46**, 263–280 (1955).

[74] *Software & field maps*, www.cern.ch/Atlas/GROUPS/SOFTWARE/MUON /magfield/mag_software.html

[75] ATLAS Software Group, *DICE-95, a Detector Integration CodE*, ATLAS Internal Note SOFT-NO-014, CERN, Geneva, 22 March 1995.

[76] *Muon Spectrometer Layout - Home Page -*, www.cern.ch/Atlas/GROUPS /MUON/layout_home.html

[77] www.cern.ch/Atlas/GROUPS/SOFTWARE/OO/dist/1.0.1/dice/util/atlsgeo.age

[78] www.cern.ch/Atlas/GROUPS/SOFTWARE/OO/dist/1.0.1/Applications /DiceMain/src/gustep.F

[79] www.cern.ch/Atlas/GROUPS/SOFTWARE/OO/dist/1.0.1/Applications /AtreconMain/src/

[80] ATLAS Collaboration, *ATLAS Calorimeter Performance Technical Design Report*, Technical Report CERN/LHCC 96-40, CERN, Geneva, 13 January 1997.

[81] www.cern.ch/Atlas/GROUPS/SOFTWARE/OO/dist/1.0.1/gcalor/

[82] www.cern.ch/Atlas/GROUPS/SOFTWARE/OO/dist/1.0.1/geant3/gheisha/

[83] www.cern.ch/Atlas/GROUPS/SOFTWARE/OO/dist/1.0.1/geant3/fluka/

[84] www.cern.ch/Atlas/GROUPS/SOFTWARE/OO/dist/1.0.1/Applications /AtreconMain/src/include/zebcom.inc

[85] www.cern.ch/Atlas/GROUPS/SOFTWARE/OO/dist/1.0.1/Applications /AtreconMain/src/include/pawcom.inc

[86] www.cern.ch/Atlas/GROUPS/SOFTWARE/OO/dist/1.0.1/atlsim/atgeant /agsbegm.age

[87] www.cern.ch/Atlas/GROUPS/SOFTWARE/OO/dist/1.0.1/Applications /AtreconMain/datacard/README

[88] V. Innocente & E. Nagy, *Trajectory fit in presence of dense materials*, Nucl. Instr. & Meth. **A324**, 297-306 (1993).

[89] V. Innocente, M.Maire & E.Nagy, *GEANE: Average Tracking and Error Propagation Package (CERN Program Library Long Writeup W5013)*, CERN, Geneva Switzerland, 13 January edition, 1994.

[90] www.cern.ch/Atlas/GROUPS/SOFTWARE/OO/dist/1.0.1/slug/slugmast /uginit.F

[91] A. Poppleton & R. Clifft, *IPATREC: inner detector pattern-recognition and track-fitting*, ATLAS Internal Note SOFT-NO-009, CERN, Geneva, 14 June 1994.

[92] I. Gavrilenko, *Description of Global Pattern Recognition Program (XKalman)*, ATLAS Internal Note INDET-NO-165, CERN, Geneva, 25 April 1997.

[93] L. Vacavant, *PIXLRec, a pattern recognition algorithm based on pixels*, marpix1.in2p3.fr/Pixel/Plan/lv.html

[94] M. Virchaux et al., *Muonbox: a full 3D tracking programme for Muon reconstruction in the ATLAS Spectrometer*, ATLAS Internal Note MUON-NO-198, Saclay, Paris, 1997 (unpublished).

[95] www.cern.ch/Atlas/GROUPS/SOFTWARE/OO/dist/1.0.1/muonbox /muonbox_dice/muon_mod.age

[96] www.cern.ch/Atlas/GROUPS/SOFTWARE/OO/dist/1.0.1/MuonSpectrometer /MuonboxInterface/

[97] www.cern.ch/Atlas/GROUPS/SOFTWARE/OO/dist/1.0.1/MuonSpectrometer /MuonboxInterface/MuonboxInterface/cointr.inc

[98] www.cern.ch/Atlas/GROUPS/SOFTWARE/OO/dist/1.0.1/muonbox/include /muonbox/cofidr.inc

[99] www.cern.ch/Atlas/GROUPS/SOFTWARE/OO/dist/1.0.1/MuonSpectrometer /MuonboxInterface/MuonboxInterface/comcan.inc

[100] www.cern.ch/Atlas/GROUPS/SOFTWARE/OO/dist/1.0.1/MuonSpectrometer /MuonboxInterface/MuonboxInterface/cosupo.inc

[101] www.cern.ch/Atlas/GROUPS/SOFTWARE/OO/dist/1.0.1/muonbox/include /muonbox/ibox.inc

[102] www.cern.ch/Atlas/GROUPS/SOFTWARE/OO/dist/1.0.1/muonbox/include /muonbox/mbox.inc

[103] www.cern.ch/Atlas/GROUPS/SOFTWARE/OO/dist/1.0.1/muonbox/include /muonbox/vbox.inc

[104] www.cern.ch/Atlas/GROUPS/SOFTWARE/OO/dist/1.0.1/muonbox/include /muonbox/tbox.inc

[105] www.cern.ch/Atlas/GROUPS/SOFTWARE/OO/dist/1.0.1/muonbox/include /muonbox/dbox.inc

[106] www.cern.ch/Atlas/GROUPS/SOFTWARE/OO/dist/1.0.1/muonbox/include /muonbox/sbox.inc

[107] www.cern.ch/Atlas/GROUPS/SOFTWARE/OO/dist/1.0.1/Tools/AgeToCxx/

[108] C. Arnault, *AGE (ATLAS GEANT language), Version v1*, ATLAS Internal Note SOFT-NO-020, LAL - Orsay, France, 29 June 1995.

[109] www.cern.ch/Atlas/GROUPS/SOFTWARE/OO/dist/1.0.1/muonbox /muonbox_rec/recomu.F

[110] www.cern.ch/Atlas/GROUPS/SOFTWARE/OO/dist/1.0.1/muonbox /muonbox_rec/supoin.F

[111] www.cern.ch/Atlas/GROUPS/SOFTWARE/OO/dist/1.0.1/muonbox /muonbox_rec/wrican.F

[112] www.cern.ch/Atlas/GROUPS/SOFTWARE/OO/dist/1.0.1/Applications /AtreconMain/src/arecon.F

[113] Offline Software group, *DRAFT ATLAS ATRECON manual (Version 0.015)*, ATLAS Internal Note SOFT-NO-015, CERN, Geneva, 5 September 1994.

[114] www.cern.ch/Atlas/GROUPS/SOFTWARE/DOCUMENTS/ATRECON /atrecon_1.4_evolution.html

[115] A. Poppleton, *MuonIdentification Ntuple (MUID)*, home.cern.ch/~pop/muid /ntuple.html

[116] D. Rousseau, *Combined Physics Ntuple (CBNT)*, home.cern.ch/~droussea /cbnt/cbnt.html

[117] www.cern.ch/Atlas/GROUPS/SOFTWARE/OO/dist/1.0.1/atrecon/cbnt /cbnt.age

[118] www.cern.ch/Atlas/GROUPS/SOFTWARE/OO/dist/1.0.1/atrecon/cbnt /cbnttrack.age

[119] www.cern.ch/Atlas/GROUPS/SOFTWARE/OO/dist/1.0.1/atrecon/cbnt /cbntkine.age

[120] www.cern.ch/Atlas/GROUPS/SOFTWARE/OO/dist/1.0.1/atrecon/cbnt /cbntuser.age

[121] www.cern.ch/Atlas/GROUPS/SOFTWARE/OO/dist/1.0.1/Reconstruction /MuonIdentification/src/cbntMuid.cxx

[122] www.cern.ch/Atlas/GROUPS/SOFTWARE/OO/dist/1.0.1/atlsim/atgeant /agdatcar.age

[123] www.cern.ch/Atlas/GROUPS/SOFTWARE/OO/dist/1.0.1/geant3/erdecks /ertrak.F

[124] www.cern.ch/Atlas/GROUPS/SOFTWARE/OO/dist/1.0.1/geant3/erdecks /ertrgo.F

[125] www.cern.ch/Atlas/GROUPS/SOFTWARE/OO/dist/1.0.1/geant3/erdecks /ertrch.F

[126] www.cern.ch/Atlas/GROUPS/SOFTWARE/OO/dist/1.0.1/geant3/gtrak /gtrack.F

[127] www.cern.ch/Atlas/GROUPS/SOFTWARE/OO/dist/1.0.1/geant3/gtrak /gtmuon.F

[128] T. Sjöstrand, L. Lönnblad & S. Mrenna, PYTHIA *6.2: Physics and Manual*, Technical Report LU TP 01-21, hep-ph/0108264, Lund University, Sweden, 10 April 2002.

[129] T. Hansl-Kozanecka, *Proposal for the organization of the top level of the ATLAS off-line software*, Technical report, LPNHE-IN2P3, Paris 6&7, 1994.

[130] T. Hansl-Kozanecka, *Top level of reconstruction*, ATLAS Internal Transparencies GEN-TR-155, CERN, Geneva, 4 April 1993.

[131] Offline Software Group, *DRAFT ATLAS ATRECON manual (Version 0.015)*, ATLAS Internal Note SOFT-NO-015, CERN, Geneva, 5 September 1994.

[132] ATLAS Collaboration, *ATLAS Detector and Physics Performance Technical Design Report*, Technical Report CERN/LHCC 99-14, CERN, Geneva, 25 May 1999.

[133] G. Battistoni, A. Ferrari & P.R. Sala, *Background calculations for the ATLAS detector and hall*, ATLAS Internal Note GEN-NO-010, INFN, Sezione di Milano, Italy, 13 October 1994.

[134] A. Ferrari & P.R. Sala, *Background rates in the muon system: recent results and the effect of the tungsten plug*, ATLAS Internal Note MUON-NO-090, INFN, Sezione di Milano, Italy, 5 September 1995.

[135] A. Ferrari & P.R. Sala, *Shielding modifications and their influence on the background values*, ATLAS Internal Note MUON-NO-162, INFN, Sezione di Milano, Italy, 31 May 1997.

[136] H. Eichinger & M. Regler, *Review of track-fitting methods in counter experiments*, Yellow report CERN 81-06, CERN, Geneva, 22 January 1981.

[137] W. Krischer, *Note on Pattern Recognition in the ATLAS Muon Chambers*, ATLAS Internal Note MUON-NO-087, CERN, Geneva, 8 August 1995.

[138] O. Palamara & S. Petrera, *Pattern recognition at the second level muon trigger in the ATLAS barrel region*, ATLAS Internal Note DAQ-NO-017, INFN, Italy, 27 December 1994.

[139] Boston Muon Consortium, *A method for a level 2 muon trigger for ATLAS*, ATLAS Internal Note ATL-COM-DAQ-98-019, Boston University, USA, 11 December 1998.

[140] W.T.L.P. Lavrijsen, *COmBined muon Reconstruction for Atlas*, PhD thesis, University of Nijmegen, 22 May 2001.

[141] W.T.L.P. Lavrijsen, *Cobra Overview*, ATLAS Internal Note ATL-SOFT-2001-001, University of Nijmegen, The Netherlands, 16 January 2001.

[142] W.T.L.P. Lavrijsen, *Cobra Performance*, ATLAS Internal Note ATL-SOFT-2001-008, University of Nijmegen, The Netherlands, 1 June 2001.

[143] www.cern.ch/Atlas/GROUPS/SOFTWARE/OO/dist/1.0.1/geant3/erpremc /trprop.F

[144] W. Wittek, *Propagation of errors along a particle trajectory in a magnetic field*, Technical Report EMC/80/15+addendum, CERN, Geneva, November 1980.

[145] W. Wittek, *Transformation of Error Matrices for Different Sets of Variables which describe a Particle Trajectory in a Magnetic Field*, Technical Report EMCSW/80/39, CERN, Geneva, December 1980.

[146] W. Wittek, *Error propagation along a helix*, Technical Report EMCSW/81/18, CERN, Geneva, August 1981.

[147] W.T.L.P. Lavrijsen, private communication.

[148] U. Egede, *Reconstruction and analysis in the ATLAS Inner Detector*, ATLAS Internal Note SOFT-NO-31, Lund University, Sweden, 25 October 1996.

[149] G. Stavropoulos, *Minutes of the INDET Pattern Recognition meeting (8 and 9/1/96).*

[150] I. Gavrilenko, D. Rousseau, J.F. Laporte, *Combined Muon Working Group: STACO*, www.cern.ch/Atlas/GROUPS/PHYSICS/MUON/StatComb.html

[151] R. Bergman, *A Study of Hadronic Punchthrough at the RD5 Experimental Setup*, PhD thesis, University of Nijmegen, 10 April 1997.

[152] J. Dupré, *The Disorder of Things, Metaphysical Foundations of the Disunity of Science*, Harvard University Press, Cambridge, Massachusetts, 1993.

[153] G. Fraser, E. Lillestøl, I. Sellevåg, *The Search for Infinity, solving the mysteries of the Universe*, Reed International Books Ltd, Great Britain, 1994.

[154] N. Solomey, *Het Ongrijpbare Neutrino, Een subatomair detectiveverhaal*, volume **61** of *Wetenschappelijke Bibliotheek van Natuur & Techniek*, Veen Magazines, Amsterdam, 1999.

[155] N.M.E.M.A. Wildiers, *Wereldbeeld en teologie, Van de middeleeuwen tot vandaag*, Standaard Wetenschappelijke Uitgeverij, Antwerpen, 1973.

[156] W.R. Cook & R.B. Herzman, *The Medieval World View, An Introduction*, Oxford University Press Inc, New York, 1983.

[157] J. Dalton, J.-L. Gay-Lussac & A. Avogadro, *Foundation of the Molecular Theory: Comprising Papers and Extracts*, The University of Chicago Press, Chicago, 1906.

[158] D.I. Mendeleev, *The Dependence Between the Properties of the Atomic Weights of the Elements*, formal presentation at the Russian Chemical Society, 6 March 1869.

[159] E. Rutherford, *The Scattering of* α *and* β *Particles by Matter and the Structure of the Atom*, Philosophical Magazine, Sixth Series **21**, 669–688 (1911).

[160] N.H.D. Bohr, *On the Constitution of Atoms and Molecules*, Philosophical Magazine, Sixth Series **26**, 1–26 (1913).

[161] I. Newton, *Philosophiæ Naturalis Principia Mathematica*, Joseph Streater for the Royal Society, London, 1687.

[162] A. Einstein, *Zur Elektrodynamik bewegter Körper*, Annalen der Physik IV. Folge, **Band 17**, 891–921 (1905).

[163] A. Einstein, *Die Grundlage der allgemeinen Relativitätstheorie*, Annalen der Physik IV. Folge, **Band 49**, 769–822 (1916).

[164] J. Clerk Maxwell, *A Dynamical Theory of the Electromagnetic Field (read before the Royal Society on 8 December 1864)*, Phil. Trans. Roy. Soc. **155**, 459–512 (1865).

[165] J. Clerk Maxwell, *A Treatise on Electricity and Magnetism*, Clarendon Press, Oxford, 1873.

[166] C.A. de Coulomb, *Mémoires sur l'électricité et le magnétisme*, Extraits des Mémoires de l'Académie Royale des Sciences de Paris, Bachelier, Paris, 1785-1789.

[167] E. Fermi, *Tentativo di una teoria dell'emissione dei raggi "beta"*, La Ricerca Scientifica IV - **II**(12), 491–495 (1933).

[168] E. Fermi, *Tentativo di una teoria dei raggi* β, Il Nuovo Cimento **11**, 1–19 (1934).

[169] W.E. Pauli, *announcement 16 June at public meeting*, in *Minutes of the Pasadena Meeting, California, 15-20 June 1931 (Proceedings of the American Physical Society)*, Phys. Rev. **38**, 579–592 (1931).

[170] S.L. Glashow, *Partial-symmetries of weak interactions*, Nucl. Phys. **22**, 579–588 (1961).

[171] S. Weinberg, *A Model of Leptons*, Phys. Rev. Lett. **19**, 1264–1266 (1967).

[172] A. Salam, *Weak and Electromagnetic Interactions*, in *Elementary Particle Theory*, edited by N. Svartholm, page 367, Almqvist and Wiksells, Stockholm, 1968.

[173] J.-E. Berendt, *Nada Brahma: De wereld is geluid, Een speurtocht door muziek, wording en bewustzijn*, East-West Publications, Den Haag, 1988.

[174] G. Verkerk (editor), *Binas, Informatieboek vwo/havo voor het onderwijs in de natuurwetenschappen*, Groningen, 1992.

[175] Y. Hara, *Unitary Triplets and the Eightfold Way*, Phys. Rev. **134**, B701–B704 (1964).

[176] S.L. Glashow, J. Iliopoulos & L. Maiani, *Weak Interactions with Lepton-Hadron Symmetry*, Phys. Rev. **D2**, 1285–1292 (1970).

[177] UA1 Collaboration, G. Arnison et al., *Experimental Observation of Lepton Pairs of Invariant Mass around* 95 GeV/c^2 *at the CERN SPS Collider*, Phys. Lett. **B126**, 398–410 (1983).

[178] UA2 Collaboration, P. Bagnaia et al., *Evidence for* $Z^0 \rightarrow e^- e^+$ *at the CERN* $p\bar{p}$ *Collider*, Phys. Lett. **B129**, 130–140 (1983).

[179] UA1 Collaboration, G. Arnison et al., *Experimental Observation of Isolated Large Transverse Energy Electrons with Associated Missing Energy at* $\sqrt{s} = 540$ GeV, Phys. Lett. **B122**, 103–116 (1983).

[180] UA2 Collaboration, M. Banner et al., *Observation of Single Isolated Electrons of High Transverse Momentum in Events with Missing Transverse Energy at the CERN* $p\bar{p}$ *Collider*, Phys. Lett. **B122**, 476–485 (1983).

[181] M.L. Perl et al., *Evidence for Anomalous Lepton Production in* e^+-e^- *Annihilation*, Phys. Rev. Lett. **35**, 1489–1492 (1975).

[182] S.W. Herb et al., *Observation of a Dimuon Resonance at* 9.5 GeV *in* 400 GeV *Proton-Nucleus Collisions*, Phys. Rev. Lett. **39**, 252–255 (1977).

[183] CDF Collaboration, F. Abe et al., *Observation of Top Quark Production in* $p\bar{p}$ *Collisions with the Collider Detector at Fermilab*, Phys. Rev. Lett. **74**, 2626–2631 (1995).

[184] D0 Collaboration, S. Abachi et al., *Observation of the Top Quark*, Phys. Rev. Lett. **74**, 2632–2637 (1995).

[185] S.J. de Jong, *Alles en niets*, inaugurele rede aan de Katholieke Universiteit Nijmegen, 18 maart 1999.

[186] W.K. Heisenberg, *Über den anschaulichen Inhalt der quantentheoretischen Kinematik und Mechanik*, Zeitschrift für Physik **43**, 172–198 (1927).

[187] W.K. Heisenberg, *Die physikalischen Prinzipien der Quantentheorie*, Verlag von S. Hirzel, Leipzig, 1930.

[188] D.H. Perkins, *Introduction to High Energy Physics, Third edition*, Addison-Wesley Publishing Company Inc, 1987.

[189] H.B.G. Casimir, *On the attraction between two perfectly conducting plates*, Proc. Kon. Ned. Akad. Wetensch. **51**, 793–795 (1948).

[190] J.F. Cornwell, *Group theory in physics*, Techniques of physics 7, Academic Press Ltd, London, 1984.

[191] H. Goldstein, *Classical Mechanics, Second Edition*, World Student Series, Addison-Wesley Publishing Company Inc, Menlo Park, California, 1980.

[192] C. Itzykson & J.-B. Zuber, *Quantum Field Theory*, International Series in Pure and Applied Physics, McGraw-Hill Publishing Company, New York, 1980.

[193] J.D. Bjorken & S.D. Drell, *Relativistic Quantum Mechanics*, International Series in Pure and Applied Physics, McGraw-Hill Publishing Company, New York, 1964.

[194] K. Huang, *Quarks, Leptons and Gauge Fields, Second edition*, World Scientific Publishing Co. Pte. Ltd, Singapore, 1992.

[195] E. Noether, *Invariante Variationsprobleme*, Nachrichten v.d. Königl. Gesellschaft der Wissenschaften zu Göttingen, Math.-phys. Klasse **2**, 235–257 (1918).

[196] W.K. Heisenberg, *Über den Bau der Atomkerne I*, Zeitschrift für Physik **77**, 1–11 (1932).

[197] W.K. Heisenberg, *Über den Bau der Atomkerne II*, Zeitschrift für Physik **78**, 156–164 (1932).

[198] W.K. Heisenberg, *Über den Bau der Atomkerne III*, Zeitschrift für Physik **80**, 587–596 (1933).

[199] T. Nakano & K. Nishijima, *Charge Independence for V-Particles*, Progr. Theor. Phys. **10**, 581–582 (1953).

[200] M. Gell-Mann, *Isotopic Spin and New Unstable Particles*, Phys. Rev. **92**, 833–834 (1953).

[201] M. Kobayashi & T. Maskawa, *CP-Violation in the Renormalizable Theory of Weak Interaction*, Progr. Theor. Phys. **49**, 652–657 (1973).

[202] N. Cabibbo, *Unitary Symmetry and Leptonic Decays*, Phys. Rev. Lett. **10**, 531–533 (1963).

[203] C.N. Yang & R.L. Mills, *Conservation of Isotopic Spin and Isotopic Gauge Invariance*, Phys. Rev. **96**, 191–195 (1954).

[204] R.P. Feynman, *The Theory of Positrons*, Phys. Rev. **76**, 749–759 (1949).

[205] A. Cohen, *Field Theory*, in *Proceedings 1996 European School of High-Energy Physics, Carry-le-Rouet, France, 1-14 September 1996*, pages 1–43, CERN 97-03, 2 July 1997.

[206] A. Anselm, *Standard Model*, in *Proceedings 1996 European School of High-Energy Physics, Carry-le-Rouet, France, 1-14 September 1996*, pages 45–47, CERN 97-03, 2 July 1997.

[207] J.M. Frère, *Standard Model of Electroweak Interactions*, 5th Annual Graduate School of Particle Physics, Conference Center De Bron Dalfsen, September 1993.

[208] T.D. Lee & C.N. Yang, *Question of Parity Conservation in Weak Interactions*, Phys. Rev. **104**, 254–258 (1956).

[209] C.S. Wu et al., *Experimental Test of Parity Conservation in Beta Decay*, Phys. Rev. **105**, 1413–1415 (1957).

[210] G. 't Hooft, *Renormalization of massless Yang-Mills fields*, Nucl. Phys. **B33**, 173–199 (1971).

[211] G. 't Hooft, *Renormalizable Lagrangians for massive Yang-Mills fields*, Nucl. Phys. **B35**, 167–188 (1971).

[212] G. 't Hooft & M. Veltman, *Regularization and renormalization of gauge fields*, Nucl. Phys. **B44**, 189–213 (1972).

[213] P.W. Higgs, *Spontaneous Symmetry Breakdown without Massless Bosons*, Phys. Rev. **145**, 1156–1163 (1966).

[214] P.W. Higgs, *Broken symmetries, massless particles and gauge fields*, Phys. Lett. **12**, 132–133 (1964).

[215] F. Englert & R. Brout, *Broken Symmetry and the Mass of Gauge Vector Mesons*, Phys. Rev. Lett. **13**, 321–323 (1964).

[216] R. Laterveer, *Studies in Higgs Physics*, PhD thesis, University of Amsterdam, 10 September 1993.

[217] J. Goldstone, *Field Theories with 'Superconductor' Solutions*, Il Nuovo Cimento **19**, 154–164 (1961).

[218] J. Goldstone, A. Salam, S. Weinberg, *Broken Symmetries*, Phys. Rev. **127**, 965–970 (1962).

[219] J.F. Gunion, H.E. Haber, G. Kane, S. Dawson, *The Higgs Hunter's Guide*, volume **80** of *Frontiers in Physics*, Addison-Wesley Publishing Company, Menlo Park, California, 1990.

[220] European Organization for Nuclear Research, *LEP design report, volume 2: The LEP main ring*, Technical Report CERN/LEP 84-01, CERN, Geneva, June 1984.

[221] M. Jacob (editor), *Large Hadron Collider in the LEP Tunnel*, volume **I-II** of *Proceedings of the ECFA-CERN Workshop*, (Lausanne and Geneva, 21-27 March 1984), CERN 84-10, ECFA 84/85, 5 September 1984.

[222] The LEP2 Team, C. Wyss (editor), *LEP design report, volume 3: LEP2*, Technical Report CERN/AC 96-01 (LEP2), CERN, Geneva, June 1996.

[223] J. Schmitz, *The Microstrip Gas Counter and its application in the ATLAS inner tracker*, PhD thesis, University of Amsterdam, 14 October 1994.

[224] J.H. Mulvey (editor), *Workshop on Physics at Future Accelerators*, volume **I-II**, (La Thuile and Geneva, 7-13 January 1987), CERN 87-07, 4 June 1987.

[225] E. Fernández & G. Jarlskog (editors), *ECFA Study Week on Instrumentation Technology for High-luminosity Hadron Colliders*, volume **I-II**, (Barcelona, 14-21 September 1989), CERN 89-10, ECFA 89/123, 24 November 1989.

[226] G. Jarlskog & D. Rein (editors), *Large Hadron Collider Workshop*, volume **I-III**, (Aachen, 4-9 October 1990), CERN 90-10, ECFA 90/133, 3 December 1990.

[227] The LHC Study Group, *Design Study of the Large Hadron Collider, A multiparticle collider in the LEP tunnel*, Technical Report CERN 91-03, CERN, Geneva, 2 May 1991.

[228] (Evian-les-Bains, 5-8 March 1992), *Towards the LHC experimental programme*, General Meeting on LHC Physics and Detectors, ECFA 92/146, 1992.

[229] R.J. Dankers, *The physics performance of and level 2 trigger for the inner detector of ATLAS*, PhD thesis, University of Twente, 29 October 1998.

[230] M. Spegel, *On the lifetime of proportional counters*, PhD thesis, CERN, Geneva, January 1998.

[231] LHCb Collaboration, *LHCb Technical Proposal: A Large Hadron Collider Beauty Experiment for Precision Measurements of CP-Violation and Rare Decays*, Technical Report CERN/LHCC 98-4, CERN, Geneva, 20 February 1998.

[232] P. Giubellino & E. Crescio, *The ALICE experiment at LHC: A Large Ion Collider Experiment physics prospects and detector design*, Technical Report ALICE-PUB-2000-35, INFN, Torino, 29 January 2001.

[233] The LEP working group for Higgs boson searches, *Search for the Standard Model Higgs Boson at LEP: ALEPH, DELPHI, L3 and OPAL Collaborations*, Technical Report CERN/EP 2001-055, CERN, Geneva, 11 July 2001.

[234] M. Hohlfeld, *On the determination of Higgs parameters in the ATLAS experiment at the LHC*, ATLAS Internal Note ATL-PHYS-2001-004, Institute of physics, University Mainz, 10 May 2001.

[235] CERN Press & Publications, *LEP shutdown postponed by one month*, CERN Press Release 08.00, press.web.cern.ch/Press/Releases00 /PR08.00ELEPRundelay.html, 14 September 2000.

[236] CERN Press & Publications, *LEP shuts down after eleven years of forefront research*, CERN Press Release 14.00, press.web.cern.ch/Press/Releases00 /PR14.00ELEPstop.html, 8 November 2000.

[237] U. Egede, *The search for a standard model Higgs at the LHC and electron identification using transition radiation in the ATLAS tracker*, PhD thesis, Lund University, 16 January 1998.

[238] M. Spira, *QCD Effects in Higgs Physics*, Technical Report CERN-TH/97-068, CERN, Geneva, 19 May 1997.

[239] E. Richter-Wąs et al., *Standard Model and Minimal Supersymmetric Standard Model Higgs rates and backgrounds in ATLAS*, ATLAS Internal Note Phys-NO-048, CERN, Geneva, 17 July 1995.

[240] J.-C. Chollet et al., *Update on latest particle level simulations for* $H \rightarrow ZZ^* \rightarrow 4l^{\pm}$, ATLAS Internal Note Phys-NO-019, CERN, Geneva, 22 May 1993.

[241] E. Richter-Wąs & B.P. Kersevan, *The* $gg, q\bar{q} \rightarrow Z/\gamma^*(\rightarrow ll)b\bar{b}$ *processes: matrix element implementation to* PYTHIA *6.1*, ATLAS Internal Note ATL-PHYS-2001-021, CERN, Geneva, 10 November 2001.

[242] O. Linossier & L. Poggioli, $H^0 \rightarrow ZZ^* \rightarrow 4l^{\pm}$ *channel in ATLAS, Signal reconstruction and Reducible backgrounds rejection*, ATLAS Internal Note Phys-NO-101, CERN, Geneva, 11 April 1997.

[243] P. Clarke, Z^0 *Lineshape Results From LEP-1993*, Technical Report UCL/HEP 94-03, University College London, 12 March 1994.

[244] A. Djouadi, J. Kalinowski & M. Spira, *HDECAY: a Program for Higgs Boson Decays in the Standard Model and its Supersymmetric Extension*, Technical Report CERN-TH-97-254, CERN, Geneva, April 1997.

[245] W.T.L.P. Lavrijsen, *COmBined muon Reconstruction for Atlas*, PhD thesis, University of Nijmegen, 22 May 2002.

[246] S.I. Bityukov & N.V. Krasnikov, *On the observability of a signal above background*, Nucl. Instr. & Meth. **A452**, 518–524 (2000).

[247] S.I. Bityukov & N.V. Krasnikov, *New Physics Discovery Potential in Future Experiments*, Mod. Phys. Lett. **A13**, 3235–3249 (1998).

[248] S.I. Bityukov & N.V. Krasnikov, *Uncertainties and Discovery Potential in Planned Experiments*, in *Advanced Statistical Techniques in Particle Physics*, (Grey College, Durham, 18-22 March 2002), University of Durham, UK, 2002.

[249] I. Narsky, *Estimation of upper limits using a Poisson statistic*, Nucl. Instr. & Meth. **A450**, 444–455 (2000).

[250] C. Onions, *FORTRAN Programming Conventions for ATLAS offline software*, ATLAS Internal Note SOFT-NO-007, CERN, 9 December 1993.

[251] M. Metcalf & J. Reid, *Fortran 90 Explained*, Oxford University Press, Oxford, 1992.

[252] M. Nessi, P. Nevski, G.Poulard, *ATLAS reconstruction banks*, ATLAS Internal Note SOFT-NO-003, CERN, 7 October 1993.

[253] P. Nevski, *Oh-Oh-Ah-Ah-Rh . . . ! Object Oriented Approach for Atlas Reconstruction*, ATLAS Internal Note SOFT-NO-002, CERN, 13 July 1993.

[254] R. Frühwirth, *Application of Kalman filtering to track and vertex fitting*, Nucl. Instr. & Meth. **A262**, 444–450 (1987).

Summary

The prime focus of this thesis is on software for the ATLAS/LHC detector and in particular on the muon track fitting package MuFit. In the second part of the thesis, the "golden" Higgs decay channel is studied in conjunction with the muon reconstruction software to get an impression of its performance. Examining, as a benchmark, this Higgs decay, into four muons exclusively, has the advantage that it allows for a comparison with previous studies. These comparisons provide a particularly firm base for the conclusions that have been drawn and are summarized below.

An important conclusion is that all parts of the software should be well understood. In preparing this thesis, the first production release of the standard ATLAS software was used and found to exhibit unwanted features. Extremely narrow gaps between calorimetric detector volumes were identified as well as unphysical behaviour of the GEANE track propagation. However, the fitting method was proven to be robust, which explains why these effects turn out not to be disastrous for subsequent analyses.

Neglecting several types of background in this analysis, e.g. minimum-bias, pile-up, electronic noise, et cetera, which are claimed not to have a big effect, had the advantage that particle/detector simulation could be sped up, thus resulting in a shorter turnround. This allowed for a more rigorous testing of the fitting method and software itself, which was found to perform as well as its modern competitors. It is believed that this good performance is caused by the underlying pattern recognition package Muonbox and by the usage of well defined, small seeds for track matching with the inner detector. A set of Monte Carlo independent quality requirements has been proposed in order to quantify the performance obtained.

Many methodological improvements with respect to previous benchmark studies were tried. While some had a positive influence on the results, others were found to have a negative effect. Most important is the correct treatment of four-muon signal and background with the corresponding significance. In this thesis, the suggestion is made to use $s = 2(\sqrt{S+B} - \sqrt{B})$ as the proper significance. It is more accurate but also smaller for small numbers of signal events (S) and/or background events (B) than the usual significance $s = S/\sqrt{B}$. It was also found that previous studies treat the irreducible background too optimistically.

Given the uncertainty on the measured signal width, the suggestion is to take an integration window of $m_{\mathrm{H}} - 3\sigma_{m_{\mathrm{H}}}$ to $m_{\mathrm{H}} + 3\sigma_{m_{\mathrm{H}}}$ for all four-muon backgrounds. The

effect is larger than expected, due to the non-uniformity of the four-muon invariant mass of the background. In the end, the conclusion is that the ATLAS collaboration should be able to claim discovery of the Higgs boson after a couple of years, if present in the mass range 130 to 550 GeV/c^2. When only the decay into four muons is considered, it would take several years longer, however, for a Higgs boson mass around 170 GeV/c^2.

The final remark is that future studies should include backgrounds, like minimum-bias, et cetera, to prove their negligible negative influence on the performance of the present muon reconstruction software. K-factors should be used for the calculation of production cross sections both for the signal as well as for the background. These more accurate cross sections have not been used in this thesis since they are not available for the four-muon background. Furthermore, it was argued to include every possible decay chain for the evaluation of the reducible background to understand it better. This knowledge could lead to a relaxation of rejection cuts thereby increasing the measured Higgs signal and its significance.

Samenvatting

Dit proefschrift behandelt computerprogrammatuur voor de reconstructie van muonsporen en de analyse van het verval van Higgsdeeltjes om zodoende aan te tonen dat de ontwikkelde ATLAS-detector gebruikt kan worden voor onderzoek naar de oorsprong van massa. Maar: Wat is massa en waarom is er massa?

Deze existentiële, filosofische vragen worden niet direct beantwoord in dit proefschrift, maar komen in een iets gewijzigde vorm aan bod. Namelijk in de vragen: Hoe fundamenteel is massa en hoe wordt het fenomeen massa gemeten?

Om antwoord te kunnen geven, is het nodig terug te gaan naar het verleden zodat vanuit een historische context de ontwikkelingen gevolgd kunnen worden. De ontdekking van het reductionisme door de oude Grieken is zeer belangrijk geweest. Volgens hun reductionistisch wereldbeeld bestond de wereld uit de vier elementen aarde, lucht, water en vuur. Hoewel deze elementen niet direct de wereld om ons heen lijken te verklaren, is het bijzondere juist de abstractie die erachter schuilgaat. In de loop der tijd is namelijk ontdekt dat er fundamentele bouwstenen bestaan waaruit de natuur is opgebouwd. Hierbij is de kracht van het reductionisme en de abstractie cruciaal gebleven.

Momenteel denken wij dat de wereld om ons heen opgebouwd is uit moleculen en kristallen. Deze zijn op hun beurt opgebouwd uit atomen, die weer bestaan uit een atoomkern, met daarin protonen en neutronen, en enkele zogenaamde schillen van elektronen. Deze elektronen hebben een negatieve elektrische lading, terwijl de protonen een exact even grote positieve lading bezitten. Neutronen zijn, zoals de naam al aangeeft, neutraal geladen.

De atomen vormen stabiele bouwstenen vanwege het feit dat elektromagnetische krachten ervoor zorgen dat de elektronen in hun schillen blijven, terwijl de kern zelf bijeengehouden wordt door de sterke wisselwerking of sterke kernkracht. Daarnaast bestaat ook nog een zwakke wisselwerking of zwakke kernkracht die ervoor zorgt dat af en toe een neutron spontaan vervalt in een proton, een elektron en een anti-elektronneutrino.

Naast deze fundamentele natuurkrachten is er nog de zwaartekracht. Dit is de aantrekkingskracht tussen objecten met massa. Vertaald naar het dagelijks leven betekent dit dat de zwaartekracht verklaart hoe sterk we door de aarde aangetrokken worden en andersom, simpelweg gewicht genoemd. Er wordt echter nog op geen enkele manier verklaard hoeveel massa we hebben, zodat hieruit mag blijken dat massa en

gewicht welbeschouwd twee verschillende zaken zijn. De zwaartekracht geeft daarom geen antwoord op de onderzoeksvraag wat het fenomeen massa behelst.

Voordat naar de onderliggende theorie van de natuurkrachten gekeken wordt, is het nuttig enkele begrippen te behandelen. Allereerst zijn het neutrino en het elektron leptonen en vormen tezamen de zogeheten eerste familie. Bij hoogenergetische botsingen, bijvoorbeeld in het heelal bij sterexplosies, kunnen andersoortige leptonen gevormd worden, zoals het muon en het tau-deeltje. Samen met het muon-neutrino en het tau-neutrino vormen deze de tweede en derde familie. De huidige experimenten tonen aan dat er niet meer dan deze drie families bestaan. Ten tweede is het van belang te weten dat elk elementair deeltje vergezeld gaat van een antideeltje met dezelfde massa maar verder tegengestelde eigenschappen.

Ten derde, het feit dat het neutron relatief eenvoudig in een proton kan vervallen komt omdat deze deeltjes sterk op elkaar lijken, bijvoorbeeld wat betreft massa. Dit wordt isospin-symmetrie genoemd en is fundamenteel aan de theorie. Het proton en neutron vormen de twee componenten van een isospin-doublet. Ten vierde is uiteindelijk uit experimenten gebleken dat protonen en neutronen, alsook de andere hadronen, uit nog fundamentelere bouwstenen bestaan: de quarks. Quarks komen altijd in groepjes van drie of in combinatie met een anti-quark in de natuur voor. Er bestaan zes varianten van quarks: up, down, strange, charm, bottom en top, die eveneens drie families vormen bestaande uit isospin-doubletten.

De theorie die uitgaat van de hiervoor aangegeven bestanddelen is ontwikkeld in de jaren zestig en staat bekend onder de naam Standaard Model. De (wiskundige) essentie van het Standaard Model wordt in deze alinea zeer beknopt beschreven. Als de verwaarloosbare invloed van de zwaartekracht buiten beschouwing wordt gelaten, dan is de interne symmetrie van de Lagrange dichtheid, of Lagrangiaan, gelijk aan $\mathrm{SU(3)_C} \otimes \mathrm{SU(2)_W} \otimes \mathrm{U(1)_Y}$. De hier niet gegeven, zeer complexe, Lagrangiaan is renormaliseerbaar omdat er onder andere geen expliciete massatermen in voor komen. De ijking van de theorie komt voort uit het feit dat het vacuüm een geprefereerde richting aanneemt in de isospinruimte. Deze zogeheten spontane symmetriebreking hangt samen met de introductie van het Higgsveld, dat bestaat uit een isospin-doublet van complexe velden. De geprefereerde richting in de isospinruimte komt overeen met de rotatie van het Higgsveld in diezelfde isospinruimte, die ervoor zorgt dat drie van de vier componenten door andere ijkbosonen opgenomen worden. Wat overblijft is de vierde component, namelijk een massief scalair boson met spin 0: het Higgsdeeltje. De $\mathrm{SU(2)_W} \otimes \mathrm{U(1)_Y}$ symmetrie met de vier bijbehorende massaloze spin 1 ijkbosonen is nu eveneens gebroken, hetgeen resulteert in een $\mathrm{U(1)_{EM}}$ symmetrie met bijbehorend (massaloos) foton terwijl de drie overgebleven ijkbosonen (zeer) massief zijn geworden. Echter de acht typen gluonen die behoren bij de $\mathrm{SU(3)_C}$ symmetrie blijven massaloos. Massa's van fermionen komen juist voort uit Yukawa-termen die de wisselwerking met het Higgsveld beschrijven. De Yukawa-interactie vormt hiermee een renormaliseerbare vervanging voor massatermen in de Lagrangiaan. Terwijl interacties tussen fermionen onderling, dat wil zeggen de fundamentele natuurkrachten, voortkomen uit het principe van minimale substitutie van co-variante afgeleiden, waar-

door deze ijkinvariant worden, omdat hierin de ijkbosonen expliciete interacties aangaan met de fermionen. Op deze manier is door invoering van het Higgsveld een consistente theorie verkregen.

De echte kracht van deze theorie schuilt in het feit dat voorspellingen hieruit daadwerkelijk allemaal zijn waargenomen. Behalve één, namelijk het bestaan van het Higgsdeeltje als manifestatie van het Higgsveld. Metingen van de directe en de indirecte gevolgen van de aanwezigheid van het Higgsveld duiden erop dat het Higgsdeeltje zelf, met grote waarschijnlijkheid, een grotere massa zal hebben dan 115.6 GeV/c^2, waarbij de massa is uitgedrukt in de potentiële energie die vrijkomt bij het verval van het Higgsdeeltje (volgens Einsteins formule $E = mc^2$). Een complicerende factor is de levensduur van het Higgsdeeltje waardoor dit zelf nooit gemeten kan worden, maar slechts alleen de vervalsproducten ervan.

Voor het meten van die vervalsproducten wordt de ATLAS-detector gebouwd samen met de LHC versneller. Deze zal ervoor zorgen dat Higgsdeeltjes uit het vacuüm onttrokken worden. Gezien de relatief grote hoeveelheid energie die vrijkomt voor de vervalsproducten van de Higgsdeeltjes, zullen deze een grote kinetische energie hebben. Dit betekent dat ze een hoog doordringend vermogen hebben in materie en de geladen vervalsdeeltjes onder invloed van een magneetveld slechts minimaal van het rechte pad afwijken. Om toch nauwkeurig te kunnen meten, is het noodzakelijk een bijzonder grote detector te bouwen. De afmetingen van ATLAS kunnen met die van een groot gebouw vergeleken worden. De detector is namelijk 28 meter hoog en breed en heeft een lengte van 46 meter. Alleen door gebruik te maken van bijzonder hoogwaardige technieken kan uiteindelijk over dit soort afstanden een meetnauwkeurigheid van enkele tientallen micrometers worden behaald. Doordat op deze manier de vervalsproducten nauwkeurig genoeg worden gemeten, kunnen kwantitatieve uitspraken worden gedaan over het Higgsdeeltje. Echter, in eerste instantie is het doel het bestaan van het Higgsdeeltje aan te tonen. Mocht dit niet kunnen worden aangetoond, zoals verwacht, dan vormt dit juist een extra uitdaging aangezien er volgens huidige, alternatieve theorieën in dat geval een veelheid aan nieuwe elementaire deeltjes zal zijn.

In dit proefschrift is zeer gedetailleerd gekeken naar bepaalde aspecten van de ATLAS-detector en het verval van Higgsdeeltjes naar vier muonen. Er is berekend dat door dergelijke vervallen het bestaan van het Higgsdeeltje aangetoond kan worden, binnen enkele jaren na de start van het experiment in 2007, zolang de massa ervan tussen 130 GeV/c^2 en 550 GeV/c^2 ligt. Voor een hogere of lagere massa van het deeltje zullen andere vervalskanalen een beduidend groter belang hebben om tot een ontdekking van het Higgsdeeltje te kunnen komen. Tevens is gesuggereerd en beargumenteerd op welke punten de analyse verbeterd is en kan worden ten opzichte van eerdere studies. Wat het signaal betreft, is opgemerkt dat deze voor Higgsmassa's onder de ZZ-limiet hoger is dan bij voorgaande studies en lager voorbij deze limiet, terwijl de meetefficiëntie beduidend beter is. Gezien de onnauwkeurigheid op de gemeten signaalpiek gedurende de eerste jaren is beargumenteerd dat eerdere studies de breedte van deze piek te bekend veronderstellen en daardoor de bijbehorende achtergrond te positief inschatten. Daarnaast werden achtergrondgebeurtenissen te gunstig behandeld

door deze als uniform verdeeld aan te nemen of als te snel afvallend met de vier muon (invariante) massa. Naast een verbeterde behandeling van de niet-reduceerbare achtergrond, wordt in dit proefschrift de aanbeveling gedaan om de reduceerbare achtergrond volledig te simuleren, onder andere om zo alle cascades van mogelijke vervallen naar vier muonen goed in de berekening mee te nemen. Een belangrijke vooruitgang zal er zijn wanneer toekomstige studies voor alle berekeningen de benodigde hogere orde correcties op de gemaakte benaderingen gebruiken. Dit zijn de K-factoren, zodat de statistische significantie van het signaal ten opzichte van de achtergrond beter vast komt te staan. Belangrijk is dan ook de gesuggereerde methode voor een betere behandeling van deze significantie die daarmee betrouwbare voorspellingen doet voor lage aantallen signaal- en achtergrondgebeurtenissen.

Kern van de analyse en dus ook van het proefschrift, is de gebruikte software. De aspecten van de ATLAS-detector die bekeken zijn, zijn feitelijk onderzocht met behulp van de beschikbare software. Die bootst niet alleen de werking van de ATLAS-detector zo nauwkeurig mogelijk na, maar ook de botsing van de protonenbundels en het verval van het Higgsdeeltje in het centrum van de detector. Een kanttekening die hierbij gemaakt moet worden, is dat enkele fysische processen, zoals onder andere temperatuurveranderingen, trillingen en elektronische ruis, ter vereenvoudiging van de simulatie juist niet nagebootst zijn. In onafhankelijke studies is aangegeven dat deze vereenvoudigingen praktisch geen negatieve consequenties hebben voor de eindresultaten.

Zodra de detectorrespons bekend is, zowel voor de nagebootste als voor de echte detector, is reconstructiesoftware nodig die uit deze respons de sporen door de detector berekent van de muonen en andere elementaire deeltjes. De speciaal voor dit proefschrift gemaakte software, namelijk het MuFit pakket, is volledig geanalyseerd. Hierbij zijn ongewenste gedragingen van de standaard software aan het licht gekomen, maar er is vooral aangetoond dat de relatief oude MuFit software net zo goed presteert als de hedendaagse muonspoor-reconstructiepakketten. Met behulp van de MuFit software is aangetoond dat de nauwkeurigheid van de muon impulsmeting in de buurt van de maximaal gewenste afwijking van 1% komt, terwijl de nauwkeurigheid van de Higgsmassameting eveneens een afwijking van 1% dicht benadert. Uit de analyse komen duidelijk gebieden naar voren met een grotere onnauwkeurigheid op de metingen dan die hierboven aangegeven zijn. Kenmerkend aan deze gebieden is dat zich hier relatief veel materiaal bevindt omdat de subdetectoren binnen de muondetector ondersteund moeten worden en ook van allerlei leidingen zijn voorzien. Hoewel er uitermate veel werk verzet is om de negatieve invloed van deze gebieden op het eindresultaat te beperken, is aangetoond dat de huidige software hiermee nog moeilijk om kan gaan. Het belangrijkste advies dat voortkomt uit dit proefschrift is dan ook om de spoorherkenning al in een vroeg stadium te laten profiteren van de meetgegevens in de andere subdetectoren.

Curriculum Vitae

In het dorpje Hintham, vlakbij Rosmalen, kwam ik ter wereld rond middernacht van 10 op 11 januari 1969. Toen op het lijntje getekend moest worden op de kleuterschool in Wageningen diende zich een glansrijke carrière aan, die resulteerde in mijn eerste bril. Daarna volgden er nog vele van de + naar de –. Na de lagere school doorlopen te hebben van 1975 tot 1981 op de Oranjeschool te Bennekom, was al enige interesse in computers en computertechniek te bespeuren. Deze interesse werd gevoed door een lezing over computer graphics in 1978 met als onderwerp het levensecht laten overkomen van een gesimuleerde sinaasappel. Met enthousiasme heb ik daarna de ontwikkelingen gevolgd, startend met een *Sinclair ZX81* aan het begin van mijn middelbare schooltijd. Deze heb ik doorlopen op het Christelijk Streeklyceum te Ede en in 1987 afgesloten met een eigen homecomputer en het behalen van het vwo-diploma. De computers moesten tijdelijk wijken omdat ik natuurkunde ging studeren aan de Katholieke Universiteit Nijmegen (KUN), alwaar ik in 1988 het propedeutisch examen natuurkunde heb behaald. Aangezien het uitvoeren van experimenten en het schrijven van verslagen niet mijn sterkste punt was, koos ik voor de richting theoretische fysica. Vlak voor het einde van mijn studietijd is de overstap naar de studierichting informatische fysica overwogen, aangezien ik alle vakken daarvan reeds gevolgd had. Uiteindelijk ben ik in mei 1993 afgestudeerd in de theoretische hoge-energiefysica bij prof. dr. C. Dullemond. Het onderwerp van mijn scriptie, getiteld *Grassmann algebra*, heeft te maken met het zogeheten bag-model: een beschrijving voor de opsluiting van quarks.

Op 1 juni 1993 ben ik begonnen als AIO op de afdeling experimentele hoge-energiefysica onder begeleiding van prof. dr. E.W. Kittel. De overstap vanuit de theorie was mogelijk doordat ik me niet zozeer met experimentele opstellingen zou gaan bezighouden maar juist met (theoretische) computermodellen. Ik heb mij vier jaar ingezet voor het toekomstige ATLAS-experiment te Genève, voornamelijk met betrekking tot specialistische software voor het reconstrueren van 'track' parameters van muonen in de ATLAS-detector. In de zomer van 1994 ben ik voor dit werk voor twee jaar naar Genève gegaan. Daar heb ik een hoogstnodige cursus Franse taal gevolgd, naast skilessen en cursussen Object Oriented Programming, Analysis & Design. Dit resulteerde in mijn deelname aan het MOOSE project (RD41), waarbij de 'Object Oriented' benadering voor LHC-software onderzocht is.

Als AIO heb ik in een twintigtal voordrachten mijn onderzoek gepresenteerd o.a. op de 6th *Annual Joint Belgium-Dutch-German Graduate School of Particle Physics*

te Witten-Bommerholz in 1994 en de *NIKHEF Jamboree* van 1995. Verder heb ik deelgenomen aan de 5th *Joint Belgium-Dutch-German Graduate School of Particle Physics* te Dalfsen in 1995 en de *European School of High-Energy Physics* te Carry-le-Rouet in 1996 (met een poster). Na mijn verblijf in Genève begon ik met het schrijven van dit proefschrift, maar toen bleek dat de onderliggende softwareketen dusdanig veranderd was, dat de resultaten opnieuw berekend moesten worden. Terwijl de ATLAS-groep hard sleutelde aan de (simulatie)software, kreeg ik de kans actief te worden in het verenigingsleven. Vanaf 1997 ben ik enkele jaren actief geweest als penningmeester en secretaris in het bestuur van het *Nijmeegs Studentenkoor Alphons Diepenbrock*. Zowel tijdens mijn studie als tijdens mijn promotietijd heb ik onderwijservaring opgedaan als werkcollegeassistent bij de vakken lineaire algebra, introductie groepentheorie en statistiek, computer graphics, kwantummechanica en voortgezette mechanica.

In 2000 ben ik opnieuw begonnen met mijn onderzoek, aangezien de benodigde software weer beschikbaar was, om zo het proefschrift te kunnen voltooien. Vanaf januari 2001 combineerde ik dit met mijn baan als ICT-specialist bij het Universitair Centrum Informatievoorziening (UCI) te Nijmegen, waar ik momenteel nog werkzaam ben.

Nawoord

Aan het einde van dit langdurig promotietraject wil ik vele personen bedanken en ook nog uitwijden over enkele zaken. Het zal niet mogelijk zijn iedereen te noemen die ik in de afgelopen (bijna) 10 jaar heb ontmoet. Bedenk dat ik een speciaal plekje in m'n hart voor je heb. Daarom allereerst, voordat ik belangrijke personen vergeet of oversla, iedereen bedankt voor de hulp en de steun die je me hebt kunnen geven.

Toch wil ik de volgende personen met name noemen. Heel bijzonder zijn papa en mama. Corrie en Aat, hoewel jullie een enkele keer hebben gesuggereerd dat stoppen een optie was, is jullie verdere steun altijd zonder aarzeling geweest. Ook jullie zullen getwijfeld hebben maar dan zonder dit te hebben gereflecteerd.

Houd ik een ongeveer chronologisch volgorde aan dan wil ik als eerste prof. Kittel noemen. Wolfram, bedankt voor alle support en vrijheid die je me hebt kunnen geven alsook natuurlijk voor het feit dat je me in eerste instantie voor deze promotieplaats aangenomen hebt. De dagelijkse ondersteuning van Frans wil ik eveneens speciaal vermelden. Vooral de discussies over gemeentelijke politiek hebben me veel geleerd, en jammer genoeg tevens het inzicht gegeven dat alles in deze wereld politiek is. Aan Wim heb ik het te danken dat mijn onderzoek voortgezet kon worden. Daarnaast wil ik je natuurlijk bedanken voor de vele nuttige discussies over ons onderwerp. Kan ik meteen ook de vrijdagmiddag pauze noemen met de vele discussies met promovendi en medewerkers. Adriaan, Carel, Cees, Charles, Ed, Frans, Jaap, Jan, Jan, Peter, Remy, Sijbrand, Thei, Wes en ook Albert, Alex, Aly, Bert, Bram, Dimitry, Dominique, Frank, Hervé, Henric, Jolanda, Jorn, Ljubisa, Martin, Michiel, Miranda, Mirna, Raymond, Rob, Roy, Serguey, Silke, Silvia, we hebben zo met z'n allen wat afgeleuterd. Speciale aandacht voor de ondersteuning door Annelies, Erna, Hanneke, Julie, Marjo en Martine waarmee de interactie op de afdeling wat aardser is geworden.

De tijd in Genève van juli 1994 tot mei 1996 is uitermate intensief geweest. Eerst de trips voor de ATLAS-weken en diners aldaar met onder andere Bob, Cees, Graziano, Harry, Henk, Hoite, Frank en enkele bovengenoemden. Daarnaast het contact met andere ATLAS-software mensen. Elemer, I want to thank you very much for providing me your source code, thereby giving me the kick-start needed to develop the MuFit package. Also special thanks to Traudl for teaching me the basics of track reconstruction and analysis. Merci aussi à Marc, Jean-François, Rob, Laurant et Claude de votre progiciel excellent: Muonbox. Help has been cordially received from Andrea, Gilbert, Leandro, Luc, Patrick and many, many others too.

Mijn verblijf in Genéve is uitzonderlijk enerverend en spannend geweest. Ronald, ik heb je dit geloof ik nog nooit gezegd maar als je die eerste week niet gebleven was dan zou ik nog sneller dan jij weer in Nederland zijn gearriveerd. Voor mij is eveneens van belang geweest dat ik tijdens thuisbezoeken het gevoel bleef houden vrienden te hebben. Esther, Francien, Harry, Philip, Pieter, Rian en m'n hele familie wil ik hiervoor bedanken. CERN and Geneva do not only mean work to me but also entertainment. Of the Softball Club, I only remember Steve and my surprisingly bad pitching. Aber, ich habe zum Glück Volleyball gespielt für den ich Thomas, Britta, Georg, Frank, Ornella und allen anderen danken möchte. Das Kanufahren mit Silvia, Alex, Georg, Marko, Werner und allen weiteren Österreichern ist immer in meinem Gedächtnis, obwohl ich nie ihre Sprache erlernen werde. Going out in Geneva and to the movies has been very enjoyable with Aaron, Chris, Els, Esther, Gerhard, Gustaaf, Jayant, Joel, Joshua, Marcel, Monty, Sandra, Tasja, Wenwen and some dutch people mentioned already before. Les leçons françaises sont devenues amusantes dû à la participation d'Anton, Claudio, Martin et Susanna. The latter, I also met at the choir, which led to a joint holiday in Norway together with Jens, Yvonne and Silvia. At the Ski Club, I have met Michal and Jane. Our days together have been many and joyful, but what not has to be did not become, as it should be. Le temps de dépense avec d'autres non physiciens à ětě trěs plaisant comme je veux mentionner particulièrement Maggie, Jacqueline, Ricardo, Deborah et Erco. Finally, I want to thank Jacqueline, Joëlle, Kathy, Kees, Muriel, Wim and many others for making the graduate schools worthwhile to visit.

Relating to work as well has been the importance of joining the MOOSE project, for which I want to thank in particular Kors, RD, Alan and Roger. For giving me the opportunity of joining the tube measurement facility, I want to thank Frank and the Austrians.

Eind 1996, na terugkomst in Nederland, kostte me het moeite hier weer gewend te raken, bijvoorbeeld aan de alom heersende zelfgenoegzaamheid. Speciaal daarom wil ik Corine bedanken omdat je, samen met je vriendengroep, ervoor zorgde dat ik me weer positiever ging opstellen. Daarnaast wil ik aandacht schenken aan die vrienden die ik al eerder heb genoemd en die nog altijd voor me klaar stonden.

De afgelopen jaren in Nederland is er veel gebeurd waarbij, gedurende de jaren 1997, 1998 en 1999, vooral het verenigingsleven centraal heeft gestaan. Van DVO wil ik de groep noemen met wie ik al jaren met plezier en wisselend succes samenspeel, namelijk Arjan, Carla, Aleida, René, Martin, Erik, Sandra, Wilbert, Agnes, Inge, Eelco, Jan Frans, Ilona, Matthijs en Nienke. Mijn twee NSKAD bestuursjaren met Anita, Erwin, Grietje, Hanneke, Henrike, Jochem, Maarten, Mechteld, Patricia, Patricia, Philipp, Pieter, Simone en Thorsten hebben me bijzonder veel nuttige bagage voor het dagelijks leven verschaft. Daarnaast wil ik alle penningmeesters en controleurs noemen met wie ik heb mogen samenwerken, namelijk Marc, Marcel, Dirk, Desirée, Daniëlle, Patrick, Christiaan en ook Patricia en Pieter zal ik wederom noemen. Maar natuurlijk heb ik ook goede herinneringen aan de overige honderden (oud-) koorleden, waaronder Annelies, Henk, John, Jonathan, Julika, Kirsten, Marcus,Marijn,

Patrick, Piet, Sander, Steven, Tineke, et cetera. Verder wil ik het enorme plezier bij ODEON vermelden met dank aan de ODEON-leden.

Het aarden in Nederland is tevens bespoedigd door het zeer plezierige samenwonen in 1997 en 1998 aan de Sint Annastraat met dank aan m'n oud-huisgenoten Roel, Frank, Walter, Benno, Janneke, Marijn, Judith, Marie-Claire en Jonas. In talloze gesprekken met Peter, Anne-Marie, Paul en Ton heb ik mijn (spraak)vermogens leren relativeren, terwijl ik mijn huidige baan zelfs aan de laatste te danken heb. Zodat mij dit brengt bij m'n huidige collega's bij het UCI. Het OPUS-traject met Arno, Jean, Marijn, Martijn, Tim en René is een absoluut succes geweest dat heeft geleid tot een prettig samenwerken met m'n CODI-sectiegenoten Jan, Willy, Inge, Bård, Gaston, Ulrich en de overige UCI-ers sinds 2001. Jeroen, jou wil ik nog speciaal bedanken voor je inzet en enorme hulp bij het maken van het plaatje op de kaft.

Het kan geen toeval zijn geweest, Rob, dat ik je weer op zo'n bijzondere manier in Genève ben tegengekomen. Opnieuw wil ik jou, Nadia, Marco, Danny, Virgil en Mieke vragen mijn keuze te respecteren alle tijd in m'n studie te hebben gestoken. Bijzonder vind ik ook Jan, Jolette, Mirjam en Ton, Marianne, Ronald, Annemieke, Cris dat jullie me hebben opgenomen in jullie gezinnen. Niemand zal zoveel van het proefschrift hebben meegemaakt als Patricia. Onze tijd samen is van zo'n grote waarde dat ik dat nooit zal (willen) vergeten. Met het promotiefeest en toekomstige inspanningen kan ik proberen datgene goed te maken waaraan ik de afgelopen jaren niet ben toegekomen. Ter afsluiting wil ik zeggen dat ik dit absoluut nooit meer zal doen. Hierbij eindigt het laatste proefschrift dat ik ooit zal hebben geschreven!

Stellingen

behorende bij het proefschrift

Muon tracks through ATLAS

1

Als herhaling de kracht is van de boodschap, dan spreekt een stotteraar wel heel krachtige taal. *(okt. 2000)*

2

De uitdaging is het overwinnen van de angst voor het nieuwe. *(apr 1994)*

3

Actieve en passieve leden: de overeenkomst is dat beiden van mening zijn dat activiteit uit de ander moet voortkomen. *(vrij naar Bazuin nr 9, verenigingsblad Door Vriendschap Omhoog, 22e jaargang, apr 1999)*

4

Niemand kan iets níet leren, hoogstens 't niet proberen. *(feb. 1995)*

5

Elke actie heeft tenminste twee reacties tot gevolg. *(sep. 1995)*

6

Tijdsbesef bestaat slechts door de selectiviteit van ons geheugen. *(jun. 1995)*

7

Alleen een patroonherkenning die alle detectoronderdelen integraal benut, zal beter kunnen presteren dan de huidige, op subdetectoren gebaseerde, reconstructiemethoden. *(dit proefschrift)*

8

Gebruik van de theoretische signaalpiek-breedte voor bepaling van het massa-integratiegebied geeft een te lage schatting van het aantal

achtergrondgebeurtenissen. *(dit proefschrift)*

9

Significantie- en signaalbepaling, zoals bij bestaande experimenten, aan de hand van een aantal gemeten gebeurtenissen en een schatting van het aantal achtergrondgebeurtenissen is fundamenteel fout bij geplande experimenten. *(dit proefschrift)*

10

Met het Higgsveld is de ether teruggebracht in de fysica. *(prof dr S. de Jong, dagblad Trouw d.d. 5 juni 2001, dit proefschrift)*

11

Bloemen zijn mooi; voor die schoonheid zijn echter hun wortels fundamenteel. *(vrij naar 'Toepassingen zijn belangrijk, maar hun oorsprong is fundamenteel', prof dr E.W. Kittel, Smoelenboek 1994 studievereniging Marie Curie)*

12

Omdat computers sneller printen dan dat mensen schrijven, zal verdere automatisering nóg meer informatie op papier voortbrengen. *(jul. 2000)*

13

Een interactief computerprogramma behoedt je niet voor je fouten, een mens daarentegen soms wel. *(jun. 1995)*

14

Sociaal begaafd zijn is openstaan voor andere communicatievormen. *(mei 1998)*

15

De grootte van de fles doet vermoeden dat één theelepel van het afwasmiddel Dreft niet volstaat voor de hele vaat. *(mrt. 1998)*

Erik Joost Visser, Nijmegen, 21 maart 2003

(deze stellingen vormen geen onderdeel van mijn openbare verdediging)